Design, Development and Characterisation of a Building Integrated Photovoltaic Smart Window System for Electricity Generation and Adaptive Daylighting Control

Xiao Liu

BEng, MSc

Faculty of Engineering

University of Nottingham

Thesis submitted for the degree of Doctor of Philosophy

April 2021

Abstract

Global concerns over climate change and ever-increasing energy demand have led to a growing interest in developing renewable energy technologies. Building Integrated Photovoltaic (BIPV) window, which is conventionally designed by incorporating a semi-transparent thin film solar cell or evenly spaced crystalline-silicon (c-Si) solar cells between two layers of glass, is a promising technology to generate electricity and reduce cooling demands in buildings. In this thesis, an innovative BIPV smart window system where an optically switchable thermotropic membrane is laminated with a c-Si solar cell layer and glass covers has been proposed. The thermotropic membrane layer can switch between a transparent and light-scattering state as its temperature changes; in the meanwhile, a proportion of the scattered solar radiation is trapped in the window and redirected onto the solar cell surfaces for electricity generation. Compared with conventional BIPV windows, this smart window has the potential to offer better control of the daylight transmitted into building spaces as well as higher electrical power outputs. The concept is new, and findings regarding the window performance have not been reported in the literature. To prove this concept, in this thesis, a comprehensive research including prototype design, development and characterisations has been carried out:

(1) The system was preliminarily designed and fabricated with the aid of a simplified optical model where the thermotropic membrane layer was assumed as a Lambertian reflector with no angular dependence. The thermotropic membrane was made of a thermo-sensitive natural polymer at relatively low cost, named Hydroxypropyl Cellulose (HPC), and a gelling agent with good thermal stability, named Gellan Gum type F (GGF).

(2) The thermotropic membrane was further characterised in terms of angular scattering distribution by using an optical modelling technique, which combines the Inverse Adding-Doubling (IAD) method, Double-Integrating-Sphere (DIS) spectral measurement and Monte-Carlo (MC) ray-tracing method. This IAD-MC optical model is firstly reported and can be applied to the parametric design and optimisation of smart windows based on anisotropic scattering materials.

(3) The thermotropic membrane was optimised to have a transition temperature of 31°C and a solar transmittance modulation of 76%. The optimised smart window was experimentally characterised under both controlled laboratory conditions and dynamic outdoor environmental conditions.

(4) The smart window when applied in buildings was evaluated by using EnergyPlus, a validated whole-building energy simulation program. It was found that applying the smart window could potentially reduce the annual energy consumption by 39.0% and improve the luminous environment of a cellular office under the UK climatic condition, as compared with using an ordinary BIPV window.

Acknowledgement

I am fortunate to have met many people who encouraged and helped me on the journey of my PhD study. The gratitude I feel for them could never be expressed properly in words.

First and foremost, I am deeply grateful to my supervisor Prof. Yupeng Wu for his guidance and tremendous support at every stage of this research project. He taught me how to be a good researcher and make things possible. He encouraged me to face challenges with confidence and ingenuity and keep on going. No matter I went fast or slow, he was always right there to help me. I would also like to thank my other supervisors, Dr. Xianghui Hou and Prof. Hao Liu, for their professionalism, immense knowledge and inspiration. The journey through all the successes and struggles would not have been possible without their help.

My heartfelt thanks also go to all the staffs and colleagues in the Low Carbon Energy and Technologies (LCERT) Research Group and specially Dr. Robin Wilson, Dr. Yanyi Sun, Dr. Xin Liu, Dr. Jan-Frederik Flor, Dr. Marina Aburas, Dr. Hao Gao, Mr. Manlio Salas Castillo, Mr. Kun Du, Ms. Xue Li, Ms. Dingming Liu for their help and invaluable suggestions for my PhD work.

Many thanks to the PhD studentship from the Faculty of Engineering, the University of Nottingham and the funding from the China Scholarship Council.

Finally, I would like to extend my appreciation to my parents for their unwavering support and belief in me. I will never forget the sacrifices my mother Xuyan Zhou and my father Jianxuan Liu made over the past four years. It was their love that helped me not to lose myself and give up. Thanks to my cousin Zhouran Zheng, my good friend Moxi Xu and my landlord Dr. Zhongsheng Wang, from whom I received a lot of care during the writing of this thesis. My sincere gratitude also goes to my grandmother, who passed away during the coronavirus pandemic period. Yet I know that she is watching me with great pride. Thanks to God.

Table of Contents

List of Publications

Journal publications

- **Liu, X.** and Wu, Y., 2021. Experimental characterisation of a smart glazing with tuneable transparency, light scattering ability and electricity generation function. Applied Energy, 303, p.117521.

- **Liu, X.** and Wu, Y., 2021. Design, development and characterisation of a Building Integrated Concentrating Photovoltaic (BICPV) smart window system. Solar Energy, 220, pp.722-734.

- **Liu, X.** and Wu, Y., 2021. Monte-Carlo optical model coupled with Inverse Adding-Doubling for Building Integrated Photovoltaic smart window design and characterisation. Solar Energy Materials and Solar Cells, 223, p.110972.

- **Liu, X.**, Wu, Y., Hou, X. and Liu, H., 2017. Investigation of the optical performance of a novel planar static PV concentrator with Lambertian rear reflectors. Buildings, 7(4), p.88.

- Knott, A., **Liu, X.**, Makarovskiy, O., O'Shea, J., Tuck, C. and Wu, Y., 2019. Design and optical characterisation of an efficient light trapping structure for dye-sensitized solar cell integrated windows. Building Simulation (Vol. 12, No. 1, pp. 41-49). Tsinghua University Press.

- Sun, Y., Liu, X., Ming, Y., **Liu, X.**, Mahon, D., Wilson, R., Liu, H., Eames, P. and Wu, Y., 2021. Energy and daylight performance of a smart window: Window integrated with thermotropic parallel slat-transparent insulation material. Applied Energy, 293, p.116826.

List of Figures

List of Tables

Nomenclature

A	Area (m^2)
A_w	Window aperture surface area (m^2)
C_g	Geometric concentration ratio
C_e	Optical concentration ratio
D	Distance (m)
D_τ	Relative spectral distribution of illuminant D65
d	Thickness (m)
d_s	Thickness of substrate (m)
d_j	Thickness of the glass or material layer *j* (m)
$F(\theta)$	Normalised angular scattering intensity (sr^{-1})
G	Irradiance (W/m^2)
G_{ref}	Irradiance on the reference PV cell (W/m^2)
$G_{sim}(\theta)$	Simulated detected irradiance at a specific scattering angle (W/m^2)
$G_{exp}(\theta)$	Measured detected irradiance at a specific scattering angle (W/m^2)
G_{pv}	Global solar irradiance on solar cells (W/m^2)
G_w	Global solar irradiance on window outside surface (W/m^2)
G_i	Normal incident light intensity (W/m^2)
g	Anisotropy factor of thermotropic layer
h	Hour angle (^{o})
I_{sc}	Short-circuit current (A)
$I_{sc,ref}$	Short-circuit current of reference PV module (A)
k_s	Extinction coefficient of substrate
k_j	Thermal conductivity of the glass or material layer *j* ($W/(m\cdot K)$)
N	Day number
L	Latitude (^{o})
n	Refractive index
n_{air}	Refractive index of air
n_{glass}	Refractive index of glass
n_s	Refractive index of substrate
P_m	Maximum power output (W)
P_{pv}	Power output from the BIPV window (W)
$P(\theta)$	Single-scattering phase function

R_t	Total reflectance of thermotropic laminated glazing unit
R_{sub}	Directional-hemispherical reflectance of substrate
R_{se}	External surface resistance ((m^2·K)/W)
R_{si}	Internal surface resistance ((m^2·K)/W)
$R_{air,\,j}$	Thermal resistance of the air space *j* between two layers ((m^2·K)/W)
r_s	Reflectance at the air-substrate interface
S_τ	Relative spectral distribution of solar radiation
T_{pv}	Solar cell temperature (^{o}C)
T_{sub}	Directional-hemispherical transmittance of substrate
T_t	Total transmittance of thermotropic laminated glazing unit
T_c	Collimated transmittance of thermotropic laminated glazing unit
T_s	Transition temperature of thermotropic layer (^{o}C)
U_g	U-value of glazing (W/(m^2·K))
$V(\lambda)$	Spectral luminous efficiency for photopic vision defining the standard observer for photometry
Z_s	Surface azimuth angle (^{o})
z	Solar azimuth angle (^{o})
α	Solar altitude angle (^{o})
α_s	Absorption coefficient of substrate (1/mm)
β	Surface tilt angle (^{o})
f_{pv}	PV cell coverage ratio
ξ	Temperature coefficient of power (1/^{o}C)
Φ	Solar zenith angle (^{o})
Ω	Solid angle (^{o})
δ	Declination angle (^{o})
λ	Wavelength (nm)
$\Delta\lambda$	Interval between wavelengths (nm)
θ	Angle (^{o})
θ_c	Critical angle (^{o})
μ_α	Absorption coefficient of thermotropic layer (1/mm)
μ_s	Scattering coefficient of thermotropic layer (1/mm)
μ_s'	Reduced scattering coefficient of thermotropic layer (1/mm)
$\tau(\lambda)$	Spectral transmittance
τ_{sub}	Internal transmission of substrate

τ_{vis}	Average visible light transmittance
τ_{solar}	Solar transmittance
$\Delta\ \tau_{solar}$	Solar transmittance modulation
ρ_{vis}	Average visible light reflectance
ρ_{solar}	Solar reflectance
$\rho_o(\lambda)$	Outer-side spectral reflectance
$\rho_i(\lambda)$	Inner-side spectral reflectance
η_o	Optical efficiency
$\eta_{inverter}$	Inverter's conversion efficiency
η_{pv}	Actual power conversion efficiency of solar cells
$\eta_{pv,STC}$	Power conversion efficiency of solar cells under standard test conditions

Chapter 1 – Introduction and literature review

1.1 Background

With a growing concern about climate change, efforts to reduce fossil fuel consumption and greenhouse gas emissions are being made in various fields. The building sector is one of the leading energy consumers and carbon dioxide emitters of the world [1]. The energy used by residential and commercial buildings in developed countries represents 20-40% of the total energy consumption, and around 60% of all energy in buildings is consumed for space heating, space cooling, ventilation and electric lighting [2-5]. Energy conservation and on-site renewable energy production are two main strategies required to be adopted in the design and operation of buildings, particularly when considering the urgent need in many developed countries for the transition towards near Zero Energy Buildings (n-ZEBs) [6].

Windows are an essential part of buildings, providing access to light, heat, vision, sound and fresh air, and directly related to the comfort and health of occupants [4]. Among the functionalities offered by windows, solar heat gain and visible light transmission represent two vital factors in the energy and environmental performance of buildings.

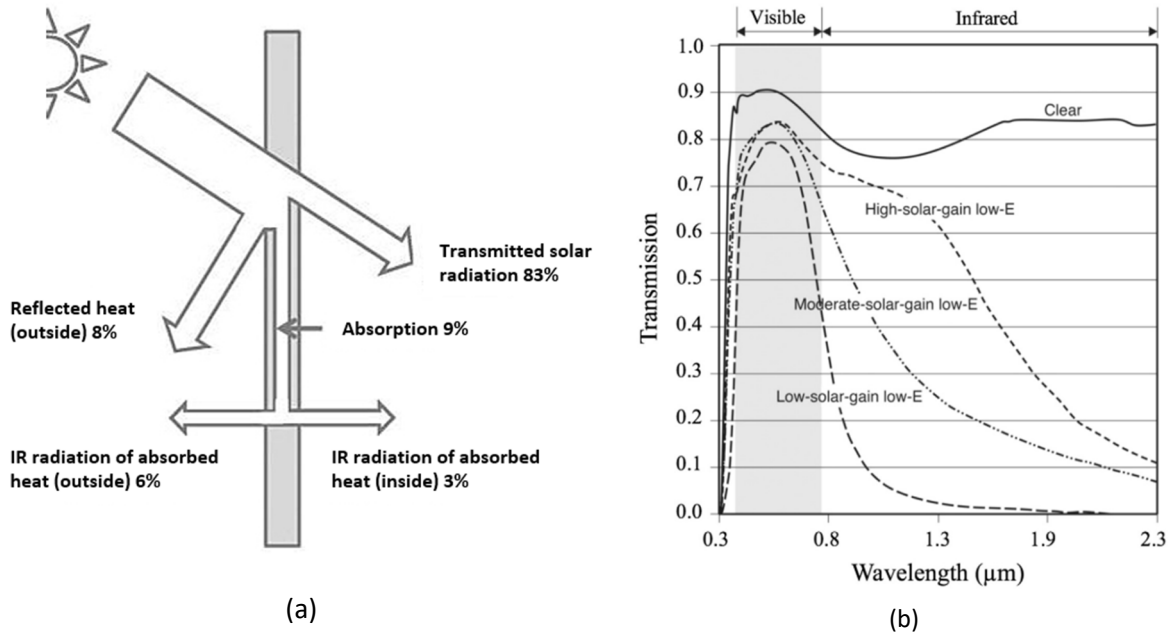

(a) (b)

Figure 1.1: (a) Solar heat gain through a single-glass window; (b) spectral transmittance of clear glass and low-e glass units. Sources: [4, 7].

Solar Heat Gain Coefficient (SHGC) is a measure of how much solar energy passes through a window, expressed by a ratio in the range of 0 to 1. **Figure 1.1** (a) illustrates an example of solar heat transfer through a traditional single-glass window. The window has a SHGC of 0.86, which equals the solar transmittance (83%) of the glass plus the glass absorbed heat that is re-radiated to the indoor space

(3%). The transmittance of a single clear glass in the visible range (380-780 nm) is about 90%, as illustrated, for example, in **Figure 1.1** (b). Traditional windows with high SHGCs and high visible light transmittances (τ_{vis}) are often the reasons for overheating and glare issues [8]. Accessory solar shading devices such as curtains or blinds are usually employed to reduce overheating and glare, however, at the expense of useful daylight so that electric lighting has to be operated in the indoor spaces despite high external light availability [9].

In order to achieve energy conservation in buildings, a critical step is to minimise the unwanted solar heat and light transferred through windows that count for substantial cooling and lighting loads. The following sections present a review focused on Building Integrated Photovoltaic (BIPV) windows (**Section 1.3**), Building Integrated Concentrating Photovoltaic (BICPV) windows (**Section 1.4**) and thermotropic smart windows (**Section 1.5**), which have been developed to overcome the drawbacks corresponding to solar heat gain and glare control.

Recent attempts to develop hybrid BIPV smart windows (**Section 1.5.4**) for on-site renewable electricity generation, adaptive solar control and building energy savings give a glimpse of the near future of n-ZEBs. This research aims to design, develop and characterise a novel BIPV thermotropic smart window system. This window technology is expected to provide enhanced energy and daylight performance as compared with an ordinary BIPV window. Details about the research gap, aim/objectives and thesis outline are given in **Sections 1.6**-**1.8**.

1.2 Overview of static and dynamic glazing technologies

Traditional windows are typically constructed of single or multiple glass panes with fixed optical properties. A single or double-glazed window consisting of clear float glass possesses high τ_{vis} (>0.8) and SHGC (>0.7) [4, 10] (see **Figure 1.2**). Both values could be reduced if changing the clear glass to body-tinted glass, also known as absorptive glass [11]. Tinted glass blocks light transmission through bulk absorption and re-emits a portion of the absorbed heat indoors as it is warming up. Such glazing allows a great reduction in τ_{vis} but yields a modest reduction in SHGC [11]. Float glass coated with a spectrally selective coating, such as low-emissivity (low-E) coating, can reduce undesirable heat exchange between the building and external environment by reflecting infrared radiation while retaining a high level of τ_{vis}. Such glazing could be formulated with a broad range of SHGC (see **Figure 1.1** (b)) to balance diverse demands from the thermal insulation, solar heat gain and daylighting points of view [4, 12]. For instance, the commercial low-E glazing products, Climaguard 80/70 with a SHGC of 0.7 and a τ_{vis} of 0.8 is intended for thermal insulation and passive solar heating in cold climates, and Climaguard 70/36 with a SHGC of 0.36 and a τ_{vis} of 0.7 is intended for solar control in warm climates [12].

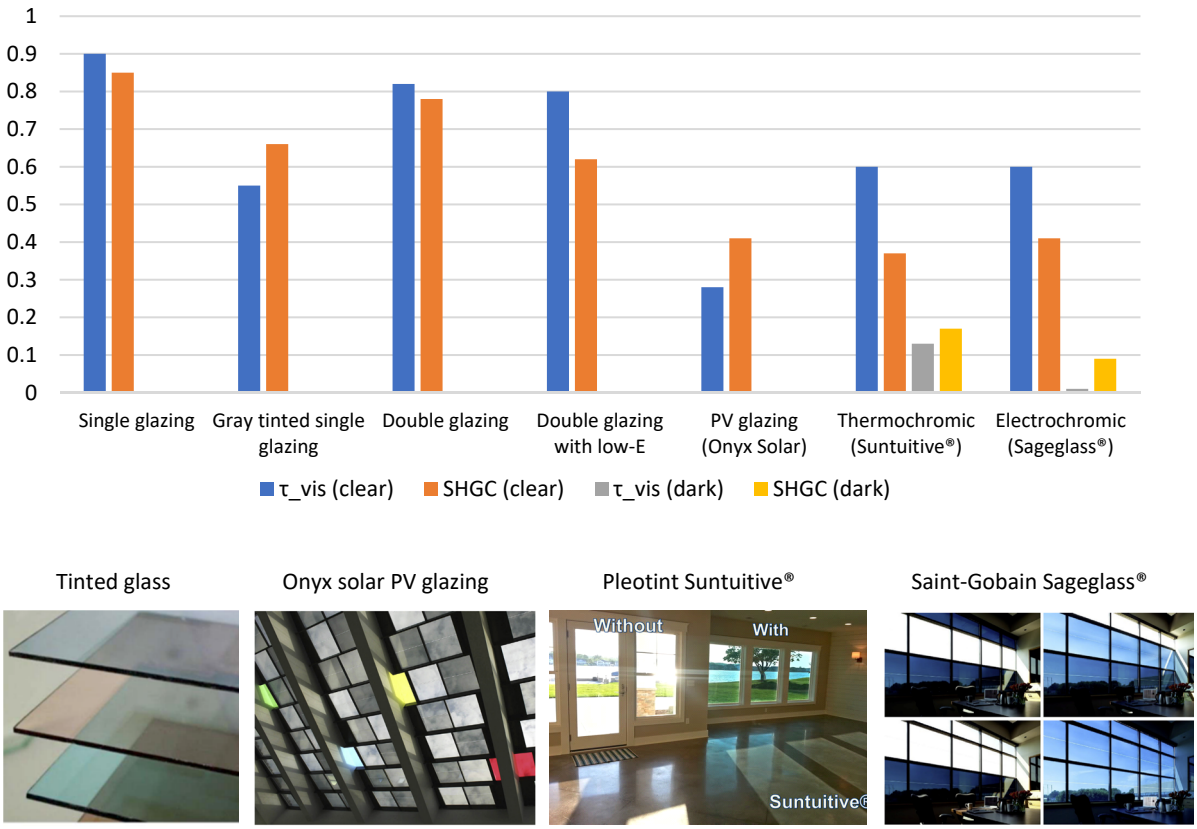

Figure 1.2: Solar heat gain coefficient (SHGC) and visible light transmittance (τ_vis) of traditional single/double glazing units and commercial dynamic glazing units. Sources: [4, 10].

In continuous efforts to enhance the window performance, various solar energy materials for applications in windows have been proposed. They include mainly phase change materials [13], water [14], aerogels [15] and photovoltaic (PV) cells [1, 16]. PV glazing can convert a fraction of the absorbed solar energy into usable electrical power instead of re-radiating it indoors, hence offering a more effective way to reduce solar heat gains through windows in comparison to tinted glazing. One of the challenges that most of the semi-transparent PV applications face is optimising τ_{vis} and power conversion efficiency (PCE) at the same time [2, 17]. In general, increasing τ_{vis} results in a decreased PCE, because PV cells utilise visible radiation to produce power [1, 10]. Therefore, most semi-transparent PV glazing products are manufactured with a τ_{vis} of below 30% in order to achieve a reasonable PCE [10, 18]. The use of PV glazing with low values of SHGC and τ_{vis} could alleviate the overheating and glare discomfort to occupants, and also contribute to reduced cooling demands in buildings. Conversely, the low values would increase the energy consumption for heating and electric lighting in buildings.

Windows integrated with smart materials such as thermochromic materials [3], photochromic materials [19] or electrochromic materials [20] can alter their SHGC and optical transmittance in response to an external stimulus such as heat, light or voltage. Due to the dynamic solar heat gain and

daylighting manipulation of the smart windows, potential energy savings are expected to derive from the reduction in cooling and electric lighting demands (see **Figure 1.3**).

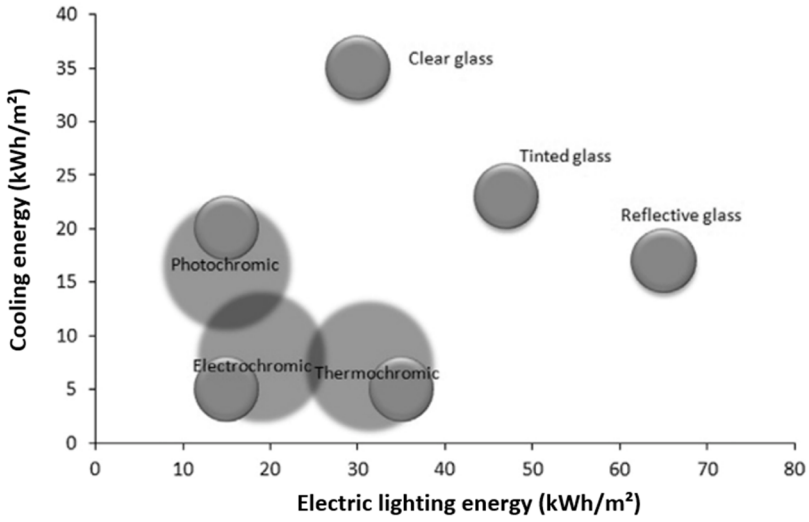

Figure 1.3: Energy consumption for space cooling versus artificial lighting by glazing type. Source: [3].

1.3 Building Integrated Photovoltaics (BIPV) glazing systems

The concept of BIPV glazing refers to the integration of photovoltaic devices into a transparent building element (e.g. window, glazed façade and skylight), purposely reducing solar heat and light transmission into buildings while providing on-site electricity generation. Most of the commercially available solar cells such as crystalline silicon (c-Si) solar cells and thin-film solar cells (e.g. amorphous silicon (a-Si), cadmium telluride (CdTe) and Dye-Sensitised Solar Cell (DSSC)) can be integrated into architectural glazing [1, 10, 17] (see **Figure 1.4**). For example, the data shown in **Table 1-1** indicate that windows or facades integrated with the listed types of solar cells can contribute to reducing the solar heat gain, possibility of glare discomfort and energy consumption in buildings.

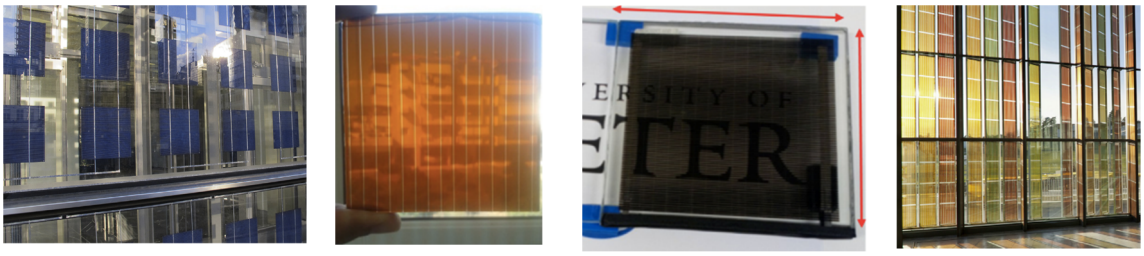

(a) c-Si (b) a-Si (c) CdTe (d) DSSC

Figure 1.4: Photographs of glazing integrated with different types of solar cells. Sources: [10, 16, 21].

Crystalline silicon (c-Si) solar cells are a well-established technology with a few advantages, such as high power conversion efficiency and long-term operational stability [1, 22-24]. The typical efficiencies of monocrystalline silicon (mono-Si) cells and polycrystalline silicon (poly-Si) cells are 16-24% and 14-18%, respectively [1, 25]. A c-Si BIPV glazing system is typically constructed by encapsulating an array

of c-Si solar cells between two panes of glass by using ethylene-vinyl acetate (EVA) films or an optically clear bonding material (e.g. polyvinyl butyral (PVB)) [1, 10]. By altering the distance between adjacent opaque c-Si cells, a varying degree of PV cell coverage ratio (i.e., the ratio between the overall solar cell area and the glazing aperture area) can be attained. A higher PV cell coverage ratio is generally associated with a higher electric energy output and a lower solar heat gain; however, this would impact the indoor daylight level, the use of electric lighting and the occupants' satisfaction with the amount of outside view [1].

Xu et al.[26] used the EnergyPlus program to simulate the building energy performance for c-Si BIPV windows in central China. The optimal PV cell coverage ratio for achieving the lowest overall energy consumption has been determined for a different combination of architectural variables, including the BIPV window orientation and Window-to-Wall Ratio (WWR) (see **Figure 1.5**). Chen et al. [27] conducted EnergyPlus simulation and field tests to evaluate the energy-saving potential of c-Si BIPV windows under various climatic conditions in southwest China. The result obtained for the BIPV window with a PV cell coverage ratio of 0.87, a WWR of 0.83 and south orientation shows a maximum of 83% reduction in annual energy consumption, compared to an ordinary double-glazed window.

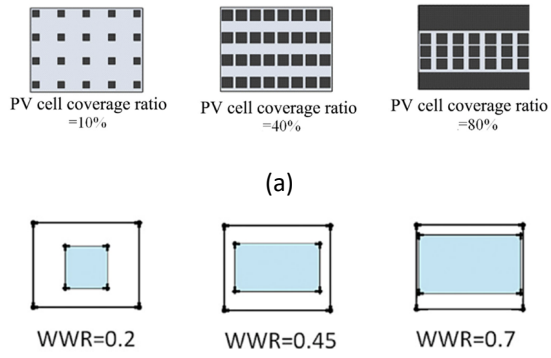

optimal PV cell coverage ratio (%)

orientation	WWR										
	0.2	0.25	0.3	0.35	0.4	0.45	0.5	0.6	0.6	0.65	0.7
E	25	40	40	45	50	60	60	60	70	70	70
SE	25	40	40	45	50	60	60	65	70	70	75
S	35	40	50	55	55	60	70	75	75	75	80
SW	35	50	50	60	65	65	70	75	75	75	80
W	35	50	50	60	65	65	70	75	75	75	80

(c)

Figure 1.5: (a) Different PV cell coverage ratios; (b) different WWRs; (c) optimal PV cell coverage ratios for different combinations of WWR and BIPV window orientation. Source: [26].

Thin-film solar cells, which are semi-transparent, uniform in appearance, flexible and lightweight, are of particular interest for BIPV glazing applications. Unlike c-Si solar cells with a thickness of up to 200 μm, thin-film solar cells have a thickness of the order of a few microns [28]. Thin-film manufacturing techniques such as Plasma-Enhanced Chemical Vapour Deposition (PECVD) allow thin films of varying thickness to be deposited on transparent substrates such as glass and plastic [29, 30]. For enhanced transparency, thin-film solar cell layers can be either made extremely thin or patterned by laser cutting [17, 31, 32]. Amorphous silicon (a-Si) cell is a well-developed thin-film PV technology [1]. Due to the thinner layer produced, an a-Si cell requires less amount of silicon for its manufacture and thus costs less compared to a c-Si cell. Moreover, a-Si cells are less affected than c-Si cells by high operating

temperature, shading and air pollution, allowing greater flexibility in building integration [10, 33]. Although many efforts such as surface texturisation and adding anti-reflection coatings have been made to enhance the optical absorption of a-Si cells, the power conversion efficiency can hardly exceed 12% [29, 31, 34].

Cadmium Telluride (CdTe) cells are well suited for BIPV glazing applications with cost and performance advantages over a-Si cells. The record laboratory efficiency of CdTe cells is 21.0±0.4% [35]. In addition, CdTe can be deposited onto large-area substrates easier and faster when compared with a-Si [33, 36]. So far, CdTe is the only thin-film material to compete with c-Si in terms of cost per watt [33]. On the other hand, CdTe is a potentially toxic material and could pose some adverse effects on the ecological environment and human health.

Dye-sensitised solar cells (DSSCs) have gained widespread attention for their unique properties: inherent semitransparency, colour tunability (depending on the dye used), substrate flexibility and ability to operate in variable lighting conditions, which make them a promising candidate for BIPV glazing applications [1, 22]. However, their commercial uptake is still hindered by several problems such as low power conversion efficiency (up to 12%), chemical degradation and electrolyte leakage [23, 37].

Table 1-1: Studies on BIPV glazing technologies.

Ref	Type	Objective	Method	Region	Major outcome
[38]	c-Si	To develop a 1D transient heat transfer model	EnergyPlus simulation	Hong Kong	About 70% reduction in total heat gain for a PV cell coverage ratio of 0.8
[39]	c-Si	To assess the temperature effect on the electrical performance of a BIPV façade module	Indoor & Outdoor experiments	Korea	0.52% reduction in power output per 1℃ increase in the module's operating temperature
[40]	a-Si	To find the optimal solar cell transmittance and WWR for a semi-transparent BIPV	EnergyPlus	Tokyo	Largest energy saving potential for 50% WWR and 40% solar cell transmittance
[41]	a-Si	To investigate the energy-saving potential of a semi-transparent PV insulating unit	EnergyPlus	Hong Kong	25.3% reduction in annual building energy consumption compared to a clear single-glass window
[42]	CdTe	To evaluate the energy and daylight performance	EnergyPlus & RADIANCE	Five cities in China	Up to 73% energy saving and lower possibility of glare compared to a conventional double glazing
[43]	DSSC	To investigate the electrical characteristics under varying sky conditions	Outdoor experiment	Daejeon	Enhanced power conversion efficiency at a lower solar intensity

1.4 Building Integrated Concentrating Photovoltaics (BICPV) systems

Low electric power output per unit solar cell area is one of the major barriers to the widespread adoption of BIPV systems. A viable solution to improve the rate of power generation is to incorporate a solar concentrator in BIPV design [44]. The idea behind solar concentrators is to concentrate sunlight onto PV cell areas by using low-cost optical devices made of materials such as plastic, glass and mirror [45, 46]. For building integration, the majority of Concentrating Photovoltaics (CPV) systems are designed to be stationary with low concentration ratios (<10 suns) [47]. Although CPVs with medium concentration ratios (10-100 suns) or high-concentration ratios (>100 suns) could potentially offer a higher electric power output per unit solar cell area, they require one or two-axis tracking systems to cater for the sun movement and maximise the solar radiation collection through a day, which prevents them from architectural integration. A review on the suitability of CPVs for building integration was presented by Chemisana [44].

A variety of concentrating optics have been proposed for BICPV applications, classified by geometric shape, including planar optics (e.g. diffused reflector [48], holographic film [49] and Luminescent Solar Concentrator (LSC) [50, 51]) and non-planar optics (e.g. Fresnel lens [52], wedge prism [53, 54] and Compound Parabolic Concentrator (CPC) [55]). Such optics are generally designed and optimised using ray-tracing techniques [56]. The following sub-sections will describe the two categories of BICPV systems in detail and their research findings.

1.4.1 Flat-plate static solar concentrators

Flat Plate Static Concentrators (FPSCs) usually feature a transparent planar waveguide with reflectors placed in between adjacent solar cells or at the waveguide's backside, as illustrated in **Figure 1.6**. The reflector can be in the form of a metal-coated v-grooved sheet [57, 58], a Lambertian diffused sheet [59-61] or a plate doped with luminescent species [62-64]. When light rays enter an FPSC, some rays are specularly reflected or scattered from the reflectors. A fraction of the reflected rays are trapped within the waveguide through Total Internal Reflection (TIR) and subsequently redirected to the solar cells for power generation. The light-trapping ability is determined by the critical angle of the waveguide (e.g. 42° for glass cover with a refractive index of 1.5 [65]) and also affected by the usage of secondary optical elements (e.g. mirrors and lenses at the waveguide's edges [48]).

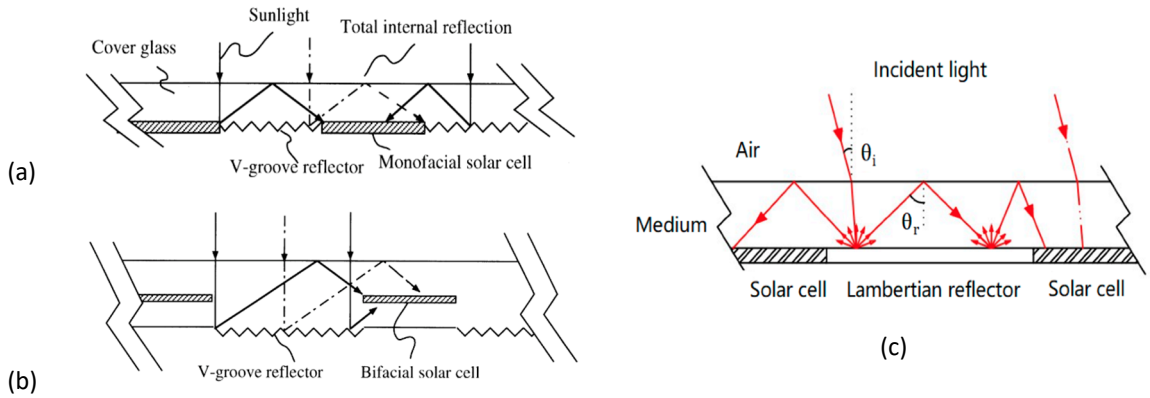

Figure 1.6: Cross-section of FPSC modules incorporating (a) v-grooved reflectors and monofacial solar cells, (b) v-grooved reflectors and bifacial solar cells, (c) Lambertian diffused reflectors. Sources: [57, 66].

Uematsu et al. [57, 67, 68] proposed two FPSC modules consisting of v-grooved reflectors with monofacial solar cells (**Figure 1.6** (a)) and bifacial solar cells (**Figure 1.6** (b)) respectively. The short-circuit current densities of the monofacial-cell-type and bifacial-cell-type FPSC modules are 1.31 and 1.71 times higher as compared to their counterparts without v-grooved reflectors. A further optimisation study of the monofacial-cell-type FPSC module was carried out by Yoshioka et al. [58]. The simulation result showed that the FPSC module with the optimised parameters, including a v-groove slope angle of 30°, a reflector width of 8 mm and a cell width of 14.5 mm, could reduce the coverage area of solar cells to 75% of a conventional PV module. The findings of a ray-tracing study by Weber et al. [69] revealed that the optical performance of FPSC modules based on v-grooved reflectors is strongly dependent on the modules' elevation angle and orientation.

In contrast to v-grooved reflectors, Lambertian type diffused reflectors scatter light uniformly regardless of the angle of light incidence. Hence, a Lambertian solar concentrator provides similar optical concentration effects over a wide range of incidence angles [66, 69]. Chou et al. [70] developed a flexible FPSC module consisting of a polydimethylsiloxane (PDMS) plate with edge-adhered poly-Si solar cells and a white-diffuse rear reflector, as shown in **Figure 1.7** (a). The white-diffuse rear reflector, which was made from another PDMS layer doped with TiO_2 nanoparticles, behaved as a near-Lambertian reflector. By ray-tracing simulation, it was found that the FPSC module has nearly constant optical concentration ratios (C_e) for incidence angles up to 50° (see **Figure 1.7** (b)). Moreover, the FPSC module with four poly-Si cells has an optical efficiency (η_o) of 35.07% and a power conversion efficiency of 4.63%. Here, C_e is defined as the ratio of the irradiance (W/m^2) on the PV cell surface to that on the module aperture; η_o is defined as the ratio of the radiant energy flux (W) received by the solar cells to the flux incident on the module aperture.

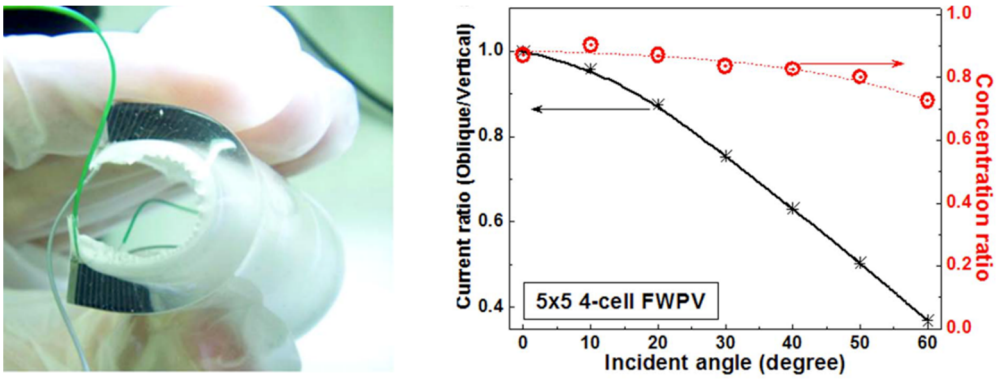

(a) (b)

Figure 1.7: (a) Photograph of a bendable FPSC module with a PDMS/TiO_2 composite bottom layer; (b) optical concentration ratio (red curve) of a 5 cm × 5 cm FPSC module with four poly-Si cells as a function of incidence angle. The optical concentration ratios are less than 1, because the solar cells were mounted at the module's edges where receive the light scattered from the white-diffuse rear reflector and have lower irradiances compared with the direct normal irradiance on the module's front aperture. Source: [70].

Hazel [71] proposed a new design of solar shading device based on bifacial solar cells in combination with a white semi-transparent rear reflector, as illustrated in **Figure 1.8** (a). The solar shading devices were installed with a tilt angle of 45° at the top of the south-oriented windows, to allow glare-free diffuse light to enter the office room, as shown in **Figure 1.8** (b). This design enables the collection of the solar radiation falling on the front sides of the bifacial cells as well as the light backscattered to the rear sides, which achieves up to 58% enhancement in power output compared to the monofacial-cell-type counterpart.

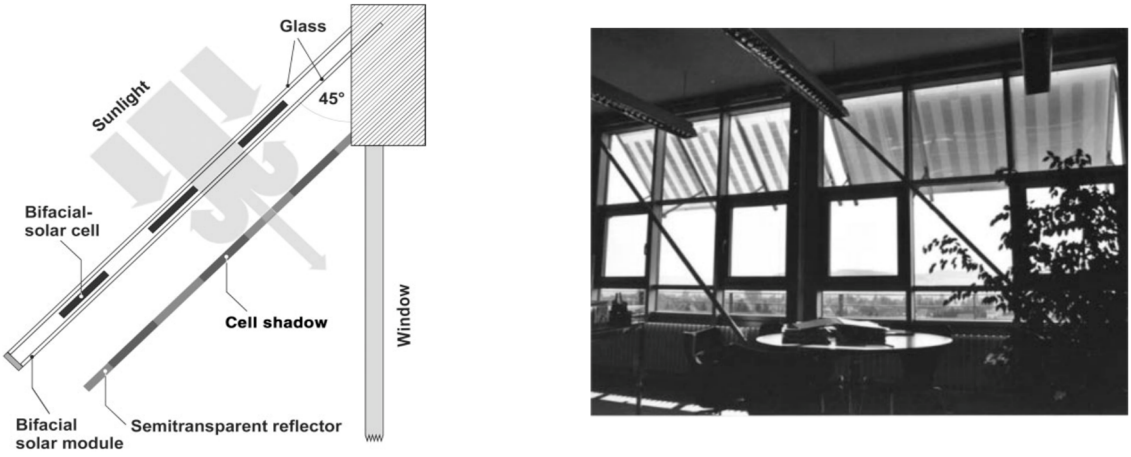

(a) (b)

Figure 1.8: (a) Schematic of the bifacial PV shading device with a semi-transparent rear reflector; (b) photograph of the shading devices installed above the south-oriented windows. Source: [71].

An FPSC module utilising Luminescent Solar Concentrator (LSC) panels as rear reflectors was introduced by Leow et al. [62-64]. In contrast to the traditional LSC windows in which solar cells are attached along the perimeter of an LSC layer [72-74], the proposed system is constituted of a transparent acrylic waveguide with solar cells mounted front-facing and interspaced with LSC panels. As can be seen from **Figure 1.9** (a), the incident light is absorbed by the organic dyes (LR305) dispersed

in the LSC panels and re-emitted isotropically, with a fraction redirected towards the solar cells through total internal reflection. The result of ray-tracing simulation in **Figure 1.9** (b) shows that the system yields a power gain of about 1.6 (i.e., about 60% increment in power output relative to the counterpart with no LSC panel) when the LSC distance between adjacent cells is increased to 10 cm. A further increase in LSC distance sees minor power gain improvement because of exacerbated photon losses by re-absorption and escaping [62].

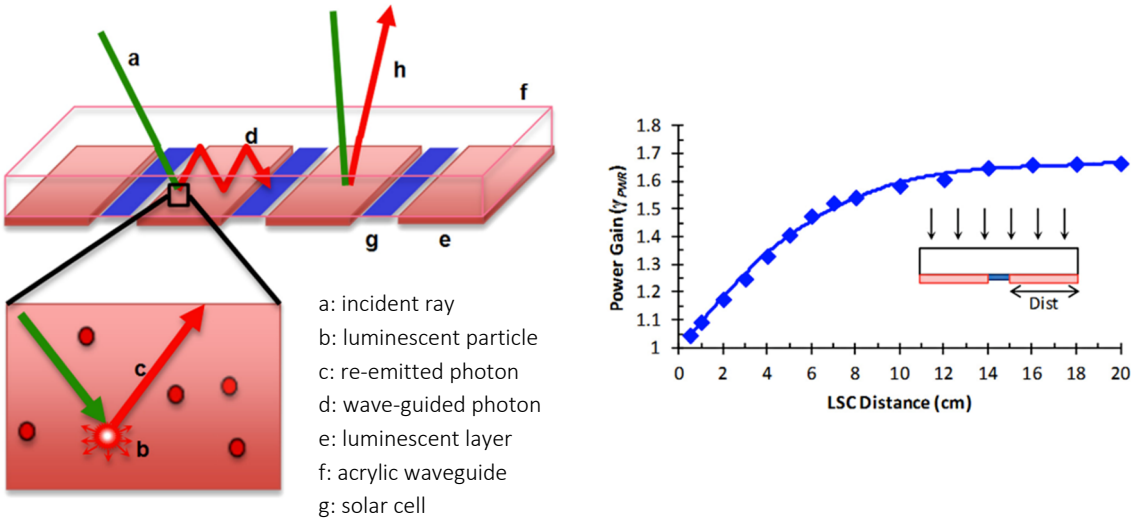

(a) (b)

Figure 1.9: (a) Schematic illustrating the transport of photons in an acrylic waveguide coupled with LSC rear panels; (b) power gain as a function of the LSC distance between adjacent solar cells. Source: [63].

1.4.2 Dielectric based compound parabolic concentrators

A significant problem associated with FPSCs for window integration is their low transparencies caused by the use of highly reflective/scattering materials for the sake of attaining high optical concentration ratios. Transparent dielectric material based solar concentrators provide a practical approach to improve PV power generation and allow access to daylight. Dielectric Compound Parabolic Concentrators (DiCPCs) forms a category of static solar concentrators widely studied, especially for building integration [75, 76]. The reported dielectric materials for DiCPCs include polycarbonate [77], polyurethane [78], polymethyl-methacrylate (PMMA) [79] and Topas® (cyclic olefin copolymer) [77], which are electrical insulators with high visible transparency (i.e., in the range of 70% to 90%) [77, 80]. Different geometrical profiles of DiCPCs such as three-dimensional crossed CPC [78, 79], rotational asymmetric CPC [81], linear asymmetric CPC [82, 83] and lens-walled CPC [84] have been introduced, and the DiCPCs' performance in terms of optical efficiency, I-V characteristics and temperature distribution have been investigated by numerical simulations and experiments.

Baig et al. [78, 79] brought forward a CPV system based on 3D Crossed Compound Parabolic Concentrator (3DCCPCs), as shown in **Figure 1.10**. An array of 3DCCPCs made from a clear

polyurethane material (Crystal-clear 200®) were optically bonded to solar cells using an encapsulation material (Sylguard-184), and the bonded units were placed between two glass panes. **Figure 1.10** (d) illustrates the trajectories of light rays entering a 3DCCPC at different incidence angles. The ray-tracing simulation results show that the 3DCCPC has a 34.5° acceptance half-angle (i.e., the incident angle at which the optical flux reaching the exit aperture falls to 90% of its maximum [78, 85]), combined with a maximum optical efficiency of 73.4%. The maximum power output of the CPV system was found to be 2.65 times higher than that of its counterpart without 3DCCPCs at normal light incidence.

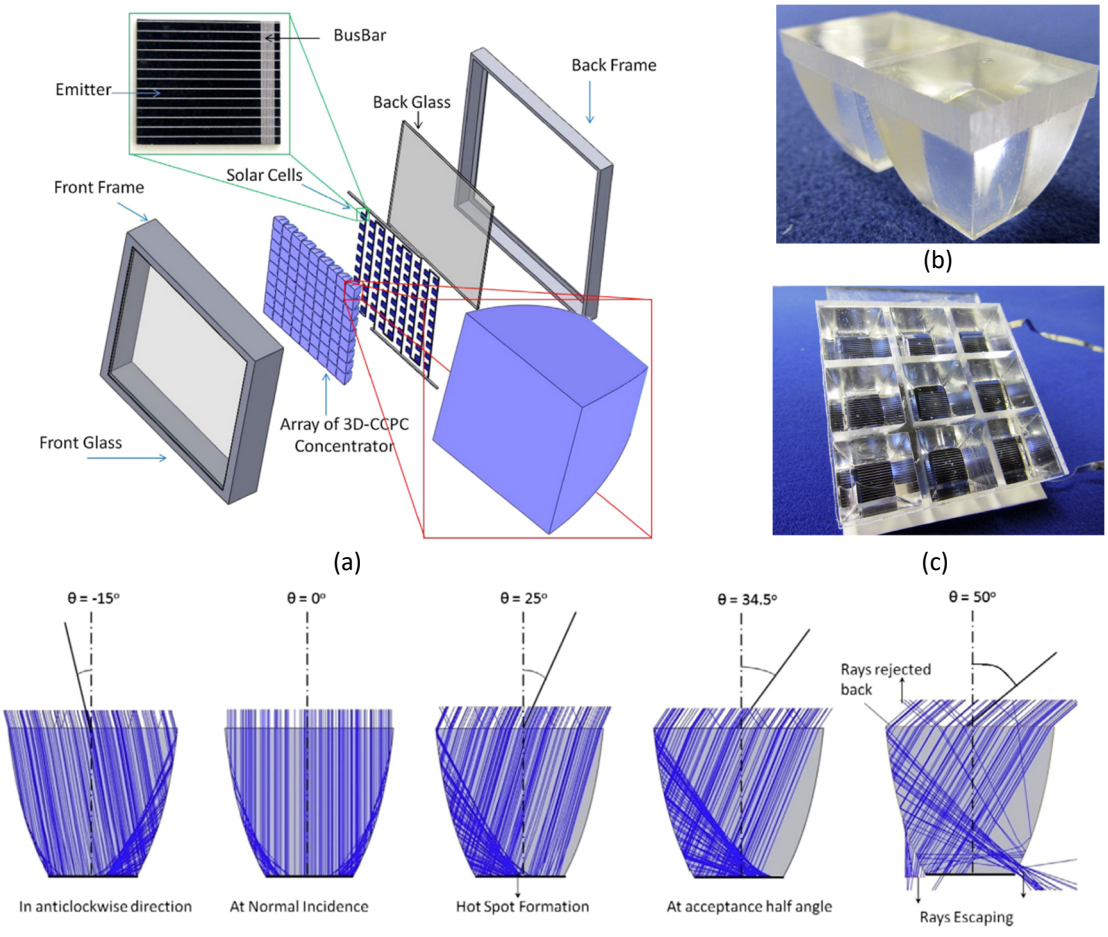

Figure 1.10: (a) Components of the 3DCCPC based BICPV system; (b) 3DCCPCs made from a clear polyurethane material; (c) prototype with nine solar cells and 3DCCPCs; (d) ray-tracing graphs of the 3DCCPC for different angles of light incidence. Source: [78, 79].

The research team at the University of Exeter [56, 76, 86, 87] developed a CPV system consisting of linear Asymmetric Compound Parabolic Concentrators (ACPCs), as shown in **Figure 1.11**. The designed ACPCs allows the incident light within the range of acceptance angles (0°-55°) to be efficiently collected for power generation, and in the meantime, allowing some light to escape at the air-dielectric interfaces and transmit through the system for daylighting purposes. The outcome from an indoor experiment shows that the CPV system has a maximum optical efficiency of 80.5% and a maximum power ratio of 2.27 (i.e., the ratio of power output relative to a non-concentrating

counterpart) at the incidence angle of 20° [86]. The CPV system was further characterised by an outdoor experiment in Edinburgh under different weather conditions (sunny, cloudy and rainy). An average power ratio of 2.19 was reported for the CPV system tested on a sunny interval day in October.

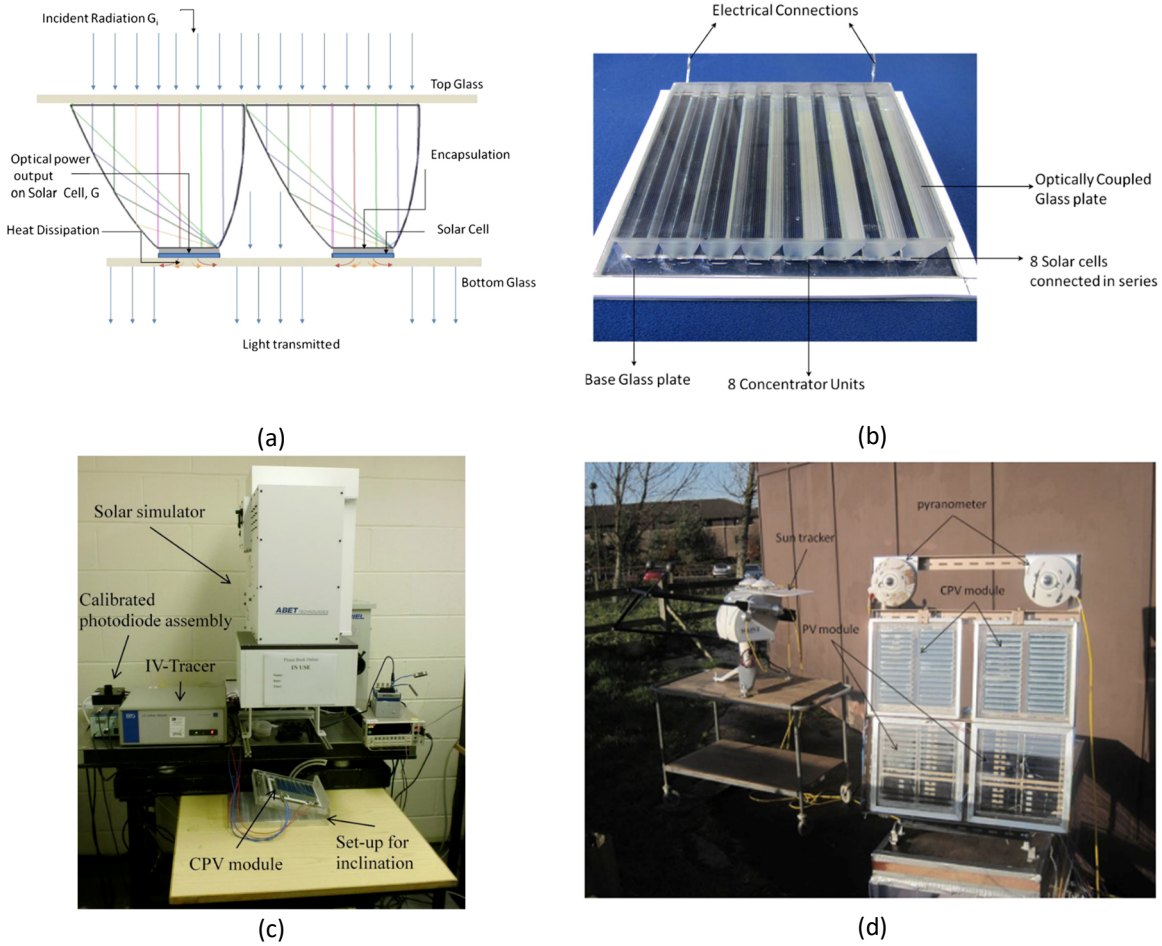

Figure 1.11: (a) Schematic of the ACPC-PV glazing system; (b) prototype fabricated for indoor characterisation; (c) indoor experimental setup; (d) outdoor experimental setup. Source: [56, 87].

Despite the significant increment in power output, the use of dielectric CPCs usually leads to high solar cell temperature and non-uniform illumination on the solar cell surface [56, 78]. Baig et al. [56] simulated the thermal and electrical performance of the linear ACPC system (**Figure 1.11**) under the standard solar irradiation (AM1.5, 1000 W/m^2). A 51°C maximum increase in solar cell temperature was observed, which brought down the power conversion efficiency from 18.5% (at 23°C) to 15.6% (at 74°C). The non-uniformity in flux distribution along the solar cell tends to cause detrimental hot-spots, current mismatch and degradation in cell performance [44, 56]. The overheating problem can be relieved by combining the CPV systems with passive cooling mechanisms such as natural ventilation and Phase Change Material (PCM) [88]. However, these would increase cost and complexity with regards to architectural integration.

1.5 Smart window technologies

Smart or switchable windows can change their optical properties reversibly to adapt to time-varying weather conditions or user requirements, hence offering selective and dynamic modulation of incoming solar radiation [9, 89]. Such functionality has become possible by exploiting chromogenic materials (e.g. thermochromic, photochromic, electrochromic and gasochromic), thermotropic materials, Suspended Particles Devices (SPDs) and Polymer Dispersed Liquid Crystals (PDLCs) [20, 89].

Thermo-sensitive materials which achieve transmittance modulation via tunable scattering behaviours are usually denoted as "thermotropic materials" in distinction to "thermochromic materials" characterised by colour change. When used in windows, thermotropic materials offer an interesting possibility for the passive control of solar heat and visible light into buildings by varying ambient temperature. This feature helps in reducing the building energy consumption for cooling in summer without compromising much of the solar radiation for space heating and daylighting in winter. In addition, thermotropic windows act on the basis of scattering effect, thereby imparting effective glare reduction. One disadvantage of thermotropic windows is that the optical switching cannot be actively controlled; therefore, they are not suitable for use in the areas where a permanent view from the inside out is required. The subsections provide a brief review of smart windows based on thermotropic hydrogels with relevant data to aid in understanding their optical behaviours and effects on building energy performance.

1.5.1 Mechanism of thermotropic hydrogels

Thermotropic hydrogels are water (or solvent) poured cross-linked polymer networks with both hydrophilic and hydrophobic groups within their structures [90, 91]. **Figure 1.12** illustrates the reversible transition of a poly(N-isopropylacrylamide) (PNIPAm) based hydrogel between a transparent state and a translucent state during heating and cooling. Below the transition temperature (approximately 32°C), also referred to as Lower Critical Saturation Temperature (LCST), the PNIPAm polymer is hydrophilic with hydrogen bonds prevailing between the polymer chains and water molecules. The polymer and water are mixed homogeneously at a molecular level; therefore, the hydrogel has a median refractive index and is highly transparent [90, 92]. Once the hydrogel temperature goes above the LCST, the polymer-water hydrogen bonds break, and the hydrophobic polymer-polymer interactions become dominant [91]. Subsequently, phase separation occurs with the polymer chains aggregating and free water quenched out from the polymer network. Therefore, light scattering takes place at the interfaces between the aggregated polymer particles (scattering domain) and the free water (matrix) which have different refractive indices (see **Figure 1.13**) [92, 93], resulting in a translucent appearance of the hydrogel.

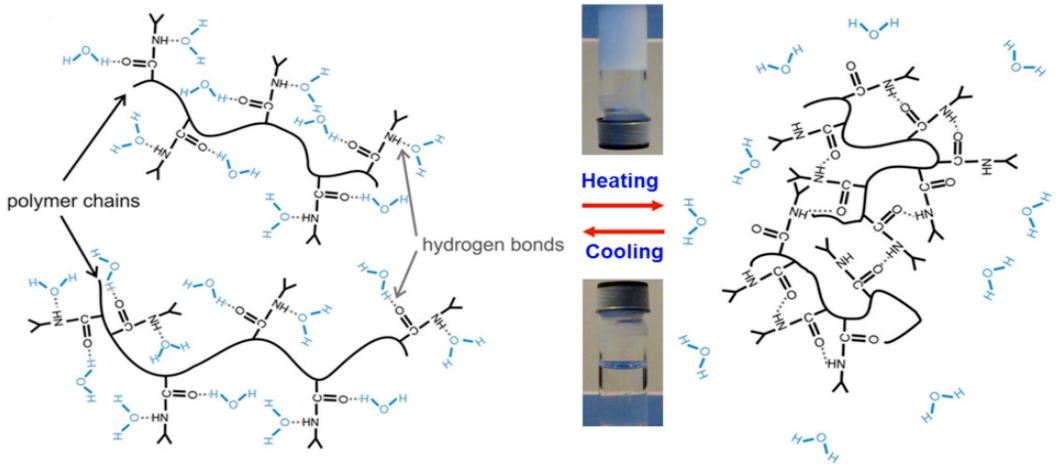

(a) (b)

Figure 1.12: Molecular structure of PNIPAm hydrogel in (a) the hydrated transparent state and (b) the dehydrated translucent state. Source: [94].

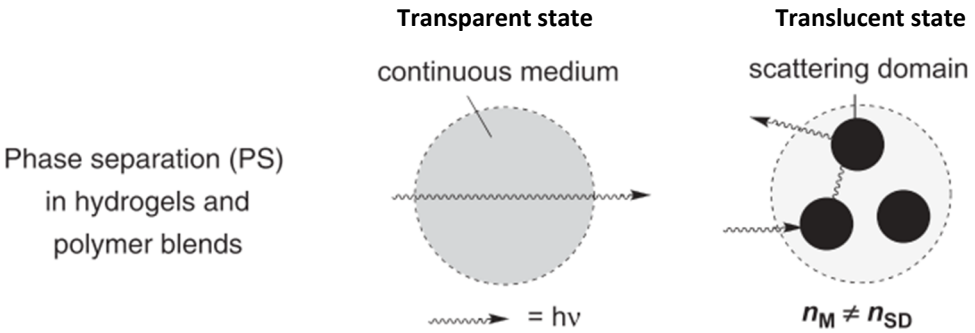

Figure 1.13: Light scattering induced by the difference between the refractive indices of the scattering domains (n_{SD}) and the matrix (n_M). Source: [92].

In practical terms, the thermotropic hydrogel used in a smart window needs to fulfil a number of requirements [90, 91, 95-97]:

- High visible light transmittance (380-780 nm) (>70%);
- Near-room-temperature transition (between 25 and 35°C);
- Steep switching gradient (<10°C);
- High reversibility and low hysteresis in the heating-cooling process;
- High viscosity to distribute the internal hydrostatic pressure evenly in the interspace of a glazing unit and not to run out;
- Non-toxic, non-freezing, stable against UV radiation;
- Low cost and good scalability.

1.5.2 Thermal and optical properties of thermotropic hydrogels

Thermotropic hydrogels are commonly produced from synthetic polymers or biopolymers [90]. As a typical member of synthetic polymers, poly(N-isopropylacrylamide) (PNIPAm) has been extensively investigated due to its unique features, such as reversible abrupt transparent-opaque transition, good

resistance to UV radiation and simplicity of synthesis [98, 99]. Pure PNIPAm hydrogels have an LCST of approximately 32°C [100]. The LCST of PNIPAm hydrogels is tunable with the approaches including copolymerisation [101, 102], adding co-solvents [98] and adding salts [103]. Mizuntani et al. [101] prepared PNIPAm hydrogels with LCST in the range of 25 and 40°C by copolymerising with hydrophobic amide-monomer (to increase LCST) or hydrophilic ester-monomer (to decrease LCST). Wang et al. [98] proposed PNIPAm microgel colloids based on a binary solvent of water and glycerol mixture. The LCST was found to decrease from 32.2 to 20.4°C by increasing the glycerol content from 0 to 35 wt % (of total solvent). The researchers also found that adding glycerol co-solvent can enhance the freezing tolerance and reduce the water evaporation rate of PNIPAm hydrogels [98].

Li et al. [104] demonstrated a prototype smart window with an interlayer of thermotropic hydrogel containing co-polymerised PNIPAm-AEMA microparticles. It can be seen from **Figure 1.14** that the PNIPAm-AEMA hydrogel layer with a thickness of 240 μm exhibits a visible light transmittance (380-780 nm) of 87.2%, a Near-Infrared (NIR) transmittance (780-2500 nm) of 81.6% and a solar transmittance (250-2500 nm) of 84.1% at 25°C, together with a solar energy modulation of 81.3% (i.e., the difference between the solar transmittances in the clear and translucent states). However, as commented by Maiorov [99], the transmittance modulations given in **Figure 1.14** are overestimated, because the authors only considered the change in directional (or collimated) transmittance, neglecting the diffuse radiation transmitted through the PNIPAm-AEMA layer.

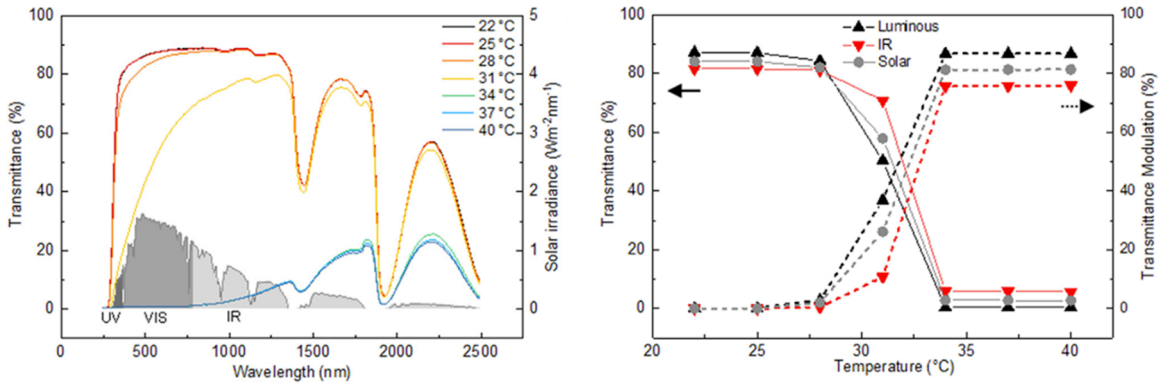

(a) (b)

Figure 1.14: (a) Transmittance spectra of the PNIPAm-AEMA layer at various temperatures; (b) integral luminous (or visible light) transmittance, IR transmittance, solar transmittance and corresponding transmittance modulations of the layer as a function of layer temperature. Source: [104].

The spectral transmittance of a PNIPAm hydrogel at varying layer thicknesses was investigated by Zhou et al. [95]. As can be seen from **Figure 1.15**, increasing the layer thickness from 26 to 78 μm has no significant effect on the spectral transmittance at 20°C, however, resulting in lower spectral transmittance at 40°C. The directional visible, NIR and solar transmittance modulations of the 78-μm-thick hydrogel layer were reported to be 65.9%, 31.7% and 49.6%, respectively. The relatively

ineffective light shielding in the NIR region may be attributed to the small PNIPAm particle sizes that are not comparable to the wavelength of the NIR spectral range [104, 105].

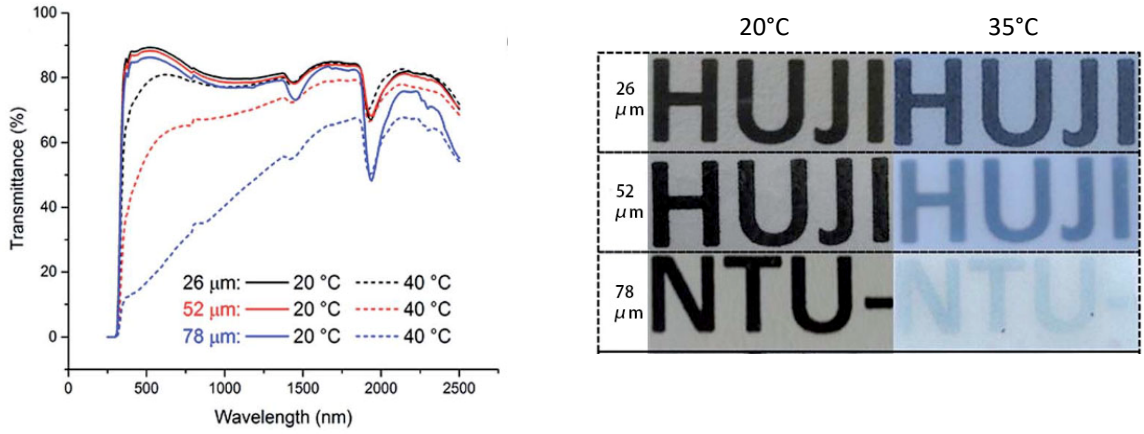

(a) (b)

Figure 1.15: (a) Spectral transmittance of the PNIPAm hydrogel with different layer thicknesses; (b) images of the PNIPAm films in the clear and translucent states. Source: [95].

Recent attempts were considering natural hydrogels based on cellulose derivatives, such as Hydroxypropyl Cellulose (HPC) [106-108] and Hydroxypropyl Methyl Cellulose (HPMC) [109, 110], for the development of thermotropic windows. HPC is a non-toxic, biodegradable, water-soluble solid polymer [90, 106]. Its advantages over synthetic polymers regarding price and availability make it economically feasible for large scale applications [90]. Furthermore, the scattering domain sizes of HPC hydrogels could reach as high as 1-2 μm in diameter; therefore, radiation in both visible and NIR regions can be effectively scattered [99, 106]. As illustrated in **Figure 1.16**, the HPC aqueous solution turns cloudy and milky-white at temperatures above 42°C. The HPC hydrogel layer at 70°C becomes nearly opaque to light over a broad range of the solar spectrum.

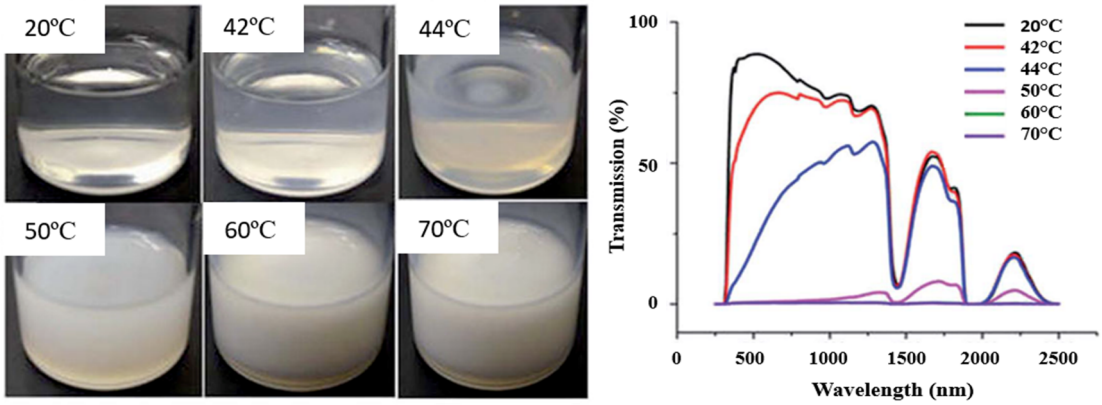

(a) (b)

Figure 1.16: (a) Photographs of 0.5 wt % HPC aqueous solution at different temperatures; (b) spectral transmittance of a 0.5 wt % HPC hydrogel film with 0.35 mm thickness at different temperatures. Source: [106].

Watanabe [111, 112] developed an Affinity Intelligent Window™ with a glazing aperture area of 1 m^2. The thermotropic hydrogel laminated between two glass panes was synthesised of HPC, water,

sodium chloride and an amphipathic compound, the latter of which acts as a spacer to avoid the irreversible sedimentation of HPC aggregates during phase separation. Schneider and Seeboth [97] suggested integrating HPC with Hydroxyethyl Cellulose (HEC) or gellan gum, instead of an amphipathic substance to prevent ageing [90]. Connelly et al. [107] developed a thermotropic hydrogel based on 6 wt % HPC thickened with 1.5 wt % gellan gum. As can be seen from **Figure 1.17**, The HPC membrane with a thickness of 0.5 mm changes its transmittance from approximately 90% in the clear state to approximately 20% in the translucent state; meanwhile, its reflectance increases by approximately 40%. The cloudy point or isotropic-to-biphasic transition temperature of a salt-free aqueous solution of ≤40 wt % HPC is around 40°C, as shown in **Figure 1.18**. Adding salt enables the cloudy point to shift down or up depending on the sorts of the associated anion and cation [113] (see **Figure 1.18**). For instance, the cloudy point of HPC aqueous solution can be decreased from 42 to 20°C by increasing the content of sodium chloride (NaCl) salt from 0 to 1.4 mol/litre [114].

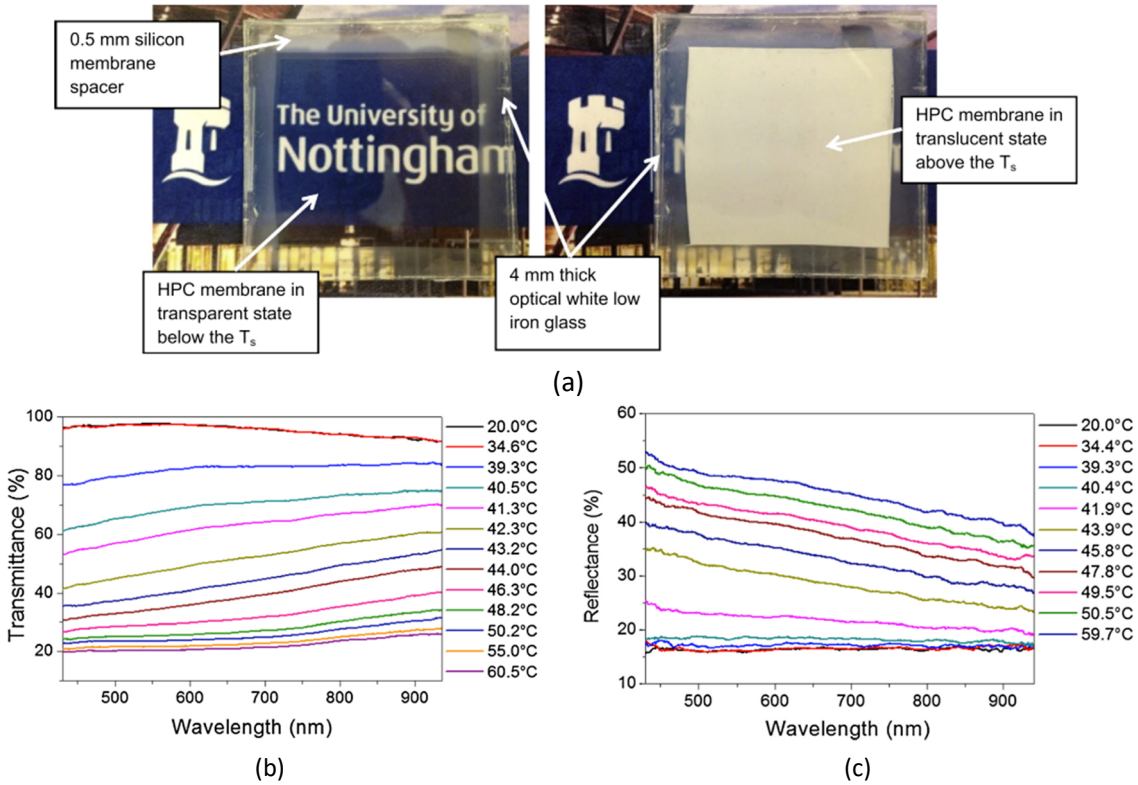

Figure 1.17: (a) Photos of an HPC hydrogel window sample at room temperature (left) and above the transition temperature (right); (b) transmittance spectra and (c) reflectance spectra of the 0.5-mm-thick membrane made of 6 wt % HPC and 1.5 wt % gellan gum for various temperatures. Source: [107].

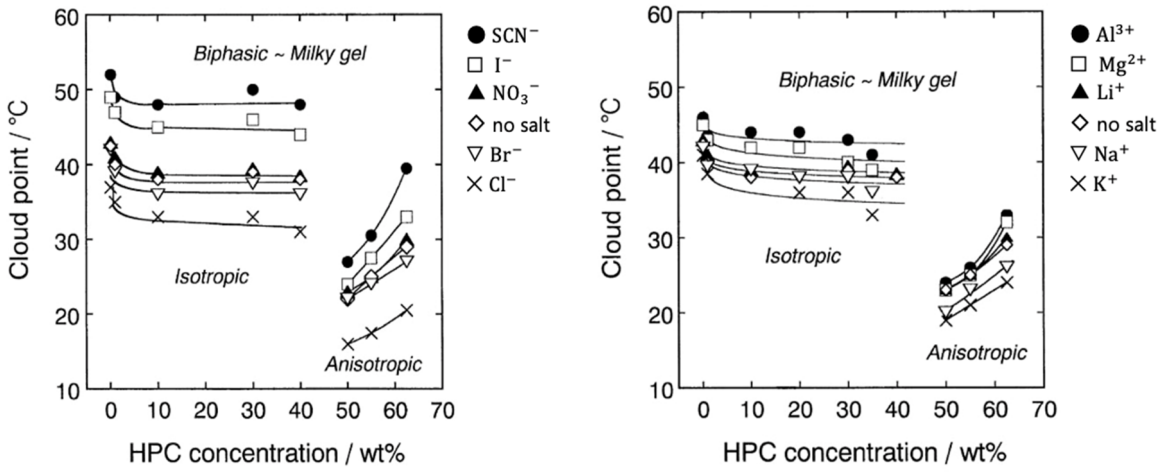

(a) (b)

Figure 1.18: Cloudy points of the HPC aqueous solutions added with (a) lithium salts with different anions and (b) metallic nitrates with different cations, at a salt concentration of 0.5 mol/litre. Source: [113].

1.5.3 Design and simulation of thermotropic windows

A thermotropic window can be simply manufactured by filling the intervening space between two glass panes with a thermotropic hydrogel and then sealing around the edges. If the thermotropic window is intended to be used in regions with cold winters, it is usually combined with one or more additional glass panes with a low-E coating for enhanced thermal insulation [115] (see **Figure 1.19** (a)). In order to enable visual contact with the outdoor environment, a window/façade can be designed with its upper and side parts covered with thermotropic glazing units while its lower and middle parts covered with visually clear glazing units (see **Figure 1.19** (b) and (c)).

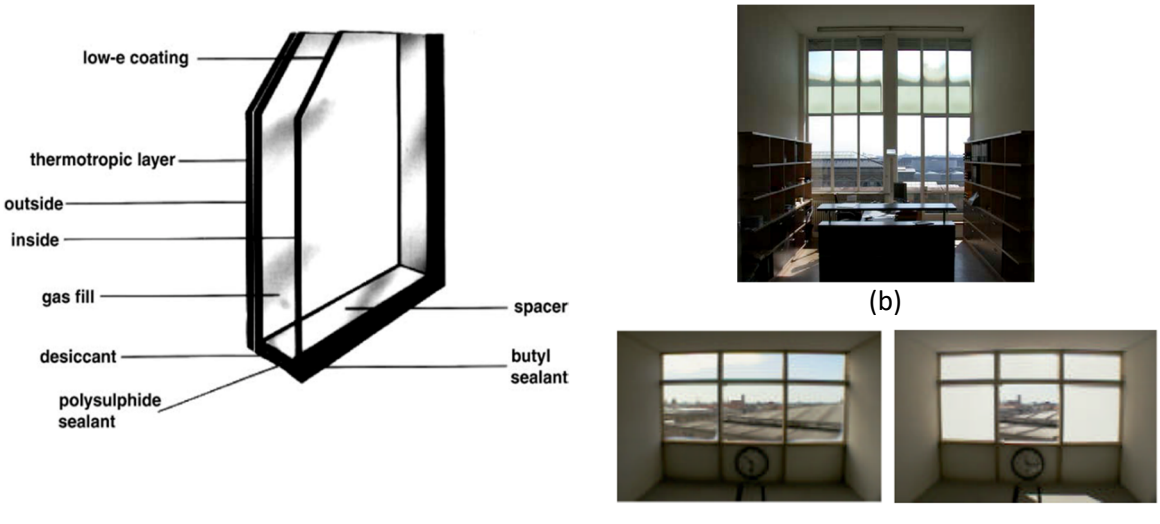

(a) (b) (c)

Figure 1.19: (a) Structure of a thermotropic insulating glazing unit (TT-IGU). Windows composed of (b) TT-IGUs in the upper section and clear-glass units in the lower section, (c) TT-IGUs and a central clear glass. Source: [115].

Allen et al. [91] conducted EnergyPlus simulation to explore the potential of thermotropic roof skylights (with 0°, 30° and 60° inclinations) as a means of reducing solar heat gain and improving building energy efficiency under the climate of Palermo, Italy. From **Figure 1.20** (b), it can be seen that

the horizontal skylight based on 6 wt % HPC hydrogel can provide considerable reductions in peak solar heat gains at approximately 44% and 25% compared to an Ordinary Double Glazing (ODG) unit and a low-E glazing unit, respectively, during the representative cooling period. The difference in overall energy consumption between the glazing units can be seen from **Figure 1.20** (c), where the horizontal skylights with the 6 wt % HPC thermotropic layer with different temperature ranges of phase separation offer annual energy savings of from 17.5% to 23% over the ODG unit.

Yao and Zhu [116, 117] used the building simulation program DeST to investigate the potential effect of double-glazed windows filled with an HPMC-NaCl thermotropic hydrogel (LCST = 31°C) on the indoor thermal environment of a residential building in Hangzhou, China. The results suggest that installing the thermotropic windows on the west-facing façade (WWR=30%) could reduce the occurrence of overheating in the indoor space by 70% and the annual cooling energy consumption by 19% when compared with ordinary double-glazed windows.

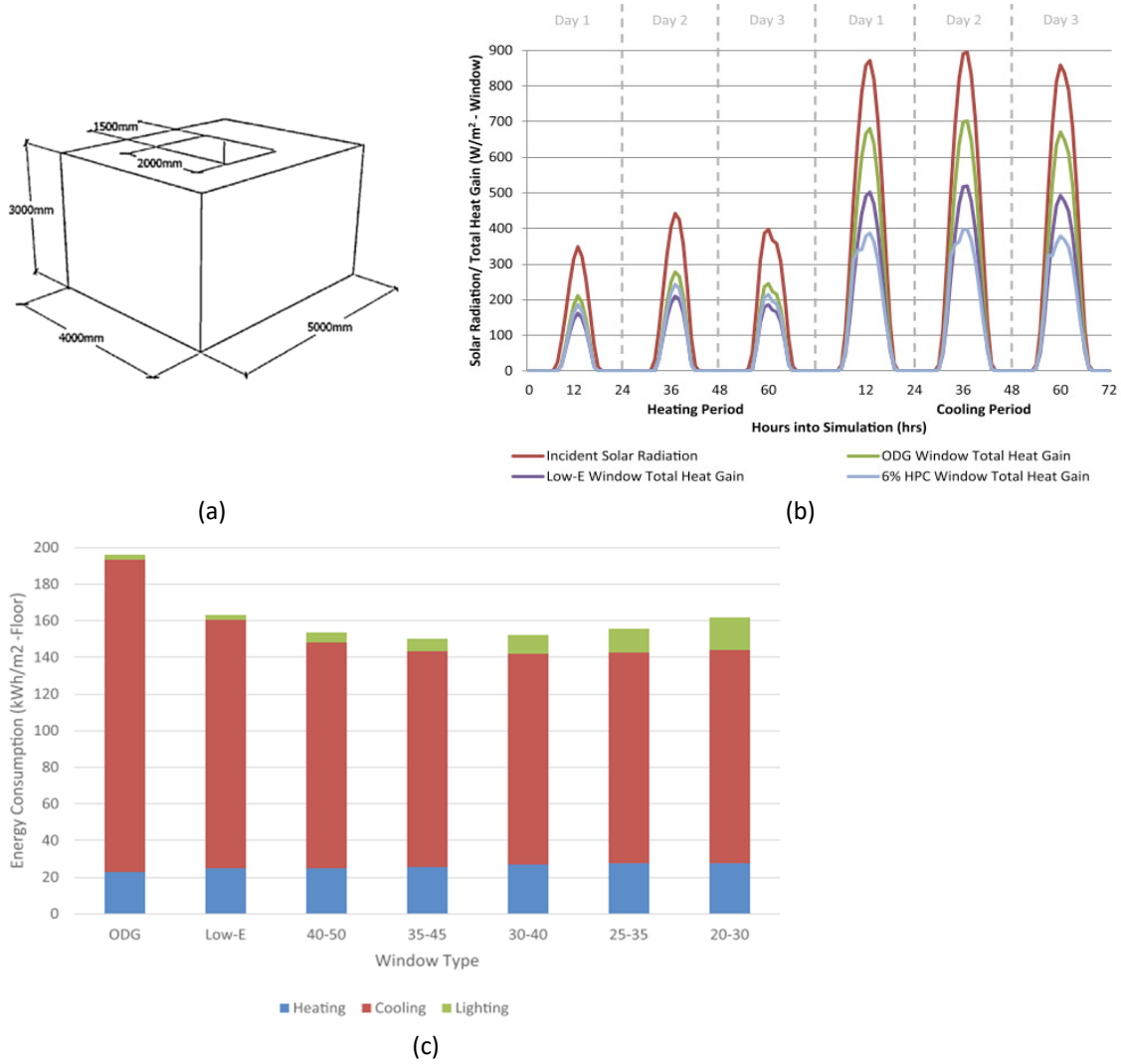

Figure 1.20: (a) Office room geometry in EnergyPlus. (b) Hourly incident solar radiation and hourly total heat gains through the ODG window, Low-E window and 6 wt % HPC thermotropic (TT) window. (c) Annual energy consumptions of the office room for different window types and TT transition temperature ranges. Source: [91].

1.5.4 BIPV smart window systems

The combination of the two fields of BIPV window and smart window has given rise to a new discipline, termed Building Integrated Photovoltaics (BIPV) smart window system. Few particular ideas have been put forward combining photovoltaic devices with optically switchable materials such as electrochromic (EC) materials [118], liquid crystals [24, 119, 120] and thermochromic materials [121]. Ma and Chen [118] presented a self-powered smart window comprised of a c-Si BIPV panel coupled with an electrochromic stack (four layers: indium tin oxide (ITO)-coated glass, tungsten oxide (WO_3), electrolyte and ITO-coated glass), as shown in **Figure 1.21** (a). The EC stack could be tuned between a fully-darkened state and fully-bleached state under the voltage (in the range of 0-3.5 V) supplied by the front BIPV panel via a voltage controller. Murray et al. [120] developed a smart window based on a Polymer Dispersed Liquid Crystals (PDLC) device for daylighting control, which is powered by an a-Si absorbing layer deposited on the glass coverslip, as shown in **Figure 1.21** (b). The PDLC device scatters incident light in the absence of an electric field (0V, OFF state) and is transparent to visible light under applied voltage (150V, ON state). The visible light transmittances are 41% and 68% for the smart window in the OFF and ON states, respectively. However, concerning its limited transmission modulation for visible light and NIR radiation, the BIPV-PDLC smart window may not be fully competent to address glare and overheating problems. Moreover, most of commercially available PDLC films demand a comparatively high voltage in order to maintain its transparent state, which could result in high electricity consumption and also a potential safety risk [122].

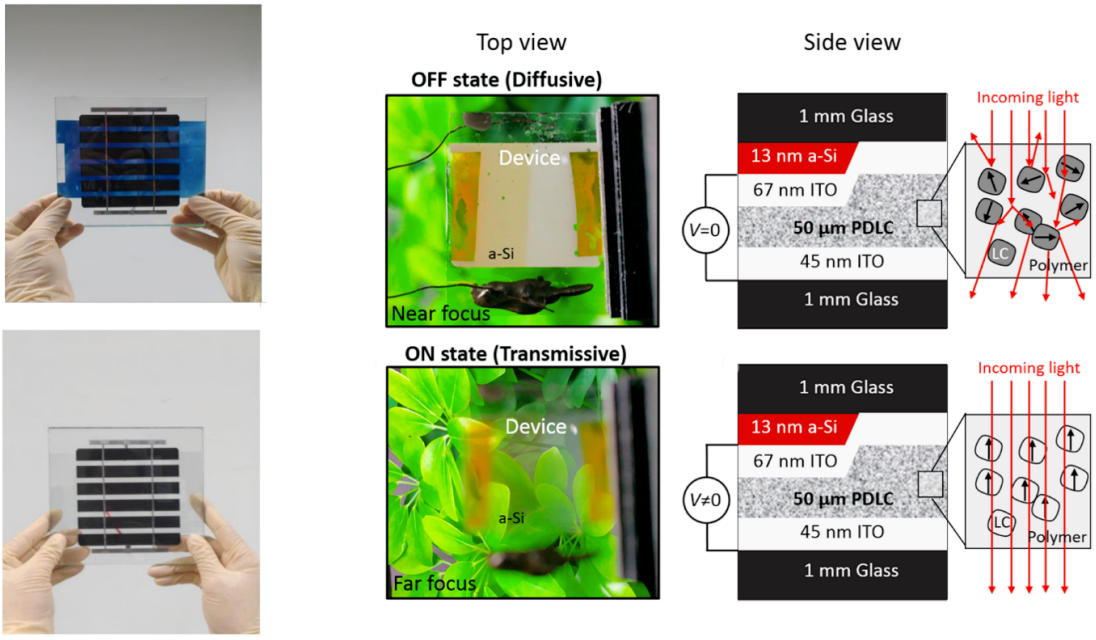

(a) (b)

Figure 1.21: (a) Photographs of the BIPV-EC smart window in a coloration (top) state and a bleached state (bottom). (b) Photographs and schematics of the BIPV-PDLC smart window; a-Si absorbers in amber colour are deposited on the sides of the glass coverslip. Source: [118, 120].

Zhao et al. [121] reported an electricity-generating smart window that utilises a VO_2-based thermochromic film to regulate the near-infrared transmittance in response to temperature change and simultaneously scatter a portion of incident light to the edge-attached poly c-Si solar cells for electricity production. Power conversion efficiencies of only up to 0.52% were realised by the scattering effect. Moreover, the applied VO_2 film has a transition temperature as high as 68°C, which limits the use of the window for practical applications.

Wu and co-workers [123] proposed an HPC based thermotropic reflective layer for integration with a BIPV window/facade in order to realise passive solar control and electricity generation within buildings (see **Figure 1.22**). Optical models developed with the aid of a 3D ray-tracing technique were used for the CPV system design and optical analysis. The optical efficiency and optical concentration ratio of the system were predicted to be 10% and 0.5 respectively when the diffuse reflectivity of the thermotropic layer is 50%. The study provides a rough picture of the relationship between the CPV performance, geometric design specifications and components' optical properties. The applicability of the proposed system needs to be further explored and validated in the context of laboratory conditions and building environments.

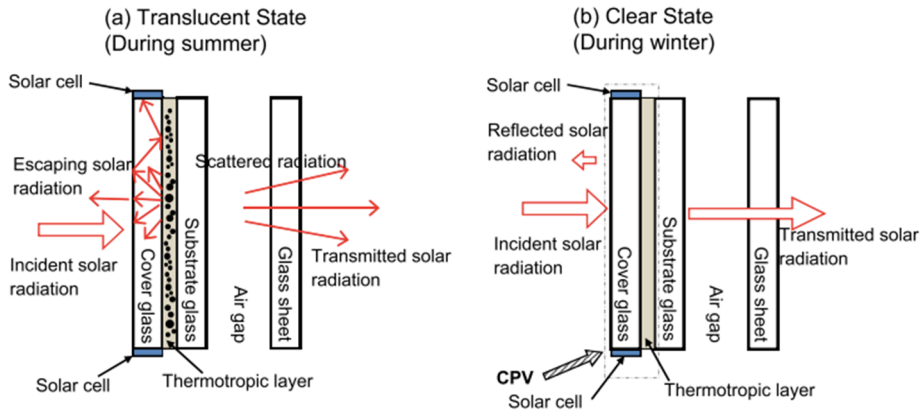

Figure 1.22: Cross-sections of a window integrated with edge-attached solar cells and a reflective thermotropic layer (a) in the translucent state and (b) in the clear state. Source: [123].

1.6 Summary of the literature and research gap

There is a wide range of static, dynamic and smart glazing options for daylighting control and energy-saving purposes. BIPV glazing that provides effective solar shading together with on-site electricity generation occupies a pivotal position. PV cells such as c-Si, a-Si, CdTe and DSSC find their applications in BIPV glazing, each of which has advantages and disadvantages (see **Table 1-2**). Of these, c-Si BIPV glazing is a mature and well-developed technology, but the critical aspects are still the opaqueness and insufficiently high power output per unit area of c-Si solar cells.

A viable strategy is to integrate c-Si BIPV glazing with inexpensive concentrating optics, enabling a reduction in the PV cell coverage area with least significant sacrifice of the power output. The solutions offered so far include developing BICPV windows based on semi-transparent rear reflectors and dielectric based Compound Parabolic Concentrators (CPCs) (see **Table 1-2**). The major shortcoming associated with the BICPV designs using Lambertian diffuse reflectors or luminescent-dye-doped backplates, is that they could not encompass both features: high transparency (for daylighting and viewing) and high scattering (for solar concentration and glare control). This issue may be potentially solved through incorporating switchable reflective layers in BIPV windows.

Hydrogels based on Hydroxypropyl Cellulose (HPC) polymer are a type of optically switchable thermotropic materials receiving attention for their application in smart windows. HPC hydrogel has numerous advantages over synthetic thermotropic hydrogels (e.g. PNIPAm) in terms of visible-near-infrared spectrum modulation, availability, environmental sustainability and cost. In recent decades, a few researches have been carried out to explore the thermal and optical characteristics of HPC based thermotropic smart windows and their performance in buildings.

The novel design of combing a BIPV window with an optically switchable thermotropic layer intends to overcome the technological challenge faced by the Lambertian-diffuse-reflector-based BICPV windows mentioned above. Although simplified ray-tracing models (assuming the thermotropic layers as Lambertian diffuse reflectors) have been developed for the window design and optical analysis, the model accuracy has not been demonstrated. The concept needs to be further validated under quasi-static or dynamic environmental conditions and examined on the building scale, in order to fully understand the window's thermal, optical and electrical behaviours as well as its effect on the energy consumption and comfort in buildings.

Table 1-2. Performance and challenges of BIPV and BICPV glazing technologies.

		Features	Challenges	Effect on building performance
BIPV glazing system	c-Si	* Well-developed PV technology * High power conversion efficiency of solar cell and BIPV module	* Opaque and thick solar cell * PCE is susceptible to PV operating temperature and shading	* Solar heat gain and daylighting reductions * Inhomogeneous daylighting for the interior space
	a-Si	* Semi-transparent, thin, lightweight, bendable * Low cost in large scale production * Better heat resistance than c-Si * Long operational lifetime	* Low power conversion efficiency * Increasing the PCE would sacrifice the cell transparency	* Lower cooling loads in summer but higher heating loads in winter * Better uniformity of illumination in the indoor space than c-Si BIPV glazing * Auxiliary shading devices are needed to eliminate glare
	CdTe	* High PCE, low generation cost and low energy payback time * Good performance at elevated temperature * Fast deposition process	* Detrimental effects on human health and environment * Dark colours	
	DSSC	* Various transparencies & colours * Good performance in variable lighting conditions * Simple manufacture and low cost	* Low power conversion efficiency * Chemical degradation * Electrolyte leakage	
BICPV glazing system	Luminescent solar concentrator (LSC)	* Various degrees of transparency and colour * Large acceptance angle * Simple manufacture and low cost	* High optical loss due to light escaping, reabsorption, etc. * Low optical efficiency	
	Compound parabolic concentrator (CPC)	* High optical efficiency and optical concentration ratio	* Non-uniform solar irradiation and temperature distribution on PV cell * Cell deterioration due to hot spot * Non-planar and bulky structure	* The coverage area of solar cells in BIPV glazing is reduced without compromising the power output * The concentrating optics may distort the view out of building
	Lambertian rear reflector	* Light-scattering effect * More uniform irradiation on solar cell than BICPV with V-grooved rear reflector, CPC, etc.	* High reflectance but low transparency, potentially not suitable for glazing application.	* Glare reduction * Poor passive solar heating and daylighting

1.7 Research aim and objectives

The research presented here aims to design, develop and characterise a novel BIPV thermotropic smart window system for electricity generation and adaptive daylighting control. The system incorporates a new thermotropic hydrogel, which is made of HPC polymer, gellan gum and sodium chloride, for controlling the heat gains and daylight through the window and also serving as a concentrating optics to redirect sunlight to integrated PV cells. In the transparent state, the proposed system is expected to work similarly as a conventional PV window (i.e., with no thermotropic layer) in terms of solar heating, daylighting and visual effect. In the light-scattering state, the system is expected to provide more effective solar shading as well as higher electric power outputs (up to 15%) in comparison with the conventional PV window.

The main research objectives are:

- To develop a thermotropic hydrogel membrane suitable for application in BIPV windows, with an appropriate transition temperature, high visible/solar transmittance at room temperature, large solar transmittance modulation and strong scattering in the wavelength region which is compatible with the spectral response of c-Si solar cells.
- To develop a reliable optical modelling method for predicting the scattering characteristics of translucent materials including the proposed thermotropic hydrogel and also for aiding the design and optimisation of the proposed BIPV smart window system.
- To experimentally characterise the thermal, optical and electrical performance of the prototype BIPV smart window system in controlled laboratory conditions as well as real climatic conditions. These experiments are expected to prove the above concept and show the effectiveness of the proposed system in modulating its optical properties (e.g., the system automatically varies its visible and solar transmittance between 10% and 90% upon heating or cooling) and also electrical properties (e.g., the power output is increased by 15-20% when the state is switched from transparent to light-scattering).
- To conduct building performance simulation to explore the potential of the proposed BIPV smart window system in building energy saving, on-site renewable energy generation, solar heat gain and daylighting control. The annual energy saving is expected to be 40-50% provided by the proposed system, as compared with the conventional double-glazed windows that are widely used in the UK.

1.8 Thesis outline

The thesis structure is shown in **Figure 1.23**.

In **Chapter 2,** a simple Monte-Carol ray tracing model has been developed to design and predict the performance of the proposed BIPV smart window system. A thermotropic hydrogel membrane consisting of Hydroxypropyl Cellulose (HPC) and Gellan Gum type F (GGF) was synthesised as the optically switchable layer for the BIPV smart window system. Subsequent to the optical design and material development, a small-scale prototype for the BIPV smart window system was fabricated. Finally, proof-of-concept indoor experiments were conducted.

Chapter 3 presents an advanced optical modelling technique for the design and optimisation of the BIPV smart window system. This technique involved an Inverse Adding-Doubling (IAD) method combined with a Double-Integrating-Sphere (DIS) spectral measurement, from which the volume scattering properties of the thermotropic membrane at varying temperatures were obtained and used

for ray-tracing analysis. The accuracy of the advanced optical modelling technique has been validated by experiments.

In **Chapter 4**, the HPC-GGF based thermotropic membrane (developed in **Chapter 2**) was optimised in terms of transition temperature, solar transmittance modulation and light-scattering ability through the addition of salt such as sodium chloride (NaCl). A prototype for the BIPV smart window system with the optimised thermotropic membrane and the optimised window design parameters (determined through the parametric analysis in **Chapter 3**) was fabricated. The thermal, optical and electrical performance of the prototype BIPV smart window system was subsequently evaluated by indoor experiments.

In **Chapter 5**, the developed BIPV smart window system and a conventional BIPV window system (reference) were characterised and compared by outdoor experiments under the UK climatic conditions. Different window inclinations, window dimensions and weather conditions were considered in the outdoor experiments.

In **Chapter 6**, EnergyPlus simulations were conducted to explore the potential of the proposed BIPV smart window system in reducing the energy consumption and improving the luminous environment in an UK office building. The EnergyPlus models were developed using the measured/calculated window properties as input, which were derived with the aid of the advanced optical modelling technique (**Chapter 3**) and the spectroscopic measurement (**Chapter 4**). The effects of different window design parameters, such as Window-to-Wall Ratio (WWR), window orientation and hydrogel transition temperature, on the building energy and environmental performance were numerically investigated.

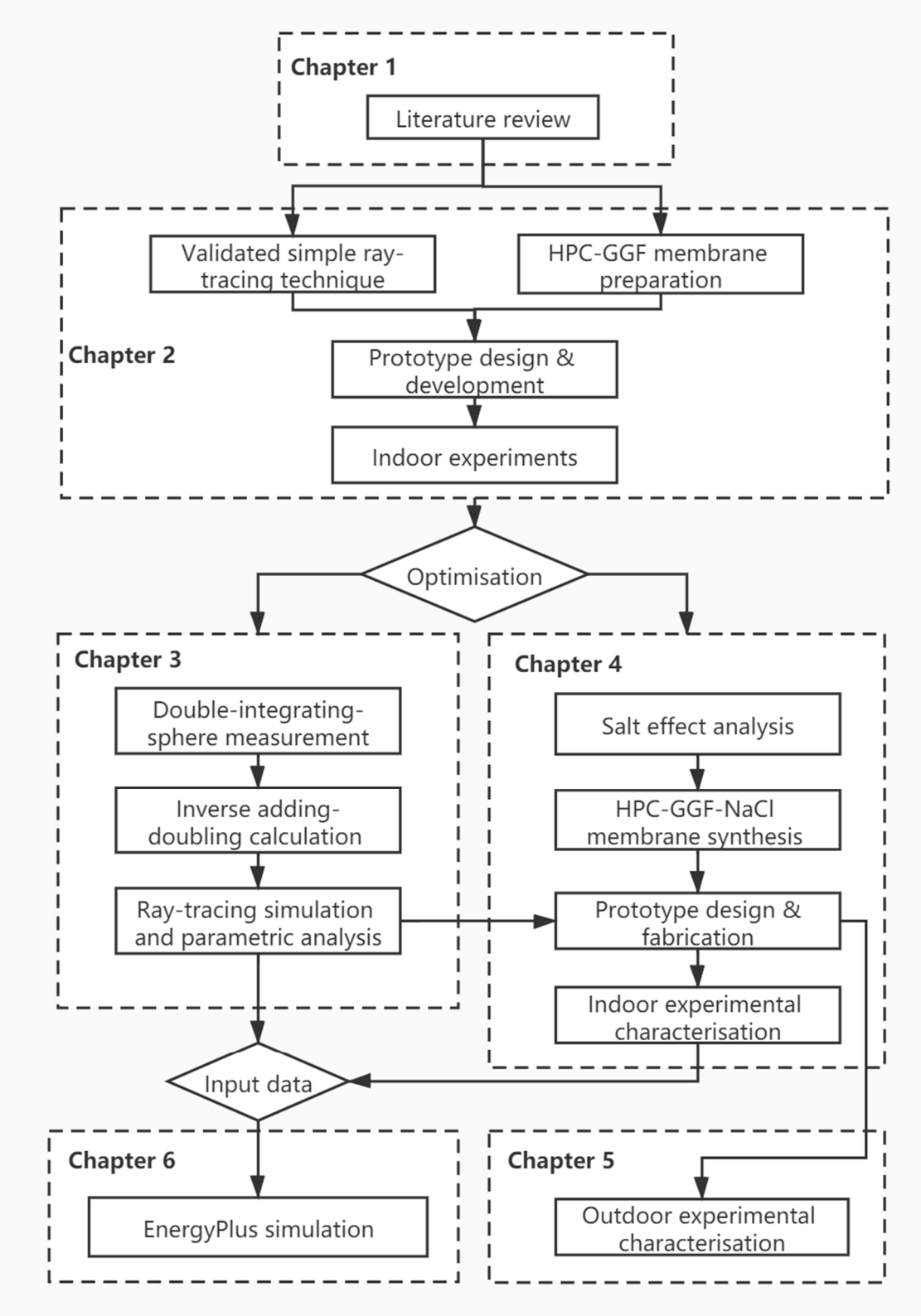

Figure 1.23: Structure of this thesis.

Chapter 2 – Preliminary window design and characterisation based on a simplified optical model

2.1 Introduction

Diffuse reflectors made of opaque white materials with high reflectivity can be incorporated in solar modules to realise static (i.e., non-tracking) concentrators [65, 69, 70, 124]. However, these diffuse reflectors may not be suited for BIPV window or façade applications, where good glazing transparency is essential for indoor space heating, daylighting and viewing. The contradiction between reflectivity and transparency can be resolved by using an optically switchable diffuse reflector. Connelly et al. [107] synthesised a thermotropic diffuse reflective membrane based on Hydroxypropyl Cellulose (HPC) hydrogel for application in BIPV smart windows. The developed membrane has a transition temperature of approximately 42°C, with an average visible light transmittance of over 90% below its transition temperature and an average visible light reflectance of up to ~50% above the transition temperature. Wu et al. [123] proposed a BIPV smart window system that mainly consists of two traditional glass panes, a thermotropic diffuse reflective layer and commercially available solar cells mounted at the glass cover edges. A 3D ray-tracing technique was applied to predict the optical performance of the CPV system under different window design parameters, such as the thickness, aperture area and refractive index of its front glass cover. Nevertheless, neither prototype has been developed, nor experiment has been conducted so far to prove the concept and verify the optical simulation.

In this chapter, a novel BIPV smart window system consisting of an optically switchable thermotropic membrane layer with integrated PV cells has been designed, fabricated and experimentally characterised. The thermotropic membrane was synthesised by dissolving HPC polymer and gellan gum in distilled water, and its dynamic optical properties was obtained by spectroscopic measurement. A wavelength-dependent Monte-Carlo ray-tracing model was developed to predict the dynamic behaviour of the novel system and also in aid of the system design. A prototype of the BIPV smart window system was subsequently fabricated and comprehensively investigated under controlled indoor environmental conditions, in terms of the electrical and optical performance with respect to different temperatures and HPC concentrations of the thermotropic membrane as well as different intensities and angles of light incidence.

2.2 Concept of the BIPV smart window system

The BIPV smart window system is mainly comprised of a front glass pane, an encapsulation layer with evenly spaced c-Si solar cells, a thermotropic layer and a back glass pane, as shown in **Figure 2.1**. The

thermotropic layer switches from a transparent state to a translucent/light-scattering state when its temperature increases from below a designed transition temperature to above it. In other words, when below the transition temperature, the window appears transparent; a portion of the incident solar radiation strikes the solar cells for electricity generation, while most of the rest radiation passes through the window for indoor space heating and daylighting, with a small amount lost due to the reflection off the front glass pane. When the thermotropic layer is in the translucent state, as shown in **Figure 2.1**, a fraction of the scattered radiation is trapped within the window and redirected to the solar cells for electricity generation through Total Internal Reflection (TIR). Some of the scattered radiation escapes from the front and back glass panes because the angles of incidence at the glass-air interface are less than the critical angle expressed by **Equation (2.1)**. As heated to a higher temperature, the thermotropic layer becomes increasingly reflective, potentially resulting in a higher electricity generation rate. Meanwhile, less solar heat and light penetrate through the window into the building interior, potentially reducing the risks of overheating and glare.

$$\theta_c = \sin^{-1} \frac{n_{air}}{n_{glass}} \tag{2.1}$$

Where θ_c is the critical angle at the glass-air interface, n_{air} is the refractive index of air and n_{glass} is the refractive index of the glass pane.

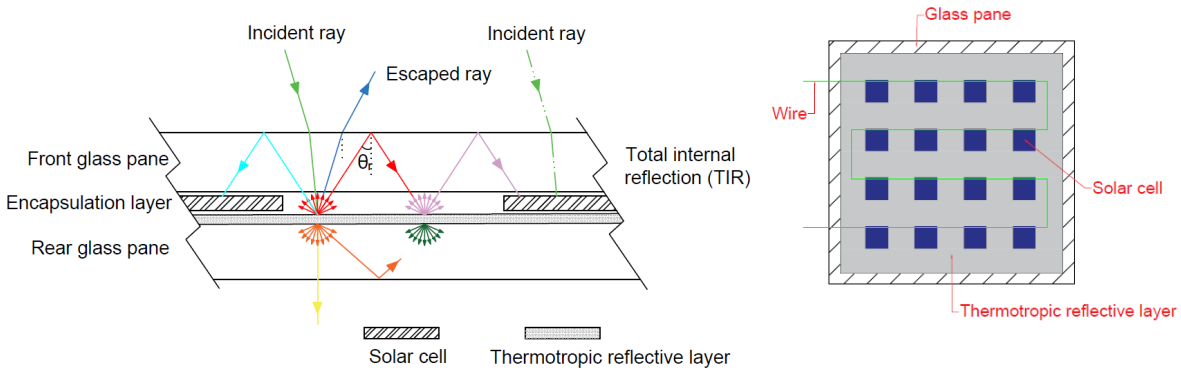

Figure 2.1. (a) Cross-sectional and (b) front-view schematic diagrams of the BICPV smart window system.

2.3 Methodology

To show the effectiveness of the proposed concept, a small-scale prototype system was developed and evaluated. The system development process applied a series of steps combing experiments and optical simulation (see **Figure 2.2**). Initially, a HPC-based thermotropic hydrogel membrane was synthesised and characterised by optical spectroscopy. The temperature variation of the spectral transmittance and reflectance of the thermotropic hydrogel membrane was measured and then

imported to a validated optical model for the design of the prototype system. The optical model was established based on a wavelength-dependent Monte-Carlo ray-tracing technique, which was validated in advanced by experimental tests with commercially available solar control films, which have different static optical properties (i.e., different films with static transmittances and reflectances). With the aid of the optical model, the prototype system was designed, optimised and fabricated. Finally, indoor experiments were carried out to obtain the prototype system performance and verify the proposed concept.

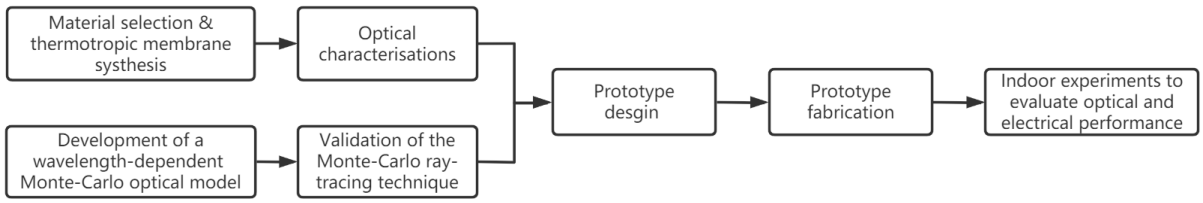

Figure 2.2. Flow chart showing the BIPV smart window development process.

2.3.1 Prototype development and experimental characterisation

2.3.1.1 Material selection and thermotropic hydrogel synthesis

To fit for window application, thermotropic materials would need to fulfil requirements of [90, 91, 97, 108]: (1) reversible switching between a clear state with >85% transmittance and a light-scattering state with <15% transmittance; (2) steep switching gradient within a small temperature range (<10°C); (3) transition temperature in the range between 25°C and 40°C; (4) low hysteresis upon heating and cooling; (5) long-term stability and good weatherability; (6) availability in a large area at low costs.

Hydroxypropyl cellulose (HPC) based hydrogels have been proved to be a promising candidate to meet most of the above demands [91, 97, 107]. Moreover, HPC based hydrogels can effectively scatter solar radiation in the wavelength range of 350-1100 nm, which is compatible with the spectral response of c-Si solar cells [107, 108]. These features make HPC based hydrogels potentially well suited for use in the proposed BIPV smart window system. In this study, the thermotropic reflective layer of the BIPV smart window was synthesised based on HPC and gellan gum (gelling agent) by the following steps:

HPC polymer (weight average molecular weight M_w ~80,000 and number average molecular weight M_n ~10,000) received as an off-white powder from Sigma Aldrich was magnetically stirred into distilled water at room temperature (25°C). The stirring was maintained at 100 rpm for several hours until all the HPC had dissolved. For example, it took approximately 2 hours to prepare an aqueous solution with 6 wt % HPC invisible to the naked eye. A gel matrix was prepared by dissolving Gellan Gum type F (GGF) powder supplied by Special Ingredients in distilled water at 80°C. A pipette was used to slowly add the HPC aqueous solution into the gel matrix at 60°C with a stirring speed of 200 rpm. After the

addition was completed, the HPC-GGF based aqueous solution was left stirring at 100 rpm with heating off for 10 minutes. After naturally cooled to the gel state, the HPC-GGF based hydrogel was cast between two GPE Scientific low-iron glass slides spaced by a 1-mm-thick gasket. After squeezed to expel trapped air, the HPC-GGF based hydrogel membrane fully filled the cavity between the glass slides with no empty areas, implying a uniform membrane thickness (1 mm).

2.3.1.2 Optical characterisations

The spectral transmittance of the HPC-GGF based hydrogel membrane was measured using an Ocean Optics USB2000+UV-VIS-ES spectrometer with an Ocean Optics FOIS-1 integrating sphere. The spectral reflectance was measured with the same spectrometer and an Ocean Optics ISP-REF integrating sphere. The measured spectra had been baseline-corrected (i.e., excluding the spectra of the low-iron glass slides) using the method presented by Connelly et al. [108]. Specifically, prior to measure the sample spectrum (i.e., the intensity of light transmitted through the laminated glass unit), a single GPE Scientific low-iron optical glass with 8 mm thickness was placed on the FOIS-1 integrating sphere to obtain a reference spectrum. With the reference spectrum, dark spectrum (i.e., no light entering the integrating sphere) and sample spectrum, the spectral transmittance of the HPC-GGF based hydrogel membrane was calculated in the software OceanView. Similarly, the membrane's reflectance was obtained by measuring the reference, dark and sample spectrums through the ISP-REF integrating sphere. In contrast, the baseline standard for the reflectance tests was an Ocean Optics WS-1 diffuse reflectance standard (>98% reflective from 250-1500 nm) combined with a 4-mm-thick GPE Scientific low-iron optical glass.

A GyroStir-DH hotplate was applied to heat the surface of the laminated glass unit uniformly (within ±1°C). Meanwhile, the temperature of the HPC-GGF based hydrogel membrane was monitored by an embedded T-type thermocouple that had been waterproofed with epoxy resin adhesive. After the hydrogel membrane was heated to a required temperature, 15 minutes were allowed for temperature equilibrium before taking the transmittance and reflectance measurements.

2.3.1.3 Prototype fabrication procedures

A prototype for the designed BIPV smart window system was fabricated following the steps plotted in **Figure 2.3**. Firstly, a Dow-Corning® 1-2577 transparent silicone-based coating with a thickness of 1 mm was cast on a GPE Scientific low-iron glass slide (50 mm x 50 mm x 4 mm), and left to cure at room temperature for 20 minutes to allow solvents to flash off and blisters to disappear. Next, a Talesun c-Si solar cell (1 cm^2 active area) with its front side facing down was placed at the centre of the coated glass substrate and encapsulated by a second layer of Dow-Corning® 1-2577 coating with 1 mm thickness. The coating was left to solidify at room temperature for 24 hours. Subsequently, the

synthesised HPC-GGF based hydrogel (following the steps 3-6 detailed in **Section 2.3.1.1**) was poured onto a second GPE Scientific low-iron glass slide (50 mm x 50 mm x 4 mm) that has a 1-mm-thick gasket attached to it. Then, the HPC-GGF based hydrogel was covered by the PV-adhered glass substrate (prepared in step 2) with pressing to get rid of air bubbles. Finally, the laminated glass unit was sealed around the edges using glass sealant and butyl tape to prevent the hydrogel from leaking and drying out, and mounted in a frame made by a 3D printer. For making a commercial normal-sized window, a process similar to the above description can be applied, but may require more advanced skills and equipment, especially when dealing with large-scale material preparation and weather-proof sealing.

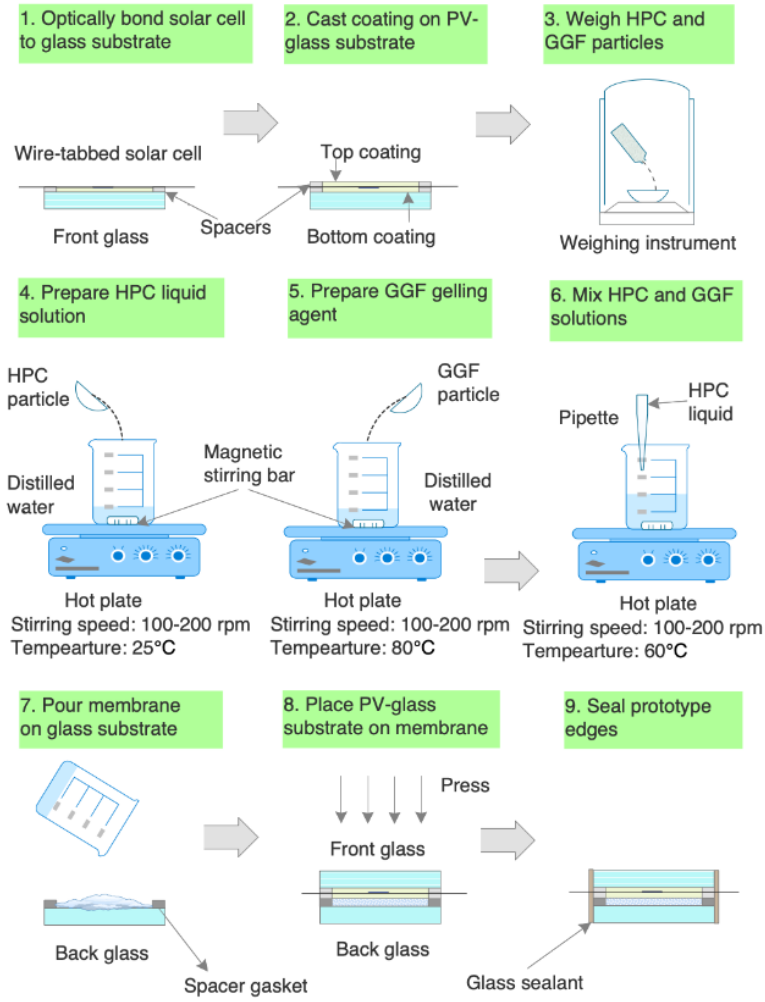

Figure 2.3: Prototype fabrication steps.

2.3.1.4 Indoor experimental setup

The prototype BIPV smart window was characterised under indoor conditions using the experimental setup shown in **Figure 2.4** (a-c). The sample was mounted on a height-and-angle adjustable holding platform and irradiated by a tungsten halogen lamp. The irradiation level at the sample aperture height was measured with an Ocean Optics optical sampling system consisting of a USB2000+VIS-NIR-

ES spectrometer, a CC-3-UV-S cosine corrector and a 200-µm-core-diameter optical fibre. The optical sampling system had been calibrated for absolute spectral irradiance against an Ocean Optics LS-1-CAL halogen light source, and its accuracy had been verified by a Kipp & Zonen CMP11 pyranometer (see **Figure 2.4** (d)). The irradiation spectrum of the tungsten lamp is presented in **Figure 2.7**. The uniformity of the total irradiance (i.e., the integral value of irradiance spectrum) over the sample aperture area (50 mm × 50 mm) was measured to be within ±5%. The sample was connected to a Keithley 2420 Source Meter Unit (SMU) via a 4-wire remote sensing method (also known as Kelvin configuration) [87, 125, 126] for electrical characterisations. The solar cell temperature and membrane temperature of the sample were detected using a DT85 data logger with T-type thermocouples. The measurements were performed at least in triplicate, and data were expressed as mean ± standard deviation. The specifications of the equipment and sensors are listed in **Table 2-1**.

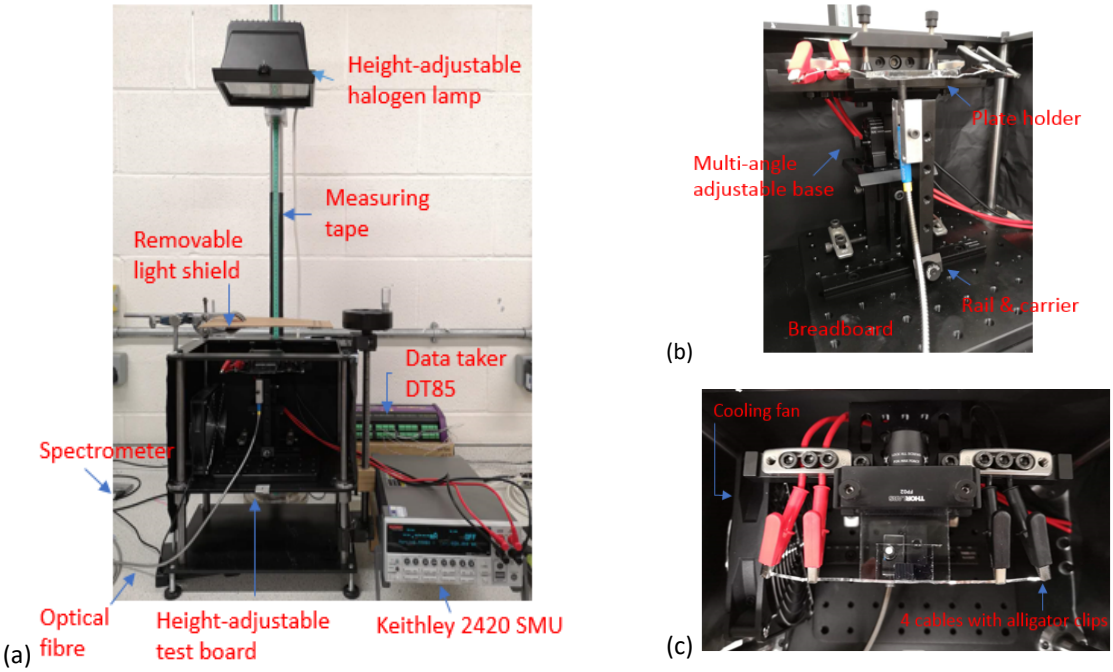

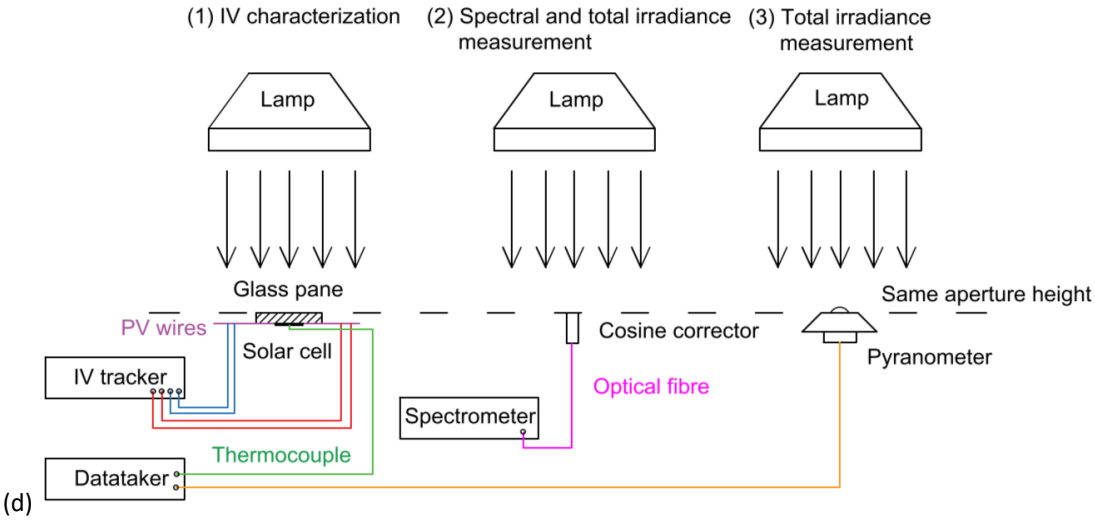

(e)

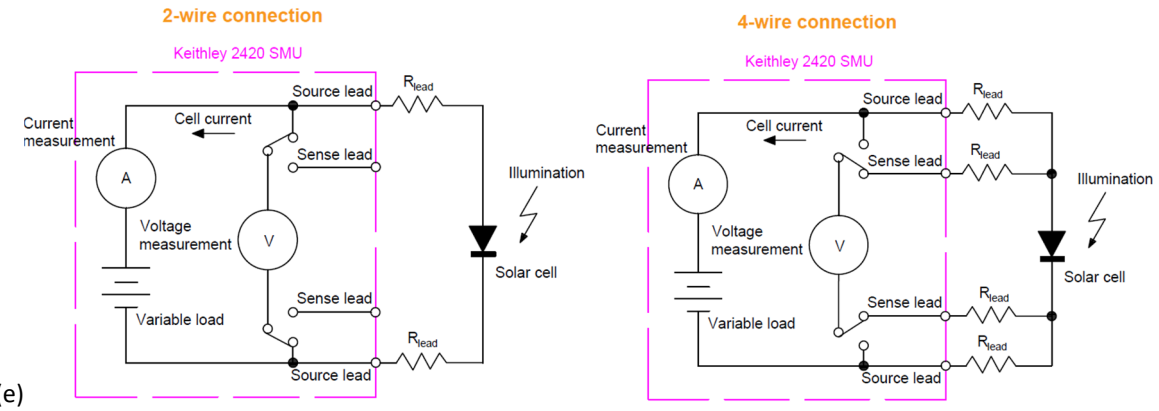

Figure 2.4: (a-d) Photographs and schematic diagram of the indoor experimental setup, (e) 2-wire and 4-wire methods for the connection between the SMU and solar cell.

The purpose of using 4 wires (instead of 2 wires) for the connection of the Keithley 2420 SMU to an illuminated solar cell is to eliminate the effect of wire (or lead) resistance. As depicted in **Figure 2.4** (d), the current generated in the solar cell flows through a pair of source leads and is measured by an ammeter inside the SMU. In terms of 2-wire connection (see the left diagram), voltage measurement is performed using a voltmeter inside the SMU, the value of which equal the voltage drop across the solar cell plus that in the sense leads. If a large photocurrent flows through the circuit, the voltage drop in the sense leads can be significant (i.e., voltage drop = current × lead resistance) [127]. As a result, the voltage measurement on the solar cell may be incorrect. In terms of 4-wire connection (see the right diagram), the current generated in the solar cell is measured using the source leads, while the voltage is measured using the sense leads. Since almost no current flows to the voltmeter, the voltage drop in the sense leads is negligible and only the voltage drop across the solar cell is measured [127]. The 4-wire method can provide a more accurate I-V measurement than the 2-wire method, especially when using large-area solar cells with long wires.

Table 2-1: Specifications of the experimental devices.

Equipment	Model	Specification and measurement range	Measurement accuracy
Data logger	Datataker DT85	Measuring voltage output from thermocouples; calibrated to ITS-90 standard for thermocouple reading;	0.1% variance for DC voltage (5 to 40°C)
Thermocouple	T-type thermocouple	Temperature range of -75 to 250°C;	±0.5°C
Spectrometer	Ocean Optic USB2000+UV-VIS-ES spectrometer	Measuring irradiance, transmittance, reflectance and absorptance; spectral resolution: 0.5 nm;	Signal-to-noise ratio: 250:1
Irradiance detector	Ocean Optics CC-3-UV-S cosine corrector	Collecting light from a 180° Field of view; diffuser diameter: 3900 µm; spectral range: 200 to 2500 nm;	
Optical fibre	Ocean Optics UV-Visible patch cord	Transmitting light; fibre core diameter: 200 µm	
Calibration light source	Ocean Optics LS-1-Cal halogen light source	Calibrating the absolute spectral response of an optical sampling system;	
Pyranometer	Kipp & Zonen CMP11	Spectral range: 285 to 2800 nm; Field of view: 180°; maximum solar irradiance: 4000 W/m^2	<0.2% non-linearity (100 to 1000 W/m^2)
I-V tracker	Keithley 2420 source meter	Maximum sourcing current: 3A; maximum sourcing voltage: 60V; minimum resolutions: 1µV and 100 pA;	0.012% basic measurement accuracy for voltage

2.3.2 Development and validation of the wavelength dependent Monte-Carlo optical model

Ray-tracing techniques have been widely adopted in the design and performance analysis of solar concentrating systems. The principle is to launch a bundle of rays from a light source and track their trajectories in a solar concentrating system to obtain the irradiance/illuminance at the surface of interest [128]. For a mirror or lens-based solar concentrator, the incident ray paths are altered by specular reflection or refraction at the geometrical surfaces [84, 129]. For a diffuse type solar concentrator, when light encounters a diffuse surface/body, it is scattered into a wide range of directions. This phenomenon can be modelled using a stochastic sampling method, named Monte-Carlo ray-tracing technique. In principle, the continuous light scattering distribution is approximated by a set of random rays with possible directions [130] (see **Figure 2.5**). The directions of scattered rays are randomly selected according to a prescribed probability distribution function [131, 132]. Due to the stochastic nature of the Monte-Carlo ray-tracing process, a large quantity of rays is required to be traced in order to achieve a good approximation [123, 133].

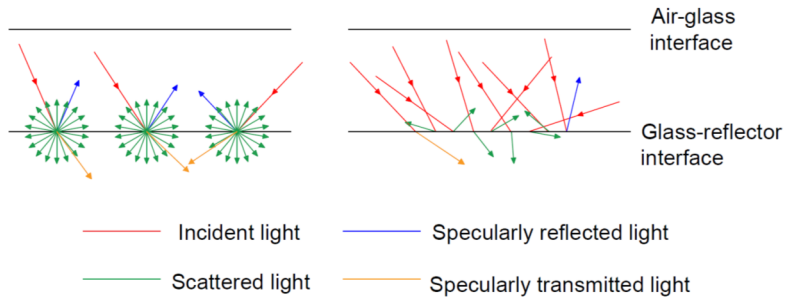

Figure 2.5: Schematic diagrams of light scattering at a surface in reality (left diagram) and modelled by a Monte-Carlo ray-tracing technique (right diagram). Note: scattering is a 3D phenomenon, but here shown in 2D.

2.3.2.1 Optical model description

A Monte-Carlo ray-tracing simulation approach coupled with measured material properties was developed to predict the radiation characteristics of the BIPV smart window system. A Monte-Carlo ray-tracing model was set up in the software TracePro, involving four steps: (1) constructing the geometry of the system; (2) applying measured spectral properties to the geometrical components; (3) defining rays emitted from a light source; (4) propagating rays through the system and calculating the flux on the absorber surfaces (solar cells).

In designing the prototype system, a 3D model geometry was created with a single solar cell and a four-layer stacked structure: front glass cover, optical coating layer, thermotropic membrane layer and back glass cover, similar as seen in **Figure 2.1**. The geometric design parameters, such as glass cover thickness and aperture area, were determined through a parametric analysis (detailed in **Section 2.4.1.2**). The optical model assumed the thermotropic membrane layer as a Lambertian-type diffused reflector, i.e., a surface reflecting light equally in all view directions (i.e., no angular dependence) [134-136]. The spectral reflectance and transmittance at different temperatures of the thermotropic membrane layer were measured (see **Figure 2.12**) and used as the Lambertian surface properties. The glass covers and optical coating were defined with the wavelength-dependent optical constants, including refractive index (n_s) and absorption coefficient (α_s), calculated by **Equations (2.2)-(2.7)** [137] and shown in **Figure 2.6**. For simplicity, the front side of the solar cell was assumed as a perfect absorber of light (with 100% optical absorptance), while its back side was assumed as a perfect Lambertian surface (with 100% diffuse reflectance). To match the laboratory conditions as closely as possible, the spectral irradiance of the light source was equal to the result measured for the applied tungsten halogen lamp (see **Figure 2.7**). The number of the rays, which were emitted from the light source and perpendicularly applied to the aperture of the front glass cover of the prototype system, was set to 1,000,000 according to a ray-independence study.

In the process of tracing a ray through the system, the outcome of events (transmission, reflection, scattering and absorption) was determined by the Monte-Carlo method [62, 138, 139]. Specifically,

each time the ray intersects a surface, the surface properties (specular/diffuse transmittance, specular/diffuse reflectance and absorptance) are used as probabilities and compared to a randomly generated number (between 0 and 1); for example, for a non-absorbing surface with 30% reflectance and 70% transmittance, if the number is between 0 and 0.3, the ray is reflected, otherwise the ray is transmitted. The process continues until the ray is lost from the system, absorbed by the solar cell or attenuated with its energy flux below the predefined threshold 5% (i.e., fraction value of starting energy flux).

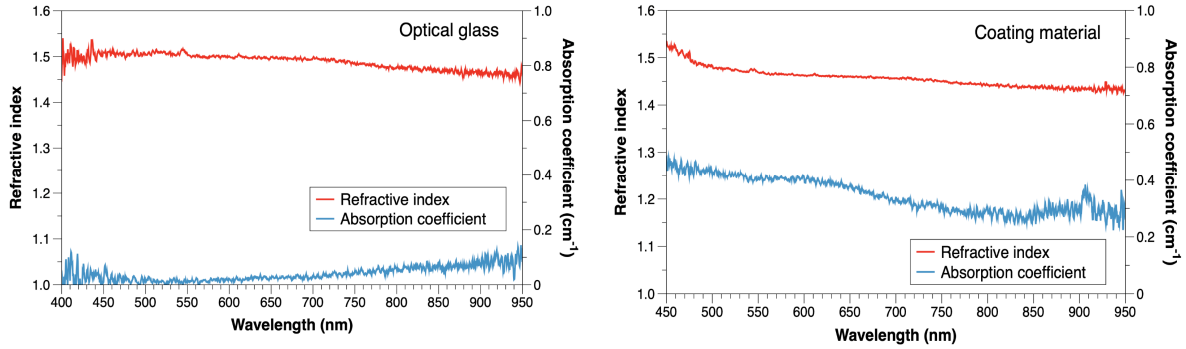

(a) (b)

Figure 2.6: Spectral absorption coefficient and refractive index for (a) the GPE Scientific low-iron glass slide and (b) the Dow-Corning® 1-2577 coating layer. The spectral values were calculated based on the directional-hemispherical reflectance and transmittance of the materials which were measured over the 450-950 nm wavelength range by an Ocean Optics USB2000+VIS-NIR-ES spectrometer with integrating spheres.

$$n_s = \frac{1+\sqrt{r_s}}{1-\sqrt{r_s}} \tag{2.2}$$

$$\alpha_s = \frac{4\pi k_s}{\lambda} \tag{2.3}$$

$$r_s = \frac{\psi - \sqrt{\psi^2 - 4(2-R_{sub})R_{sub}}}{2(2-R_{sub})} \tag{2.4}$$

$$\psi = T_{sub}^2 - R_{sub}^2 + 2R_{sub} + 1 \tag{2.5}$$

$$k_s = -\frac{\lambda}{4\pi d} ln\, \tau_S \tag{2.6}$$

$$\tau_S = \frac{R_{sub} - r_s}{r_s\, T_{sub}} \tag{2.7}$$

Where n_s is the refractive index of the substrate, α_s is the absorption coefficient of the substrate, r_s is the reflectance at the air-substrate interface, τ_s is the internal transmission of the substrate, R_{sub} and T_{sub} are the directional-hemispherical reflectance and transmittance of the substrate obtained from spectroscopy measurements, k_s is the extinction coefficient of the substrate, d_s is the substrate thickness, λ is wavelength, ψ is a parameter used to simplify Equation (2.4).

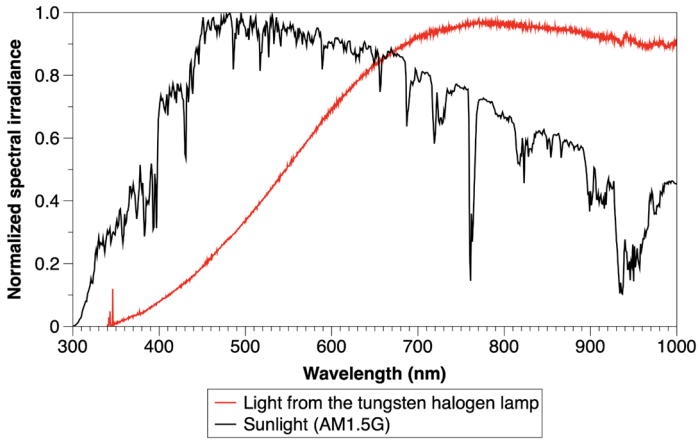

Figure 2.7: Normalised irradiation spectrum of the tungsten halogen lamp compared with the normalised standard AM1.5G solar spectrum.

2.3.2.2 Validation of the Monte-Carlo ray-tracing model

Prior to the design of the prototype system, a preliminary verification of the proposed Monte-Carlo ray-tracing technique by indoor experimental tests was carried out. The validation samples were manufactured with a GPE Scientific low-iron glass slide (50 mm x 50 mm x 4 mm), a Talesun c-Si solar cell and different types of static diffuse reflective film, as shown in **Figure 2.8**. The c-Si solar cell has dimensions of 1 cm × 1.2 cm (1 cm^2 active area) and the electrical properties: 35 mA short-circuit current, 611 mV open-circuit voltage, 0.768 fill factor and 16.5% power conversion efficiency at standard test conditions (100 mW/cm^2 illumination, AM1.5 solar spectrum and 25°C cell temperature). The solar cell was tabbed with Ulbrich tin-coated copper PV wires (1.8 mm wide and 0.1 mm thick) using a low-melting-point tin/lead solder. The wire-tabbed solar cell and the static diffuse reflective film were optically bonded to the low-iron glass slide. The optical bonding was achieved using a Dow-Corning® 1-2577 transparent silicone coating, whose thickness on the glass substrate was uniformly controlled at 0.5 mm through the tape casting technique (also called doctor-blade method) [140, 141]. Before testing, it is important to ensure that the active area of the solar cell is in complete contact with the coated glass substrate with no solder bump and air gap in-between; otherwise, these would affect the experiment validation due to a reduced amount of light collected by the solar cell [72].

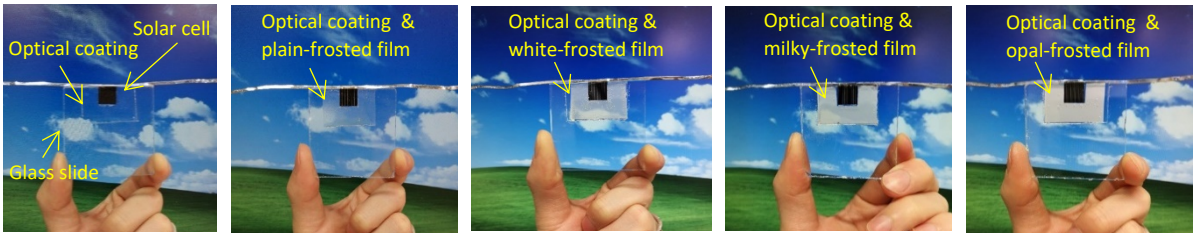

Figure 2.8: PV modules with (a) no film, (b) a plain-frosted film, (c) a white-frosted film, (d) a milky-frosted film and (e) an opal-frosted film. The ratio between the solar cell area and the frosted film area is 1:5.

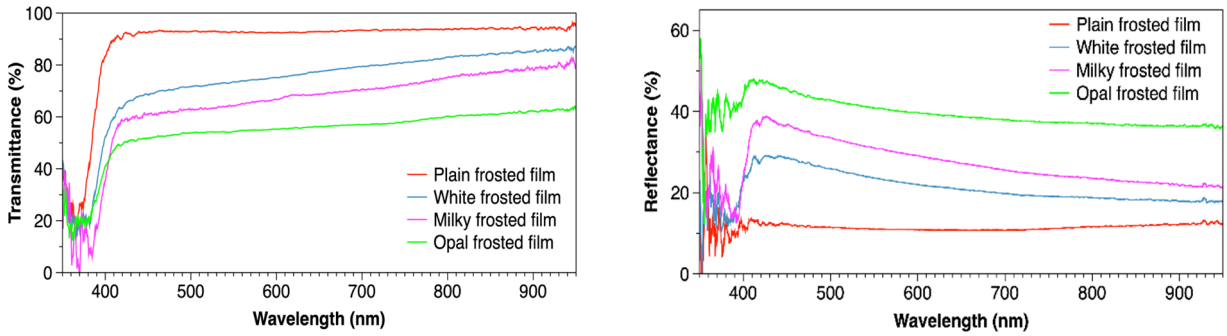

(a) (b)

Figure 2.9: (a) Spectral transmittance and (b) spectral reflectance of the frosted films from 350 to 950 nm.

The static diffuse reflective films are commercially available frosted films, named plain frosted film (Purlfrost®), white frosted film (Purlfrost Ltd®), milky frosted film (d-c-fix®) and opal frosted film (Purlfrost®). These frosted films are a type of solar control film for windows to scatter sunlight in the visible range and reduce glare. Their spectral transmittance and reflectance films were measured using the same spectroscopy method and optical devices as for the thermotropic membrane.

It can be seen from **Figure 2.9** (a) that the plain frosted film has the highest transmittance in the wavelength range from 400 to 950 nm, followed by the white frosted, milky frosted and opal frosted films; for example, the values at the 600 nm wavelength are 92.5% (plain frosted film), 75.2% (white frosted film), 66.8% (milky frosted film) and 55.3% (opal frosted film), respectively. Conversely, the opal frosted film has the highest reflectance over the 400-950 nm spectrum, followed by the milky frosted, white frosted and plain frosted films, as shown in **Figure 2.9** (b); for example, the values at 600 nm are 40.4% (opal frosted film), 30.2% (milky frosted film), 22.9% (white frosted film) and 10.1% (plain frosted film), respectively. In some cases, the sum of measured transmittance and reflectance is slightly greater than 100%, which is not realistic in practice, probably due to errors related to measurement noise (i.e., the background noise from the spectrometer can cause fluctuations in measured data). The purpose of using these different static diffuse reflective films is to acquire preliminary observations on the effect of the dynamic reflectance of the developed thermotropic membrane on PV electricity generation.

The electrical characteristics of the fabricated samples including the reference PV module (with no film) were measured using the experimental setup shown in **Figure 2.4**. The current-voltage (I-V) curve of the samples (see **Figure 2.10** (a)) was captured by sweeping the source voltage linearly through the range of 0 V to 0.62 V with a step size of 0.0031 V while measuring the corresponding current from the PV cells at each voltage step. The power-voltage (P-V) curve of the samples (see **Figure 2.10** (b)) was obtained by using linear voltage sweeps with a similar setup as described above while recording the power output from the PV cells at each voltage step.

From **Figure 2.10** and also **Figure 2.11** (a), it can be seen that the sample based on the opal frosted film has both the highest short-circuit current (17.6 mA) and maximum power output (8.5 mW), followed by the samples based on the milky frosted film (17.0 mA and 8.3 mW), the white frosted film (16.8 mA and 8.1 mW), the plain frosted film (16.1 mA and 7.8 mW) and with no film (15.1 mA and 7.3 mW). The sequence is the same as that found for the reflectance measurement. The result suggests that using a diffuse reflective film with higher reflectance for application in PV glazing can contribute to improved electricity generation.

The fabricated samples were optically modelled using the proposed Monte-Carlo ray-tracing technique. The model settings are the same as those described in **Section 2.3.2.1**, except using the measured spectral properties for the static diffuse reflective films as input. The simulated irradiance on the solar cell surface for the samples is shown in **Figure 2.11** (b). The irradiance is increased from 423.1 to 447.7 W/m^2 when the reference PV module is integrated with the plain frosted film, and further to 489.5 W/m^2 when integrated with the opal frosted film with higher reflectance. The result indicates that increasing the reflectance of the diffuse reflective film yields a more substantial solar concentration effect.

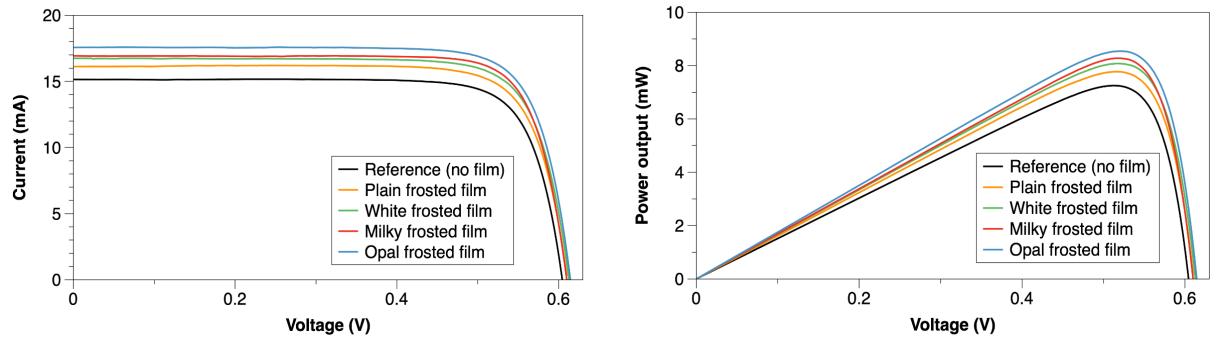

(a) (b)

Figure 2.10: (a) Current-voltage (I-V) characteristics and (b) power-voltage (P-V) characteristics of the PV modules at a cell temperature of 25°C and under an incident radiation level of 460 W/m^2. The results can also be presented as current density (mA/cm^2) and power density (mW/cm^2) without the need to change the values in these figures, because the solar cells under test have an active area of 1 cm^2.

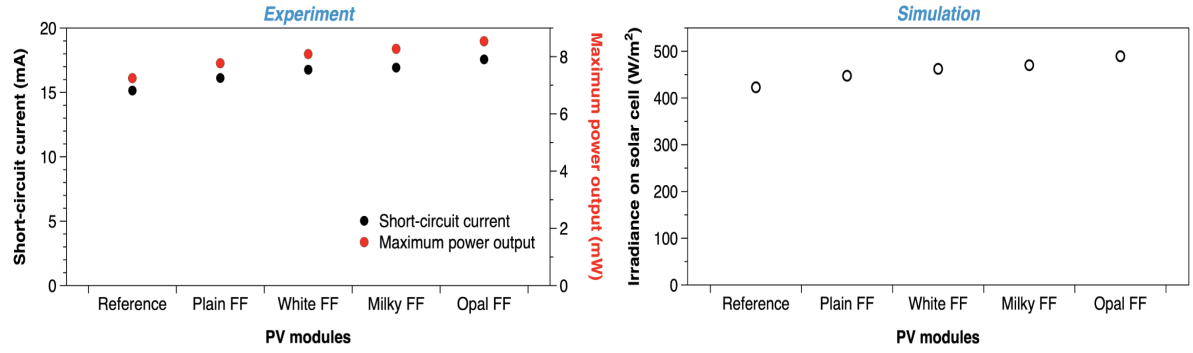

(a) (b)

Figure 2.11: (a) Measured electrical properties and (b) simulated irradiance on the solar cell for the PV modules based on different frosted-films (FF) and the reference PV module with no film.

As known from the literature [85, 142], the short-circuit current produced by a crystalline-silicon solar cell can be taken as directly proportional to the solar irradiance on it, which allows using irradiance or optical concentration ratio as an indication of short-circuit current. Therefore, the short-circuit current of a concentrating PV module could be expressed by **Equation (2.8)** [143-145] with respect to a reference case. This equation together with the experimental result was applied for validating the developed optical models. As compared in **Table 2-2**, the deviation between the ratio of short-circuit-currents (from the experiment) and the ratio of irradiances (from the optical simulation) is less than 2% for all the static diffuse reflective film cases. Therefore, the proposed Monte-Carlo ray-tracing technique can be considered as a reliable approach for the design and optical analysis of diffuse-type solar concentrators.

$$\frac{I_{sc}}{I_{sc,ref}} = \frac{G}{G_{ref}} \tag{2.8}$$

Where I_{sc} is the short-circuit current of the concentrating PV module, $I_{sc,ref}$ is the short-circuit current of the reference PV module with no concentrator, G is the irradiance on the PV cell under solar concentration, G_{ref} is the irradiance on the reference PV cell.

Table 2-2: Comparison between the simulated and measured results for the tested PV modules.

	Reference	Plain FF	White FF	Milky FF	Opal FF
Reflectance at 600 nm		10.1%	22.9%	30.2%	40.4%
Measured short-circuit current (mA)	15.1	16.1	16.8	17.0	17.6
Current ratio ($I_{sc}/I_{sc,ref}$)	-	1.07	1.11	1.13	1.17
Simulated irradiance (W/m^2)	423.1	447.7	462.5	470.4	489.5
Irradiance ratio (G/G_{ref})	-	1.06	1.09	1.11	1.16
Difference between the ratios		0.8%	1.7%	1.2%	0.7%

2.4 Results and discussion

2.4.1 BIPV smart window prototype design and development

2.4.1.1 Thermotropic membrane properties

Figure 2.12 shows the spectral transmittance and reflectance of a 1-mm-thick thermotropic hydrogel membrane synthesised of 6 wt % HPC and 1.5 wt % GGF. The average light transmittance (τ_{vis}) and reflectance (ρ_{vis}) in the visible region (380-780 nm) of the hydrogel membrane were calculated by **Equation (2.9)** and **Equation (2.10)** [146], respectively. From **Figure 2.12** (a), it can be seen that the spectral transmittance reduces from over 90% to about 10% with an increase in membrane temperature from 25 to 58°C. A transition temperature of 40.5°C is recorded (see **Figure 2.12** (c)). Here, the transition temperature is quoted as the temperature at which the average visible light

transmittance equals to 50% of the transmittance at 25°C. On the other hand, the spectral reflectance increases from approximately 10% to over 40% when the temperature increases from 25 to 58°C, as shown in **Figure 2.12** (b). The sharp changes in transmittance and reflectance are caused by phase separation in the hydrogel membrane, where HPC polymer chains aggregate and free water quenches out of the polymer network, owing to the weakening of hydrogen bonding between HPC polymer chains and surrounding water molecules by heating [91, 108]. The formation of local differences in refractive index between the HPC aggregation and water matrix induces light scattering in the hydrogel membrane [90]. As can be seen from **Figure 2.12** (a-c), the further temperature elevation from 54 to 58°C leads to insignificant changes in transmittance and reflectance, indicating the near completion of phase separation. At 58°C, the average visible light transmittance and reflectance are 11.7% and 47.1%, respectively.

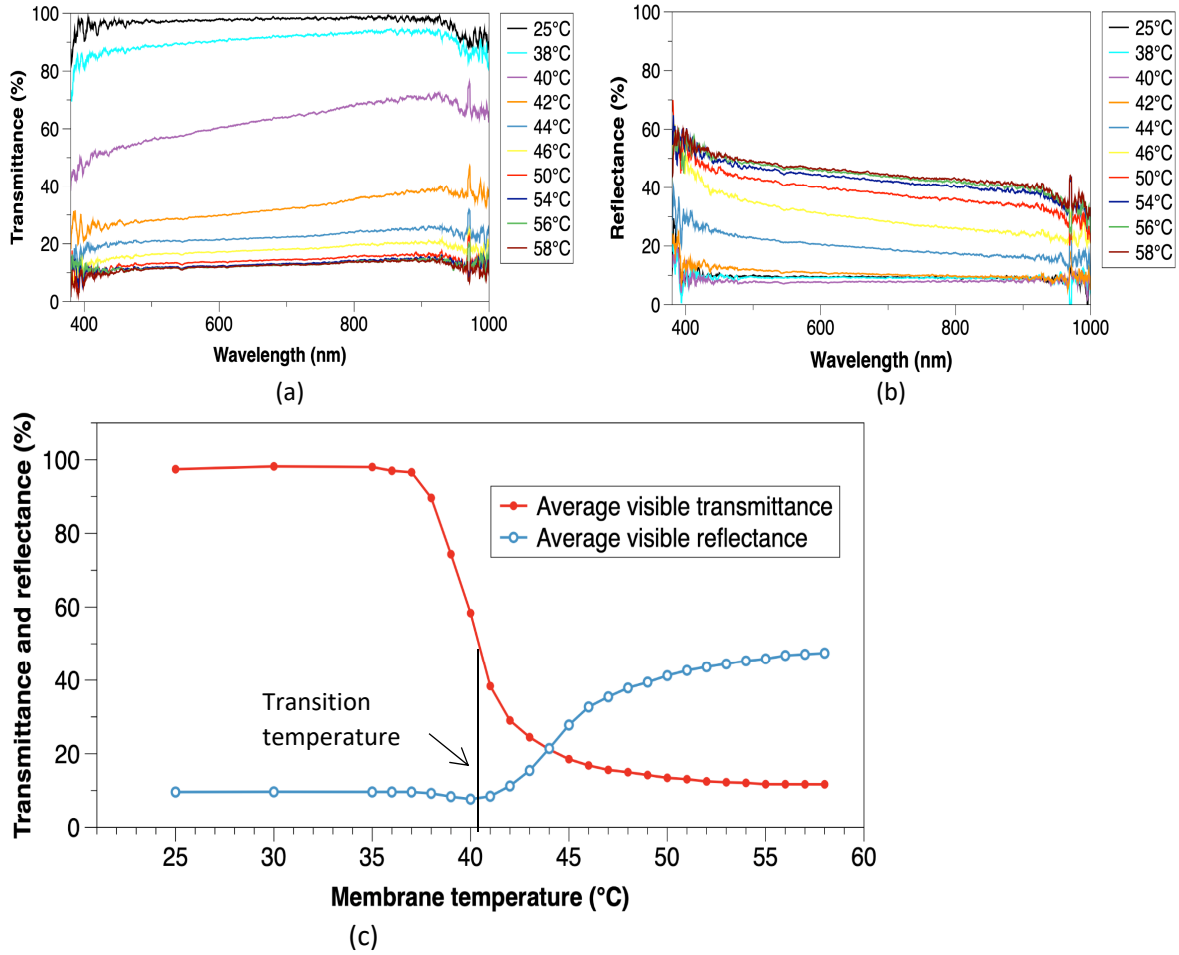

Figure 2.12: (a) Spectral transmittance, (b) spectral reflectance and (c) average visible light transmittance and reflectance of the 6 wt % HPC and 1.5 wt % GGF based hydrogel membrane with 1 mm thickness under various membrane temperature conditions.

$$\tau_{vis} = \frac{\sum_{380\ \mathrm{nm}}^{780\ \mathrm{nm}} D_\tau \tau(\lambda) V(\lambda) \Delta\lambda}{\sum_{380\ \mathrm{nm}}^{780\ \mathrm{nm}} D_\tau V(\lambda) \Delta\lambda} \quad (2.9)$$

$$\rho_{vis} = \frac{\sum_{380\ \mathrm{nm}}^{780\ \mathrm{nm}} D_\tau \rho(\lambda) V(\lambda) \Delta\lambda}{\sum_{380\ \mathrm{nm}}^{780\ \mathrm{nm}} D_\tau V(\lambda) \Delta\lambda} \quad (2.10)$$

Where $\tau(\lambda)$ is the measured spectral transmittance, $\rho(\lambda)$ is the measured spectral reflectance, $\Delta\lambda$ is the interval between wavelengths, $V(\lambda)$ is the spectral luminous efficiency for photopic vision defining the standard observer for photometry, and D_τ is the relative spectral distribution of illuminant D65.

2.4.1.2 Predicted optical performance

A prototype for the BIPV smart window system was designed with the aid of the validated Monte-Carlo ray-tracing model. **Figure 2.13** shows the main components comprising the prototype. The thermotropic reflective layer was for simplicity modelled as a Lambertian surface between the back glass cover and the optical coating layer. The dynamic reflectance of the Lambertian surface was assumed to be in the range of 10% to 47%, according to the optical measurement (displayed in **Figure 2.12)**. Optical simulations were conducted for a series of the designed prototypes with respect to different glazing aperture areas (between 20 mm x 20 mm and 80 mm x 80 mm) and different glazing cover thicknesses (between 1 and 8 mm). The optical concentration ratio, which is denoted as the ratio of the irradiance on the solar cell surface to the irradiance on the front glazing aperture, was calculated for the different design scenarios.

As can be seen from **Figure 2.14** (a), the optical concentration ratio of the designed prototypes is strongly dependent on the reflectance of the thermotropic layer. Take the prototype with the front glass cover dimensions of 50 mm × 50 mm × 4 mm as an example: the optical concentration ratio increases from 0.96 to 1.15 when the reflectance increases from 10% to 47%. Significant improvements in optical concentration ratio are observed by increasing the glazing aperture area until it exceeds 70 mm × 70 mm. This indicates that further extensions of the glazing aperture area could not contribute to more photons being collected by the solar cell, due to the losses of photons caused by multiple scattering, absorption and escaping. In terms of the front glass cover thickness, the optical concentration ratio is maximum at the thickness of 3 or 4 mm, as shown in **Figure 2.14** (b). This may be because a higher thickness results in longer paths for the photons travelling in the front glass cover before reaching the solar cell and thus higher optical absorption; however, reducing the thickness may cause more scattered photons escaping from the front glass cover, due to an increased number of light pass between the boundaries of the front glass cover, i.e., a higher possibility for light entering the glass-air interface at angles less than the critical angle.

Considering the balance between the predicted optical concentration ratio and the uniformity of the indoor lamp irradiation over the sample aperture area (>5% errors when the sample aperture area is greater than 50 mm × 50 mm), the dimensions of the front glazing cover were selected as 50 mm × 50 mm × 4 mm for the prototype fabrication. Optical simulations have also been conducted for different thicknesses of the back glass cover, however, which show only a minor effect on the optical concentration ratio.

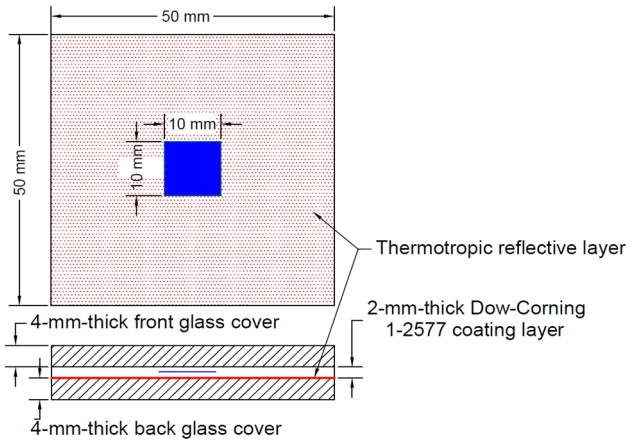

Figure 2.13: Model geometry of the BIPV smart window prototype.

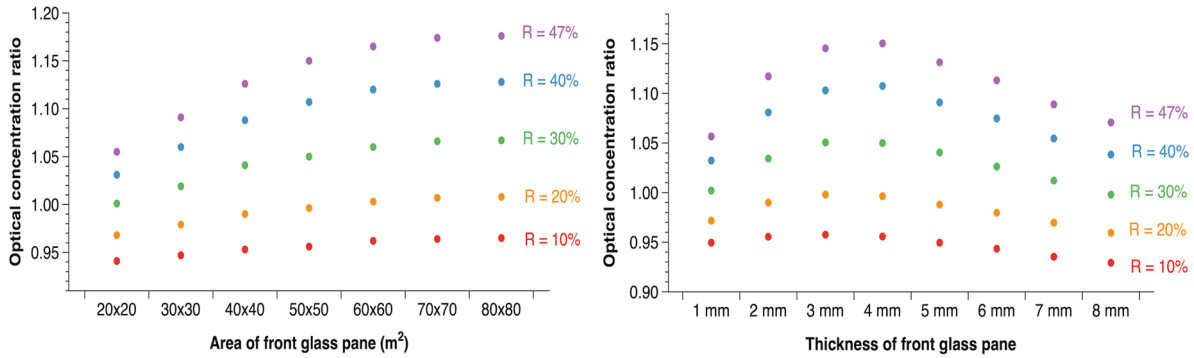

Figure 2.14: Optical concentration ratio of the BIPV smart window (a) for different aperture areas of the front glazing with the same thickness 4 mm and (b) for different thicknesses of the front glazing with the same aperture area 50 mm × 50 mm; the reflectance (R) of the thermotropic layer is assumed to vary between 10% and 47%.

2.4.2 Electrical and solar control performance

A prototype of the optimised design (**Figure 2.13**) for the BIPV smart window system was fabricated and evaluated by an indoor experiment. The electrical and optical performance of the prototype along with the membrane temperature and solar cell temperature were measured simultaneously. **Figure 2.15** shows the transition process of the prototype from a clear state to a light-scattering state with an increase in membrane temperature. The light transmitted through the prototype was detected by the cosine-corrected irradiance probe held against the prototype's backside. The solar cell

temperature and membrane temperature were monitored by the T-type thermocouples, which had been calibrated and wrapped with aluminium foil to avoid any light exposure.

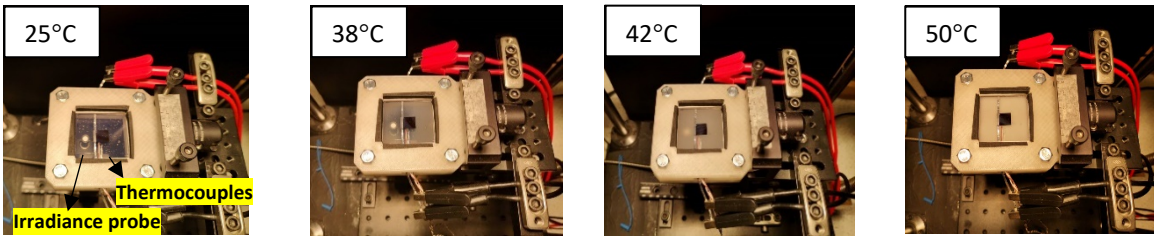

Figure 2.15: Images illustrating the state transition of the BIPV smart window prototype with the membrane temperature increasing.

2.4.2.1 Effect of membrane temperature

Figure 2.16 shows the electrical characteristics of the BIPV smart window prototype with a 6 wt % HPC and 1.5 wt % GGF based hydrogel membrane under varying membrane temperatures. No significant differences in short-circuit current (i.e., current at the voltage of 0 V) and maximum power output (i.e., the peak point of a P-V curve) are observed between 28°C and 40°C. Further increasing the membrane temperature to above 40°C yields significant increases in short-circuit current and maximum power output. This is because the HPC-GGF based hydrogel membrane above 40.5°C transitions from a transparent state to a light-scattering state, resulting in more light being collected by the solar cell. As can be seen from **Figure 2.17** (a), the short-circuit current produced by the BIPV smart window prototype increases from 26.9 to 31.9 mA with the membrane temperature increasing from 40 to 50°C; meanwhile, the maximum power output increases from 12.1 to 14.1 mW. In contrast, the counterpart PV window system, which has a similar structure but without the hydrogel membrane, shows a continuous decline in maximum power output and a slight increase in short-circuit current with the solar cell temperature increasing (see **Figure 2.17** (b)). This is because, a higher cell temperature reduces the amount of energy required (or bandgap) to excite the electrons bonded to an atom into a free state, which promotes the generation of electron-hole pairs and hence yields a slight increase in the short-circuit current; on the other hand, more recombination of electrons-holes pairs takes place as a result of the increased reverse saturation current with temperature, which leads to a decrease in the open-circuit voltage; since the voltage of a crystalline-silicon solar cell is more temperature-dependent than the current, increasing the cell temperature can results in a lower power output and conversion efficiency [147, 148]. By comparison, the maximum power output and short-circuit current of the counterpart PV window system are 12.7% and 17.4% lower than those of the BIPV smart window prototype, respectively, when the solar cell temperature reaches 54°C.

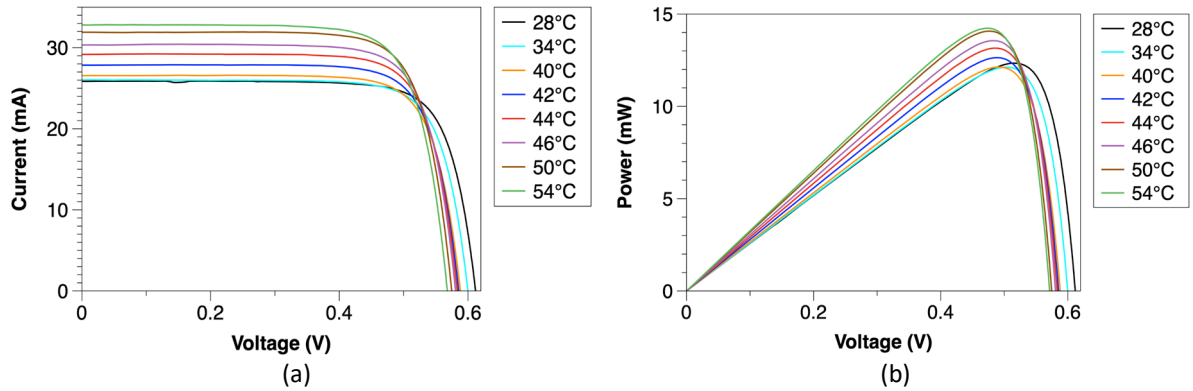

Figure 2.16: (a) I-V and (b) P-V characteristics of the 6 wt % HPC and 1.5 wt % GGF based BIPV smart window prototype under different membrane temperatures and an irradiation level of 550 W/m^2.

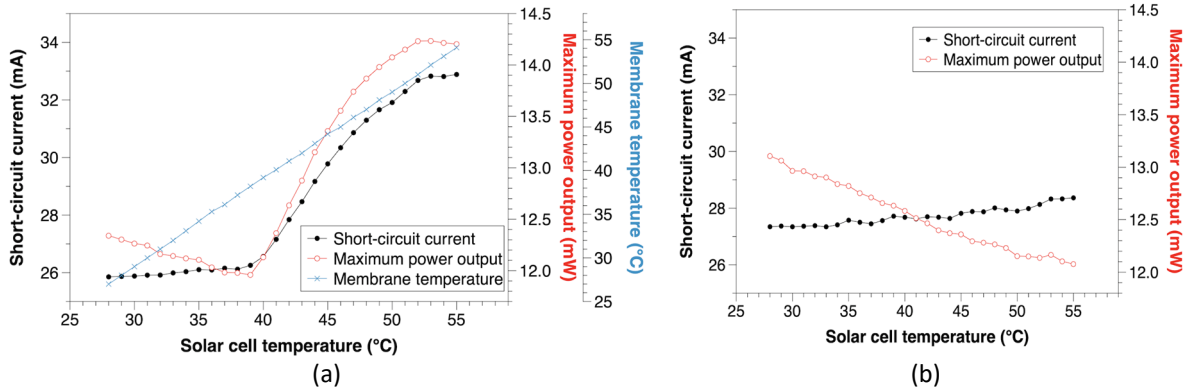

Figure 2.17: Short-circuit current and maximum power output of (a) the BIPV smart window prototype and (b) its counterpart with no membrane, as a function of solar cell temperature.

The electrical characteristics of the BIPV smart window prototype and its counterpart system with no membrane were also compared under different conditions of incident light intensity and angle. **Figure 2.18** (a) shows the I-V characteristics at a solar cell temperature of 50°C under the three irradiation levels: 550, 600 and 700 W/m^2. The short-circuit current of the BIPV smart window prototype is observed to increase from 31.9 to 41.0 mA when the irradiation level is elevated from 550 to 700 W/m^2. Under the same irradiation levels, the BIPV smart window prototype has both higher short-circuit currents and power outputs (i.e., current times voltage) compared with its counterpart system. From **Figure 2.18** (b), it can be seen that the short-circuit current of the BIPV smart window prototype under 700 W/m^2 irradiation decreases from 41.0 to 21.3 mA when the incident light angle is increased from 0° (normal to the plane) to 60°. At the same incident light angles, the BIPV smart window prototype offers better electrical performance than its counterpart system.

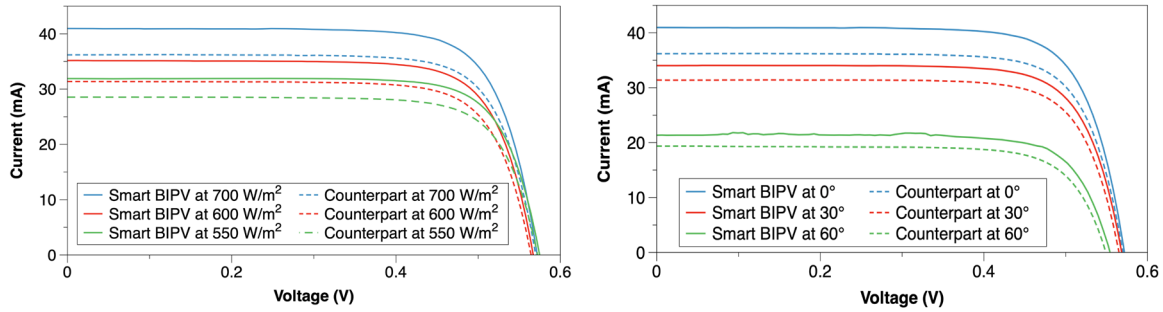

Figure 2.18: I-V characteristics of the BIPV smart window prototype and its counterpart system (a) under the irradiation levels of 550, 600 and 700 W/m^2 at the incident light angle of 0°, and (b) at the incident light angles of 0°, 30° and 60° under the irradiation level of 700 W/m^2.

2.4.2.2 Effect of HPC concentration

The effect of HPC concentration on the electrical and optical performance of the BIPV smart window prototype has been investigated. Three hydrogel membranes consisting of 1.5 wt % GGF and different HPC concentrations (2, 4 and 6 wt %) were prepared for the comparative analysis. As can be seen from **Figure 2.19** (a), the maximum power outputs of the three BIPV smart window prototypes show decreasing trends when the membrane temperature increases from 28 to 39°C. This is because of the fact that under constant irradiation, the power conversion efficiency of c-Si solar cells decreases with an increase in operating temperature [149]. The maximum power outputs of the three prototypes start to increase once the membrane temperature exceeds 40°C, due to the occurrence of phase separation. The 6 wt % HPC based prototype shows a 17.1% increase in the mean value of maximum power output with the membrane temperature increasing from 40 to 54°C, followed by the prototypes based on 4 wt % HPC (11.5%) and 2 wt % HPC (8.9%). On the other hand, the mean values of the intensity of the light transmitted through the prototypes based on 6 wt %, 4 wt % and 2 wt % HPC reduce by 70.9%, 66.5% and 57.3%, respectively, when the membrane temperature increases from 28 to 54°C, as shown in **Figure 2.19** (b). The outcomes may be attributed to higher reflectance and lower transmittance of the hydrogel membranes with greater HPC concentrations [107, 108], because of more HPC aggregates formed in the water matrix during phase separation.

The above experimental results demonstrate that the BIPV smart window system has the potential to provide lower solar heat gains and higher electricity generation when subjected to higher membrane temperatures, which could protect the building interior from overheating in summer and improve the building energy efficiency. The optical analysis reveals that the effectiveness of solar concentration via total internal reflection is related to the thermotropic membrane reflectance as well as the optical losses due to escaping of light from the system. The thermotropic membrane reflectance could potentially be further enhanced by increasing the HPC concentration, HPC particle size or membrane thickness. The optical losses may be reduced by applying low-iron glass covers with a higher refractive

index. The optimisation, however, should also take into account the reduction in daylight transmission and the impacts on occupant comfort and building energy consumption.

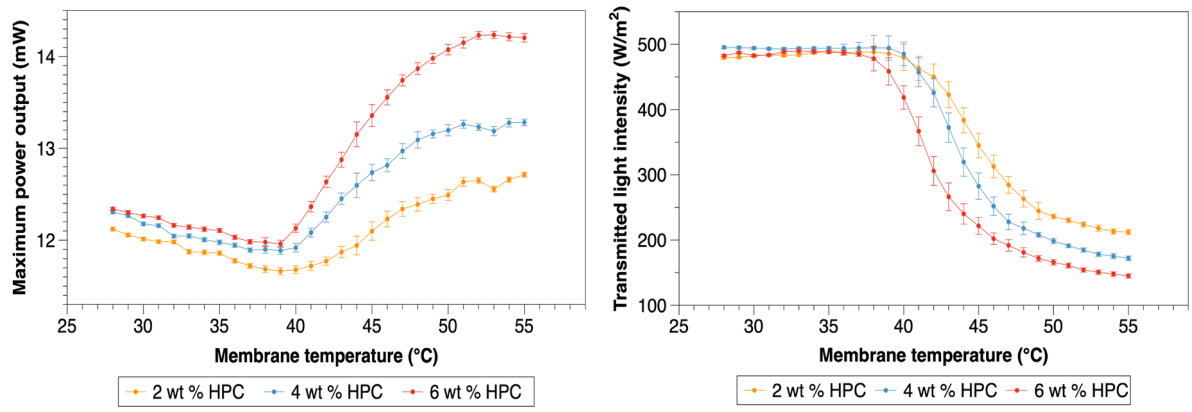

(a) (b)

Figure 2.19: (a) Maximum power output and (b) transmitted radiant intensity of the 2, 4 and 6 wt % HPC based BIPV smart window prototypes as a function of membrane temperature under an irradiation level of 550 W/m ^{2}. Error bars represent one standard deviation.

2.5 Summary

A Building Integrated Photovoltaic (BIPV) smart window with a dual function of electricity generation and adaptive solar radiation control is introduced in this chapter. A validated Monte-Carlo ray-tracing technique has been applied for the system design and performance prediction. A thermotropic hydrogel membrane comprised of 6 wt % HPC and 1.5 wt % GGF has been selected for the BIPV smart window system due to its higher reflectance above switching temperature and also meet most of the window requirements. From the optical prediction, it can be seen that when the prototype has a 50 mm × 50 mm × 4 mm front glass cover with a 10 mm x 10 mm solar cell exhibits the best performance. A prototype with this suggested design has been subsequently fabricated and characterised experimentally. Some key findings from the BIPV smart window characterisations are presented below:

1. The maximum power output of the BIPV smart window system decreases with an increase in membrane temperature until reaching the HPC thermotropic membrane transition temperature of 40.5°C; it increases significantly thereafter.
2. The BIPV smart window system offers a higher short-circuit current and higher maximum power output by up to 12.7% and 17.4%, respectively, compared to its counterpart system with no HPC thermotropic membrane.
3. An approximately 70% reduction in light transmittance for the BIPV smart window is observed when the membrane temperature increases from 28 to 54°C.
4. Using a higher HPC concentration could potentially enhance both solar transmittance modulation and electricity generation of the system.

Chapter 3 – A Monte-Carlo optical model coupled with an IAD method for the window performance prediction

3.1 Introduction

In **Chapter 2**, a BIPV smart window system was developed based on a simplified ray-tracing optical model, where the thermotropic layer in its translucent state was assumed as a Lambertian-type reflective surface with a uniform reflectance distribution [134, 150]. However, in practice, the light reflection from a translucent medium with a slab geometry is anisotropic (angle dependent) in almost all situations [151]. The simplified ray-tracing technique applied in the previous chapter might not be accurate enough to predict the optical performance of a solar system where a translucent medium is involved. Therefore, an optical model considering the non-Lambertian scattering with angular distribution is required.

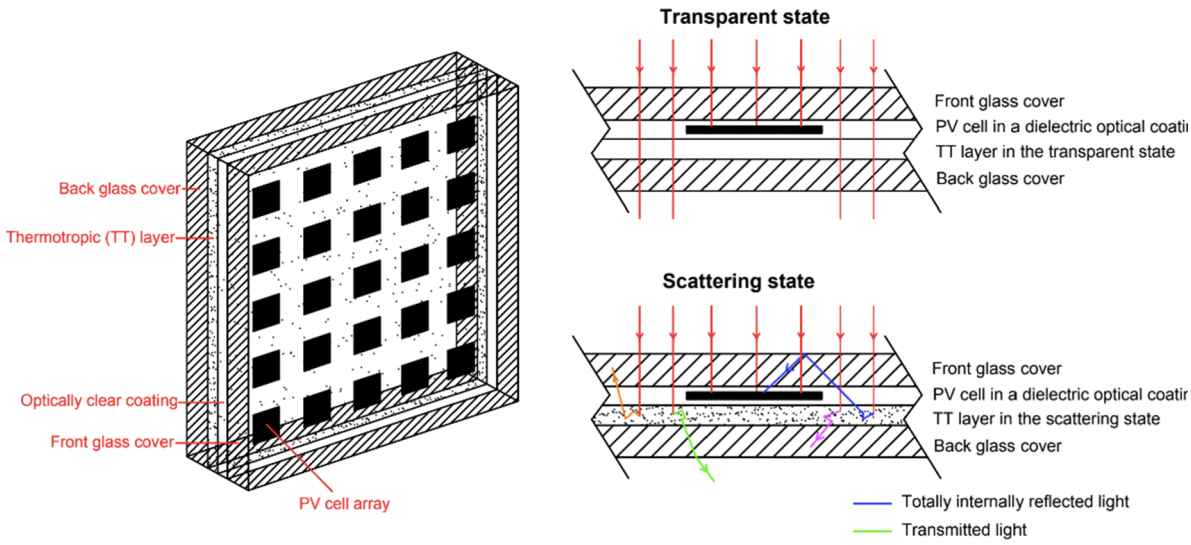

(a) (b)

Figure 3.1. (a) Schematic diagram of the BIPV smart window system and (b) possible light paths in the system.

An alternative method is to model the spatial light distribution, involving volume (or bulk) scattering, when a light ray propagates through the thermotropic layer, as sketched in **Figure 3.1** (b). Typically, the light distribution in a translucent medium can be modelled based on its intrinsic optical properties, including absorption coefficient (μ_α), scattering coefficient (μ_s), anisotropy factor (g) and reduced scattering coefficient (μ_s') [152-155]. These volume scattering properties can be estimated by the direct methods and the inverse methods [152, 156, 157]. In the direct methods (e.g. Lorenz-Mie theory), the physical properties of a diffuse medium and its constituent particles, such as refractive index, particle size, shape and concentration, are measured with specialised equipment and used as input in Maxwell's equations to yield solutions for the volume scattering properties [157-159]. If these experimental data are not available, the volume scattering properties can be estimated by the Inverse

or fitting approaches, such as the Kubelka-Munk method [160], the diffusion approximation [161] and the Inverse Adding-Doubling (IAD) method [159]. The prerequisites for these inverse methods are the macroscopic quantities of a diffuse medium, such as reflectance and transmittance, which can be obtained using the experimental setups such as integrating spheres and goniometers [158].

The IAD method is regarded as a standard reference approach to estimate the volume scattering properties of diffuse media, with advantages such as fast computation, good flexibility and broad applicability [154, 156]. In the IAD method, an initial guess is made for the volume scattering properties of a sample. The guessed values are used for calculating the sample's reflectance and transmittance with the Adding-Doubling (AD) method, and iteratively adjusted until a good fit between the calculated and measured values is obtained. The IAD method applies to any diffuse medium for which the Radiative Transport Equation (RTE) is valid, and places no restrictions on albedo, optical depth and scattering anisotropy [162, 163]. Typically, three input variables are required for the IAD calculation: the total reflectance, total transmittance and collimated transmittance of a diffuse medium. These data are usually available from the measurement with a single/double integrating sphere system [154, 164] or a Bi-directional Scattering Distribution Function (BSDF) device [155, 158, 159].

The IAD method has been used to investigate the light scattering in a host of diffuse media such as fruit and vegetable tissues [154, 165, 166], tissue-mimicking phantoms for clinic use [163, 167, 168], translucent liquids [152, 159] and plastic diffusers [159, 169]. Leyre et al. [159] used the IAD method to estimate the volume scattering properties for a concentration series of diluted milk in glass cuvettes, which were used as input to Monte-Carlo ray-tracing simulations to predict the angular scattering intensity distribution of the samples with different milk concentrations and thicknesses. Good agreement was obtained between the simulated results and the data measured using a BSDF device. Xie et al. [170] investigated the optical characteristics of Quantum dots (QDs)-Polymethyl methacrylate (PMMA) films by using a combination of IAD calculation and double-integrating-sphere measurement. It was found that the QDs-PMMA films exhibit stronger scattering and absorption at higher QDs concentrations and for the incident laser with a lower wavelength.

In this chapter, an advanced optical modelling approach based on a Monte-Carlo ray-tracing technique with the volume scattering properties of the thermotropic membrane layer determined by the IAD method has been developed. This developed optical model has been subsequently used to optimise the BIPV smart window design, where the effects of HPC concentration, geometric concentration ratio, thermotropic membrane thickness and glass refractive index on PV power outputs have been

evaluated. This novel optical model can be applied to most variants of smart windows that involve anisotropic scattering materials. The accuracy of this model has been validated by experiments.

3.2 Methodology

A flow chart showing the procedure of the development and validation of the proposed advanced optical model is illustrated in **Figure 3.2**. At first, the total reflectance (R_t), total transmittance (T_t) and collimated transmittance (T_c) of a thermotropic laminated glazing sample (4-mm-thick glass pane/1-mm-thick 2 wt % HPC based thermotropic membrane layer/4-mm-thick glass pane) were measured and used as input to an IAD algorithm. The volume scattering properties of the thermotropic membrane, including absorption coefficient (μ_α), reduced scattering coefficient (μ_s') and anisotropy factor (g), were derived from the IAD calculation and then imported into a Monte-Carlo ray-tracing model. The intensities of light transmitted through the thermotropic laminated glazing sample observed at multiple scattering angles ($G_{sim}(\theta)$) were simulated with the Monte-Carlo ray-tracing technique and compared to experimental data ($G_{exp}(\theta)$). To gain deeper insight into the thermotropic membrane performance, its angular scattering profile and spatial flux distribution were simulated under varying membrane temperatures and HPC concentrations. The developed model was subsequently used for the design and optimisation of the proposed BIPV smart window system. The simulated results for the optimised prototype were compared to the data obtained from an indoor experiment, as further validation of the developed numerical method for BIPV and smart window applications.

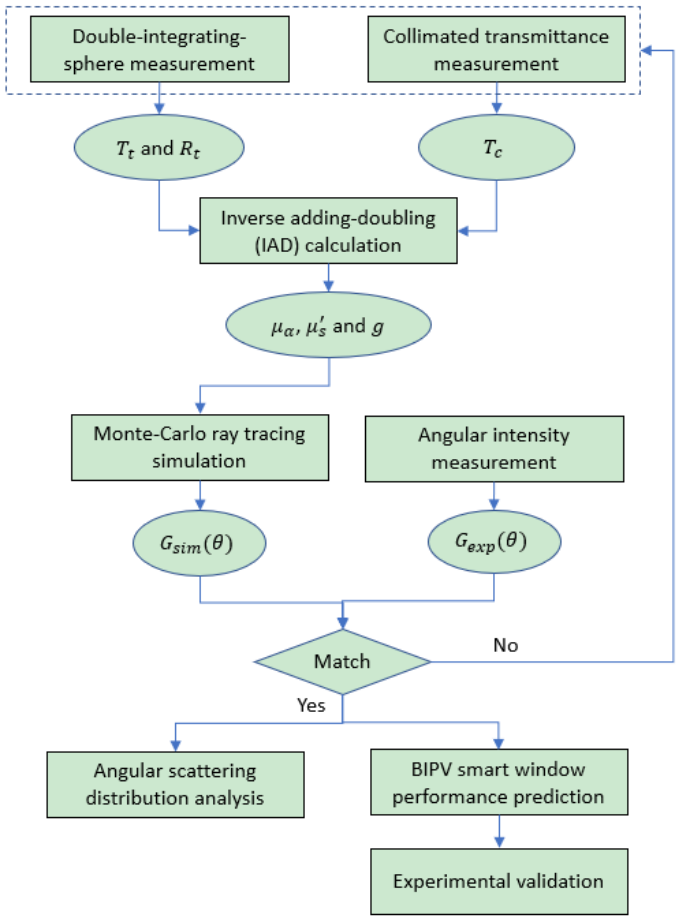

Figure 3.2: Flow chart presenting the process for optical simulation and validation.

3.2.1 Optical measurements

The thermotropic membranes were synthesised using HPC polymer and Gellan Gum type F (GGF) (gelling agent). The detailed synthesis procedures are presented in **Section 2.3.1.1**. The total reflectance (R_t) and total transmittance (T_t) of a laminated glazing sample with an HPC-GGF thermotropic membrane layer were measured using a Double-Integrating-Sphere (DIS) system illustrated in **Figure 3.3** (a). In the DIS system, the totally reflected light (including the specularly and diffusely reflected light) from the sample was collected by an Ocean Optics ISP-REF integrating sphere; and the totally transmitted light (including the specularly and diffusely transmitted light) through the sample was collected by an Ocean Optics FOIS-1 integrating sphere. The spheres were connected to an Ocean Optics USB2000+UV-VIS-ES spectrometer via 400 µm core diameter optical fibres. The collimated transmittance (T_c) of the sample, which is defined as the light transmitted through the sample without being scattered [157, 164], was measured using the setup illustrated in **Figure 3.3** (b). A collimated detector consisting of an Ocean Optics 74-UV collimating lens and a 400 µm core diameter optical fibre was positioned at a distance of 20 cm from the sample with its centre aligned with the incident beam. The collimated detector was connected to the Ocean Optics USB2000+UV-VIS-ES spectrometer. A distance independence test has been conducted for the collimated

transmittance measurement. As can be seen from **Figure 3.4**, the measured collimated transmittance decreases exponentially with increasing the distance between the sample and detector, indicating less diffuse light being detected. No significant decrease in collimated transmittance has been observed when the distance is over 20 cm.

Before the optical measurements, a GyroStir-DH hotplate was used to heat the thermotropic membrane to a defined temperature with an equilibrium time of at least 10 minutes. The membrane temperature was recorded and monitored by a T-type thermocouple embedded in the membrane (see **Figure 3.5**) and connected to a DT85 data taker. The uniformity of temperature distribution across the membrane was checked by using a FLIR E40BX infrared camera. The thermal and optical measurements were repeated at least triplicate, to account for the uncertainty due to membrane temperature fluctuation.

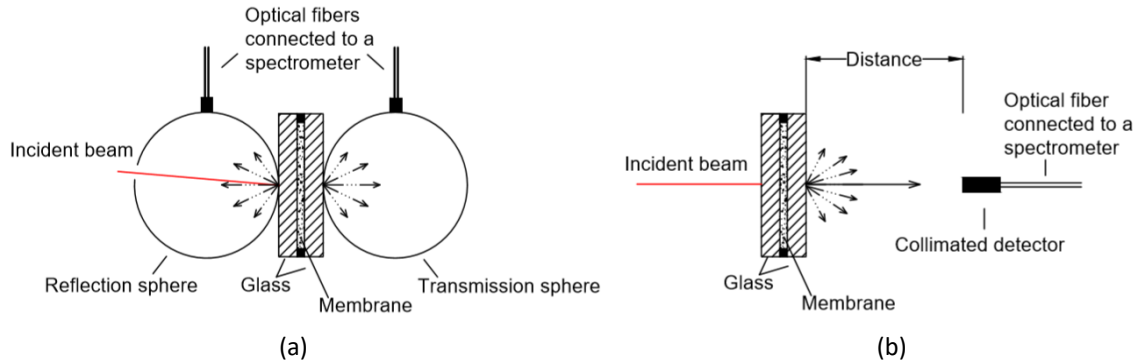

Figure 3.3: (a) Double-integrating-sphere system and (b) collimated transmittance measurement setup.

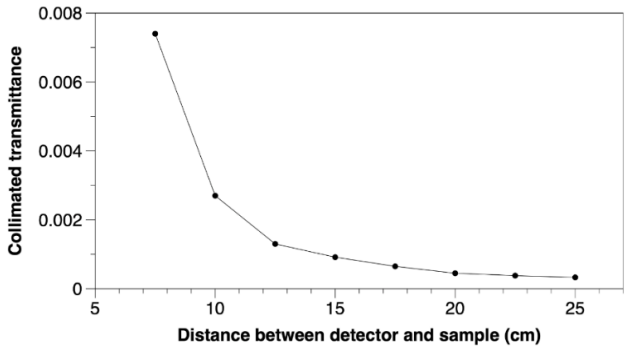

Figure 3.4: Measured collimated transmittance of the sample with a 2 wt % HPC, 1.5 wt % GGF based TT membrane in the translucent state against sample-detector distance.

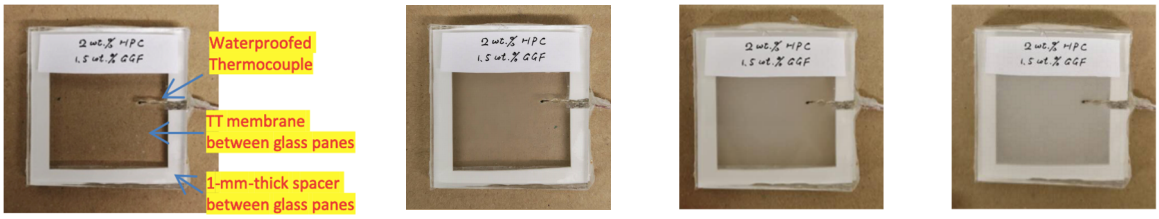

Figure 3.5: Images illustrating the states of the sample with a 2 wt % HPC, 1.5 wt % GGF based TT membrane at different temperatures.

3.2.2 IAD calculation and ray-tracing simulation

The measured spectral data of R_t, T_t and T_c were imported to an IAD algorithm [164, 171, 172], with which μ_α, μ_s' and g as a function of wavelength were calculated [166, 173]. A flow chart of the IAD algorithm is shown in **Figure 3.6**. The additional input parameters for the IAD calculation include the average refractive index of the low-iron optical glass panes (1.51), the average reflective index of the thermotropic layer (1.34), the glass pane thickness (4 mm), the thermotropic layer thickness (1 mm), the illumination beam diameter (1.5 mm), the diameters of the integrating spheres (38 mm), the diameters of the sample ports (10 mm) and the sphere wall reflectivity (98%). In the IAD algorithm, the refractive indices of the glass panes and thermotropic layer are used to calculate the Fresnel reflection at boundaries, and the geometrical dimensions are used to correct the light loss when using the DIS measurement setup [164]. The refractive index of 2 wt % HPC aqueous solution is 1.34 according to the literature [174, 175] and is considered as the refractive index of the thermotropic layer under study.

Monte-Carlo ray-tracing model has been developed to simulate the optical characteristics of the thermotropic laminated glazing sample. The light propagation in the thermotropic layer was approximated using its absorption coefficient μ_α, scattering coefficient μ_s (given by **Equation (3.1)** [173]) and single-scattering phase function $p(\theta)$ as input. μ_α (or μ_s) is defined as the reciprocal of the average free path that light travels between two absorption (or scattering) events [152, 170]. The single-scattering phase function describes the fraction of light scattered at an angle θ from the incident direction after a single scattering event [152, 156]. In this work, the Henyey–Greenstein phase function with a single variable g (anisotropy factor) was implemented for the simulation, given by **Equation (3.2)** [173]. Other input parameters include the refractive index and absorption coefficient of the low-iron optical glass panes, the refractive index of the thermotropic layer, the measured irradiation intensity of the light source and the number of incident rays where 1,000,000 rays were used in this study confirmed through a ray independence test.

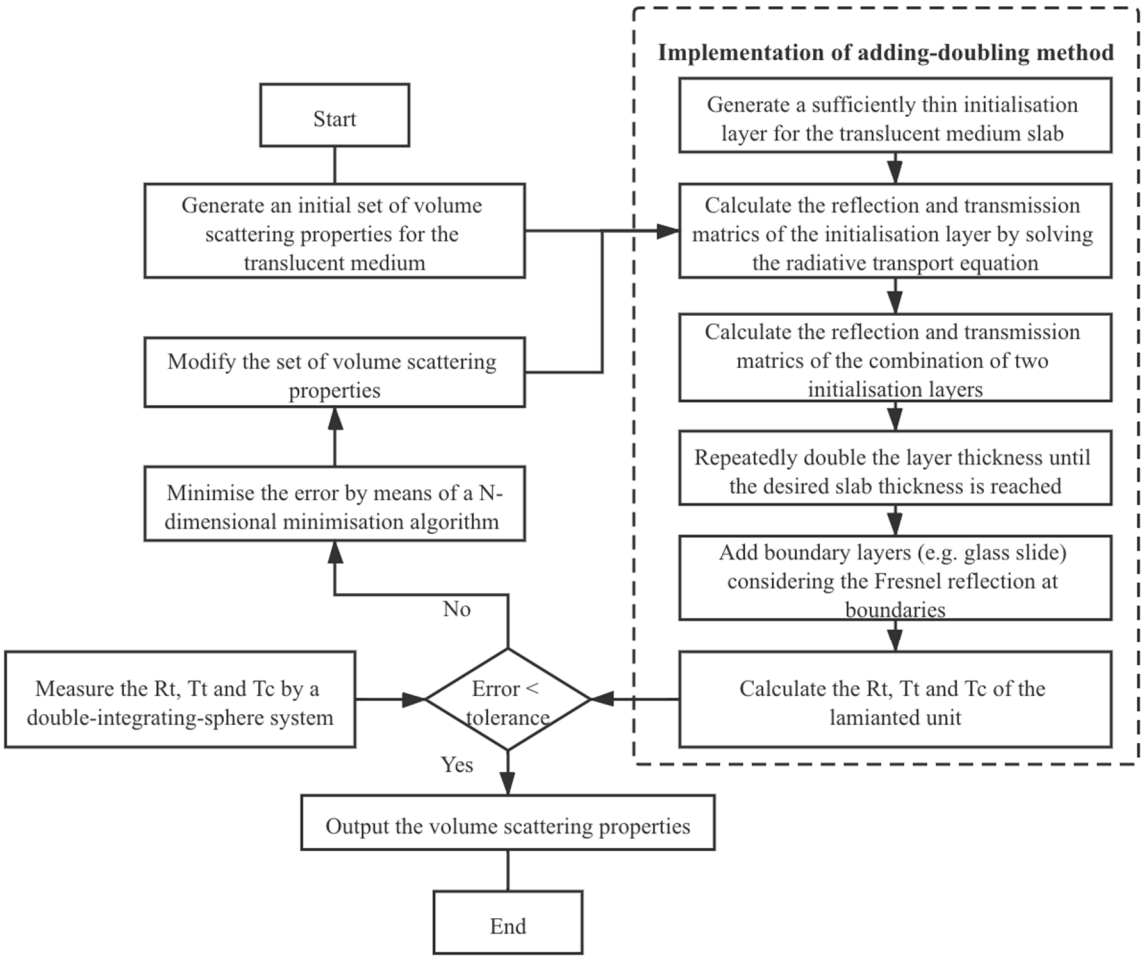

Figure 3.6: Inverse adding-doubling algorithm for determining the volume scattering properties of a translucent medium.

$$\mu_s = \frac{\mu_s'}{(1-g)} \tag{3.1}$$

$$p(\theta) = \frac{1}{4\pi} \frac{1-g^2}{(1+g^2-2g\ \cos(\theta))^{3/2}} \tag{3.2}$$

3.2.3 Validation of the optical model

The optical model was validated by an experiment using the setup shown in **Figure 3.7**. A laminated glazing sample comprised of a thermotropic layer (40 mm × 40 mm × 1 mm) between two optical glass covers (50 mm × 50 mm × 4 mm) was mounted in the centre of a rotation device. The sample was illuminated by a collimated light source that consists of an Ocean Optics 74-UV collimating lens, a 400 µm core diameter optical fibre and an Ocean Optics HL2000 halogen lamp. The normal incident beam has a diameter of 5 mm and a total irradiation intensity of 36 W/m^2 across the 350-1000 nm spectrum. A detector (at a 10 cm distance from the centre and 15 cm away from the light source) moved around the sample to collect the light scattered at a predefined set of angles. The detector consists of an Ocean Optics CC-3-UV-S cosine corrector (with an aperture diameter of 3.9 mm and a field of view 180°) and a 400 µm core diameter optical fibre connected to an Ocean Optics USB2000+UV-VIS-ES

spectrometer. The optical detection system had been calibrated for absolute spectral irradiance against an Ocean Optics LS-1-CA calibrated halogen lamp. The intensities of light transmitted through the sample observed at the angles of 0°, 15°, 30°, 45° and 60° were measured and compared to the simulation results using the developed optical model (described in **Section 3.2.2**). After validation, the normalised scattered radiant intensity of the thermotropic laminated glazing sample as a function of scattering angle was calculated, given by **Equation (3.3)** [176].

$$F(\theta) = \frac{G_s(\theta)}{G_i \times \Omega} = \frac{G_s(\theta)}{G_i \times \frac{A}{R^2}} \tag{3.3}$$

Where F(θ) is the normalised angular scattering intensity, $G_s(\theta)$ is the scattering intensity of the sample detected at the scattering angle θ (W/m^2), G_i is the normal incident light intensity (W/m^2), Ω is the solid angle of the detector, *A* is the surface area of the detector port (m^2), and *R* is the distance between the detector port and the centre of the sample.

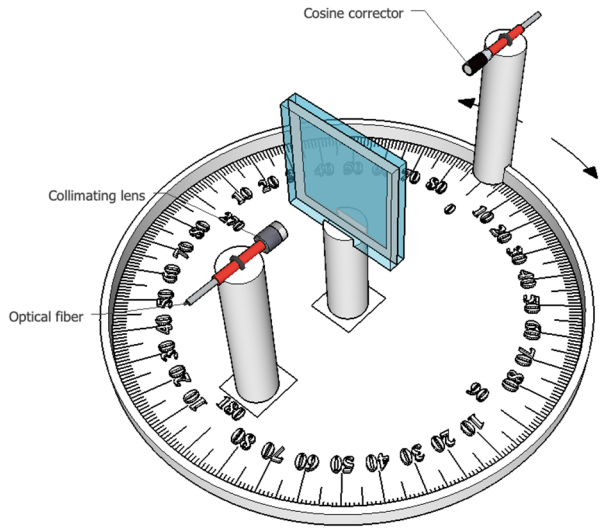

Figure 3.7: Schematic diagram of the angular intensity measurement setup.

3.3 Results and discussion

3.3.1 Total transmittance, total reflectance and collimated transmittance

Figure 3.8 shows the total transmittance and total reflectance of the sample consisting of a 1-mm-thick 2 wt % HPC, 1.5 wt % GGF based thermotropic membrane sandwiched by two pieces of 4-mm-thick optical glass panes, measured over the membrane temperature range from 27 to 56°C and the wavelength range from 400 to 1000 nm. As shown in **Figure 3.8** (a), the total transmittance of the sample decreases with increasing temperature, being approximately 90% at temperatures below 38°C and nearly 20% above 50°C. This is because HPC is freely soluble in the water below 38°C, whereas is insoluble and precipitates as white floc in water above 38°C, resulting in a translucent appearance

[108, 174, 177], as can also be seen in **Figure 3.5**. The transition temperature of the 2 wt % HPC membrane is approximately 42°C.

On the other hand, the total reflectance is below 10% at 27°C, decreases slightly when the temperature increases from 38 to 42°C, and then increases progressively with temperature, as shown in **Figure 3.8** (b). A similar phenomenon was reported by Varma et al. [178]. This might be due to the combined effect of specular reflection decrease and diffuse reflection increase. The specular reflection decrease might be attributed to an increase in the refractive index of the thermotropic hydrogel, induced by its volumetric change with temperature [179]. A possible reason for the diffuse reflection increase may be that the number and size of HPC aggregates (i.e., scattering centres) in the membrane structure increase due to continuous phase separation [95].

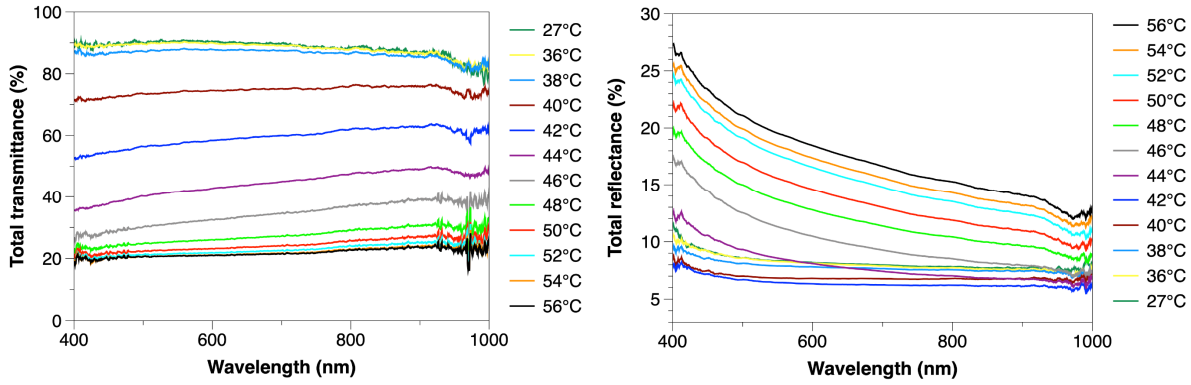

(a) (b)

Figure 3.8: (a) Spectral total transmittance and (b) spectral total reflectance of a laminated glazing sample with a 2 wt % HPC, 1.5 wt % GGF based TT membrane under various temperature conditions.

Figure 3.9 shows the average values of total transmittance (T_t), collimated transmittance (T_c) and total reflectance (R_t) in the visible region (380-780 nm) (calculated following the methods outlined in the BSI Standard BS EN 410:2011 [146]) for the laminated glazing samples with the 2, 4 and 6 wt % HPC membranes under various temperature conditions. The samples exhibit similar total transmittances (~90%), collimated transmittances (~80%) and total reflectances (~8%) when below 38°C. The differences between the total and collimated transmittances imply that the light passing through the samples in the transparent state is not entirely in the specular direction. A fraction of light incident on the samples is diffused, probably because of unsmooth surfaces and impurities. As can be seen from **Figure 3.9**, the total and collimated transmittances both start to decrease at 38°C. However, the collimated transmittance decreases faster than the total transmittance, indicating an increase in the proportion of diffusely to totally transmitted light through the sample. When the membrane temperature increases to 42°C, the collimated transmittances of the three samples are nearly 0% whereas their total transmittances are higher than 35%. The transmittance differences suggest that

the thermotropic membranes potentially can be used in windows to reduce glare caused by direct lighting. As the membrane temperature reaches 56°C, the total transmittances of the samples with 2, 4 and 6 wt % HPC decrease to ~ 21%, ~16% and ~14%, respectively. The total reflectances of the samples increase with temperature when the samples are heated above 42°C. A higher HPC concentration results in higher total reflectance but lower total and collimated transmittances in the phase separation process. This could be attributed to an increased amount of HPC aggregates within the membrane structure, increasing the opportunity for light to be scattered.

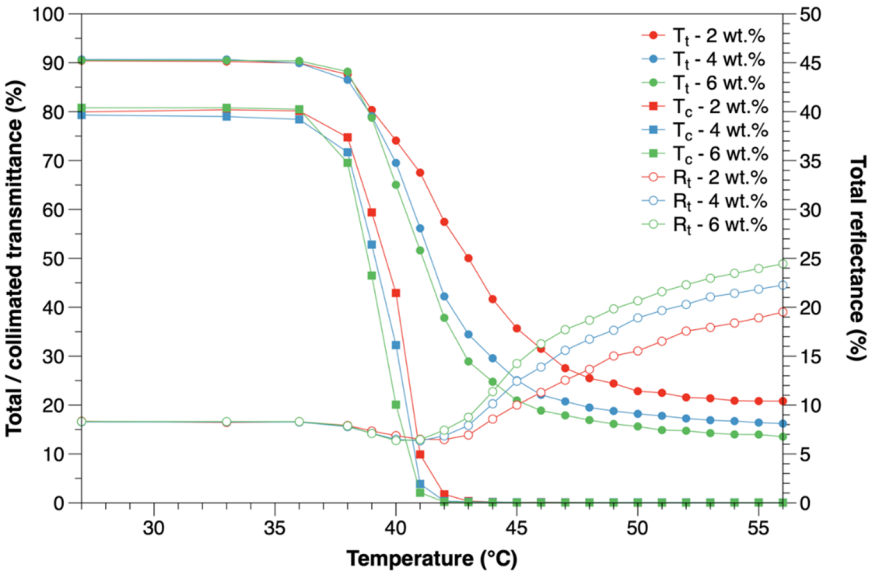

Figure 3.9: Average visible total transmittance, total reflectance and collimated transmittance of the three laminated glazing samples with the TT membranes consisting of 2, 4 and 6 wt % HPC with 1.5 wt % GGF, as a function of membrane temperature.

3.3.2 Volume scattering properties

Based on the measured spectral transmittance and reflectance, the spectral volume scattering properties of the thermotropic membrane were calculated using the IAD method. **Figure 3.10** shows the effect of membrane temperature on the volume scattering properties of the thermotropic membrane consisting of 2 wt % HPC and 1.5 wt % GGF over the wavelength range from 400 to 1000 nm. It can be seen that the reduced scattering coefficient (μ_s') increases when the membrane temperature increases from 44 to 56°C. This trend corroborates that the thermotropic membrane becomes increasingly diffusely reflective and transmissive in the heating process as aforementioned. On the other hand, the temperature effect on the sample's absorption coefficient (μ_α) is as not significant as on the μ_s'. The anisotropy factor (g) is observed to decrease with increasing temperature, indicating an increasing proportion of the incident light being scattered backwards from the thermotropic membrane.

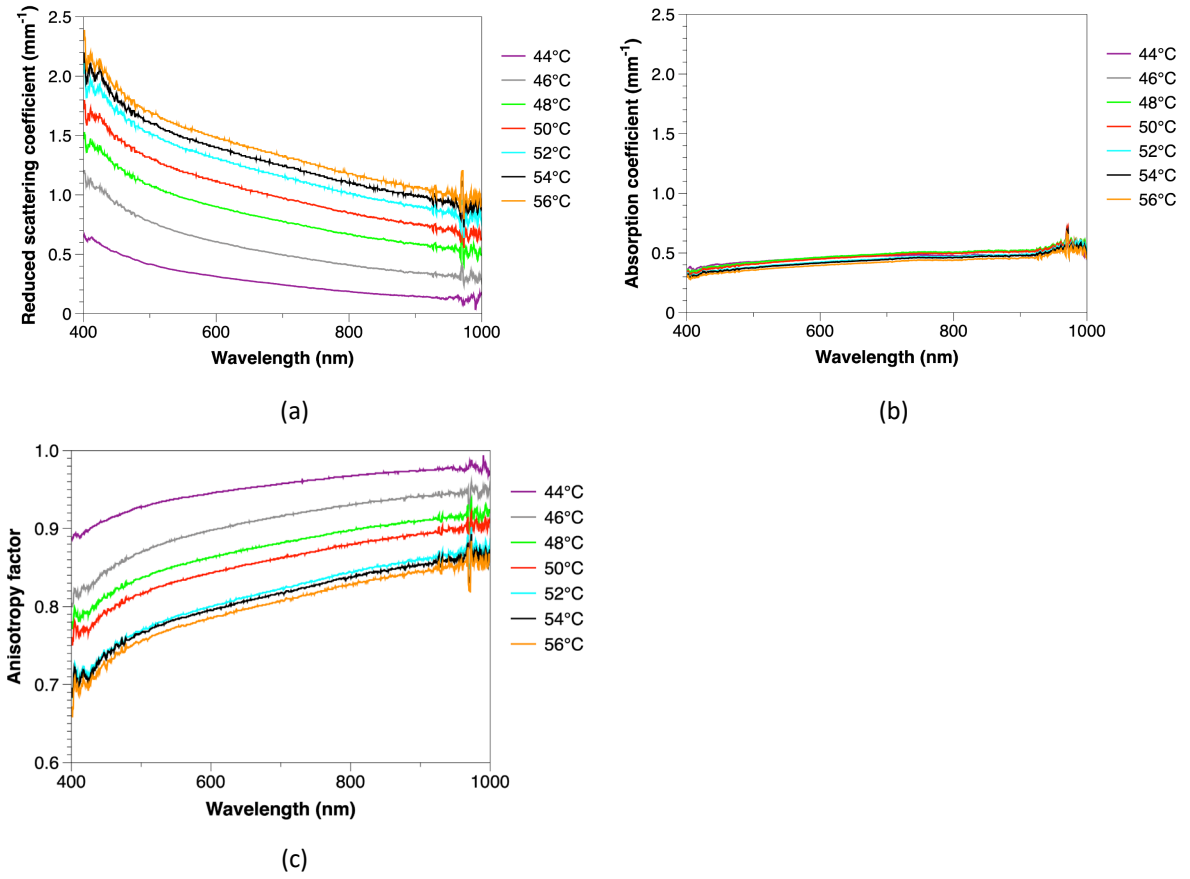

Figure 3.10: (a) Reduced scattering coefficient, (b) absorption coefficient and (c) anisotropy factor of the 2 wt % HPC, 1.5 wt % GGF based TT membrane under various temperatures.

Figure 3.11 shows the volume scattering properties calculated for the 2, 4 and 6 wt % HPC based thermotropic membranes at the wavelength of 600 nm. As can be seen from **Figure 3.11**, the three membranes exhibit similar temperature dependences of the volume scattering properties. Taking the 6 wt % HPC as an example, when the membrane temperature increases from 44 to 56°C, the μ_s' increases from 0.78 to 2.41 mm^{-1}, the μ_α reduces from 0.55 to 0.42 mm^{-1}, and the g reduces from 0.88 to 0.67. It is also found that at the same temperatures, the membranes with greater HPC concentrations have higher μ_s' but lower g. For example, at 56°C, the μ_s' increases from 1.48 to 2.41 mm^{-1}, while the g decreases from 0.79 to 0.67, with increasing the HPC concentration from 2 to 6 wt %. Similar trends regarding the effects of temperature and HPC concentration are observed at the wavelengths of 400 nm and 800 nm (see **Table 3-1**).

The effect of the wavelength of incident light on the volume scattering properties of the thermotropic membranes has also been investigated. As can be seen from **Table 3-1** and **Figure 3.10**, the μ_s' is lower and the g is higher at a longer wavelength. This might be because the radiative scattering behaviour of a translucent material is related to the particle size parameter ($x = 2\pi a/\lambda$), which is determined by the wavelength of incident light (λ) and the particle radius (a) [180, 181]. The longer the wavelength,

the smaller the value of x, therefore the less effectively light is scattered by the particles, and also the larger the angle between the incident and scattered directions [180, 181].

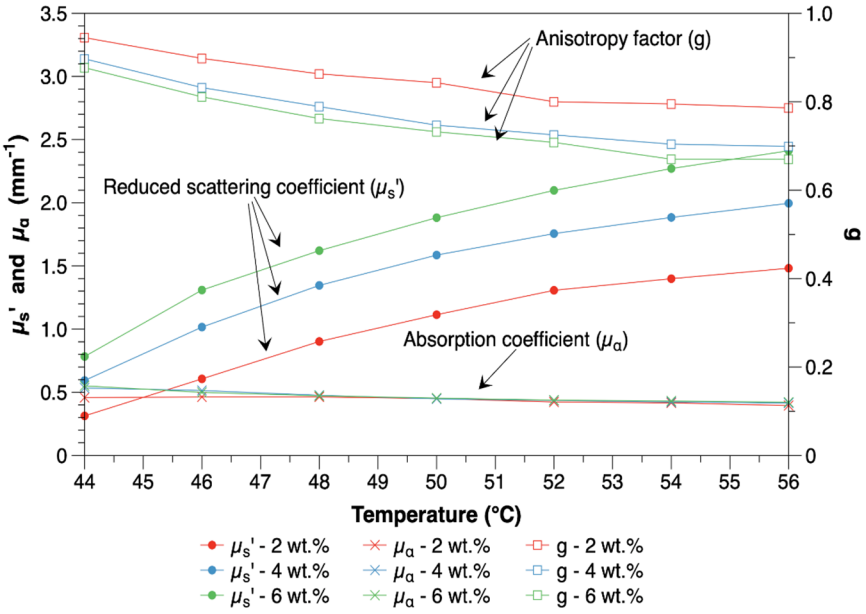

Figure 3.11: Volume scattering properties of the 2, 4 and 6 wt % HPC based TT membranes at the wavelength of 600 nm as a function of membrane temperature.

Table 3-1: Volume scattering properties with respect to different HPC concentrations, membrane temperatures and wavelengths.

		400 nm				600 nm				800 nm			
		μ_s'	μ_s	μ_a	g	μ_s'	μ_s	μ_a	g	μ_s'	μ_s	μ_a	g
Unit	°C	mm^{-1}	mm^{-1}	mm^{-1}	/	mm^{-1}	mm^{-1}	mm^{-1}	/	mm^{-1}	mm^{-1}	mm^{-1}	/
2 wt %	**44**	0.67	5.81	0.36	0.88	0.31	5.70	0.46	0.95	0.19	5.69	0.48	0.97
	50	1.72	7.22	0.33	0.76	1.11	7.10	0.45	0.84	0.85	7.05	0.49	0.88
	56	2.30	7.01	0.29	0.67	1.48	6.91	0.40	0.79	1.18	6.87	0.44	0.83
4 wt %	**44**	1.06	5.88	0.43	0.82	0.59	5.77	0.53	0.90	0.42	5.73	0.57	0.93
	50	2.53	6.35	0.36	0.60	1.59	6.26	0.45	0.75	1.27	6.21	0.50	0.80
	56	2.99	6.71	0.33	0.55	2.00	6.63	0.41	0.70	1.63	6.59	0.45	0.75
6 wt %	**44**	1.28	6.45	0.44	0.80	0.78	6.34	0.55	0.88	0.58	6.30	0.60	0.91
	50	2.86	7.11	0.35	0.60	1.88	7.01	0.45	0.73	1.51	6.96	0.50	0.78
	56	3.63	7.37	0.35	0.51	2.41	7.30	0.42	0.67	1.99	7.26	0.46	0.73

3.3.3 Angular scattering profile and spatial flux distribution

The volume scattering properties determined in the previous section were used as input data to the Monte-Carlo ray-tracing model, where an irradiance detector rotates around the thermotropic laminated glazing sample to collect the scattered light at a specific angle from the sample (**Figure 3.7**).

Figure 3.12 shows the results of detected irradiance from the optical simulation (circle points) and the measurement (cross points). Good agreement is obtained between the simulated and measured results for the selected scattering angles (0°, 15°, 30°, 45° and 60°), membrane temperatures (48, 50 and 52°C) and HPC concentrations (2, 4 and 6 wt %). The validated results give confidence in the use of the optical modelling approach to predict the angular scattering profile and spatial flux distribution of the thermotropic membranes under different conditions.

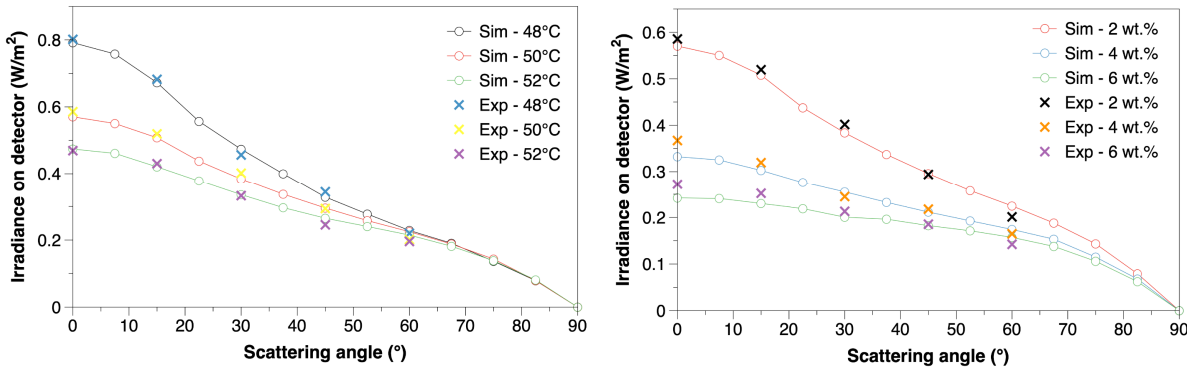

Figure 3.12: Comparison between the simulated and measured irradiances for (a) the sample with 2 wt % HPC at 48, 50 and 52°C, and (b) the samples with 2, 4 and 6 wt % HPC at 50°C.

The validated optical model has been subsequently used to investigate the angular scattering intensity distribution of the thermotropic laminated glazing sample when subjected to the changes in membrane temperature and HPC concentration. As can be seen from **Figure 3.13** (a), the 2 wt % HPC based sample at 44°C exhibits narrow-angle forward scattering, i.e., most of the incident light is scattered forwards within the angle range from 345° to 15°. The forward-scattering peak reduces significantly with the membrane temperature increasing from 44 to 56°C, as shown in **Figure 3.13** (a) and **Figure 3.13** (b). For instance, the normalised radiant intensity at the scattering angle of 0° reduces from ~1 sr^{-1} to ~0.18 sr^{-1} when the membrane temperature increases from 44 to 48°C, and further to ~0.09 sr^{-1} when above 54°C. On the other hand, the backward scattering becomes more prominent at higher membrane temperatures**.** In addition to the temperature effect, the angular scattering intensity distribution shows dependence on the HPC concentration. **Figure 3.13** (c) and **Figure 3.13** (d) illustrate that increasing the HPC concentration from 2 to 6 wt % results in suppressed forward scattering and enhanced backward scattering at the membrane temperatures of 50 and 56°C. Similar trends are observed for the other membrane temperatures in the range from 44 to 56°C (results not shown here). The results from **Figure 3.13** (c) and **Figure 3.13** (d) also show that increasing the HPC concentration results in a more uniform angular intensity distribution of the light scattered in the forward direction, which can potentially reduce the intensity contrast between the glare area and its neighbouring area thus providing more effective glare protection for buildings.

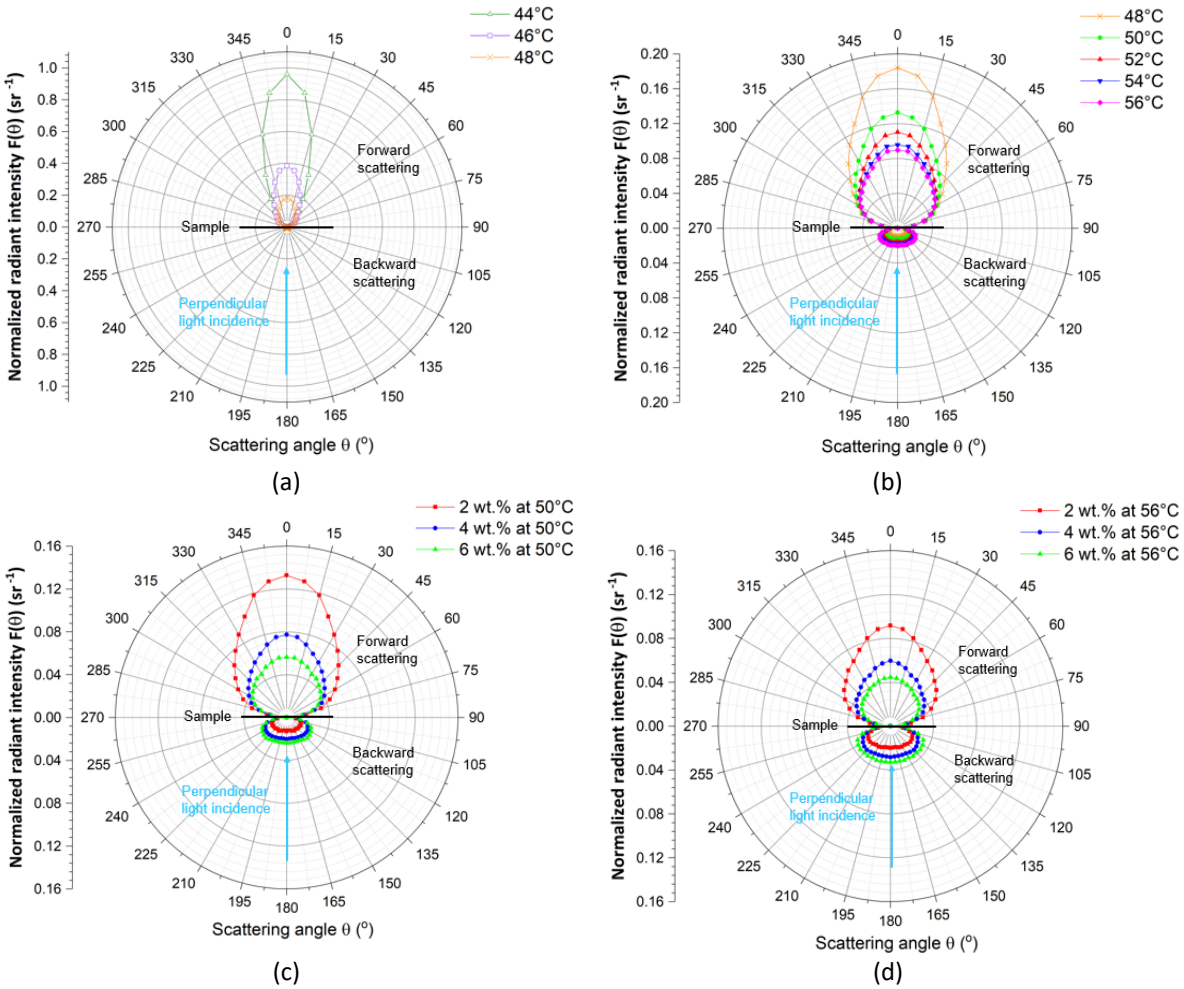

Figure 3.13: Normalised angular scattering intensity distributions of (a and b) the sample with 2 wt % HPC at the membrane temperatures from 44 to 56°C, (c and d) the samples with 2, 4 and 6 wt % HPC at the membrane temperatures of 50°C and 56°C.

Figure 3.14 illustrates the spatial flux distributions when light propagates in the 2 wt % and 6 wt % HPC based thermotropic layers at the three membrane temperatures: 44, 50 and 56°C. A light beam with a diameter of 0.5 mm was assumed to perpendicularly enter the top surface of the 1-mm-thick thermotropic layer (i.e., Y = 0). All the other settings are the same as in the previous optical simulations. As shown in **Figure 3.14**, the incident flux in the X range from -0.25 to 0.25 mm decreases with the depth increasing. The light attenuation is caused by the absorption and scattering in the thermotropic membrane. Due to the volume scattering, the light beam spreads in the transverse direction during propagation in the thermotropic layer. When the membrane temperature increases from 44 to 56°C or the HPC concentration increases from 2 to 6 wt %, the flux reaching the bottom surface (i.e., Y = -1) decreases, which results in reductions in the total transmittance (**Figure 3.9**) and forward scattering peak (**Figure 3.13**) of the thermotropic laminated glazing sample.

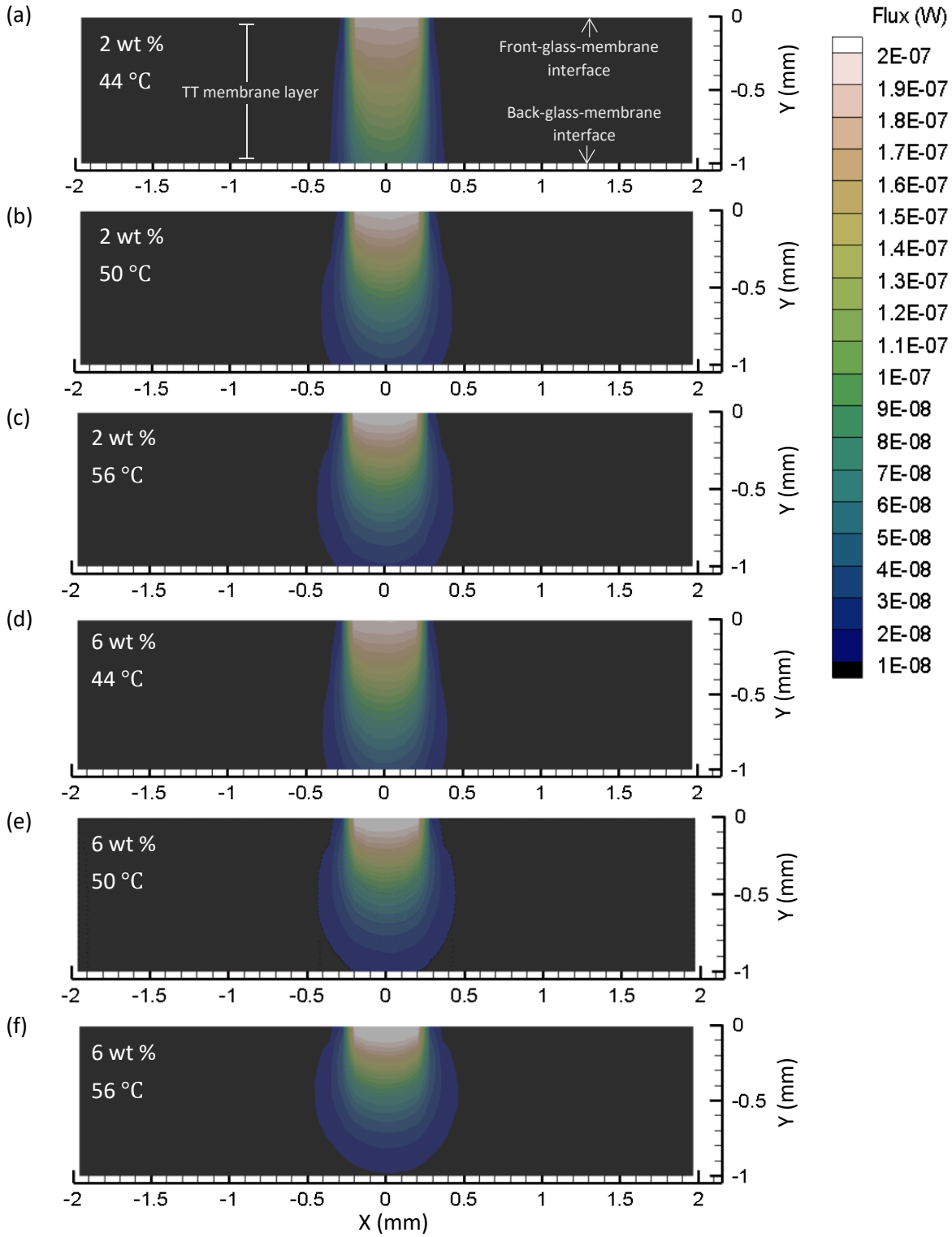

Figure 3.14: Cross-section views of the incident flux distribution in the TT membrane layer with 1 mm thickness for (a-c) 2 wt % HPC and (d-f) 6 wt % HPC at 44, 50 and 56°C, respectively, obtained from the optical simulation.

3.3.4 Optical design and characterisation of BIPV smart window

The developed optical model has been used to predict the effects of various parameters (e.g. HPC concentration, membrane thickness, geometric concentration ratio and glass refractive index) on the performance of the proposed BIPV smart window. Subsequently, a prototype for the BIPV smart

window and a prototype for the counterpart PV window of similar structure but with no HPC membrane (named reference system) have been fabricated based on the findings from the optical simulation. A schematic diagram for the BIPV smart window for initial optical modelling is illustrated in **Figure 3.15**. The BIPV smart window has a four-layer structure: a Dow Corning 1-2577 optical coating layer for encapsulating the solar cell (10 mm × 10 mm), a thermotropic membrane layer (50 mm × 50 mm × 1 mm) for modulating incident solar radiation and two GPE Scientific low-iron glass covers (50 mm × 50 mm × 4 mm). The thermotropic membrane layer was modelled using the sets of volume scattering properties (μ_a, μ_s and g) corresponding to the membrane temperatures from 44 to 56℃. The average refractive indices of the glass covers and the optical coating layer were defined as 1.51 and 1.49, respectively. The solar cell was assumed as a perfect light absorber (i.e., 100% absorptivity) for simplicity. AM1.5G sunlight with the power density of 1000 W/m^2 [182] was perpendicularly irradiated on the front glazing cover of the BIPV smart window. The ray number was set as 1,000,000 conformed by a ray independence study.

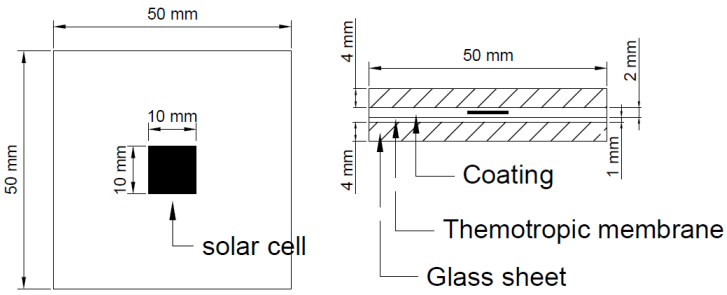

Figure 3.15: Configuration of the BIPV smart window prototype for optical analysis.

The effects of membrane temperature and HPC concentration on the optical performance of the BIPV smart window have been investigated and are shown in **Figure 3.16** (a). When the membrane temperature increases from 44 to 56°C, the optical power density (i.e., irradiance at the solar cell surface) of the BIPV smart window with the 2 wt % HPC membrane increases from 958 to 1028 W/m^2, higher than that of the reference system (930 W/m^2). This is because the thermotropic membrane offers stronger backward scattering at higher temperatures (see **Figure 3.13**), resulting in an increased fraction of incident light being reflected and redirected through Total Internal Reflection (TIR) towards the solar cell. **Figure 3.16** (a) also shows that higher optical power densities can be achieved by increasing the HPC concentration, for example, the optical power densities at 56°C for the 2, 4 and 6 wt % HPC concentrations are 1028, 1047 and 1061 W/m^2, respectively. Therefore, the HPC concentration of 6 wt % was selected for further parametric studies.

The optical performance of the BIPV smart window with a 6 wt % HPC membrane at different thicknesses is illustrated in **Figure 3.16** (b). The optical power density increases significantly with the

membrane thickness increasing from 0.1 to 0.5 mm. A possible reason may be that using a thicker membrane increases the number of scattering events along the path of propagation, thus causing more photons to be scattered to the solar cell. With further increasing the thickness above 1 mm, it is observed that there is no significant increase in optical power density, probably because the contribution of longer path length travelled photons to the light reflectance is less significant [183]. In other words, the reflected radiation is mainly contributed by the near-surface volume scattering [151].

Figure 3.16 (c) illustrates the relationship between the geometric concentration ratio (i.e., the ratio between the aperture areas of the front glazing cover and solar cell) and the optical performance of the BIPV smart window with a 1-mm-thick 6 wt % HPC membrane. Taking the membrane temperature of 56°C as an example, when the geometric concentration ratio is increased from 4 to 16, the optical power density increases from 1019 to 1057 W/m^2. This is due to a larger area of the thermotropic membrane available, resulting in more photons being reflected and concentrated on the solar cell. There is a slight increase to 1064 W/m^2 when the geometric concentration ratio is further raised to 36, indicating that most of the photons scattered from the expansion area could not be collected by the solar cell. The optical losses could be attributed to the escaping of photons from the window system and the absorption of photons in the coating/glass/membrane before reaching the solar cell.

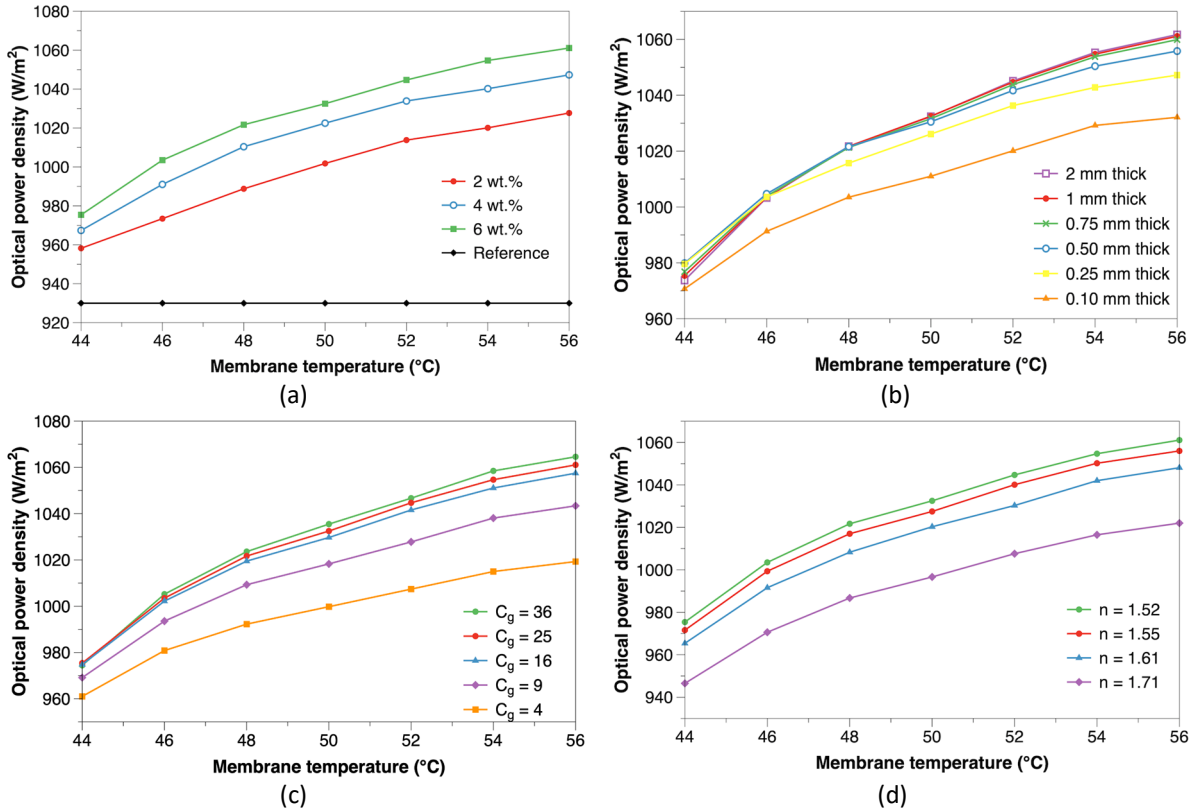

Figure 3.16: Optical power density for the BIPV smart windows based on (a) different HPC concentrations, membrane thickness d = 1 mm, geometric concentration ratio C_g = 25 and refractive index of the front glass cover n = 1.52; (b) 6 wt % HPC, different thicknesses, C_g = 25 and n = 1.52; (c) 6 wt % HPC, d = 1 mm, different C_g

and n = 1.52; (d) 6 wt % HPC, d = 1 mm, C_g = 25 and different refractive indices. N.B., the C_g was varied by maintaining the same solar cell area while changing the glass aperture area.

The refractive index of the front glazing cover is another factor affecting the optical performance of the BIPV smart window. As can be seen from **Figure 3.16** (d), the curve of optical power density plotted against membrane temperature shifts downwards as the refractive index is increased from 1.52 to 1.71. This may be because the front glazing cover with a higher refractive index has lower optical transmittance and reduces the direct sunlight received by the solar cell.

After considering all the factors affecting the BIPV smart window performance, the HPC concentration of 6 wt % with the membrane thickness of 1 mm, the geometric concentration ratio of 16 and the glass refractive index of 1.52 was selected and applied for the prototype development.

3.3.5 Experimental validation

The optimised prototype of the BIPV smart window has been characterised by an indoor environmental experiment. The electrical performance of the prototype illuminated under a tungsten halogen lamp was measured using a Keithley 2420 source meter unit. The incident light intensity and the ambient air temperature were controlled to be 90 mW/cm^2 and 25°C, respectively. **Figure 3.17** (a) shows the current-voltage (I-V) characteristics at different membrane temperatures of the prototype BIPV smart window. The short-circuit current density increases by 17.8% from 27.8 to 32.8 mA/cm^2 with the membrane temperature increasing from 42 to 54°C, and meanwhile, the maximum power output increases by 12.1%. The result demonstrates that the BIPV smart window system can produce more electricity when the integrated thermotropic membrane provides stronger light scattering while subjected to higher temperatures above its transition temperature.

Based on the experimental results, the ratio of short-circuit currents generated from the prototype BIPV smart window ($I_{sc,BIPV}$) and from its counterpart system with no membrane (reference system) ($I_{sc,ref}$) was calculated. From **Figure 3.17** (b), it can be seen that the short-circuit current ratio increases from 1.053 to 1.145, with the membrane temperature increasing from 44 to 56°C. Since the short-circuit current produced by a solar cell can be taken as directly proportional to the irradiance at the cell surface [85, 142, 184], the ratio of irradiances between the prototype BIPV smart window ($G_{s,BIPV}$) and the reference system ($G_{s,ref}$) can be expressed by **Equation (3.4)**. The irradiance ratios at various membrane temperatures derived from the experiment and optical simulation are presented in **Table 3-2**. The simulation results give good agreement with the experimental results, with differences of less than 1%. This validation confirms the usefulness of the optical modelling approach for predicting the dynamic behaviours of the BIPV smart window system.

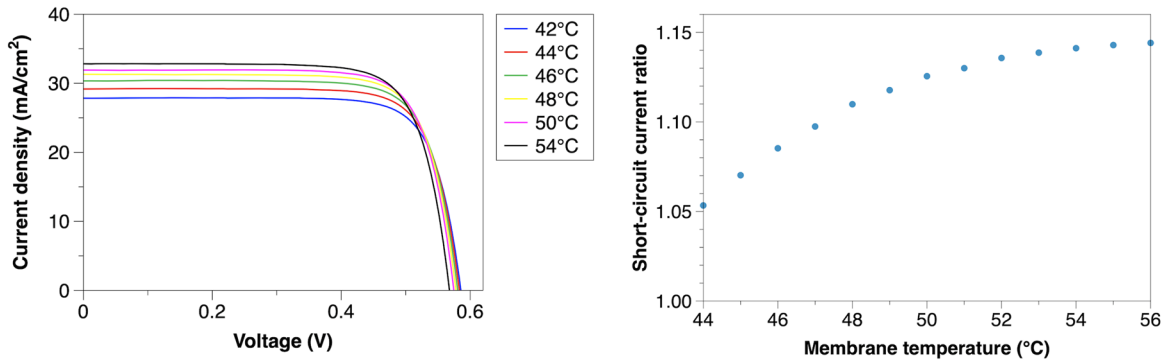

(a) (b)

Figure 3.17: (a) I-V characteristics of the BIPV smart window prototype at different membrane temperatures. (b) The ratio of short-circuit currents between the BIPV smart window and the reference system as a function of membrane temperature.

$$\frac{I_{sc,BIPV}}{I_{sc,ref}} = \frac{G_{s,BIPV}}{G_{s,ref}} \tag{3.4}$$

Table 3-2: Experimental and simulated irradiance ratios at different membrane temperatures.

		44°C	46°C	48°C	50°C	52°C	54°C	56°C
$\frac{G_{s,BIPV}}{G_{s,ref}}$	Experiment	1.053	1.085	1.109	1.125	1.135	1.141	1.145
	Simulation	1.050	1.080	1.101	1.116	1.127	1.136	1.143
	Difference	0.3%	0.5%	0.7%	0.8%	0.7%	0.4%	0.2%

3.4 Summary

This chapter presents a generalised method for evaluating the scattering characteristics of translucent materials (e.g. thermotropic hydrogels) and also for the accurate performance prediction of the proposed BIPV smart window system. To be more specific, a numerical method based on Inverse Adding-Doubling (IAD) calculation coupled with Double-Integrating-Sphere (DIS) spectroscopic measurements has been firstly used to determine the volume scattering properties of the HPC based thermotropic hydrogel membranes. Subsequently, a Monte-Carlo ray-tracing model using the volume scattering properties obtained from the IAD has been developed to predict the dynamic behaviours of the developed thermotropic membranes (2, 4 and 6 wt % HPC) and optimise the design of the proposed BIPV smart window system. The simulation predictions were found to be in good agreement with the experimental results. The key findings and conclusions are as follows:

1) The total transmittance of the thermotropic laminated glazing sample (2 wt % HPC) reduces from ~90% to ~20% and the collimated transmittance reduces from ~80% to ~0%, with the membrane temperature increasing from 27 to 56˚C. These features indicate that the

developed thermotropic membrane offers good potential for application in windows to avoid excessive solar heating and glare.

2) The optical simulation results show that increasing membrane temperature or HPC concentration leads to stronger backward scattering from the thermotropic membrane, resulting in an improved power output of the BIPV smart window.
3) There is no significant improvement in power generation when the geometric concentration ratio of the BIPV smart window (6 wt % HPC) exceeds 16× and the membrane thickness is greater than 1 mm.
4) The optimised prototype of the BIPV smart window shows an increase in short-circuit current density by 17.8% and an increase in maximum power output by 12.1% with the membrane temperature increasing from 42 to 54℃.
5) The short-circuit current of the prototype BIPV smart window is up to 1.15 times higher than that of its counterpart system of similar structure but with no membrane.

Chapter 4 – Material selection, membrane synthesis, window development and indoor experimental characterisation

4.1 Introduction

As indicated in our previous chapters, the thermotropic hydrogels prepared from aqueous blends of HPC polymer and gellan gum possess suitable properties for application in BIPV smart windows:

- High visible and near-infrared transmittance in the clear state (below T_s) and low transmittance in the translucent state (above T_s)
- High reflectance (above T_s) within the wavelength range of 350-1100 nm, compatible with the spectral response of crystalline-silicon solar cells.
- Simple synthesis process.

The transition temperatures of the HPC-gellan-gum based thermotropic hydrogels at low HPC concentrations (2-6 wt %) are found to be approximately 40-42°C. However, these hydrogels may not be suitable for use in the climates with mild temperatures during summer, such as the UK (where the average summer daytime temperature is approximately 20°C), since the hydrogels would spend most of the time in the transparent state, scarcely exploiting their potential for energy efficiency. Therefore, the thermotropic hydrogels need to be further developed to adapt to a range of climatic conditions.

According to the literature (see **Table 4-1**), the transition temperature and optical properties of the hydrogels made of the polymers such as HPC, poly(N-isopropylacrylamide) (PNIPAm) and hydroxypropyl methylcellulose (HPMC) could be adjusted by adding alcohol (e.g. glycerol), acid (e.g. acrylic acid) and salt (e.g. sodium chloride (NaCl)). Numerous researches dealing with the effect of salt addition have been conducted [103, 113, 185, 186]. The study from Xia et al. [114] suggested that the transition temperature of HPC-NaCl aqueous solution decreases linearly with the increase of NaCl concentration. Yang et al. [106] prepared a series of HPC-NaCl films with a fixed HPC concentration (0.5 wt %) and varying NaCl concentrations. The transition temperature was found to decrease from 38 to 30°C by increasing the NaCl concentration from 0.5 wt % to 5 wt %, and simultaneously the solar transmittance modulation is improved from 25.7% to 43.6%. The microscopic properties of pure HPC and HPC-NaCl aqueous solutions at varying temperatures were studied by Weißenborn and Braunschweig [185]. The results show that the mean hydrodynamic radius of scattered particles in the salt-free HPC aqueous solution starts to decrease at 45°C, due to coil-to-globule transition, whereas the transition temperature is shifted to 32.5°C by adding 0.7 M NaCl.

Table 4-1: Thermal and optical properties of thermotropic hydrogels reported in the literature.

	Compositions (weight concentration)		**d** (mm)	T_s (°C)	τ_{vis}	$\Delta\tau_{vis}$	$\Delta\tau_{solar}$	**Ref.**
1	HPC (0.05%)		-	43	-	-	-	[185]
2	HPC (6%)	+ GGF (1.5%)	0.5	42	>90%	>70%	-	[107]
3	HPC (0.5%)	+ NaCl (5%)	0.35	30	82.5%	66.9%	43.6%	[106]
4	HPC (0.5%)	+ glycerol (33%)	2	30	-	~80%	-	[187]
5	HPC (0.3%)	+ HEC (1.4%)	10	22.5	~90%	-	-	[97]
6	HPC (0.6%)	+PAA (1%)	-	17	-	-	-	[188]
7	PNIPAm (8%)		0.2	32	89.1%	88.5%	73.9%	[95]
8	PNIPAm	+ AEMA	0.24	32	87.2%	85%	81.3%	[104]
9	PNIPAm (1.6%)	+ PAM	1	30	92%	36.4%	-	[189]
10	PNIPAm	+ TDMImAc	-	25	>90%	-	-	[190]
11	PNIPAm (2.5%)	+ glycerol (35%)	2	20.4	-	~70%	~60%	[98]
12	HPMC (1%)		-	69	-	-	-	[191]
13	HPMC (0.5%)	+ PAA (7%)	-	38	-	-	-	[192]
14	HPMC (2%)	+ AuNRs	10	35	-	-	-	[109]
15	HPMC (2%)	+ NaCl (20%)	2	24	~80%	-	-	[117]

d is the layer thickness, T_s is the transition temperature, τ_{vis} is the average visible light transmittance in the clear state, $\Delta\tau_{vis}$ and $\Delta\tau_{solar}$ are the differences in average visible light transmittance and solar transmittance respectively between the clear and translucent states. HEC: hydroxyethyl cellulose; PAA: poly(acrylic acid); AEMA: 2-aminoethylmethacrylate hydrochloride; PAM: polyacrylamide; TDMImAc: 1-Methyl-3-tetradecylimidazolium acrylate; AuNRs: gold nanorods.

In this chapter, a comprehensive experimental study was conducted to optimise the HPC based thermotropic hydrogel for applications in the UK climate. The procedures include: (1) investigation of the correlation between transition temperature, composition and concentration of HPC aqueous solution (i.e., no gelling agent added); (2) synthesis of HPC based hydrogel membranes with different component concentrations and characterisation of their optical and thermal behaviours by spectroscopic measurement; (3) design and fabrication of a BIPV smart window system with the optimised hydrogel membrane; (4) experimental evaluation of the developed BIPV smart window system under controlled laboratory conditions.

4.2 Methodology

4.2.1 Material synthesis and optical measurement setup

4.2.1.1 HPC aqueous solution synthesis

HPC polymer (weight average molecular weight (M_w) ~ 80,000 and number average molecular weight (M_n) ~ 10,000) in the form of off-white powder was purchased from Sigma Aldrich and used without any purification. HPC aqueous solution was prepared by mixing the HPC powder in distilled water at room temperature until thoroughly dissolved. Salt such as NaCl sourced from Sigma Aldrich was added to the HPC aqueous solution to form an HPC-salt hybrid solution.

4.2.1.2 HPC aqueous solution tests

The prepared pure HPC or HPC-salt aqueous solution was dripped into a quartz cuvette with a pathlength (or medium thickness) of 10 mm. The cuvette was placed in an Ocean Optics Qpod-2e sample compartment (see **Figure 4.1**). The Peltier-controlled cuvette holder in the sample compartment exchanged heat with the circulating water from the water bucket and provided temperature control from -15°C to 105°C with a precision of ±0.01°C (i.e., a measure of how well the cuvette is maintained at constant temperature) for the cuvette [193]. The Qpod-2e sample compartment was connected to an Ocean Optics HL2000 halogen light source and a USB2000+UV-VIS-ES spectrometer using collimating-lens-attached optical fibres. This setup allowed the measurement of spectral transmittance (in the collimated direction) for the HPC aqueous solution with its temperature precisely controlled. Based on the HPC aqueous solution tests, the transition temperatures under different compositions (i.e., without salt added and with different types of salt) and concentrations were obtained and used as references for the subsequent membrane development.

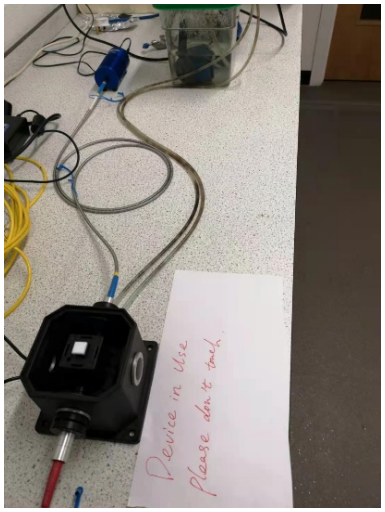

(a)

Transparent state

Translucent state

(b)

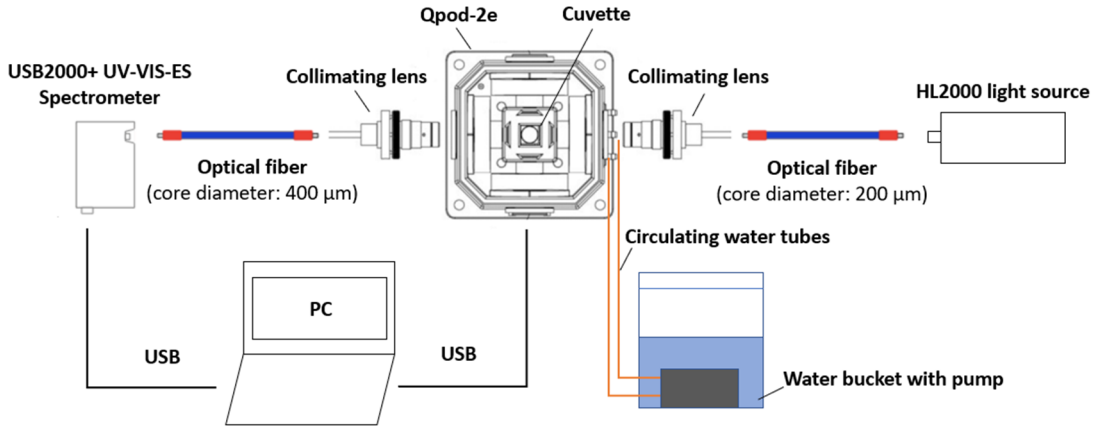

(c)

Figure 4.1: Photographs of (a) the experimental setup for the HPC aqueous solution tests, and (b) the cuvette containing the HPC aqueous solution when it was unheated (above photograph) and when heated above its transition temperature (below photograph); (c) schematic diagram of the setup.

4.2.1.3 HPC hydrogel membrane synthesis

This section outlines the procedures for the synthesis of the HPC hydrogels without salt (**Steps 1-3**) and with salt (**Steps 1-5**) and the membrane development (**Step 6-7**). **Step 1**: Gellan Gum type F (GGF) powder sourced from Special Ingredients was magnetically stirred into distilled water at 80°C for several minutes until all the GGF dissolved. **Step 2**: the GGF aqueous solution was cooled to 60°C and then fed steadily with HPC powder (average Mw ~ 80,000 and average Mn ~ 10,000) sourced from Sigma-Aldrich. **Step 3**: the HPC-GGF-water mixture was left stirring for 2-3 hours until the HPC had fully dissolved (i.e. the number of hours depends on the amount of HPC to dissolve). **Step 4**: a certain amount of NaCl-water solution needed to produce the desired concentrations of the final hydrogel composition was dripped into the HPC-GGF-water solution using a pipette while stirring vigorously. **Step 5**: after the mixing completed, the visible air bubbles trapped in the HPC-GGF-NaCl hydrogel were removed using ultrasonic vibration. **Step 6**: after naturally cooled to 25°C, the hydrogel was laminated with two 4-mm-thick low-iron optical glass slides sourced from GPE scientific; the thickness of the hydrogel layer (membrane) was controlled to be 1 mm by the use of a gasket spacer between the glass slides. **Step 7**: the laminated glass unit was sealed around the edges with butyl sealant to prevent the hydrogel from leakage and drying out.

4.2.1.4 Membrane spectroscopy measurement

The spectral transmittance and reflectance of the laminated glass unit (glass/membrane/glass) were measured by an Ocean Optics USB2000+ spectrometer (spectral range: 300-1000 nm) and an Ocean Optics NIRQuest 512-2.5 spectrometer (spectral range: 1000-2500 nm) coupled with integrating spheres and a GyroStir-DH hot plate (see **Figure 4.2**). The spectral transmittance and reflectance of the thermotropic membrane were obtained by subtracting the spectra of the low-iron optical glass

slides from the measured spectra, using the baseline-correction method presented by Connelly et al. [107, 108]. The baseline for the reflectance tests was a 4-mm-thick GPE scientific optical glass slide covered by an Ocean Optics WS-1 diffuse reflectance standard (100% reflectance). The baseline for the transmittance tests was an optical glass slide of the same type but at a thickness of 8 mm. Based on the measured spectral data, the average visible light transmittance (τ_{vis}) and average visible light reflectance (ρ_{vis}) of the thermotropic membrane were calculated using **Equations (2.9)** and **(2.10)** [146], and the solar transmittance (τ_{solar}) and solar reflectance (ρ_{solar}) were calculated using **Equations (4.1)** and **(4.2)** [146].

$$\tau_{solar} = \frac{\sum_{300\ nm}^{2500\ nm} S_\tau \tau(\lambda) \Delta\lambda}{\sum_{300\ nm}^{2500\ nm} S_\tau \Delta\lambda} \tag{4.1}$$

$$\rho_{solar} = \frac{\sum_{300\ nm}^{2500\ nm} S_\tau \rho(\lambda) \Delta\lambda}{\sum_{300\ nm}^{2500\ nm} S_\tau \Delta\lambda} \tag{4.2}$$

where $\tau(\lambda)$ is the measured spectral transmittance, $\rho(\lambda)$ is the measured spectral reflectance, $\Delta\lambda$ is the interval between wavelengths, S_τ is the relative spectral distribution of solar radiation.

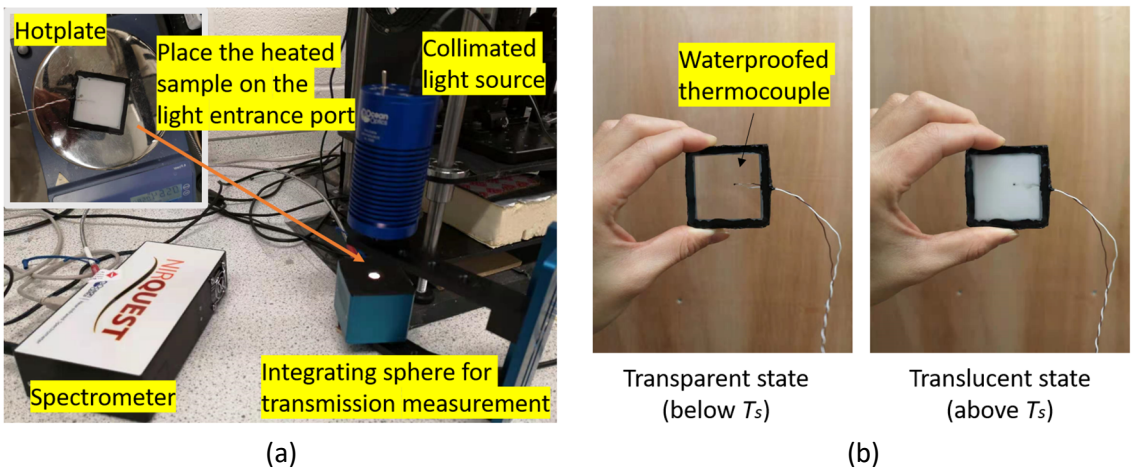

Figure 4.2: (a) Optical measurement setup, (b) sample in the transparent and translucent states.

4.2.2 Window fabrication and indoor characterisation setup

Figure 4.3 illustrates a small prototype designed for the BIPV smart window system, where the components' dimensions (e.g. aperture area and thickness of the glass covers and membrane) have been optimised using the technique of Monte-Carlo ray-tracing simulation coupled with the IAD method (described in **Chapter 3**). The window performance was experimentally characterised using the setup shown in **Figure 4.4**. In the setup, a plate holder from Thorlabs was used to clamp the prototype with its front side facing a tungsten-halogen lamp. An irradiance probe comprised of an Ocean Optics 200-µm-core-diameter optical fibre and an Ocean Optics CC-3-UV cosine corrector was held against the rear glass cover of the prototype and connected to an Ocean Optics USB2000+

spectrometer (with a wavelength range of 350-1000 nm and a resolution of 0.5 nm) to detect the transmitted radiation. The optical sampling system had been calibrated for absolute spectral irradiance measurement using an Ocean Optics LS-1-CA calibration light source. The prototype was linked to a Keithley 2420 source meter unit via a four-wire connection method to measure its current-voltage (I-V) characteristics. The temperatures of the integrated solar cell and thermotropic membrane were recorded by T-type thermocouples connected to a Datataker DT85. The optical, electrical and temperature measurements were performed simultaneously under the controlled environment conditions: ambient air temperature 25°C and total irradiation level 900 W/m^2 (determined by a Kipp & Zonen pyranometer CMP11 with the spectral response range 285-2800 nm).

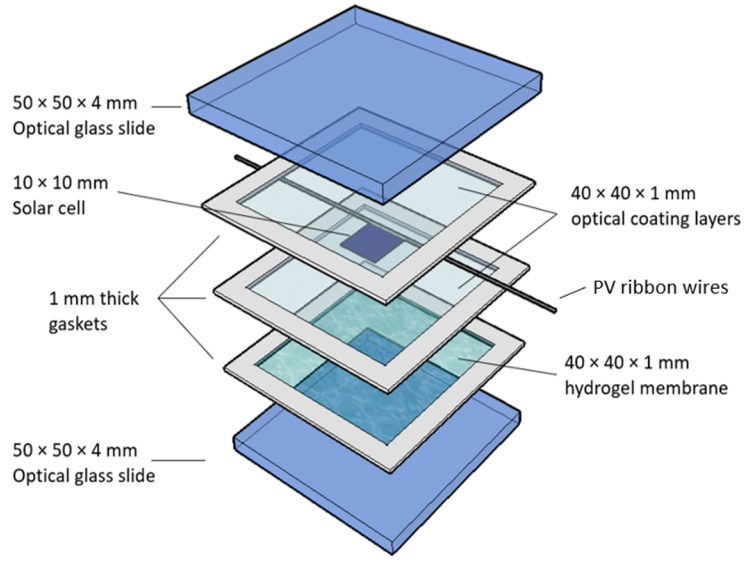

Figure 4.3: Schematic diagram of the structural design of the BIPV smart window prototype.

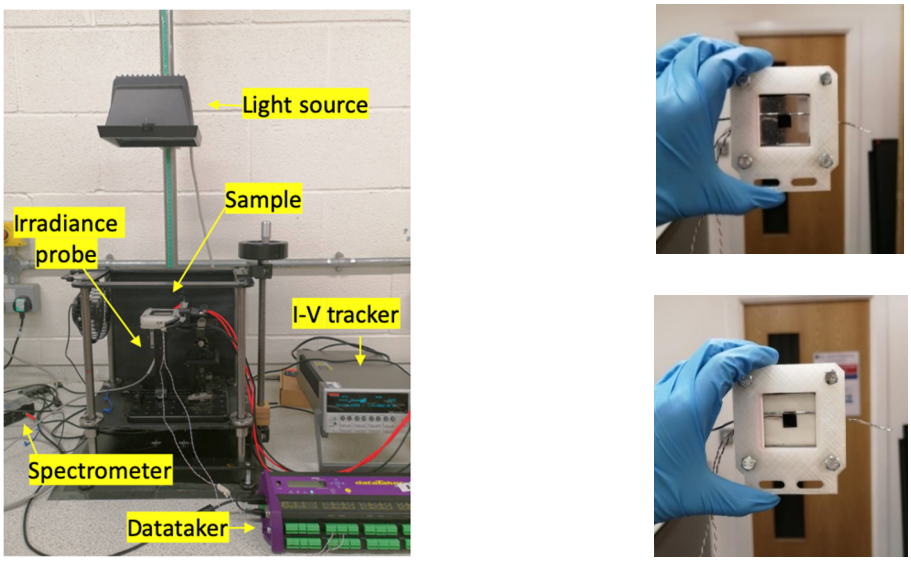

Figure 4.4: (a) Setup for indoor characterisation; (b) images illustrating the appearance change of the fabricated BIPV smart window below and above its transition temperature.

4.3 Results and Discussion

4.3.1 Thermal and optical properties of HPC aqueous solutions

Figure 4.5 shows the average visible light transmittance (τ_{vis}) of the pure HPC aqueous solutions as a function of solution temperature. As can be seen, the transition temperature (T_s) (i.e., the temperature at which the τ_{vis} is half of the clear state transmittance at 26°C) decreases from 40.2 to 39.5°C by increasing the HPC concentration from 3 to 6 wt %. However, the T_s reduces by only approximately 1°C when the HPC concentration is increased from 6 to 15 wt %. This indicates that a further increase in HPC concentration would exert a minor effect on the transition temperature.

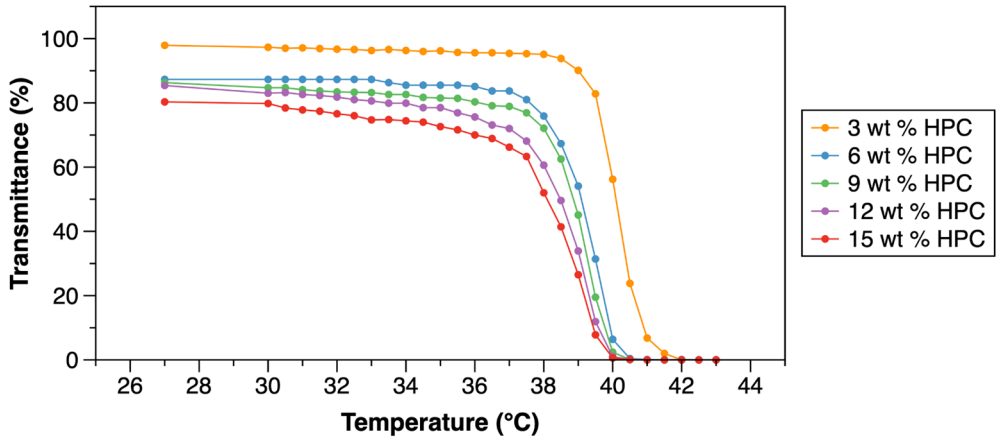

Figure 4.5: Average visible light transmittance of the HPC aqueous solutions at varying temperatures with respect to different HPC concentrations.

The effect of adding different types of salt on the transition temperature of HPC aqueous solution was investigated. As can be seen from **Table 4-2**, the HPC aqueous solution with sodium sulfate (Na_2SO_4) has the lowest T_s, followed by sodium chloride (NaCl), calcium chloride ($CaCl_2$) and sodium nitrate ($NaNO_3$), while adding potassium iodide (KI) leads to an increase in T_s. This may be because the salt addition affects the solubility of HPC polymer in water. The salting-out effectiveness follows a specific ion order (or the so-called Hofmeister series): $SO_4^{-2} > Cl^{-1} > NO_3^{-1} > I^{-1}$ and $Na^+ > Ca^{2+}$ [103, 194]. In this work, NaCl was selected as the additive for adjusting the transition temperature of HPC aqueous solution/hydrogel, considering trade-offs between salting-out effectiveness and health safety. Although Na_2SO_4 is more effective in reducing the transition temperature, it is a slightly hazardous salt that may cause irritation in the case of eye/skin contact and asthma if inhaled, while NaCl is generally regarded as non-hazardous.

Table 4-2: Transition temperatures of the aqueous solutions of 3 wt % HPC with and without salts (3 wt %).

	HPC only	HPC + NaCl	HPC + $CaCl_2$	HPC + $NaNO_3$	HPC + Na_2SO_4	HPC + KI
T_s	40.2°C	31.7°C	34.0°C	38.8°C	25.4°C	43.2°C

The τ_{vis} of the HPC aqueous solutions made at a constant HPC concentration (6 wt %) and different NaCl concentrations as function of solution temperature is shown in **Figure 4.6**. By increasing the NaCl concentration from 0 to 4.5 wt %, the T_s is found to decrease significantly from 39.5°C to 27.7°C, while the hysteresis loop width of the τ_{vis} upon heating and cooling remains narrow (<1.5°C) (see **Figure 4.7**). The effective reduction in transition temperature may be because the presence of NaCl weakens the hydrogen bonding between HPC polymer and water, facilitating the HPC polymer to aggregate and precipitate out of solution at a reduced temperature.

Further increasing the NaCl concentration is undesirable as the HPC-NaCl aqueous solution turns cloudy at or below room temperature (25°C), which would affect daylighting and viewing when applied in windows. For example, the HPC aqueous solution with 6 wt.% NaCl starts to switch at approximately 22°C. Accordingly, the NaCl concentrations of 4.5 wt % (with a T_s of approximately 28°C) and 3 wt % (with a T_s of approximately 31°C) were selected for the subsequent membrane synthesis and evaluation.

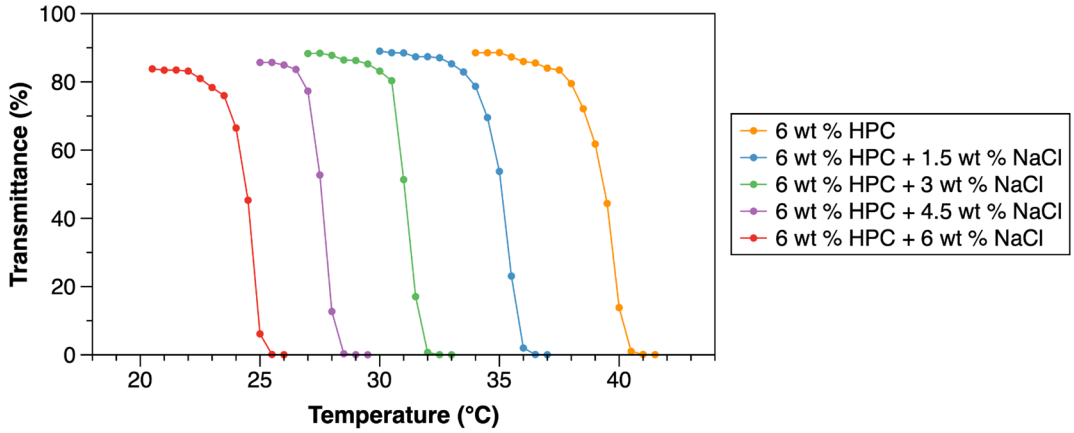

Figure 4.6: Average visible light transmittances of HPC aqueous solutions with various NaCl concentrations at different solution temperatures. The solution temperature was precisely controlled by the device in Figure 4.1.

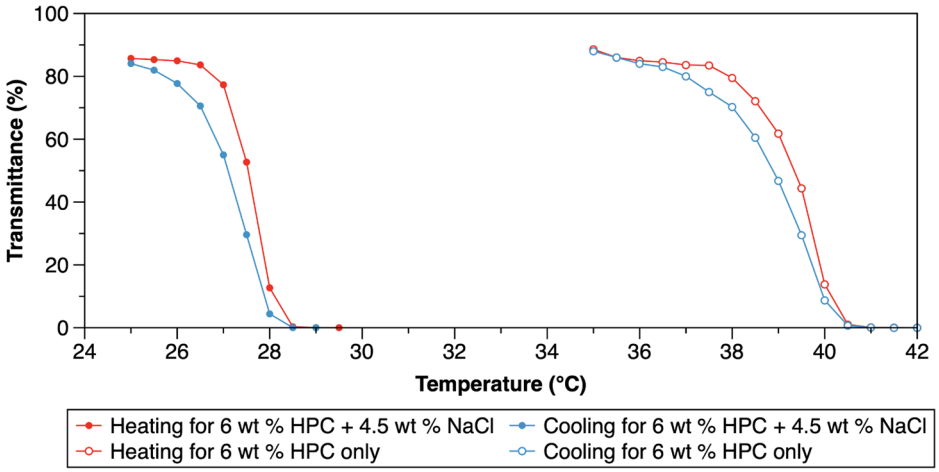

Figure 4.7: Variation in average visible light transmittance when the HPC aqueous solutions were subject to heating and subsequent cooling.

4.3.2 Thermal and optical properties of HPC hydrogel membranes

Three salt-free HPC hydrogel membranes were prepared by increasing the HPC concentration from 6 wt % to 12 wt % while maintaining the GGF concentration constant at 0.5 wt %, in order to further explore the hypothesis raised in [107], that increasing the concentration of HPC within HPC-GGF based hydrogel may potentially reduce the transition temperature. To investigate the salt effect, two NaCl-added HPC hydrogel membranes were synthesised using the same concentrations of HPC (6 wt %) and GGF (0.5 wt %) but with different concentrations of NaCl: 3 wt.% and 4.5 wt %.

The spectral transmittance and reflectance of the HPC hydrogel membranes with different compositions at 25°C and 55°C are shown in **Figure 4.8**. At 25°C, there are little differences in transmittance and reflectance across the whole investigated spectrum between the thermotropic membranes. When the temperature increases to 55°C, the spectral transmittance reduces significantly, for example, from over 90% to about 20% in the visible region (380-780 nm) for the salt-free hydrogel membranes, whereas to about 10% for the salt-added hydrogel membranes. On the other hand, raising the temperature to 55°C results in higher spectral reflectance. In this state, most reflection is observed in the wavelength range of 400-1100 nm, matching well with the spectral response of crystalline-silicon solar cells [108, 195]. It can also be seen that the hydrogel membranes with increased concentrations of HPC or NaCl have higher spectral reflectance and conversely lower spectral transmittance.

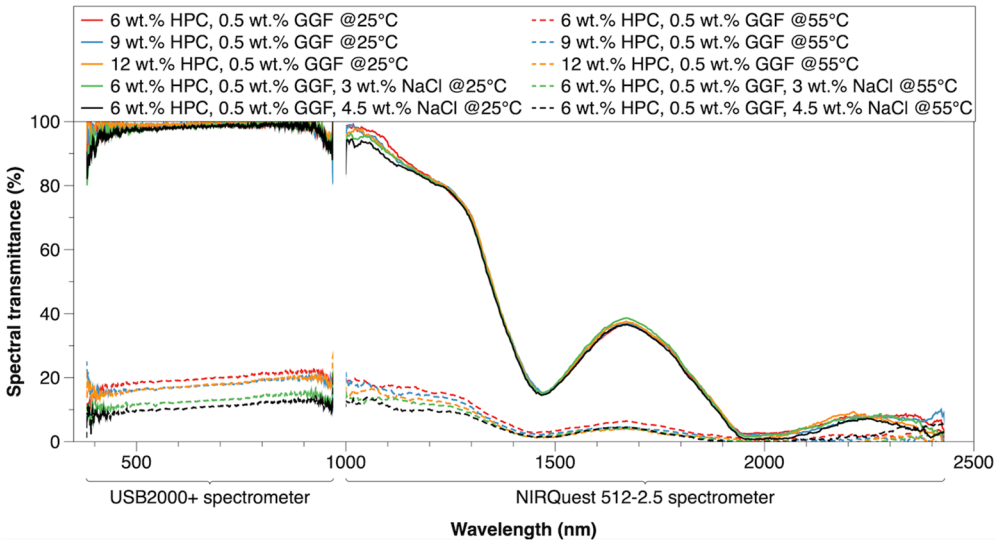

(a)

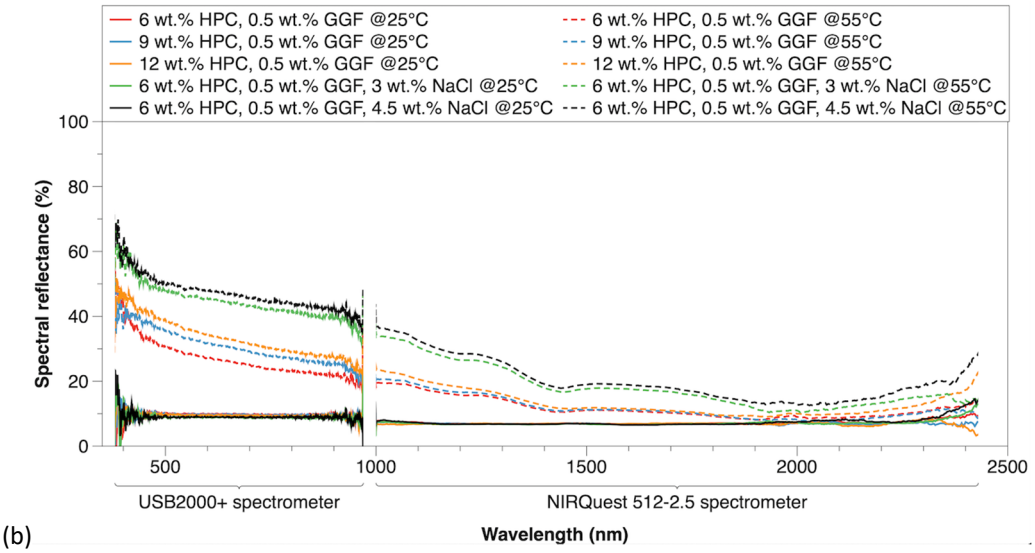

(b)

Figure 4.8: (a) spectral transmittance and (b) spectral reflectance of the thermotropic membranes (1 mm thickness) with different compositions at 25°C and 55°C.

Figure 4.9 (a) shows the variation of the average visible light transmittance (τ_{vis}) of the thermotropic membranes upon heating from 25°C to 55°C and their transition temperatures (T_s). As can be seen, the hydrogel membrane made of 6 wt % HPC and 0.5 wt % GGF exhibits the highest T_s observed to be 42.7°C. There is a slight reduction in T_s by approximately 2°C after doubling the concentration of HPC, indicating a limited effect of HPC concentration on transition temperature. In terms of NaCl salt effect, the T_s is reduced to 34.1°C and 30.7°C after adding NaCl salt to 6 wt % HPC based hydrogel membrane to the concentration of 3 wt % and 4.5 wt %, respectively. It is expected that with further increasing the NaCl concentration, the T_s would continuously decrease.

The average visible light reflectance (ρ_{vis}) with increased temperature of the thermotropic membranes is shown in **Figure 4.9** (b). At 25°C, the ρ_{vis} is approximately 10% and almost unaffected by varying the concentration of HPC or NaCl. The ρ_{vis} starts to increase at approximately 40°C for the salt-free hydrogel membranes, while it is approximately 35°C and 31°C for the hydrogel membranes with 3 wt % NaCl and 4.5 wt % NaCl, respectively. Among the tested samples, the hydrogel membrane with 4.5 wt % NaCl has the highest ρ_{vis} when above the T_s. For example, at 55°C the reflectance is 48.7% for the sample of 6 wt % HPC, 0.5 wt % GGF and 4.5 wt % NaCl, compared to 37.4% for the sample of 12 wt % HPC and 0.5 wt % GGF and 30.0% for the sample of 6 wt % HPC and 0.5 wt % GGF.

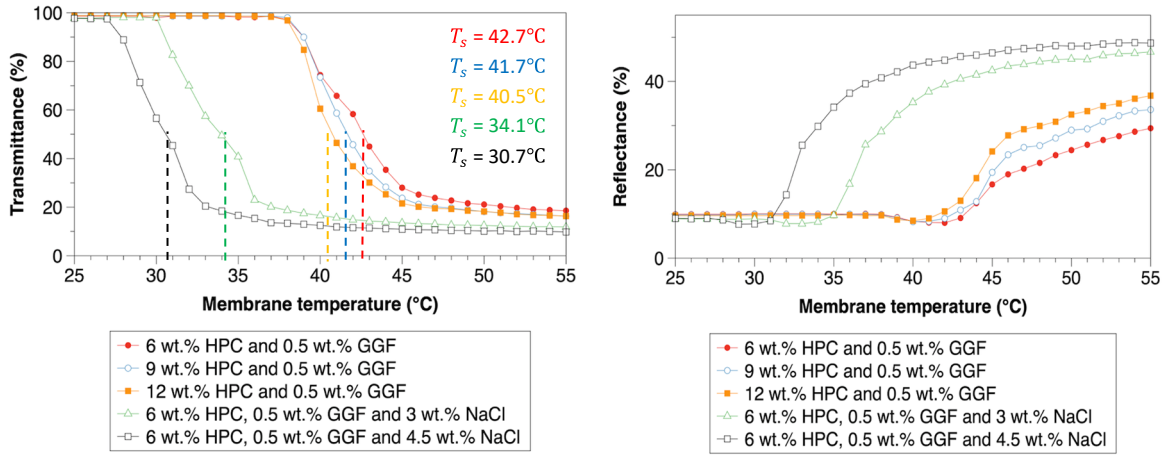

(a) (b)

Figure 4.9: (a) Average visible light transmittance and (b) average visible light reflectance of the thermotropic membranes (1 mm thickness) over the temperature range of 25°C to 55°C.

The solar reflectance (ρ_{solar}) and solar transmittance (τ_{solar}) of the thermotropic membranes at 25°C and 55°C are outlined in **Table 4-3**. From **Table 4-3** and **Figure 4.8**, it can be seen that increasing the membrane temperature results in a higher ρ_{solar} but a lower τ_{solar}. It can also be seen that the hydrogel membranes with and without NaCl have similar values of ρ_{solar} and τ_{solar} at 25°C. However, when the membrane temperature increases to 55°C, the ρ_{solar} of the hydrogel membrane with 4.5 wt % NaCl increases to 41.0%, compared to 25.9% for the hydrogel membrane with the same HPC concentration (6 wt %) and no salt added. The hydrogel membrane with 4.5 wt % NaCl shows the highest solar transmittance modulation ($\Delta\tau_{solar}$) of 76.2% (i.e., the difference in solar transmittance between 25°C and 55°C) among the tested samples.

Table 4-3: Solar reflectance (ρ_{solar}), solar transmittance (τ_{solar}) and solar transmittance modulation ($\Delta\tau_{solar}$) of the thermotropic membranes (1 mm thickness).

Properties at different Temperatures		**6 wt % HPC 0.5 wt %GGF**	**9 wt % HPC 0.5 wt % GGF**	**12 wt % HPC 0.5 wt % GGF**	**6 wt % HPC 0.5 wt % GGF 3 wt % NaCl**	**6 wt % HPC 0.5 wt % GGF 4.5 wt % NaCl**
ρ_{solar}	25°C	9.2%	8.7%	8.4%	8.3%	7.9%
	55°C	25.9%	26.6%	29.1%	38.4%	41.0%
τ_{solar}	25°C	87.2%	87.3%	87.8%	86.3%	85.8%
	55°C	17.5%	15.6%	15.0%	11.5%	9.6%
$\Delta\tau_{solar}$		69.7%	71.7%	72.8%	74.8%	76.2%

The above results demonstrate that adding NaCl salt to a HPC based hydrogel membrane reduces the transition temperature, while providing higher solar transmittance modulation as well as higher reflectance when the hydrogel membrane experiences a temperature above the T_s, which would benefit for passive overheat protection and electricity generation of the BIPV smart window system. This is likely to be attributed to the weakened strength of hydrogen bonding between HPC polymer chains and surrounding water molecules after NaCl salt addition [106, 114]. Increasing the

concentration of NaCl tends to reduce the solubility of HPC in water and drive the aggregation of HPC at elevated temperature. With an increased number of HPC aggregates (scattering domains) presenting in water, light scattering from the hydrogel membrane is enhanced.

The thermotropic hydrogel membrane composed of 6 wt % HPC, 0.5 wt % GGF and 4.5 wt % NaCl with a transition temperature of 30.7°C, which is close to the average summer daytime temperature (20 °C) [196, 197] and above the recommended upper limit of occupants' thermal comfort (26 °C) [198, 199], was selected for further studies on the development of the prototype BIPV smart window and its applicability in the UK climate.

4.3.3 Reversibility of the selected HPC hydrogel membrane

The thermal reversibility of the hydrogel made of 6 wt % HPC, 0.5 wt % GGF and 4.5 wt % NaCl has been evaluated. A 3-mm-pathlength cuvette containing the hydrogel was placed in the Qpod-2e sample compartment (**Figure 4.1**) (where the collimating lens on the spectrometer side was replaced with a cosine-corrector for normal-hemispherical transmittance measurement). The sample compartment was programmed to heat the hydrogel to 45°C (translucent state) and hold the temperature for 15 minutes, and subsequently cool the hydrogel to 25°C (transparent state) and hold the temperature for 15 minutes. The heating-cooling cycles were repeated in 100 times. **Figure 4.10** shows the collected transmittance data for the hydrogel membrane (3 mm thickness) at the selected wavelengths of 450, 700 and 900 nm at the membrane temperatures of 45°C and 25°C. No significant transmittance variations are observed for the hydrogel membrane at the same wavelengths and temperatures during the heating-cooling cycles, indicating that the transition process is reversible. For potential commercial applications, this material may need to be tested with more heating-cooling cycles (e.g., 1000 times) to confirm its long-term cycling stability.

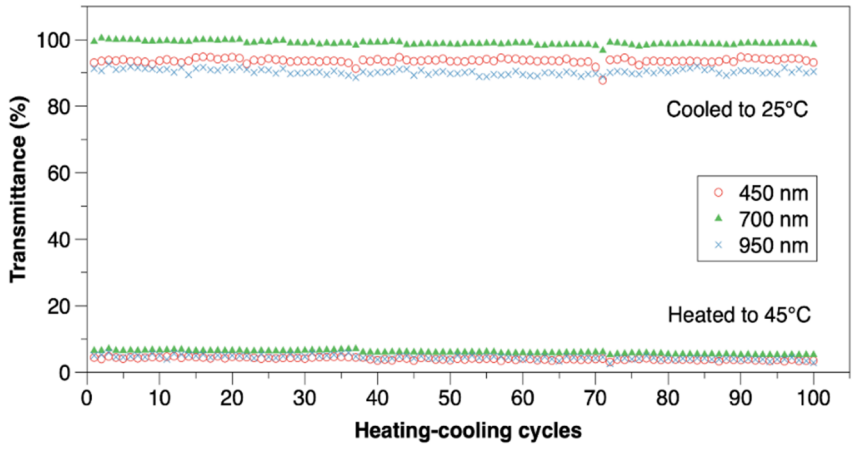

Figure 4.10: Spectral transmittances of the 6 wt % HPC, 0.5 wt % GGF, 4.5 wt % NaCl based hydrogel membrane (3 mm thickness) during 100 heating-cooling cycles.

4.3.4 Scattering characteristics of the selected HPC hydrogel membrane

The scattering characteristics of the 6 wt % HPC, 0.5 wt % GGF, 4.5 wt % NaCl based hydrogel membrane was investigated using the IAD method (described in **Chapter 3**). Firstly, the total transmittance, total reflectance and collimated transmittance of the laminated glazing unit (4 mm glass/1 mm membrane/4 mm glass) were measured (see **Figure 4.11**) and used for the IAD calculation. Then, the reduced scattering coefficient (u_s'), anisotropy factor (g) and absorption coefficient (u_a) of the hydrogel membrane (1 mm thickness) with respect to wavelength and temperature were derived from the IAD calculation (see **Figure 4.12** (a-c)). These values were subsequently imported to a Monte-Carlo ray-tracing model to predict the angular scattering intensity distribution of the laminated thermotropic glazing unit (see **Figure 4.12** (d)).

As can be seen from **Figure 4.12** (a-c), the increase of the membrane temperature leads to a higher value of u_s' and lower values of g. The temperature effect on the volume scattering properties becomes negligible, when the thermotropic membrane is heated to above 46 °C, indicating that an almost steady translucent state has been reached. From **Figure 4.12** (d), it may be seen that with the membrane temperature increasing, the laminated thermotropic glazing unit exhibits stronger backward scattering together with suppressed but more uniform forward scattering. These features could potentially benefit the enhancement of power generation and daylighting control of the BIPV smart window system, which will be discussed in the subsequent section.

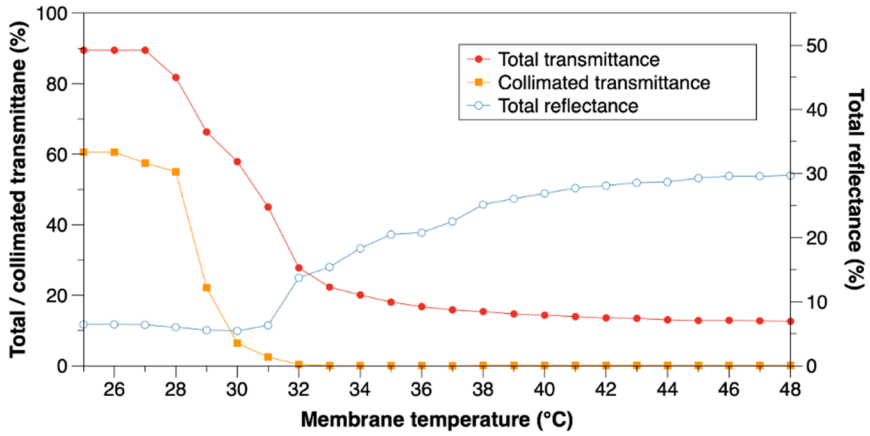

Figure 4.11: Average visible total transmittance, collimated transmittance and total reflectance of a laminated glass unit, which consists of a 1-mm-thick hydrogel membrane (made of 6 wt % HPC, 0.5 wt % GGF and 4.5 wt % NaCl) between two 4-mm-thick optical glass slides, as a function of membrane temperature.

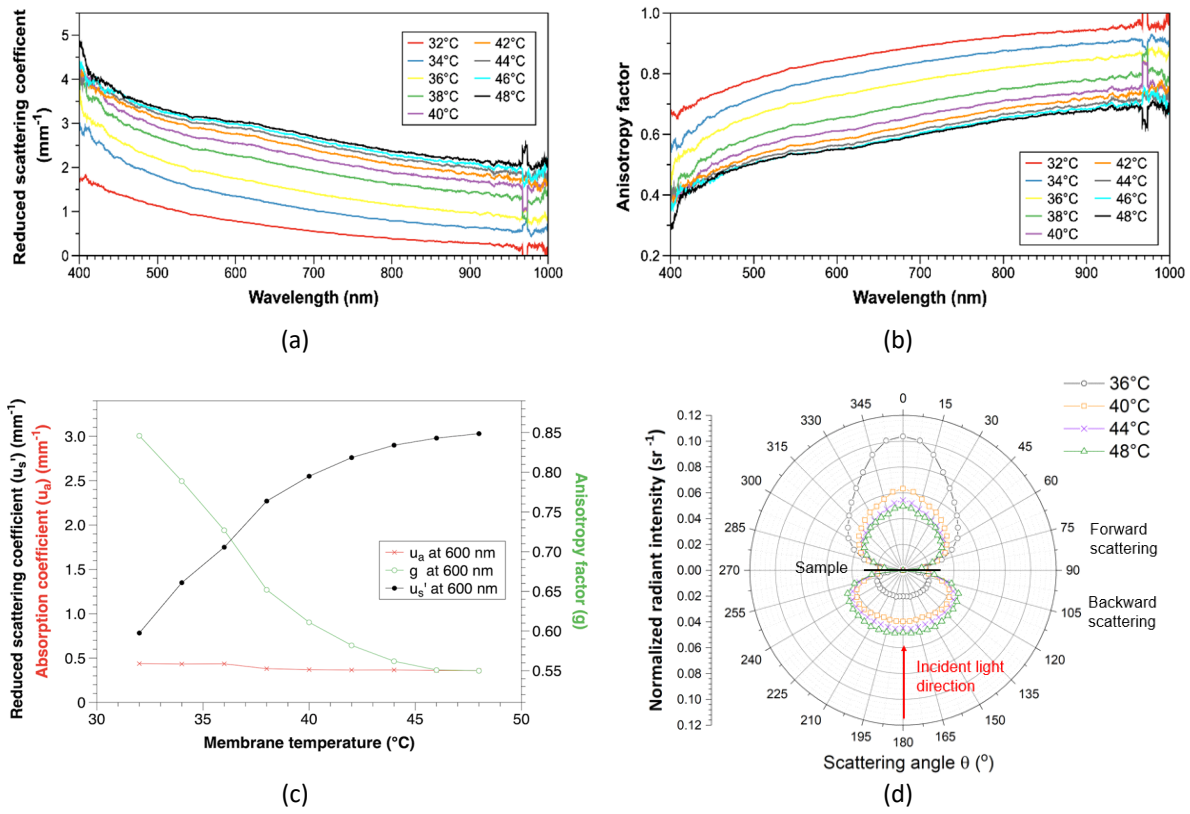

Figure 4.12: (a) Reduced scattering coefficient and (b) anisotropy factor of the 6 wt % HPC, 0.5 wt % GGF, 4.5 wt % NaCl based hydrogel membrane (1 mm thickness) at different membrane temperatures, (c) volume scattering properties at the wavelength of 600 nm, (d) normalised angular intensity distribution of the light scattered from the laminated glass unit .

4.3.5 Optical and electrical performance of BIPV smart window systems

Figure 4.13 (a) shows the spectral intensity of the light transmitted through the BIPV smart window system with the selected thermotropic membrane (6 wt % HPC, 0.5 wt % GGF and 4.5 wt % NaCl) under various membrane temperatures. The measured light incident on the window aperture has a spectral intensity of up to 120 μW/cm^2/nm over the wavelength band of 350 to 1000 nm, equivalent to a total irradiation intensity of 540 W/m^2. When the membrane temperature is 25°C, the BIPV smart window system at its transparent state allows most of the incident light across the 400 to 1000 nm spectrum to be transmitted, with a total intensity of 480 W/m^2. The total transmitted light intensity reduces significantly to 191 W/m^2 when the membrane temperature increases to 34°C and stabilises at approximately 100 W/m^2 when above 46°C.

The I-V characteristics of the BIPV smart window system at different membrane temperatures are shown in **Figure 4.13** (b). It can be seen that the short-circuit current is approximately constant below 30°C. With the temperature increasing from 30°C to 34°C, a significant increase in short-circuit current by 12.2% is observed. The enhancement in short-circuit current goes up to 28.5% as the temperature reaches 54°C. This may be a consequence of increased irradiation intensity on the solar cell, induced

by the increased reflectance of the thermotropic membrane with its temperature increasing above 30°C (see **Figure 4.9** (b)).

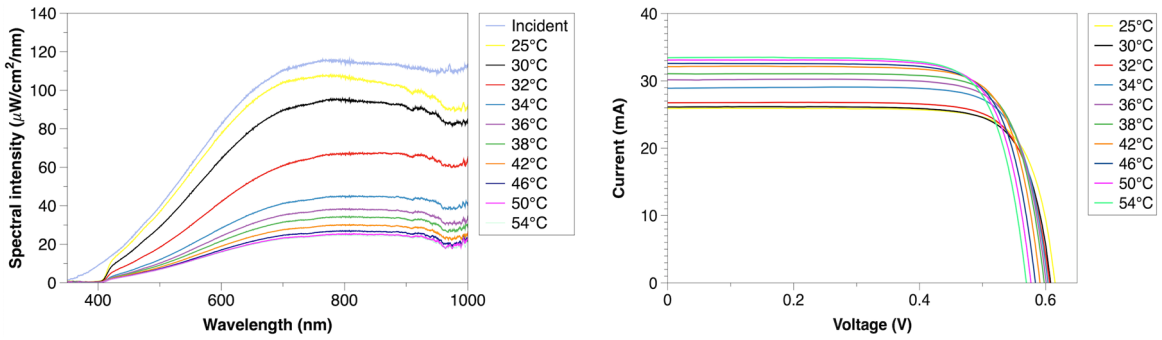

(a) (b)

Figure 4.13. (a) Spectral transmitted light intensity and (b) I-V characteristics for the BIPV smart window system with the thermotropic membrane consisted of 6 wt % HPC, 0.5 wt % GGF and 4.5 wt % NaCl under various membrane temperatures. The spectral intensity of the incident light was measured when the irradiance probe was not covered by the sample.

The total transmitted light intensity and maximum power output for the BIPV smart window systems with different hydrogel compositions are shown in **Figure 4.14**. From **Figure 4.14** (a), it can be seen that the total transmitted light intensity for the system with 4.5 wt % NaCl starts to decrease at 28°C, while it is 32°C for the system with 3 wt % NaCl and 40°C for the systems with no NaCl, respectively. Using a higher NaCl concentration is expected to shift the switching temperature to a lower value. Similar as observed in **Table 4-3**, the result in **Figure 4.14** (a) shows that the BIPV smart window system with 4.5 wt % NaCl allows 88.8% and 18.9% of incident light to be transmitted at the membrane temperature of 26°C and 54°C, respectively; However, these values are lower than 92.5% and 32.8% for the system with the same HPC concentration (6 wt % HPC) and no NaCl added at the same membrane temperatures. It can be inferred that increasing the NaCl concentration may reduce the amount of radiation transmitted through the BIPV smart window system in both transparent and light-scattering states.

Despite lower transmittance, the BIPV smart window system with 4.5 wt % NaCl provides higher solar transmittance modulation between 26°C and 54°C (69.9%) compared to its counterpart system with 6 wt % HPC and no NaCl (59.7%). Moreover, the system with 4.5 wt % NaCl offers higher maximum power outputs than the counterpart systems with less or no NaCl at the same temperatures above 32°C, as shown in **Figure 4.14** (b). These findings show that adding NaCl salt can effectively reduce the transition temperature and also improve the solar transmittance modulation and electricity generation of the BIPV smart window system, which corroborates the conclusion drawn from the spectroscopic measurement in **Section 4.3.2**.

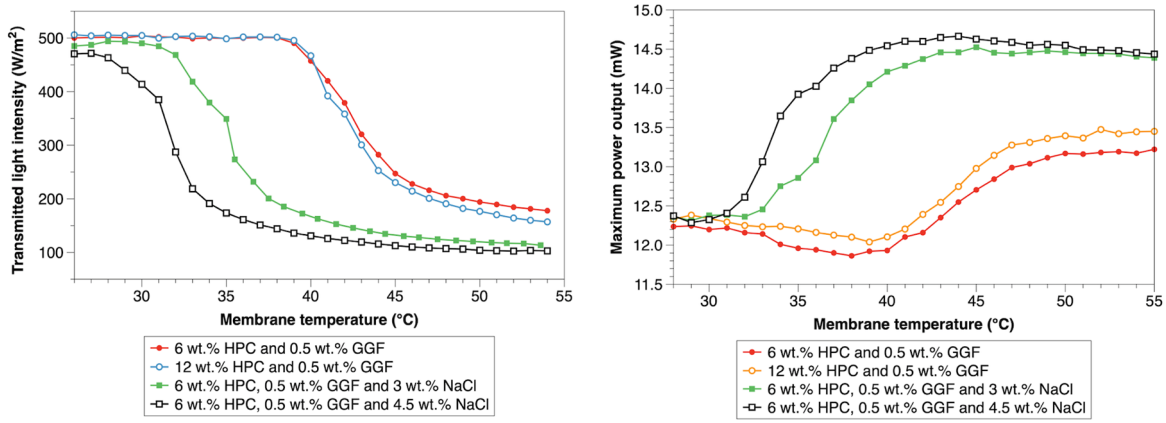

(a) (b)

Figure 4.14. (a) Total transmitted light intensity (integration over the 350-1000 nm spectrum) and (b) maximum power output of the BIPV smart window systems with different membrane compositions as a function of membrane temperature.

4.4 Summary

To optimise the BIPV smart window performance in terms of transition temperature, window transmittance and electrical power output, in this chapter, thermotropic hydrogels with a modified composition (i.e., HPC-GGF based hydrogel is added with sodium chloride (NaCl)) were synthesised and evaluated by experiments. From the HPC aqueous solution tests, it was found that the transition temperature could be adjusted between 39.5°C and 24.5°C by varying the NaCl concentration between 0 wt % and 6 wt %. This allows the hydrogel for applications in a variety of climatic conditions. Based on the spectroscopic measurement, the thermotropic membrane composed of 6 wt % HPC, 0.5 wt % GGF and 4.5 wt % NaCl was selected for further evaluation of outdoor performance in the UK climate, due to its appropriate transition temperature T_s (30.7°C) as well as high solar energy modulation (up to 76.2%) and high reflectance in the light-scattering state (up to 48.7%). Moreover, the thermotropic membrane shows good thermal reversibility and stability during heating-cooling cycles. From the indoor experimental tests, it was found that applying the thermotropic membrane with a higher NaCl concentration could potentially improve both electricity generation and light-shielding performance of the BIPV smart window system.

Chapter 5 – Outdoor experimental characterisation

5.1 Introduction

Different from tested in a controlled laboratory environment, BIPV smart windows for application in real climatic conditions are subjected to continuously varying boundary conditions such as ambient air temperature, solar radiation angle and intensity, wind speed and humidity. This chapter aims to examine the temporal associations between the performance of the developed BIPV smart window system and dynamic outdoor environmental conditions.

Following on from the indoor characterisation study (**Chapter 4**), the BIPV smart window system integrated with the thermotropic membrane made of 6 wt % HPC, 0.5 wt % gellan gum and 4.5 wt % NaCl was used for the outdoor experimental analysis. The outdoor experiment was carried out based on a small-scale test cell at the University of Nottingham (52.9° N, 1.2° W) during summer. The BIPV smart window system and its counterpart system with no thermotropic membrane were installed on the south wall of the test cell. The window performance has been analysed for different window sizes (50 mm × 50 mm and 120 mm × 120 mm), window inclination angles (90° and 45°) and weather conditions (sunny and partially cloudy weathers).

5.2 Experimental setup

A field test was conducted at the Energy Technologies Building at the University of Nottingham, the UK. **Figure 5.2** shows the block diagram and photographs of the outdoor characterisation setup. The 50 mm × 50 mm prototype BIPV smart window and its counterpart system with no thermotropic membrane were installed in a south-facing test cell (see **Figure 5.2** (b)). The window systems were linked to a Keithley 2420 I-V tracker with a 4-wire connection method [45, 87]. A custom program written in LabVIEW (National Instruments, version 14.0) was used to instruct the device to trigger current-voltage (I-V) sweeping with 1-minute intervals automatically. A CMP6 pyranometer (P1) from Kipp & Zonen with a spectral response range of 285 to 2800 nm was used to measure the global solar irradiance on the south-facing window surfaces. Another two CMP6 pyranometers (P2 and P3) were placed adjacent to the windows' interior side to measure the solar radiation transmitted into the chambers of the test cell (see **Figure 5.2** (c)). The chambers were cooled by natural ventilation to ensure similar internal air temperatures. The temperatures of the solar cells, thermotropic membrane layer, external air and internal air were monitored by T-type thermocouples wrapped in aluminium foil and calibrated with an accuracy of ±0.5°C. The pyranometers and thermocouples were connected to a Datataker DT85, with the data collected in 1-minute intervals over the experimental period starting from 9:30 am until 5:30 pm.

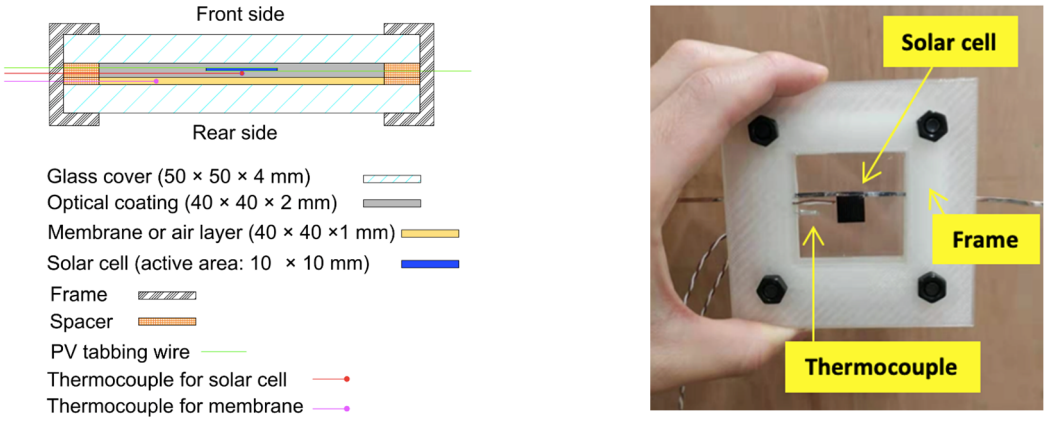

Figure 5.1: (a) Cross-sectional schematic diagram and (b) image of the prototype BIPV smart window for indoor and outdoor characterisations.

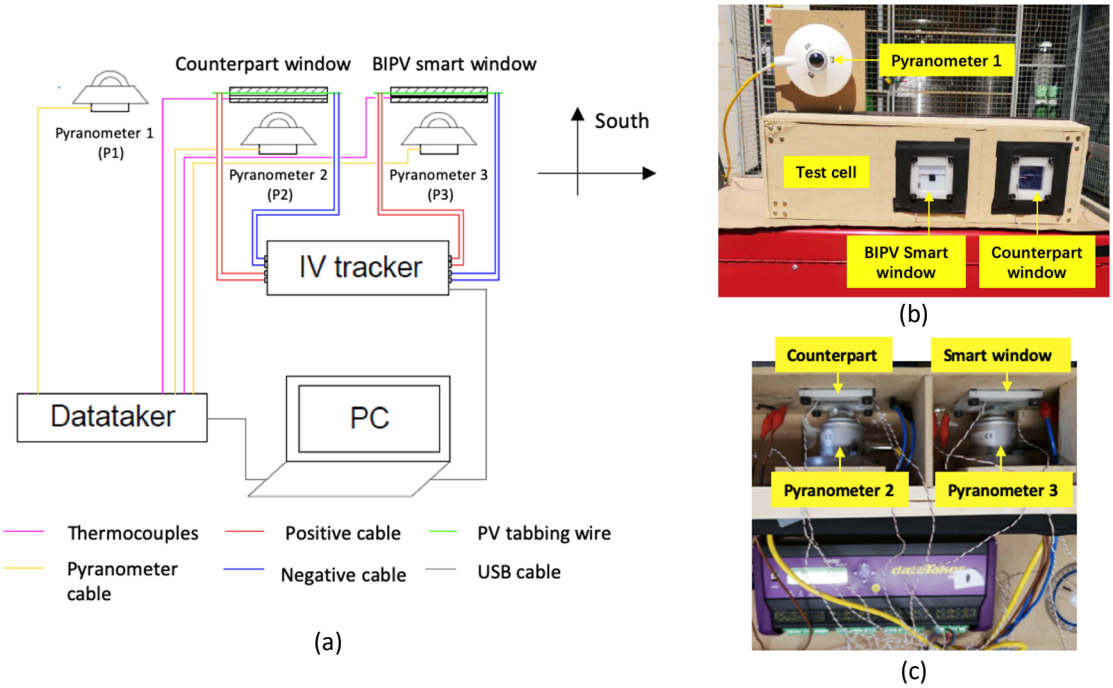

Figure 5.2: (a) Schematic of the outdoor experimental setup; (b) image of the 50 mm × 50 mm window systems installed in the test cell; (c) pyranometers in the testing chambers.

5.3 Results and discussion

5.3.1 Outdoor characteristics of the 50 mm × 50 mm window systems

5.3.1.1 Performance at 90° plane inclination

The BIPV smart window system and its counterpart system with no membrane at 90° inclination from the horizontal were characterised on a sunny interval day (24th July 2019). **Figure 5.3** shows the variation of the global solar irradiance on the south-facing vertical surfaces (detected by P1) and the temperatures of the thermotropic membrane, solar cells and outdoor ambient air during the daytime between 9:30 and 17:30. The global solar irradiance fluctuates between 100 and 600 W/m^2 in the

periods before 14:00 and after 15:00, due to intermittent cloud cover affecting solar irradiation. In the interval between 14:00 and 15:00, whilst the global solar irradiance stabilises at level of 600 W/m^2 and the average ambient air temperature is over 30°C, the temperatures of the thermotropic membrane and solar cell reach up to 44°C.

The solar radiation transmitted into the test cell was attempted to be measured using the pyranometers behind the BIPV smart window system (P3) and the counterpart PV window system (P2). However, the solar irradiances detected by P2 and P3 are found to be similar (up to about 100 W/m^2) and significantly lower than the incident solar radiation (up to about 600 W/m^2) over the entire observation period, as shown in **Figure 5.3**. This might be because the pyranometers P2 and P3 in the test cell are not exposed to the direct sunlight; in other words, only the diffuse component of the sunlight transmitted through the windows is detected, as a result of multiple factors including small window area, high solar elevation angle and existing window-to-sensor distance. Using a larger window area could potentially allow the direct beam component of the transmitted solar radiation to be sensed by the pyranometers, which will be further explored and discussed in **Section 5.3.2**.

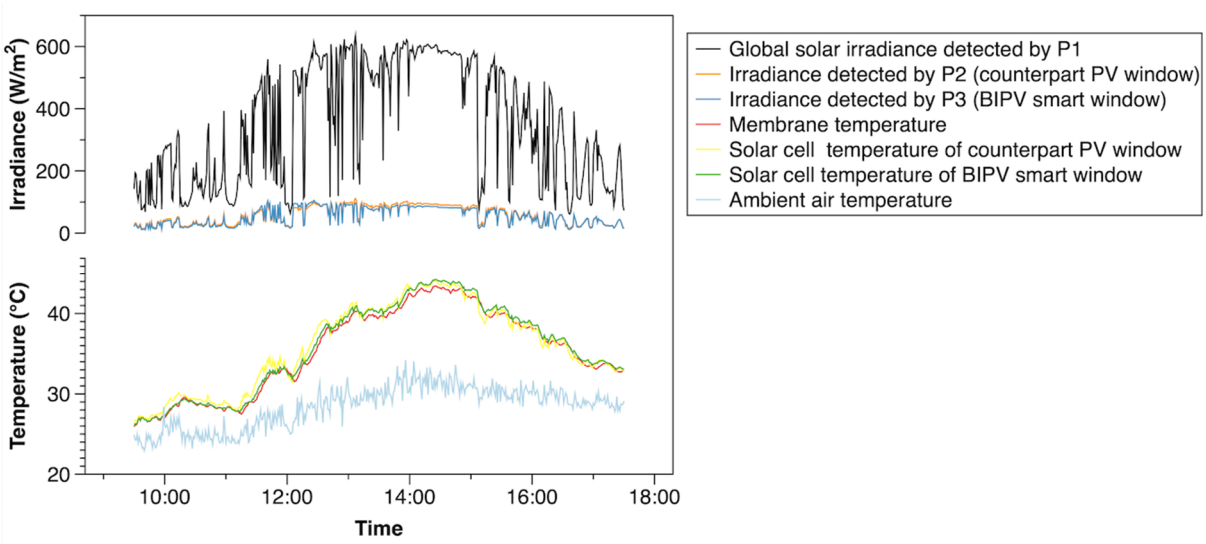

Figure 5.3: Variation of the solar irradiances and temperatures on 24th July 2019.

As can be seen from **Figure 5.4**, the short-circuit current (I_{sc}) of the PV window systems fluctuates along with the global solar irradiance at the south-facing window surfaces. The maximum short-circuit current of the BIPV smart window system is recorded to be 32.5 mA at 13:07 with a maximum global solar irradiance of 636 W/m^2 and a membrane temperature of 40.2°C, which is 8.7% higher than that of the counterpart PV window system. The difference in short-circuit current between the two window systems increases with a further increase in membrane temperature. At 14:24, when the highest membrane temperature of 43.5°C is reached, the short-circuit current of the BIPV smart window system exceeds that of the counterpart PV window system by 12.2%. It is also observed that the BIPV

smart window system and its counterpart system have similar short-circuit currents during the periods before 12:30 and after 16:30, while the membrane temperature is below 34°C. This may be because the intensity of light concentrated onto the solar cell associated with the light-scattering ability of the thermotropic membrane is relatively weak at low membrane temperatures.

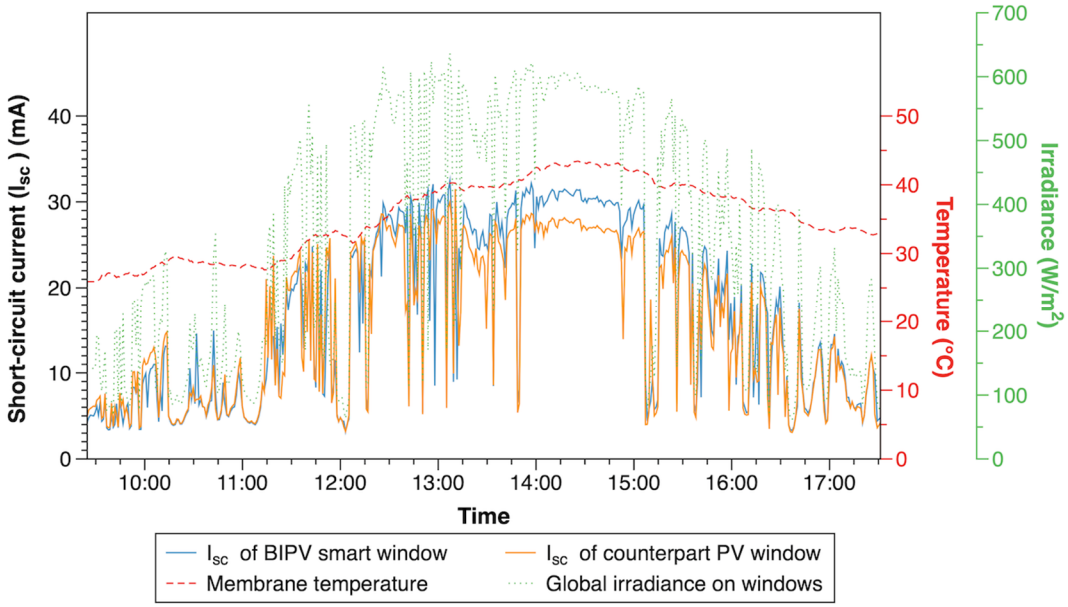

Figure 5.4: Variation of the short-circuit current of the 50 mm × 50 mm BIPV smart window system and its counterpart system with no membrane at 90° inclination.

Figure 5.5 shows the correlation between the measured short-circuit current and global solar irradiance. For the counterpart PV window system, the short-circuit current increases linearly with an increase in global solar irradiance. There is no significant difference in short-circuit current between the BIPV smart window system and its counterpart system under similar global solar irradiances, when the membrane temperature is below 34°C. However, the BIPV smart window system provides higher short-circuit currents than its counterpart system under similar global solar irradiances, when the membrane temperature is above 34°C. The result confirms the finding from the indoor I-V characterisation shown in **Figure 4.13** (b) where the short-circuit current of the BIPV smart window under constant solar irradiation increases sharply as the membrane temperature increases to 34°C or above.

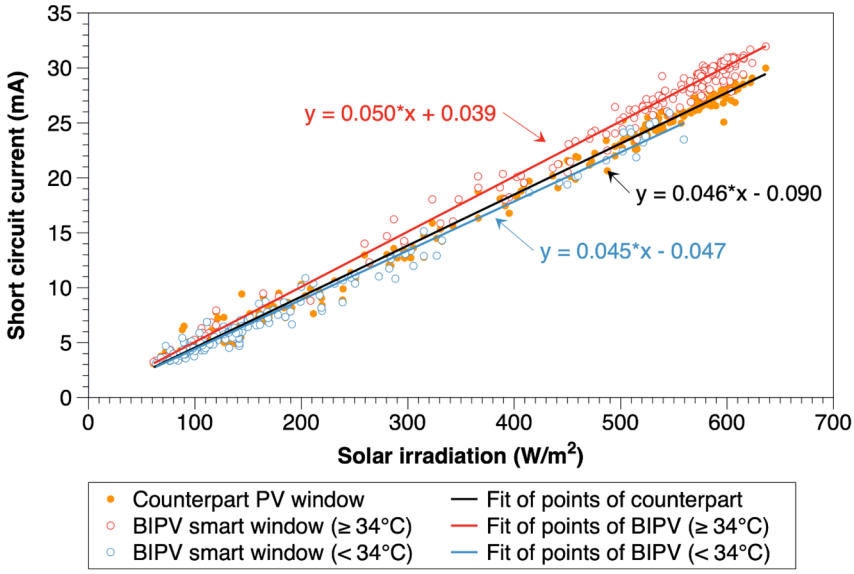

Figure 5.5: Short-circuit current of the 50 mm × 50 mm PV window systems plotted against global solar irradiance at the south-facing vertical surfaces.

The variation of the hourly maximum power output (P_m) of the two window systems over the experimental period (9:30-17:30, 24th July 2019) is shown in **Figure 5.6**. The hourly maximum power output of the BIPV smart window system increases to 13.1 mW (13:30-14:30) when the hourly global solar irradiance reaches a peak of 568 W/m^2, and then decreases to 3.6 mW (16:30-17:30) with the hourly global solar irradiance decreasing to 176 W/m^2. During 12:30 to 17:30, the BIPV smart window system offers 5.3-11.4% higher hourly maximum power outputs than its counterpart system with no membrane. The power enhancement can be explained because the thermotropic membrane has turned into its light-scattering state at temperatures above 34°C after 12:30 (see **Figure 5.6**), leading to increased irradiation intensity on the solar cell.

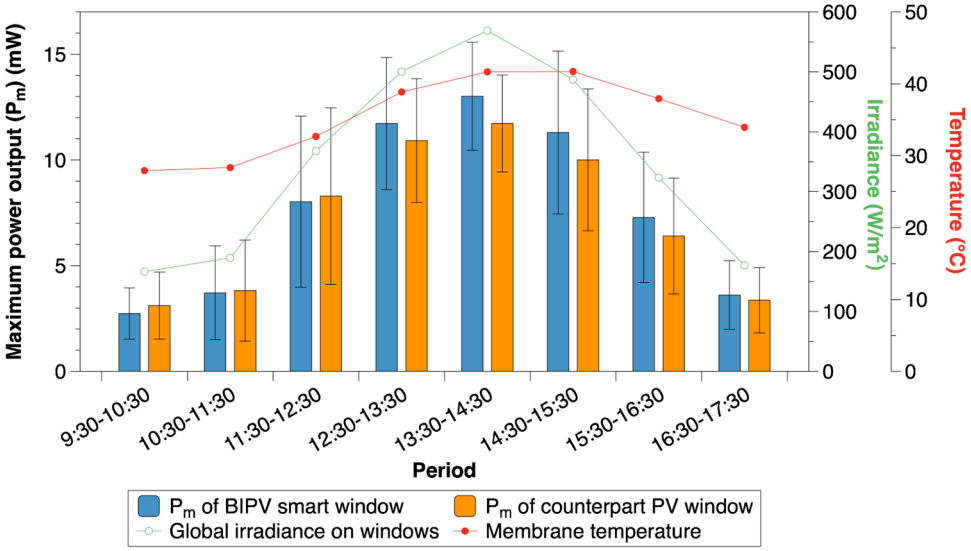

Figure 5.6: Hourly maximum power output of the 50 mm × 50 mm PV window systems at 90° inclination. Error bars represent one standard deviation.

5.3.1.2 Performance at 45° plane inclination

The 50 mm × 50 mm PV window prototypes were also characterised at a tilt angle of 45° to explore their potential when incorporated as skylights in buildings. **Figure 5.7** shows the variation of the measured solar irradiances and temperatures with local time over a clear sunny day (29th July 2019). The incident solar radiation at the inclined south-facing surfaces increases to about 1000 W/m^2 at 11:30 and remains at this level until 14:30. The irradiance detected by P2 for the counterpart PV window system has a parabolic shape between 11:30 and 14:30 with a maximum of around 600 W/m^2 (at 11:30) and a minimum of around 400 W/m^2 (at 13:00). This may be because, at noontime, the pyranometer P2 in the test cell is partially shaded by the opaque wall/frame and has a smaller area exposed to direct sunlight with the sun elevation angle increasing. As to the BIPV smart window, the irradiance detected by P3 stabilises at around 200 W/m^2 during 11:30 to 14:30. Meanwhile, the membrane temperature is observed to be higher than 40°C, and this suggests that the thermotropic membrane is in its light-scattering state and the solar radiation entering the test cell is significantly reduced.

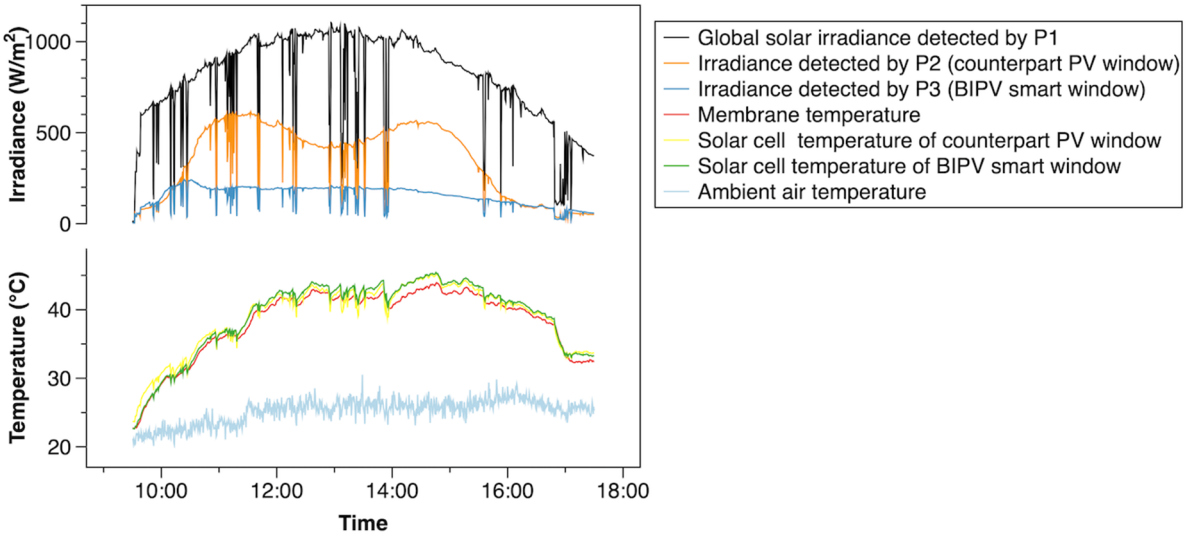

Figure 5.7: Variation of the solar irradiances and temperatures on 29th July 2019.

Figure 5.8 shows the variation in short-circuit current with global solar irradiance for the PV window systems inclined at 45°. The short-circuit current of the BIPV smart window system reaches above 50 mA during 11:30 to 13:30 while the global solar irradiance is approximately 1000 W/m^2, and then decreases gradually while the global solar irradiance decreases. A maximum increase of 12.8% in short-circuit current is observed for the BIPV smart window system compared to its counterpart system, during 11:30 to 13:30 with membrane temperatures of over 40°C. The correlation between short-circuit current and global solar irradiance is shown in **Figure 5.9**. A linear fit through the measured data for the BIPV smart window system below 34°C (blue line) yields a gradient of 0.048,

similar to that for the counterpart PV window system (black line). The gradient increases to 0.052 when above 34°C (red line), implying a higher electricity generation rate of the BIPV smart window system when switching from the transparent state to the light-scattering state.

Figure 5.10 shows that the two window systems have similar hourly maximum power outputs at the hourly membrane temperatures of below 34°C (before 10:30 and after 16:30). The hourly maximum power output of the BIPV smart window system exceeds that of its counterpart system with no membrane by 6.6% at approximately 35°C (10:30-11:30) to 12.0% at approximately 43°C (14:30-15:30). The result shows that the membrane temperature plays a pivotal role in the power generation of the BIPV smart window system.

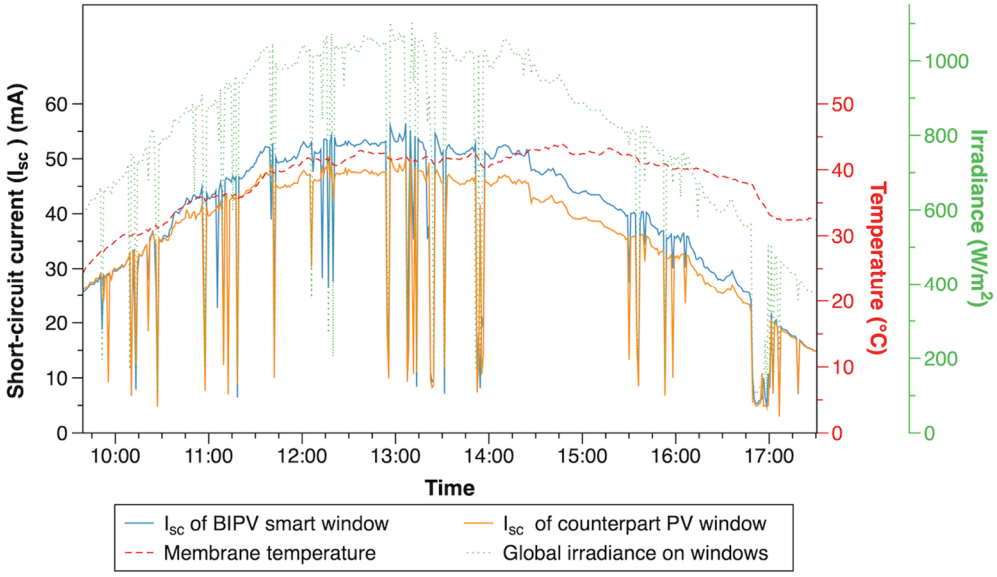

Figure 5.8: Variation of the short-circuit current of the 50 mm × 50 mm PV window systems at 45° inclination.

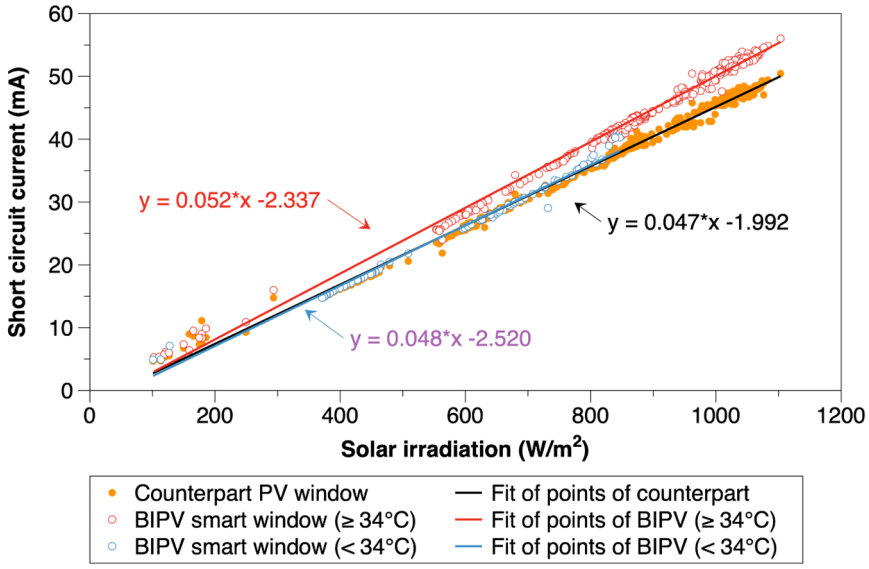

Figure 5.9: Short-circuit current of the 50 mm × 50 mm PV window systems plotted against global solar irradiation on the south-facing window surfaces at 45° inclination.

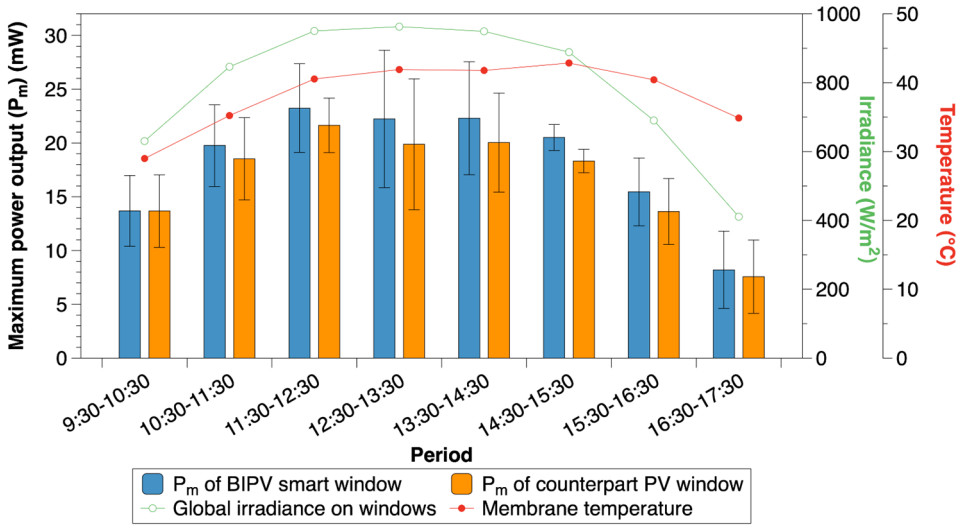

Figure 5.10: Hourly maximum power output of the 50 mm × 50 mm PV window systems at 45° inclination. Error bars represent one standard deviation.

5.3.2 Outdoor characteristics of the 120 mm × 120 mm window systems

In addition to the 50 mm × 50 mm prototype, a large-scale prototype for the BIPV smart window system was developed for outdoor characterisations. The purpose is to avoid the edge effect on the detection of solar beam irradiation by the light sensor in the test cell and accurately measure the window transmittance. The large-scale prototype was fabricated with similar configurations and materials as those for the 50 mm × 50 mm prototype (shown in **Figure 5.1**), but differing in the aperture area of the components, i.e., the glazing aperture area is 120 mm × 120 mm and the thermotropic membrane area is 110 mm × 110 mm. Two identical test boxes were constructed where the BIPV smart window system and its counterpart system with no membrane were mounted on the south side (see **Figure 5.11**). The solar radiation transmitted through the windows was detected using the Kipp & Zonen CMP6 pyranometers located in the test boxes with a similar setup as the previous tests discussed in **Section 5.3.1**. The average temperature of the thermotropic membrane layer was measured using the T-type thermocouples located at three different heights in the layer.

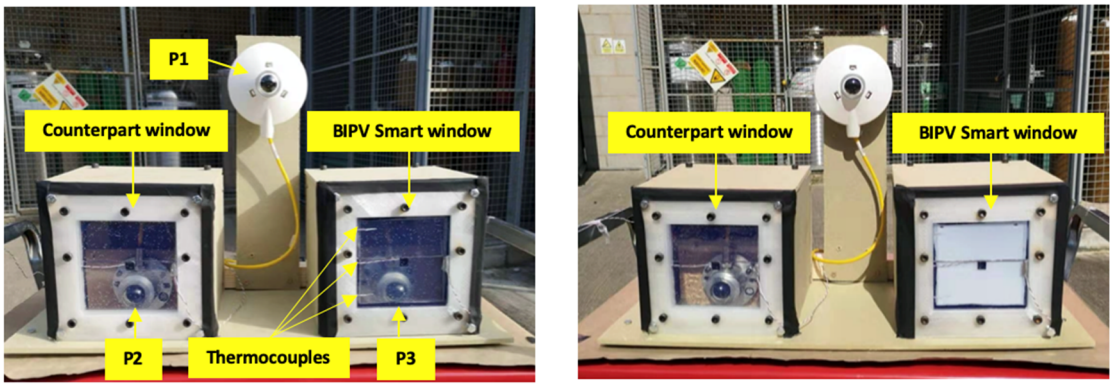

(a) Transparent state (b) Translucent state

Figure 5.11: Images of the test boxes with the 120 mm ×120 mm PV window systems.

5.3.2.1 Performance on a clear sunny day

The window performance was evaluated on a clear sunny day (25th August 2019). As can be seen from **Figure 5.12**, the global solar irradiance on the south-facing window surfaces (detected by P1) is in a parabolic shape between 9:30 and 17:00. It increases from around 400 W/m^2 to around 650 W/m^2 at 12:45 and gradually decreases to around 200 W/m^2 at 17:00. The irradiance detected by P2 for the counterpart PV window system shows a similar tendency as the global solar irradiance measured by P1, but at a lower level, reaching a maximum of around 500 W/m^2 at 12:45. The irradiance detected by P2 decreases rapidly after 16:00, because the pyranometer in the south-facing test box can hardly receive direct sunlight as the sun sets in the west. As to the BIPV smart window system, the irradiance detected by P3 is nearly constant at 100 W/m^2 during 10:00 to 15:00 where the thermotropic membrane is in its light-scattering state with temperature between 34°C and 50°C. The BIPV smart window system can significantly reduce (up to 80%) solar radiation entering the test cell when compared with its counterpart system, showing advantages in reducing overheating and glare in buildings on hot sunny days.

The variation in short-circuit current with local time is also shown in **Figure 5.12**. During the hot period between 11:00 and 17:00, whilst the ambient air temperature exceeds 30°C and the membrane temperature is over 40°C, the BIPV smart window system generates up to approximately 12% higher short-circuit currents when compared to its counterpart system with no membrane. For the same period, the hourly maximum power outputs of the BIPV smart window system are found to be 8.7-11.8% higher than those of the counterpart system, as shown in **Figure 5.13**.

It is noted that the BIPV smart window system has lower power outputs than its counterpart system between 9:00 and 10:00 in the morning. This might be because when below the T_s, the thermotropic membrane layer has a higher refractive index ($n_{TT} \approx 1.33$) than the air layer ($n_{air} = 1.0$) and thus a larger critical angle (θ_c) at its interface with the PV encapsulation layer ($n_{encapsulation} = 1.49$) according to the Snell's law ($\theta_c = \sin^{-1}\frac{n_{TT\ or\ air}}{n_{encapsulation}}$), which causes less incident light being trapped and totally reflected in the PV encapsulation layer of the BIPV smart window system. When above the T_s, the total internal reflection is enhanced with more light being scattered from the thermotropic membrane layer, and thereby the BIPV smart window has higher power outputs.

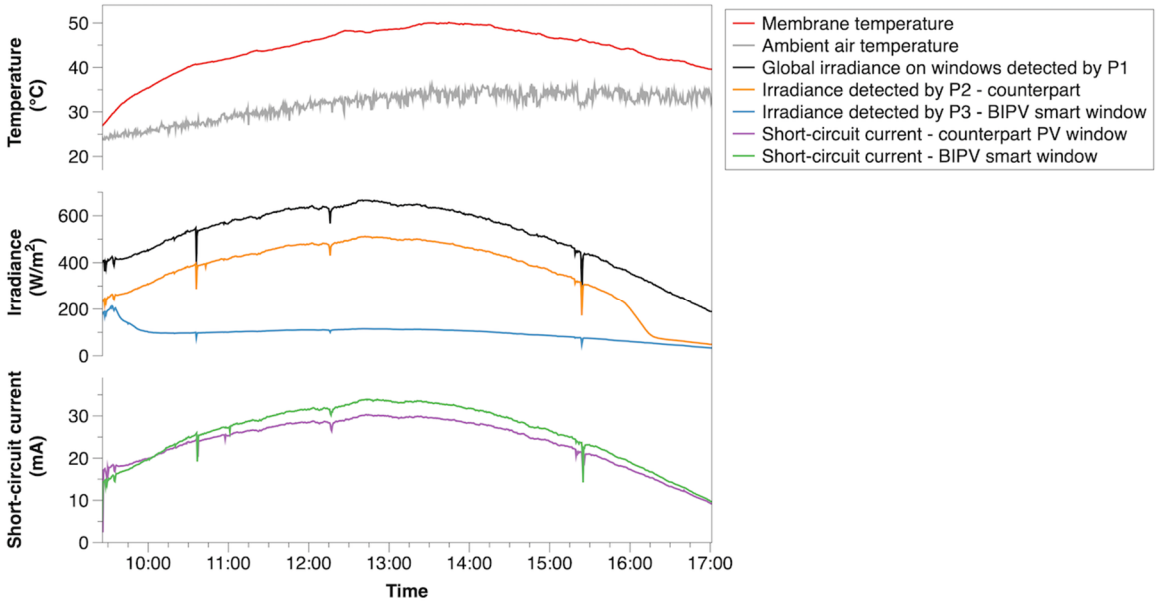

Figure 5.12: Optical and electrical performance of the 120 mm × 120 mm PV window systems at 90° inclination.

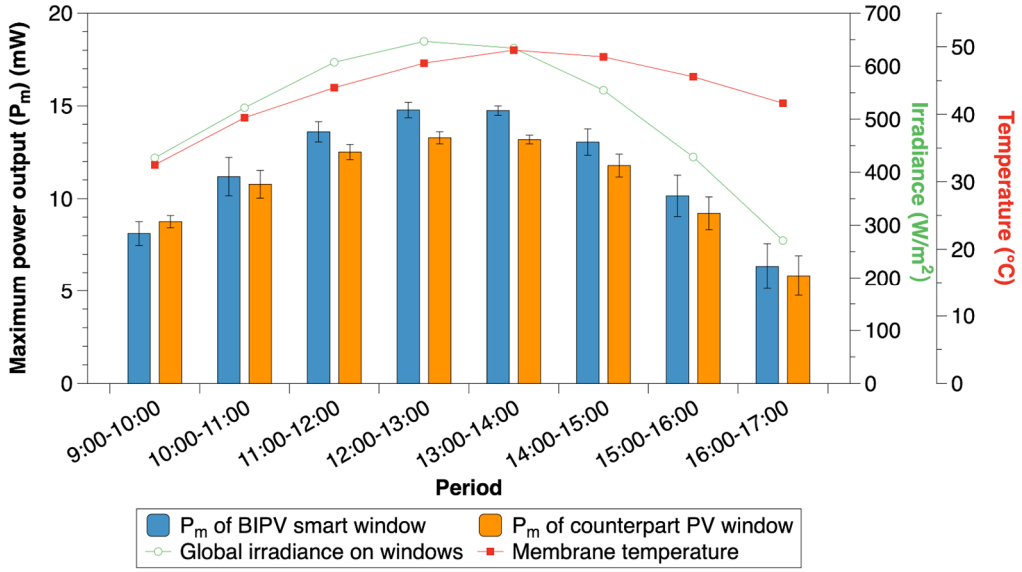

Figure 5.13: Hourly maximum power output of the 120 mm × 120 mm PV window systems at 90° inclination. Error bars represent one standard deviation.

5.3.2.2 Performance on a partially cloudy day

The 120 mm × 120 mm prototype BIPV smart window at an inclination of 90° were also characterised on a partially cloudy day in summer (21st August 2019) with intermittent solar irradiation and low ambient air temperatures shown in **Figure 5.14** (a). The global solar irradiance on the south-facing vertical surfaces (detected by P1) is observed to be less than 200 W/m^2 with overcast sky conditions in the morning (before 10:30) and in the late afternoon (after 15:00). During 10:30 to 15:00, the global solar irradiance fluctuates between 100 and 750 W/m^2 due to intermittent cloud cover. The solar irradiation measured for the counterpart PV window in the test cell (P2) follows a similar trend as the

global solar irradiation measured by P1 but with lower intensities. A similar irradiance pattern is observed for the BIPV smart window system (P3) and the counterpart PV window (P2) until 11:30, indicating similar window transmittances. However, the solar radiation transmitted through the BIPV smart window system reduces from approximately 450 W/m^2 at 11:30 to approximately 150 W/m^2 at 12:30, while that through the counterpart PV window remains at level of 500 W/m^2. This can be explained with **Figure 5.14** (b), where the thermotropic membrane changes its state between transparent and translucent with the variation of its temperature. Specifically, the thermotropic membrane turns into translucent at around 12:00 when its temperature is over 30°C and maintains this state till 15:00. The thermotropic membrane returns to its transparent state after 15:00 when the membrane temperature decreases below 30°C, when the sky becomes overcast and the ambient air temperature is approximately 20°C. This observation illustrates the dynamic solar transmittance of the BIPV smart window system in relation to the membrane temperature under the combined influence of solar irradiation and ambient air temperature.

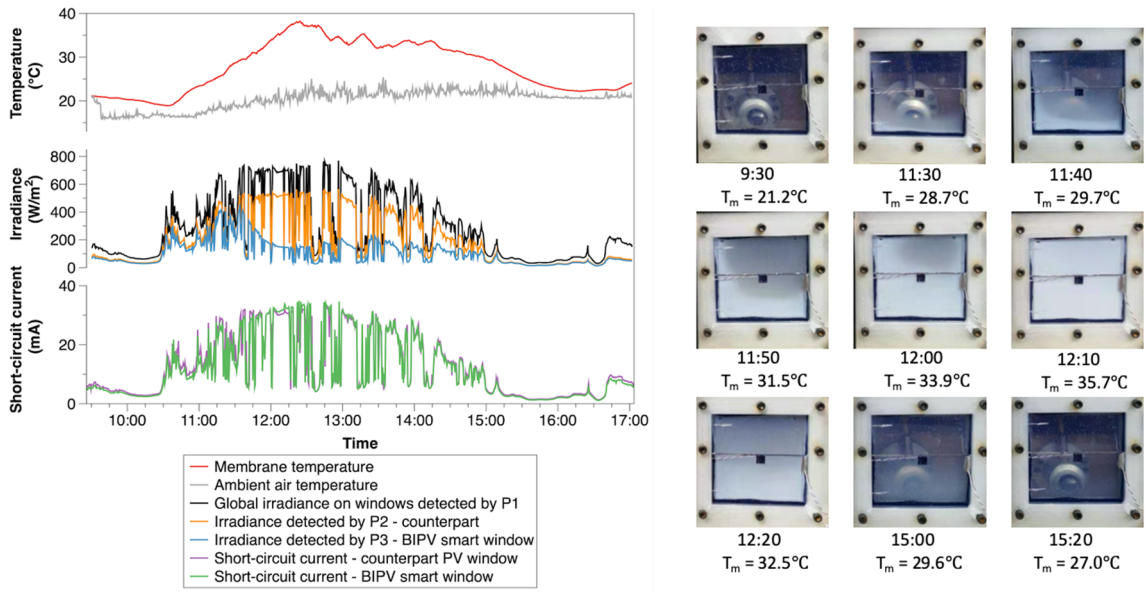

(a) (b)

Figure 5.14: (a) Variation of the parameters measured on the partially cloudy day, (b) images illustrating the appearances of the BIPV smart window system with different average membrane temperatures (T_m).

5.4 Summary

The BIPV smart window system was characterised for its electrical and optical performance under outdoor weather conditions in Nottingham (UK). The thermotropic membrane selected for the outdoor tests consists of 6 wt.% HPC, 0.5 wt.% GGF and 4.5 wt.% NaCl with a transition temperature of 30.5°C. Two similar prototypes with the glazing cover dimensions of 50 mm × 50 mm and 120 mm × 120 mm were constructed and tested at the inclination angles of 90° and 45° facing south, respectively, and their performance was analysed in comparison to the identical BIPV window systems in the absence of the thermotropic membrane. The outdoor experiments illustrate how solar

irradiation influences the temperature of the thermotropic membrane layer, thus altering the optical and electrical properties of the BIPV smart window system. It is found that the BIPV smart window can reduce up to 80% solar radiation transmitted into the interior space compared to its counterpart system with no thermotropic membrane applied, while providing up to 12% higher electrical power outputs.

Chapter 6 – Building Performance Simulation

6.1 Introduction

The outdoor characterisation of the BIPV smart window prototypes, as discussed in **Chapter 5**, provides a general picture of how varying external environmental conditions affect their electrical, thermal and optical properties. This chapter aims to provide insight into the potential of the BIPV smart window system in improving the energy efficiency and occupant comfort in buildings.

In this work, building performance simulation has been carried out in EnergyPlus (version 9.2) for a small cellular office room located in Nottingham, the UK. The office room was assumed to be equipped with a BIPV smart window system which was constituted of a glass-PV-membrane-glass laminate, an air gap and a low-emissivity (low-e) glass pane. Based on the EnergyPlus model, the performance of the BIPV smart window system in terms of solar heat gain, daylighting control and electricity generation was simulated, and compared to those for a conventional BIPV window and an ordinary low-e double-glazed window. The effects of different window design parameters, such as Window-to-Wall Ratios (WWR), window orientation and transition temperature, on the overall energy and daylight performance of the BIPV smart window system have also been investigated.

6.2 Methodology

EnergyPlus is a modular program that reads input data (e.g. building geometry, window properties, internal heat load, occupant/equipment schedule and climate data) and writes output data (e.g. window surface temperature, window solar heat gain, heating/cooling/lighting load and PV power output). **Figure 6.1** provides a flow chart illustrating the integration of the thermal, optical and electrical properties of the BIPV smart window system into the EnergyPlus model. The thermal properties (e.g. thermal conductivity and U-value) were calculated using the International Standard ISO 10077-1:2006 [200] and the optical properties (e.g. solar transmittance and visible light transmittance) were calculated following the International Standard ISO 9050:2003 [201]. These window properties were imported to a built-in module named 'thermochromic glazing module' in EnergyPlus for the simulations of heat and light transfer through the BIPV smart window system. On the other hand, the optical concentration ratio of the BIPV smart window system under varying conditions (e.g. thermotropic layer temperature and angle of light incidence) was predicted by the Monte-Carlo ray-tracing simulation technique (described in **Chapter 3**). A PV modelling algorithm based on the predicted optical concentration ratios was developed and validated, and then specified in the 'Energy Management System (EMS) module' in EnergyPlus for simulating the on-site electricity generation from the BIPV smart window system.

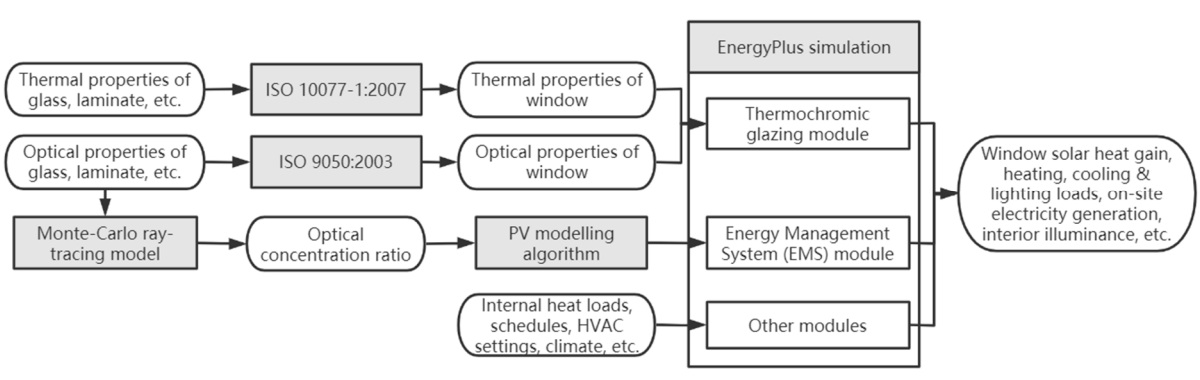

Figure 6.1: Flow chart of the workflow for modelling the BIPV smart window system.

6.2.1 Model geometry

Figure 6.2 shows the geometry of the cellular office room (3 m × 3 m × 3 m) modelled in EnergyPlus. The office room was considered as part of a large south-facing façade and buffered by mechanically conditioned spaces. It was assumed that only the south wall and horizontal roof comprising the office room were exposed to external conditions and subjected to heat transfer [91, 202]. The south wall of the office room was assumed to be installed with a BIPV smart window system with a WWR of 25%. The BIPV smart window system was assumed to consist of an array of crystalline-silicon (c-Si) solar cells with cell dimensions of 0.01 m × 0.01 m and a cell-to-cell spacing of 0.02 m. The PV cell coverage ratio, which is defined as the fraction of the window aperture surface area covered by the solar cells, is equal to approximately 11%.

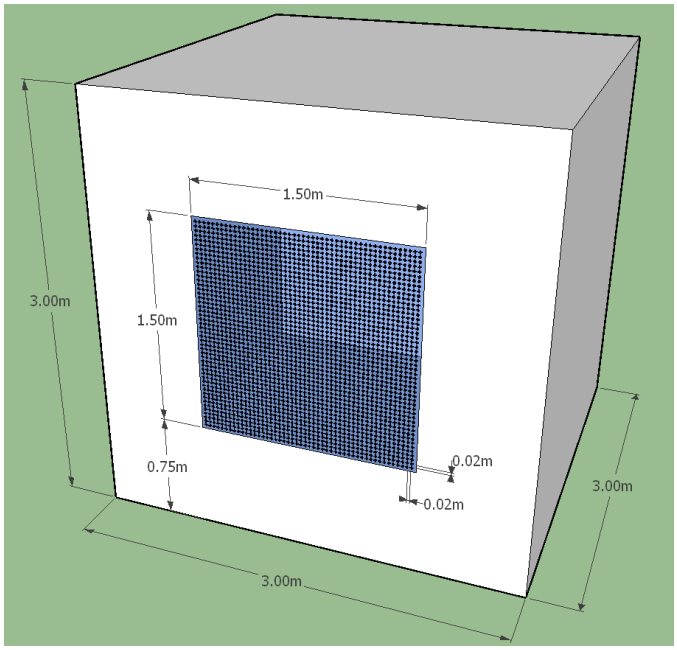

Figure 6.2: Geometry of the office room modelled in EnergyPlus.

6.2.2 Glazing configuration and properties

6.2.2.1 Glazing configuration

Three glazing systems shown in **Table 6-1** were designed for the numerical simulation and comparative analysis. The BIPV smart window system was assumed to consist of an outside laminate layer, an air gap and an inside low-e glass layer. The laminate layer was assumed to consist of a Dow-Corning 1-2577® coating layer (where c-Si solar cells were encapsulated) and a thermotropic layer between two optiwhite glass coverslips. The thermotropic layer was designed with the hydrogel composition of 6 wt % HPC, 0.5 wt % GGF and 4.5 wt % NaCl with a transition temperature of 30.5°C (details are presented in **Chapter 4**). A counterpart BIPV window system (with a similar window structure and PV cell coverage ratio, but no thermotropic layer applied) and a low-e double-glazed window (with no PV encapsulation layer and thermotropic layer) were selected as references for the window performance comparison.

Table 6-1: Window components and their thicknesses.

Type	Outer cover	Middle layer	Inner cover
BIPV smart window system	**Laminate** (from outside to inside): 3 mm GPE scientific optiwhite glass 2 mm PV encapsulation layer 1 mm thermotropic layer 3 mm GPE scientific optiwhite glass	12 mm air gap	3 mm Guardian low-e glass*
Counterpart BIPV window system	**Laminate** (from outside to inside): 3 mm GPE scientific optiwhite glass 2 mm PV encapsulation layer 3 mm GPE scientific optiwhite glass	12 mm air gap	3 mm Guardian low-e glass*
Low-e double-glazed window	6 mm GPE scientific optiwhite glass	12 mm air gap	3 mm Guardian low-e glass*

* The physical properties of the commercially available low-e glass pane can be found from the International Glazing Database (IGDB) (ClimaGuard 80/70, ID: 3238) [203].

6.2.2.2 Window thermal properties

The thermal transmittance (or U-value) of a double or multi-layer glazing system can be determined using **Equation (6.1)** and the typical values given in the International Standard ISO 10077-1:2006 [200]. For the BIPV smart window system, the thermal conductivities (k_j) of the individual layers including the optiwhite/low-e glass panes (d = 3 mm), PV encapsulation layer (d = 2 mm) and thermotropic layer (d = 1 mm) are 1.0 W/m K, 0.27 W/m K and 0.59 W/m K, respectively. As the window is vertically inclined and the normal emissivity of its external and internal surfaces is greater than 0.8, the thermal resistances of its external surface (R_{se}) and internal surface (R_{si}) can be assumed to be 0.13 m^2 K/W and 0.04 m^2 K/W, respectively, according to the ISO 10077-1:2006. The thermal resistance ($R_{air,j}$) of

the unventilated air space between the laminate and the low-e glass pane can be assumed to be 0.377 m^2 K/W, since the air space has 12 mm thickness and one side coated with a normal emissivity of 0.1, according to the ISO 10077-1:2006.

With the above inputs, the U-value of the BIPV smart window system was calculated to be 1.77 W/m^2 K. Similarly, the U-value of the counterpart BIPV window system (with no thermotropic layer) was calculated to be 1.78 W/m^2 K and that of the low-e double glazed window (with no PV encapsulation layer and thermotropic layer) was calculated to be 1.80 W/m^2 K.

$$U_g = \frac{1}{R_{se} + \sum_j \frac{d_j}{k_j} + \sum_j R_{air,j} + R_{si}} \tag{6.1}$$

where R_{se} and R_{si} are the external and internal surface resistances, d_j is the thickness of the glass or material layer j, k_j is the thermal conductivity of the glass or material layer j, $R_{air,\,j}$ is the thermal resistance of the air space j between two layers.

6.2.2.3 Window optical properties

For a window consisting of two glazing covers separated by an air gap, its spectral transmittance $\tau(\lambda)$, outer-side spectral reflectance $\rho_0(\lambda)$ and inner-side spectral reflectance $\rho_i(\lambda)$ can be calculated by **Equations (6.2)-(6.4)**, according to the International Standard ISO 9030:2003 [201]. For the BIPV smart window system, the calculation inputs include the spectral properties of the glass-PV-membrane-glass laminate (outer pane), which were obtained by spectroscopic measurement, and also the spectral properties of the low-e glass cover (inner pane), which were sourced from the International Glazing Database (IGDB) [203]. **Figure 6.3** (a) and (b) show the average transmittance and reflectance in the visible region (380-780 nm) and solar spectrum (250-2500 nm) measured for the glass-PV-membrane-glass laminate. **Figure 6.3** (c) and (d) show the calculated optical properties for the BIPV smart window system. A Similar method was applied to calculate the optical properties of the counterpart BIPV window system and the low-e double-glazed window (see **Table 6-2**).

$$\tau(\lambda) = \frac{\tau_1(\lambda)\,\tau_2(\lambda)}{1 - \rho_1'(\lambda)\,\rho_2(\lambda)} \tag{6.2}$$

$$\rho_o(\lambda) = \rho_1(\lambda) + \frac{\tau_1^2(\lambda)\,\rho_2(\lambda)}{1 - \rho_1'(\lambda)\,\rho_2(\lambda)} \tag{6.3}$$

$$\rho_i(\lambda) = \rho_2' + \frac{\tau_2^2(\lambda)\,\rho_1'(\lambda)}{1 - \rho_1'(\lambda)\,\rho_2(\lambda)} \tag{6.4}$$

where $\tau_1(\lambda)$ is the spectral transmittance of the outer pane (i.e., the laminate), $\rho_1(\lambda)$ is the spectral reflectance of the outer pane in the direction of incident light, ρ_1' is the spectral reflectance of the

outer pane in the opposite direction of incident light, $\tau_2(\lambda)$ is spectral transmittance of the inner pane (i.e., the low-e glass pane), $\rho_2(\lambda)$ is the spectral reflectance of the inner pane in the direction of incident light, ρ_2' is the spectral reflectance of the inner pane in the opposite direction of incident light, λ is the wavelength.

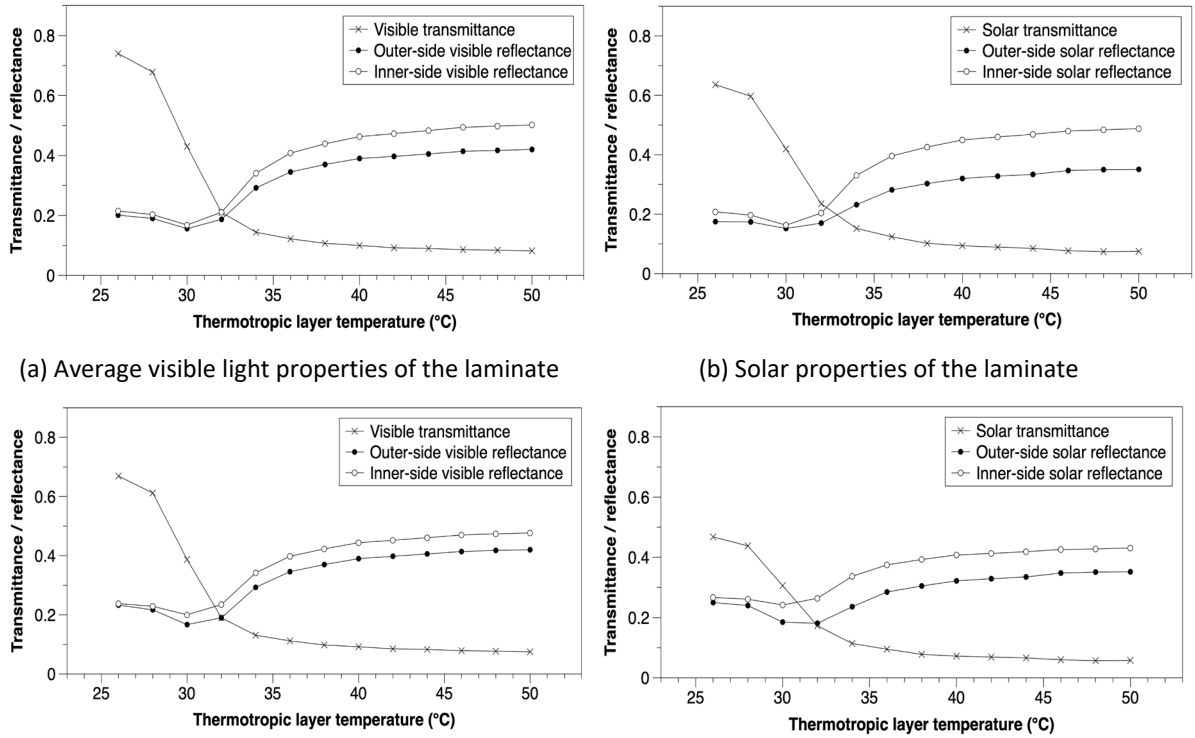

(a) Average visible light properties of the laminate

(b) Solar properties of the laminate

(c) Average visible light properties of the window

(d) Solar properties of the window

Figure 6.3: Transmittance, outer-side reflectance and inner-side reflectance measured for the glass-PV-membrane-glass laminate and calculated for the BIPV smart window system.

Table 6-2: Average visible light and solar properties of the three glazing systems.

glazing system		Solar transmittance and reflectance			Average visible light transmittance and reflectance		
		$\tau(\lambda)$	ρ_0	ρ_i	τ	ρ_0	ρ_i
BIPV smart window	25°C	0.468	0.250	0.267	0.669	0.233	0.238
	50°C	0.058	0.352	0.431	0.075	0.420	0.477
Counterpart BIPV window		0.554	0.324	0.274	0.693	0.263	0.249
Low-e double-glazed window		0.637	0.222	0.197	0.814	0.132	0.132

The above window optical and thermal properties were used for the daylight simulation and heat balance simulation in EnergyPlus. For the BIPV smart window system, due to its optical properties varying with temperature, the built-in 'thermochromic glazing module' was adopted. Specifically, at each timestep, EnergyPlus determines the temperature of the thermotropic layer, which selects the most closed specification temperature whose corresponding window optical properties will be used for the next timestep calculation. The reliability of simulation based on the 'thermochromic glazing

module' has been validated by Liang et al. [204, 205] through comparing the simulated cooling load with the measured cooling load for a thermochromic-glazing-equipped test room [206] with same boundary conditions applied.

6.2.2.4 Window electrical properties

A PV modelling algorithm was developed and specified in the 'Energy Management System (EMS)' module in EnergyPlus to predict the on-site electricity generation from the BIPV smart window system or the counterpart BIPV window system under time-varying weather conditions. The electrical power output (*P*) of the PV cells within the BIPV windows was calculated by **Equation (6.5)** [207], where the constant parameters include the window aperture surface area (A_w), PV cell coverage ratio (f_{pv}) and inverter efficiency ($\eta_{inverter}$) (listed in **Table 6-3**), and the dynamic parameters include the global solar irradiance (G_{pv}) on the PV cells and the actual power conversion efficiency (η_{pv}) of the PV cells. The G_{pv} can be calculated by **Equation (6.6)**, where the optical concentration ratio (C_e) of the BIPV windows (i.e., the ratio between the solar irradiance on the PV cells and on the window aperture surface) was predicted using the IAD and Monte-Carlo coupled optical modelling technique (described in **Chapter 3**). The η_{pv} can be calculated by **Equation (6.7)**.

$$P_{pv} = G_{pv} \times A_w \times f_{pv} \times \eta_{pv} \times \eta_{inverter} \tag{6.5}$$

$$G_{pv} = G_w \times C_e \tag{6.6}$$

$$\eta_{pv} = \eta_{pv,STC} \times \left(1 - \xi \times \left(T_{pv} - 25\right)\right) \tag{6.7}$$

Where P_{pv} is the PV power output from the BIPV window (W), G_{pv} is the global solar irradiance on the solar cells (W/m^2), A_w is the window aperture surface area (m^2), f_{pv} is the PV cell coverage ratio, η_{pv} is the actual power conversion efficiency of the solar cells, $\eta_{inverter}$ is the inverter efficiency, G_w is the global solar irradiance on the window outside surface (W/m^2), C_e is the predicted optical concentration ratio, $\eta_{pv,STC}$ is the power conversion efficiency of the solar cells under standard test conditions, ξ is the temperature coefficient of power (%/°C), T_{pv} is the solar cell temperature (°C).

Table 6-3: Input parameters for the PV modelling algorithm.

Parameter	value
Window aperture surface area (A_w)	2.25 m^2
PV cell coverage ratio (f_{pv})	11%
Power conversion efficiency of the solar cell under STC ($\eta_{pv,STC}$)	17%
Inverter efficiency ($\eta_{inverter}$)	95%
Temperature coefficient of power of the solar cells (ξ)	0.3%

In practice, the optical concentration ratio depends on the thermotropic layer temperature as well as the angle of light incidence on the window aperture, both of which change with local time. The angle of light incidence varies with the sun position, surface tilt angle and surface azimuth (see **Figure 6.4**). It can be determined using **Equation (6.8)**, which can be simplified to **Equation (6.9)** if the investigated surface is vertically inclined (β = 90°), facing south (Z_s = 0°) and in the northern hemisphere [208, 209].

Figure 6.5 shows the predicted optical concentration ratios for the BIPV smart window system under various conditions of thermotropic layer temperature and incidence angle. At the same temperatures, the optical concentration ratio remains nearly constant within the incidence angle range of 0° to 65°, while it reduces significantly with the incidence angle increasing above 65°. On the other hand, at the same angles, the optical concentration ratio of the BIPV smart window system experiences a significant increase with the thermotropic layer temperature increasing until 44°C, while it changes slightly with a further temperature increase.

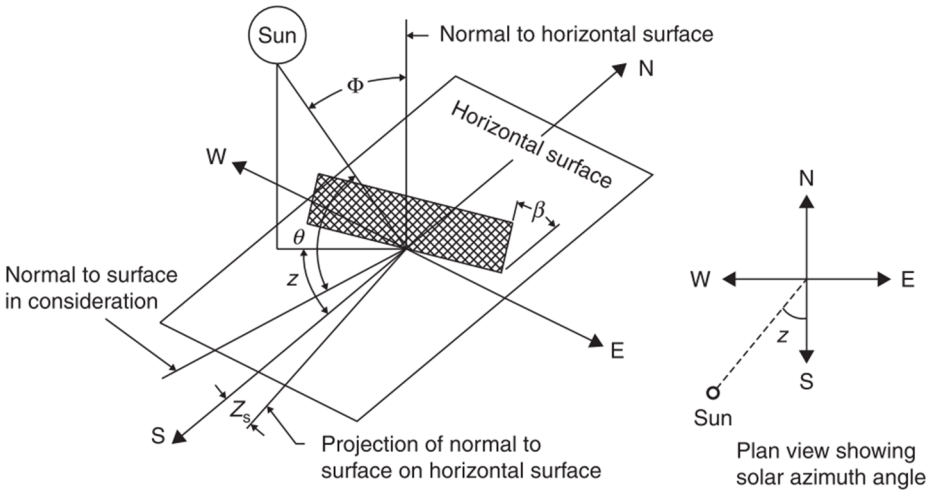

Figure 6.4: Diagram of solar radiation incident on a plane. Source: [208].

$$\cos\theta = \sin(L)\sin(\delta)\cos(\beta) - \cos(L)\sin(\delta)\sin(\beta)\cos(Z_s) + \cos(L)\cos(\delta)\cos(h)\cos(\beta) + \sin(L)\cos(\delta)\cos(h)\sin(\beta)\cos(Z_s) + \cos(\delta)\sin(h)\sin(\beta)\sin(Z_s) \quad (6.8)$$

$$\cos\theta = -\cos(L)\sin(\delta) + \sin(L)\cos(\delta)\cos(h) \quad (6.9)$$

$$\delta = 23.45 \sin\left[\frac{360}{365}(284 + N)\right] \quad (6.10)$$

$$\sin h = -\frac{\cos\alpha \sin(z)}{\cos\delta} \quad (6.11)$$

or $h = \pm 0.25$ (Number of minutes from local solar noon)

Where θ is the angle of incidence between the solar beam on a surface and the normal to the surface, δ is the declination angle, L is the local latitude, β is the surface tilt angle, Z_s is the surface azimuth

angle, h is the hour angle, N is the day number, α is the solar altitude angle, z is the solar azimuth angle, Φ is the solar zenith angle.

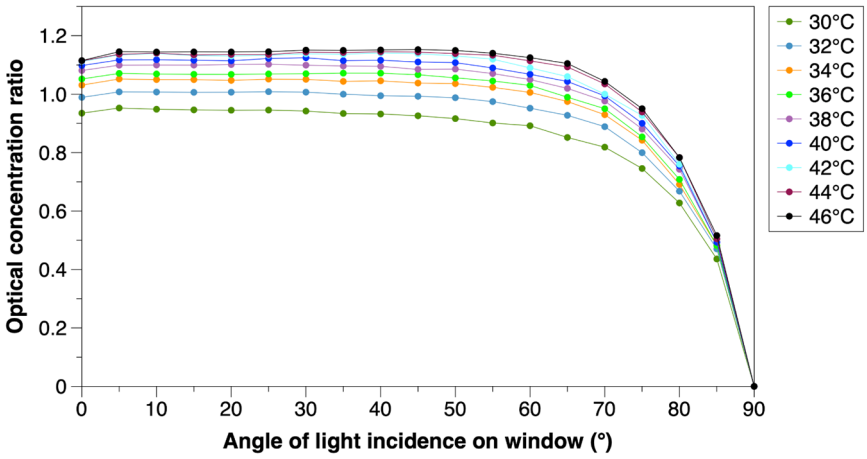

Figure 6.5: Predicted optical concentration ratio of the BIPV smart window system with respect to thermotropic layer temperature and angle of light incidence on it.

The developed PV modelling algorithm has been validated by comparisons with the results obtained from the outdoor experiment in Nottingham on the summer days, July 25th and August 25th, 2019. The details about the outdoor experimental setup and data are presented in **Chapter 5**. Given the measured thermotropic layer temperatures and the calculated angles of light incidence at the local times of the summer days, the corresponding optical concentration ratios can be derived from the predicted dataset (see **Figure 6.5** and **Figure 6.6** (a) and (b)). With the prediction of optical concentration ratio, the electrical power output of the BIPV smart window system at the local times was calculated using **Equations (6.5)-(6.7)**. From **Figure 6.6** (c) and (d), it can be seen that the calculated maximum power outputs are in a good agreement with the measured results.

By using the EMS, the time-varying parameters such as the thermotropic layer temperature, the angle of light incidence on the window and the PV cell operating temperature were detected at the beginning of each time step. Then, a corresponding optical concentration ratio for this condition was selected from the dataset (**Figure 6.5**) and a corresponding power conversion efficiency was calculated by the EMS. These data were subsequently applied in the PV modelling algorithm for the calculation of on-site electricity generation.

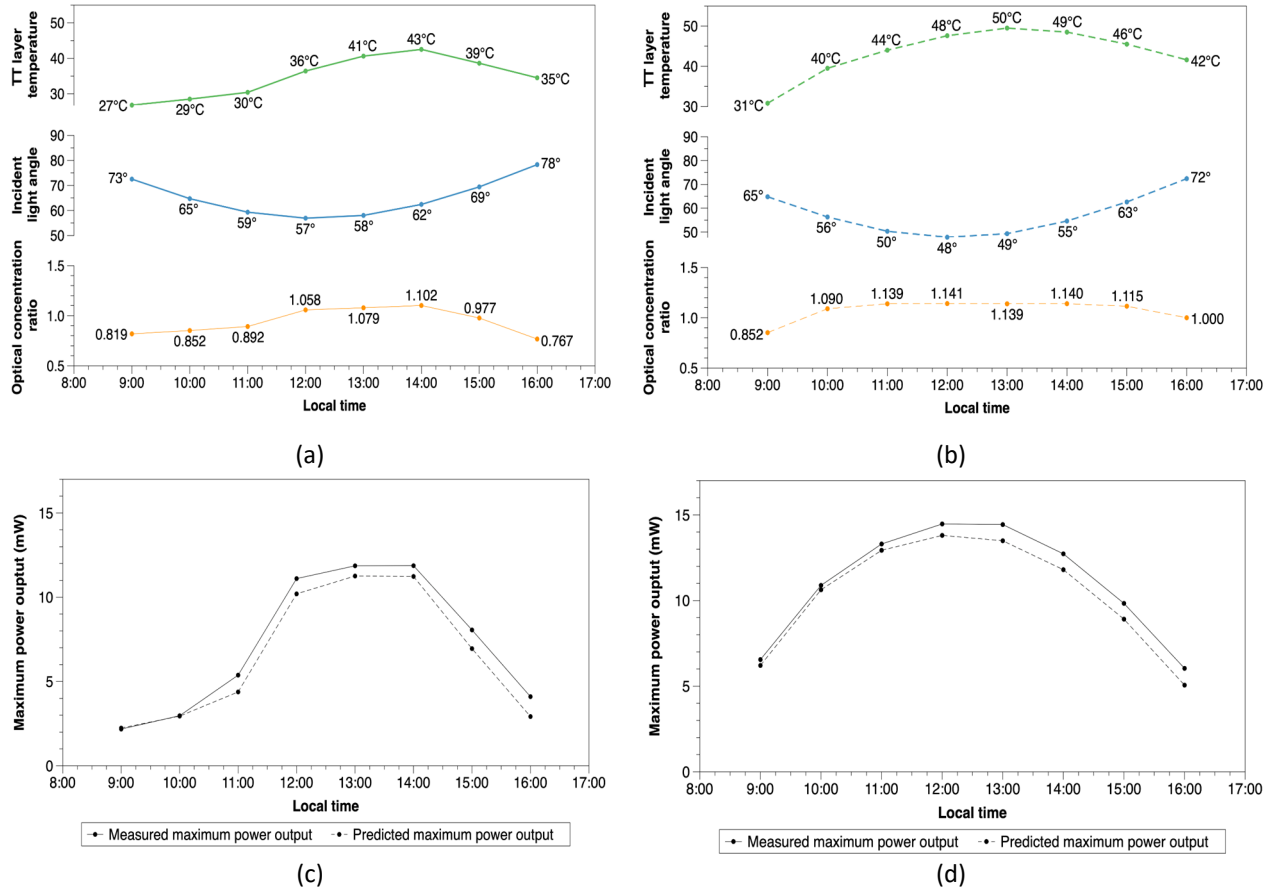

Figure 6.6: Predicted optical concentration ratios for the BIPV smart window tested in Nottingham on the dates of (a) 25/07/2019 and (b) 25/08/2019; comparison between the calculated and measured maximum power outputs on the dates of (c) 25/07/2019 and (d) 25/08/2019.

6.2.3 Other settings in EnergyPlus

In the model setup, the boundary condition of the south wall and roof of the office room was set as 'exposed to the outdoor environment', while those of the rest walls and floor was set to be adiabatic (i.e., no heat gains and losses through them). **Table 6-4** shows the U-values specified for the building elements in EnergyPlus, compared with the maximum allowed U-values for UK office buildings under the latest Building Regulation Part L2A [210]. The office room was assumed to be occupied by one person from 9:00 to 17:00 on weekdays all year long. An ideal-loads Heating, Ventilation and Air-conditioning (HVAC) system with a dual setpoint control was used to maintain the indoor air temperature between 20°C and 26°C, in accordance with the HVAC design temperatures for office buildings recommended by the American Society of Heating, Refrigerating and Air-Conditioning Engineers (ASHRAE) [211]. The internal heat load from electrical equipment was assumed to be 15 W/m^2. The light power density was assumed to be 9 W/m^2, where 80% of the electric lighting power was consumed for visible radiation and 20% was dissipated as heat to the interior space. The electric lighting was set to be automatically controlled, i.e., during the working hours, the electric lighting was

switched on when the daylight illuminance over the working plane (at the centre of the office room and at a 0.75 m height above the floor) fell below 300 lux.

Table 6-4: Simulation parameters for a UK cellular office.

Parameters		Benchmark range for building performance simulation [211]	Values used in this study
U-value ($W/m^2 K$)	Wall	≤0.35	0.35
	Roof	≤0.25	0.25
	Floor	≤0.25	0.25
	Window	≤2.2	1.8
Heating temperature setpoint (°C)		20-23	20
Cooling temperature setpoint (°C)		23-26	26
Maximum occupant density (m^2/person)		6-15	9
Infiltration rate (ACH)		0.16-1.0	0.5
Equipment heat gain (W/m^2)		10-25	15
Lighting power density (W/m^2)		4-24	9
Illuminance over a task area (lux)		300-500	300

6.3 Results and discussion

In order to understand the thermal, electrical and optical performance of the designed BIPV smart window system and its effect on building energy and environmental performance, specific evaluation criteria were applied. Firstly, the thermal behaviour in terms of the monthly solar heat gain through window and the percentage of working hours for the thermotropic layer at specific temperatures was investigated. Then, the monthly/annual energy consumptions (i.e., cooling, heating and lighting loads) and on-site electricity generation were analysed to explore the energy saving potential. The daylight performance was evaluated using the metric named Useful Daylight Illuminance (UDI). Finally, detailed energy and daylight analyses were carried out to explore the effects of different WWRs, glazing orientations and transition temperatures of the thermotropic layer.

6.3.1 Window solar heat gain

Figure 6.7 shows the monthly solar heat gains through the different windows for application in the office room with a WWR of 25% and south orientation of glazing under the climate of Nottingham. As can be seen, both BIPV windows allow less solar heat to be admitted to the indoor space when compared to the low-e double-glazed window. This occurs probably because a portion of incident solar radiation is absorbed and converted to electricity by the solar cells in the BIPV windows. During the cold months of November to February, the solar heat gains through the BIPV smart window are slightly lower than those through the counterpart BIPV window. However, during the warm months of March to October, significant reductions in solar heat gain are observed for the BIPV smart window over the counterpart BIPV window. For example, during the hottest month (July), the BIPV smart

window provides approximately 47% lower solar heat gains when compared with the counterpart BIPV window and approximately 53% when compared with the low-e double-glazed window. The BIPV smart window shows a greater potential in reducing solar heat gain during summer than during winter, which is likely attributed to the increasing number of hours during summer where the thermotropic layer has turned into translucent at temperatures above 28°C (see **Figure 6.8**).

Figure 6.9 shows the variation of the solar heat gain rate of the BIPV windows with the incident solar radiation intensity. In the graph, the data points for the BIPV smart window are separated into two groups, corresponding to the steady-state conditions: transparent (below 28°C) and translucent (above 36°C) (i.e., the steady states can be also determined according to **Figure 6.3** (d)). When the thermotropic layer is transparent, the BIPV smart window and its counterpart system with no thermotropic layer have similar solar heat gain rates under similar solar irradiation intensities; however, after switching to the translucent state, the solar heat gain rate of the BIPV smart window reduces significantly, i.e., the gradient of the linear fit (or the Solar Heat Gain Coefficient (SHGC)) decreases from 0.49 to 0.12. The above results suggest that the BIPV smart window can provide a similar passive solar heating effect as the traditional BIPV window in cold periods, but more effective overheat protection in hot periods.

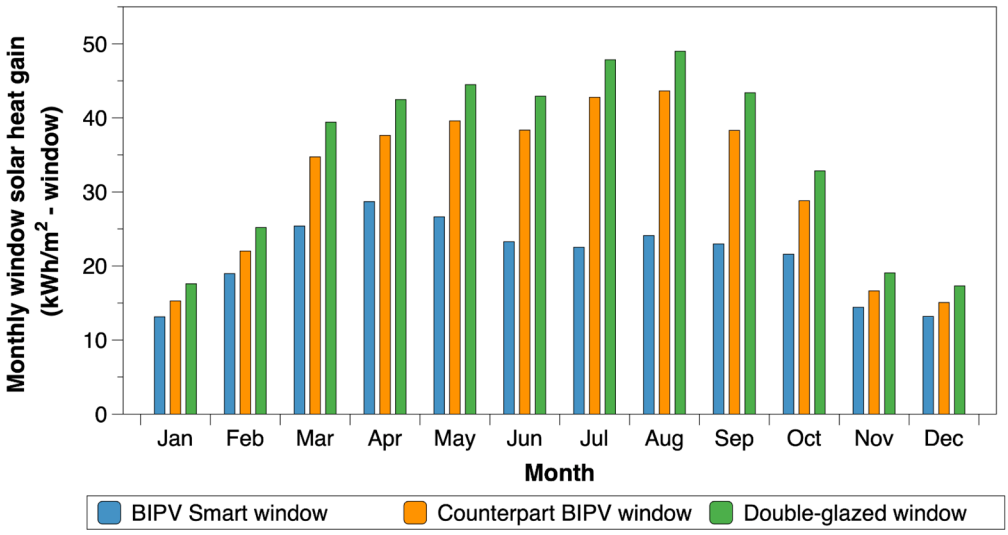

Figure 6.7: Monthly solar heat gains (kWh per window area) through the different windows for application in the office with a WWR of 25% and south orientation of glazing.

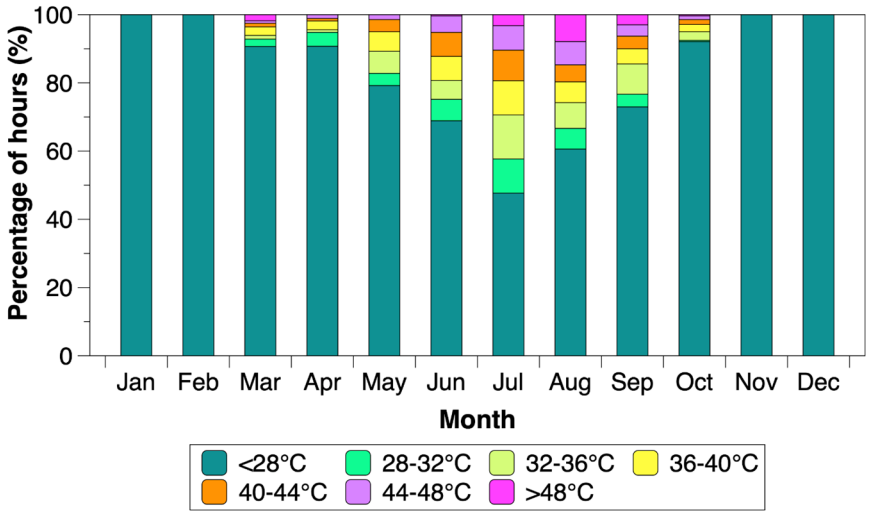

Figure 6.8: Percentages of total working hours (range: 9:00-17:00) in the months where the thermotropic layer temperature is within the specific temperature ranges.

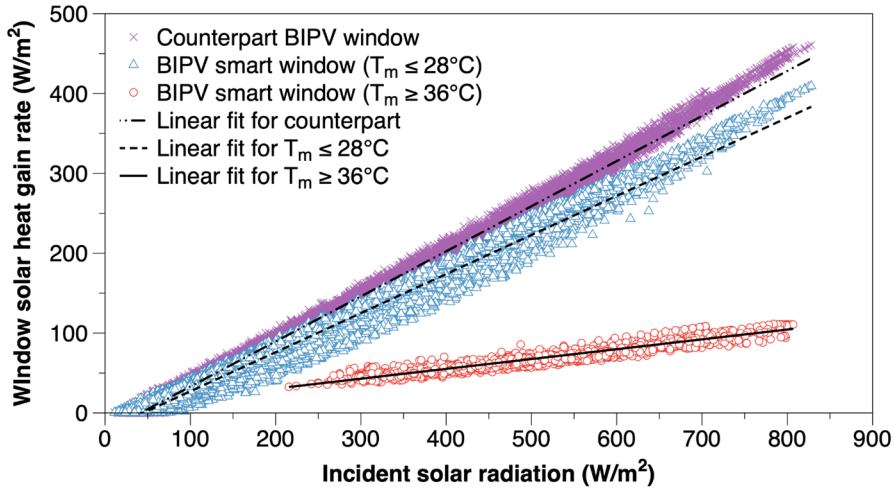

Figure 6.9: Solar heat gain rates of the BIPV smart window in the steady states and its counterpart system with no thermotropic layer. Data were retrieved at 10-minutes time steps through a year.

6.3.2 Energy consumption, electricity generation and daylight performance

Figure 6.10 shows the monthly energy consumptions for heating, cooling and electric lighting in the office room using the different window types. During the cooling-demand months of April to October, the use of the BIPV smart window contributes to significantly lower cooling loads of the office room when compared with the counterpart BIPV window and low-e double-glazed window; however, during the heating-demand months of November to March, the office room with the BIPV smart window consumes slightly more heating energy. These could be explained by the differences in monthly solar heat gain between the windows according to **Figure 6.7**. Apart from reducing cooling energy consumption, the BIPV smart window generates more quantities of electric energy compared to the counterpart BIPV window, as shown in **Figure 6.10**. The increase in the amount of electric energy generated by the BIPV smart window over its counterpart system becomes larger as the

weather warms up, reaching a maximum of approximately 12% in July. This could be explained by the fact that the thermotropic layer maintains at high temperature and in its translucent state over a longer period during summer than during winter (see **Figure 6.8**), therefore the BIPV smart window can utilise more scattered solar radiation for electricity generation, thus providing better electrical performance than its counterpart system during summer.

Table 6-5 shows the annual energy performance of the office room with the different window types. Both BIPV windows provide lower annual cooling loads but higher annual heating and lighting loads than the low-e double-glazed window. However, the BIPV smart window outperforms the counterpart BIPV window with a reduction in annual cooling load by 19.6 kWh/m^2 and an increase in annual electricity generation by 0.2 kWh/m^2. In addition, the BIPV smart window offers net energy savings of 39.0% when compared with the counterpart BIPV window and 49.6% when compared with the low-e double-glazed window.

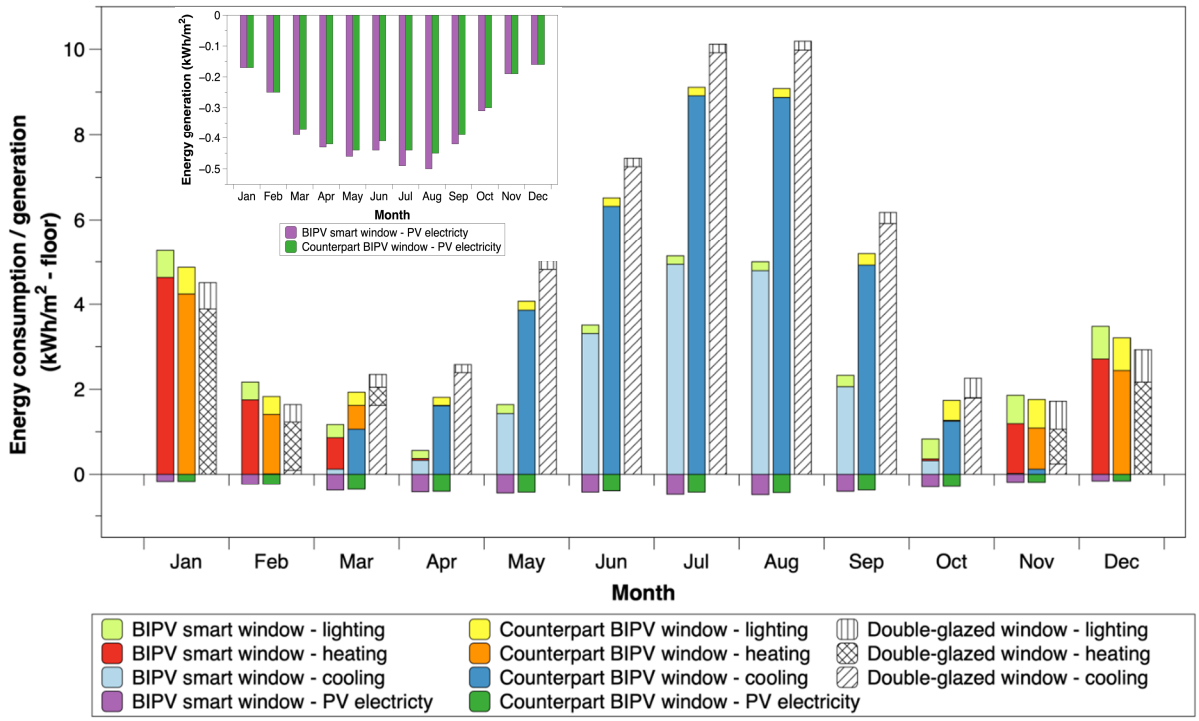

Figure 6.10: Monthly energy consumption and generation (kWh per floor area) of the office using the different window types.

Table 6-5: Annual energy consumption and generation comparison between the different window types.

	Annual Cooling (kWh/m^2)	**Annual Heating (kWh/m^2)**	**Annual Lighting (kWh/m^2)**	**Annual PV electricity (kWh/m^2)**	**Annual net Energy use (kWh/m^2)**	**Energy saving** (relative to DG
BIPV Smart window	17.3	11.1	4.5	4.2	28.7	49.6%
Counterpart BIPV window	36.9	9.6	4.6	4.0	47.1	17.2%
Low-e double glazing (DG)	44.0	8.5	4.4	0.0	56.9	-

To assess daylight availability in the building interior, Useful Daylight Illuminance (UDI) is generally used as the performance metric. In this study, the percentages of total working hours in a year where the daylight illuminance on the working plane falls within three standard UDI bins were predicted. The working plane was assumed to be at the centre of the room and a height of 0.75 m above the floor. The UDI bins include (1) an undersupply UDI bin where the hourly illuminances are lower than 100 lux (labelled as '$UDI_{<100\ lux}$'); (2) an oversupply UDI bin where the hourly illuminances exceed 2000 lux (labelled as '$UDI_{>2000\ lux}$'); (3) a useful bin where the hourly illuminances are in the range of 100 to 2000 lux (labelled as '$UDI_{100–2000\ lux}$') [202, 212]. Periods that fall into the $UDI_{<100\ lux}$ and $UDI_{>2000\ lux}$ bins often encourage some form of intervention, since the undersupply of daylight ($UDI_{<100\ lux}$) could lead to an increased demand for supplementary artificial lighting, while the oversupply of daylight ($UDI_{>2000\ lux}$) is likely to cause visual or thermal discomfort of occupants. Periods that lands in the $UDI_{100–2000\ lux}$ bin generally require neither electric lighting nor solar shading, and it may be assumed that the luminous environment meets the needs of occupants.

Figure 6.11 shows the annual UDI distribution for the different window types. For the low-e double-glazed window, the periods when exposed to oversupplied daylight ($UDI_{>2000\ lux}$), undersupplied daylight ($UDI_{<100\ lux}$) and desirable illumination ($UDI_{100–2000\ lux}$) account for 71.7%, 4.5% and 23.8%, respectively. The percentage of $UDI_{100–2000\ lux}$ is slightly increased to 27.6% when the office room is equipped with the counterpart PV window. In contrast, using the BIPV smart window significantly increases the percentage of $UDI_{100–2000\ lux}$ to 42.0% while reducing the percentage of $UDI_{>2000\ lux}$ to 52.9%. This may be because the BIPV smart window can scatter incoming sunlight and reduce its visible light transmittance in some periods of a year, thus lowering the risk of over illumination.

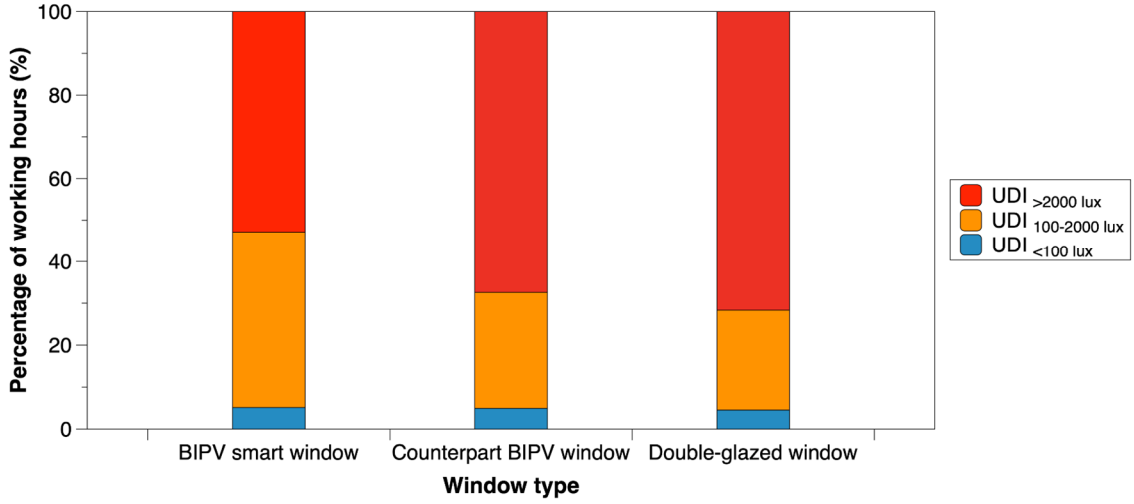

Figure 6.11: Annual UDI distribution in the office room with a south-facing window and a WWR of 25% under the climate of Nottingham.

6.3.3 Effect of window orientation and WWR

Further simulations have been carried out to specify the effects of orientation and WWR on the window performance. Four orientations, including south, west, east and top (horizontal skylight), were considered in the EnergyPlus simulations. In each orientation group, three WWRs were considered: 25%, 50% and 75% (see **Figure 6.12**), which were recommended to represent office buildings with low, medium and high levels of glazing coverage, respectively [211]. Therefore, totally 12 architecture design scenarios were numerically investigated.

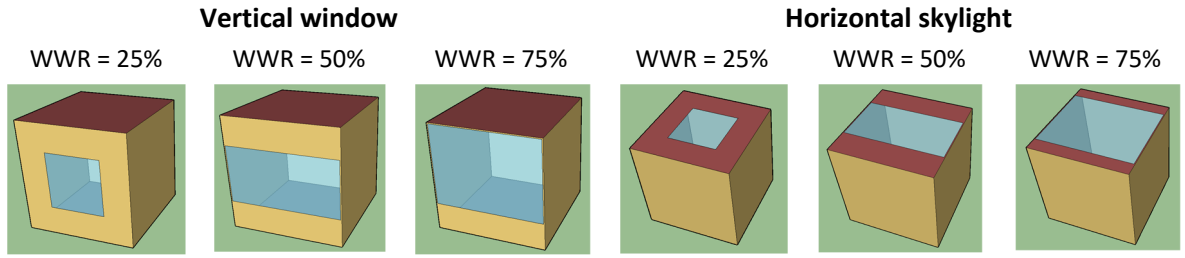

Figure 6.12: Diagrams of the office room using different window-to-wall ratios (WWR) for the south/west/east-facing window and horizontal roof skylight.

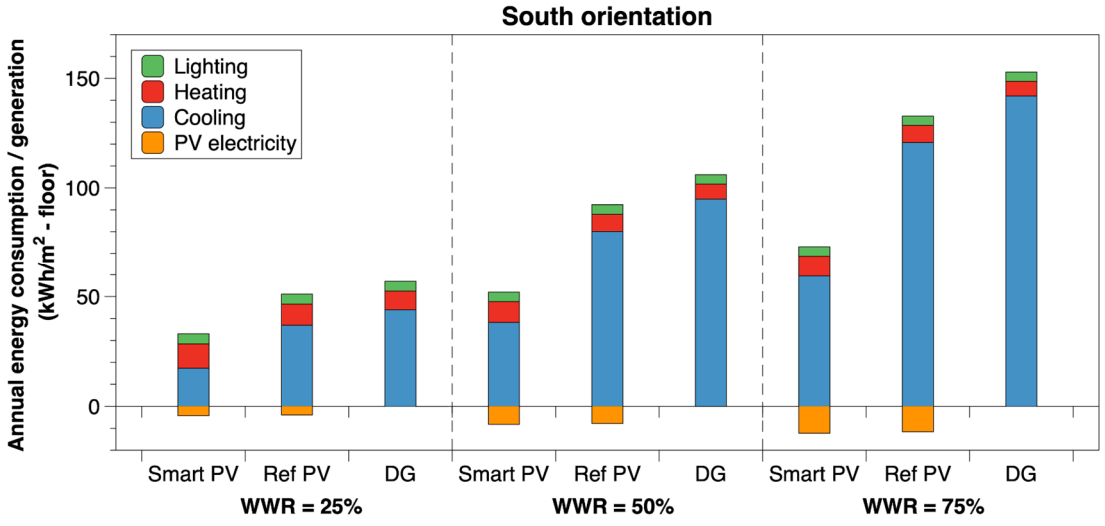

(a)

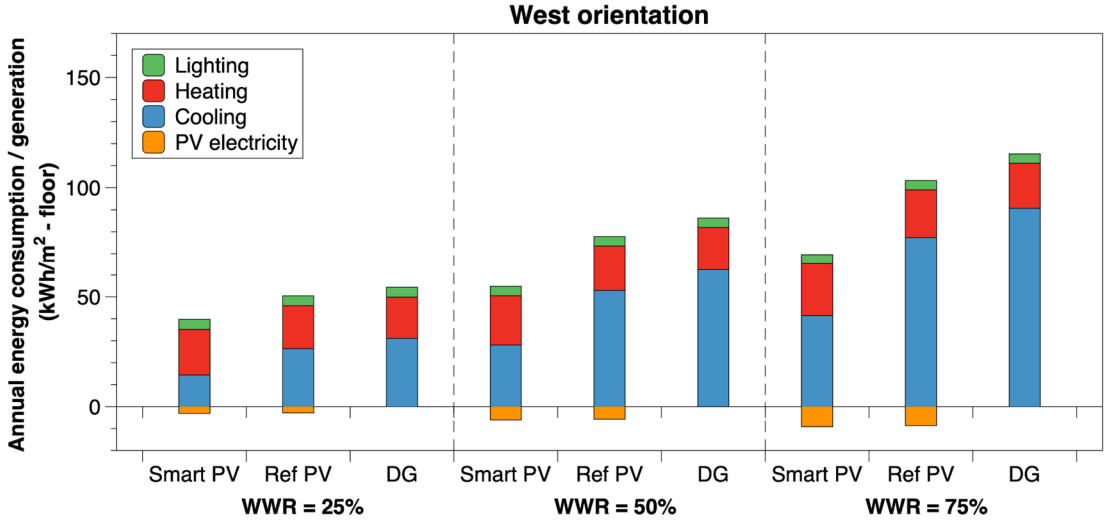

(b)

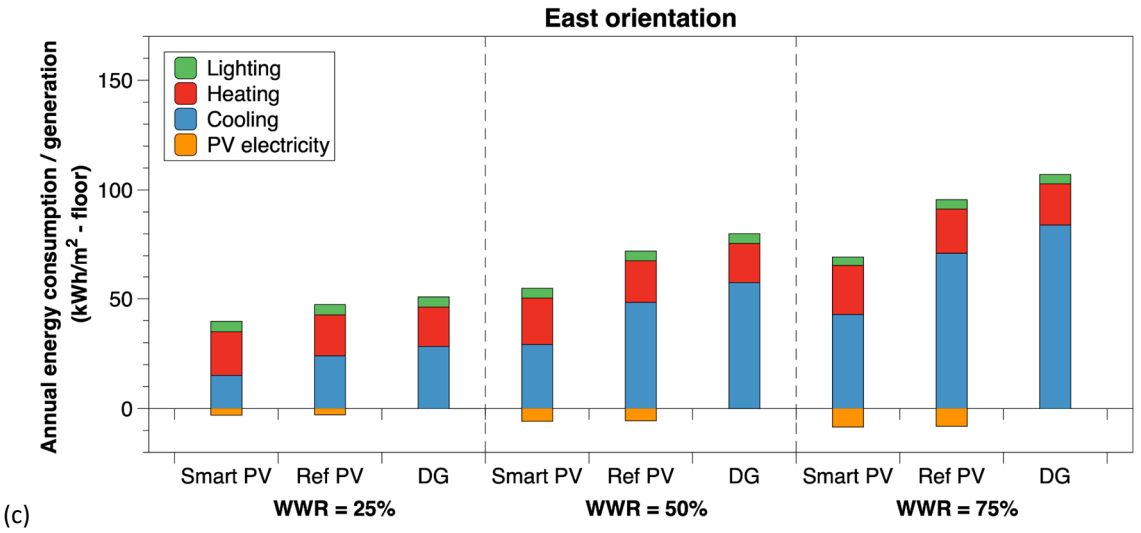

(c)

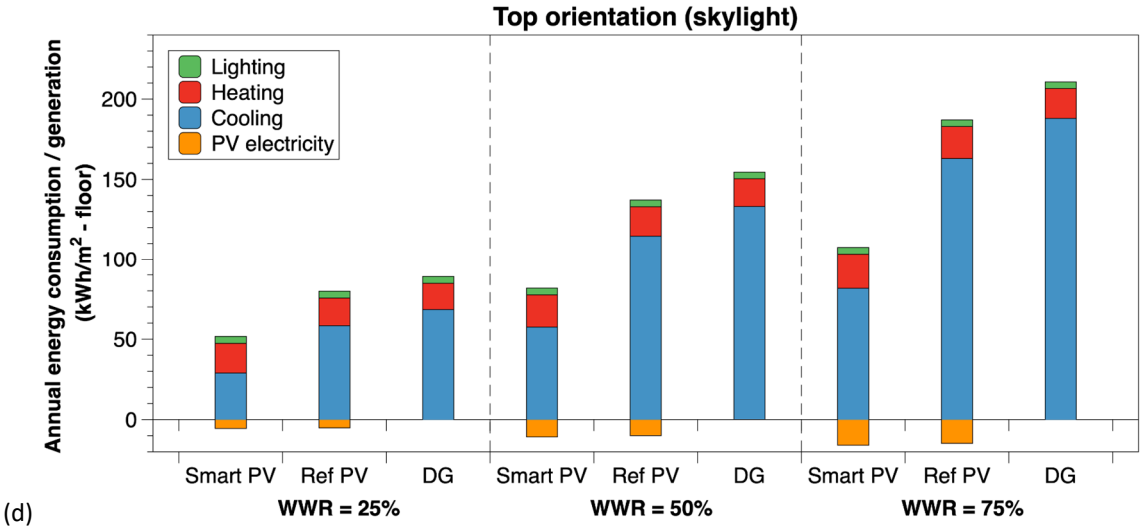

(d)

Figure 6.13: Annual energy use and generation for the (a) south-facing windows, (b) west-facing windows, (c) east-facing windows and (d) horizontal skylight under different WWRs.

The predicted annual energy consumption and electricity generation with respect to different glazing orientations and WWRs are shown in **Figure 6.13**. Under the same WWRs, all the three windows with the top orientation show the highest annual cooling loads, followed by the south, west and east orientations. This may be because the horizontal skylights receive more solar radiation than the vertical windows in hot seasons when the sun has high elevation angles. Under the same WWRs, the south orientation cases require the lowest amounts of heating energy, due to the longest exposure to direct solar radiation in cold seasons when the sun has low elevation angles. Another observation is that under the same orientations, the increase of WWR from 25% to 75% leads to both higher annual total energy consumption and annual electricity generation for the BIPV windows.

From **Table 6-6**, it can be clearly seen that under the same orientations, all the three windows with a larger WWR are associated with larger annual net energy consumption. Amongst them, the BIPV smart

window exhibits the best energy performance in all cases of orientation and WWR. For example, when the office room is facing south with a WWR of 75%, the net energy savings by using the BIPV smart window and the counterpart BIPV window are 60.2% and 20.7%, respectively, when compared with the low-e double-glazed window. In terms of daylight performance, as can be seen from **Table 6-7**, the BIPV smart window shows the highest percentages of total working hours where the office room is supplied with the desired daylight illumination ($UDI_{100–2000\ lux}$), in all cases of orientation and WWR.

Overall, the results suggest that using the BIPV smart window in place of the traditional BIPV window or low-e double-glazed window can improve both overall energy efficiency and indoor luminous environment quality for the office rooms regardless of glazing orientation and WWR.

Table 6-6: Annual net energy consumption for different WWRs and orientations. The values in brackets are the net energy savings relative to the low-e double-glazed window (DG).

	South window (kWh/m² - floor)			West window (kWh/m² - floor)			East window (kWh/m² - floor)			Horizontal skylight (kWh/m² - floor)		
	Smart	**Ref**	**DG**	**Smart**	**Ref**	**DG**	**Smart**	**Ref**	**DG**	**Smart**	**Ref**	**DG**
WWR = 25%	28.7 (49.6%)	47.1 (17.2%)	56.9	36.7 (32.5%)	47.6 (12.5%)	54.4	36.6 (27.9%)	44.4 (12.5%)	50.8	46.2 (48.1%)	74.7 (16.1%)	88.9
WWR = 50%	43.8 (58.7%)	84.5 (20.3%)	106.0	48.7 (43.5%)	72.1 (16.4%)	86.3	49.0 (38.8%)	66.6 (16.8%)	80.0	71.0 (54.1%)	127.1 (17.7%)	154.5
WWR = 75%	60.8 (60.2%)	121.2 (20.7%)	152.9	60.4 (47.6%)	94.7 (17.9%)	115.3	61.0 (43.0%)	87.5 (18.3%)	107.1	91.6 (56.5%)	172.3 (18.2%)	210.7

Table 6-7: Percentages of total working hours where the daylight illuminance in the office room lands in the $UDI_{100\text{-}2000}$ bin for different WWRs and window orientations.

	South window			West window			East window			Horizontal skylight		
	Smart	**Ref**	**DG**	**Smart**	**Ref**	**DG**	**Smart**	**Ref**	**DG**	**Smart**	**Ref**	**DG**
WWR = 25%	42.0%	27.6%	23.8%	60.4%	53.8%	47.1%	64.4%	57.4%	51.1%	44.9%	28.9%	25.4%
WWR = 50%	29.1%	17.0%	15.6%	33.8%	28.6%	25.5%	38.7%	31.9%	27.4%	29.8%	14.6%	12.9%
WWR = 75%	20.8%	13.8%	12.6%	22.3%	20.1%	17.5%	25.8%	21.2%	18.7%	15.7%	10.3%	8.6%

6.3.4 Effect of transition temperature

To better take advantage of the BIPV smart window for energy saving and daylighting control, this section takes at a more in-depth look at how the window performance is affected by the transition temperature of the thermotropic layer. A series of EnergyPlus models with the same setups as the previous model (i.e., an office room with south orientation and 25% WWR), except the transition temperature for the BIPV smart window, have been developed for the comparative analysis. The transition temperature was varied in the range of 20°C to 40°C with an interval of 2°C. For simplicity, the thermal and optical properties of the BIPV smart window derived for the transition temperature of 30.5°C (shown in **Figure 6.3**) were used in the new models; the only difference is that the original

property data were shifted to the transition temperature under testing (e.g. the curves of SHGC and τ_{vis} in **Figure 6.3** were shifted rightwards by 1.5°C for the transition temperature of 32°C).

Figure 6.14 shows the predicted annual energy consumption and electricity generation for different transition temperatures. It can be clearly seen that with the transition temperature decreasing from 40 to 20°C, the annual cooling load of the office room decreases, but in the meantime, the annual heating load increases. Moreover, the annual electricity generation by the BIPV smart window slightly increases by using a lower transition temperature. As can be seen from **Table 6-8**, the net energy saving by using the BIPV smart window over the low-e double-glazed window increases from 31.0% to 62.6% with the decrease of the transition temperature from 40 to 24 °C. A minimal difference in net energy saving is observed by further decreasing the transition temperature to 20 °C. In the perspective of daylight availability, the application of the BIPV smart window with a lower transition temperature contributes to an increased percentage of total working hours where the daylight illuminance is within the desirable range ($UDI_{100\text{-}2000\ lux}$). These results suggest that using a lower transition temperature is beneficial for improving the onsite electricity generation, cooling energy saving as well as luminous environment in the office, however, possibly causing a higher heating demand. This can be explained because with a lower transition temperature, the BIPV smart window has transitioned to its translucent state over a longer period across the year, which reduces the occurrence of over-illumination and overheating, increases the amount of solar energy concentrated on the integrated PVs through Total Internal Reflection (TIR) and in turn impacts on passive solar heating.

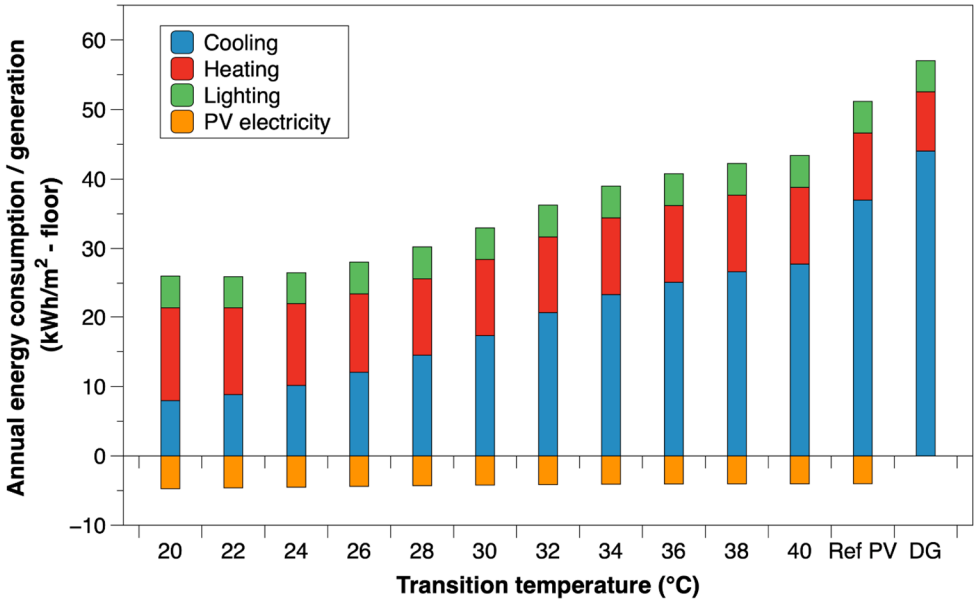

Figure 6.14: Annual energy consumption and on-site electricity generation for the BIPV smart window with different transition temperatures (from 20°C to 40°C), the counterpart BIPV window (Ref PV) and the low-e double-glazed window (DG).

Table 6-8: Window performance with respect to the transition temperature of the thermotropic layer.

	BIPV smart window											Ref PV	DG
Transition temperature	20°C	22°C	24°C	26°C	28°C	30°C	32°C	34°C	36°C	38°C	40°C		
Annual PV electricity (kWh/m^2)	4.7	4.6	4.5	4.4	4.3	4.2	4.1	4.1	4.1	4.0	4.0	4.0	/
Net energy Saving*	62.6 %	62.6 %	61.4 %	58.5 %	54.5 %	49.5 %	43.7 %	38.8 %	35.7 %	33.0 %	31.0 %	17.3 %	/
$UDI_{100\text{-}2000}$	67.9 %	62.4 %	56.6 %	51.4 %	46.2 %	42.0 %	37.3 %	34.5 %	32.5 %	31.1 %	30.0 %	27.6 %	23.8 %

* reduction of net energy consumption compared to the low-e double-glazed window (DG)

6.4 Summary

In this chapter, a comprehensive simulation method has been developed to predict the performance of the BIPV smart window system in an office-type building environment and analyse the effect of different window designs on the building energy efficiency and visual comfort of occupants. Firstly, the thermal, optical and electrical properties of a designed BIPV smart window system were calculated. Subsequently, these window properties were imported to an EnergyPlus model where the BIPV smart window system was assumed to be installed in a small cellular office under the climate of Nottingham, the UK. From the EnergyPlus simulation, the overall energy performance in terms of energy consumption (i.e., heating, cooling and artificial lighting loads) and on-site electricity generation and daylight performance (e.g. useful daylight illuminance) were predicted. The effects of different WWRs (25%, 50% and 75%), window orientations (south, west, east and top) and transition temperatures of the thermotropic layer (from 20°C to 40°C) were also investigated. The following conclusions can be drawn:

1) Using the BIPV smart window system can result in lower overall energy consumption and higher PV electricity generation in the office when compared with its counterpart system with a similar PV area but no thermotropic layer applied. For example, the net energy saving is 49.6% when the window is facing south and the WWR is 25%.
2) Using the BIPV smart window system can effectively reduce the period of over-illumination occurring in the office room and thus provide more comfortable luminous environment, compared to the counterpart BIPV window system.
3) Reducing the transition temperature of the thermotropic layer could potentially reduce the cooling energy consumption, enhance the on-site electricity generation and improve the luminous environment of the office room served by the BIPV smart window system. However, the energy saving becomes trivial when the transition temperature is decreased below 24°C, this probably attributed to increased requirements for heating and electric lighting.

Chapter 7 - Conclusions and recommendations for future work

Solar radiation transmitted through conventional single or double-glazed windows provide heat and light to the indoor space, which could exert either a positive or negative impact on the building energy performance and indoor luminous environment, depending on the circumstances. Excessive solar heat gain through windows can cause high cooling demands and thermal discomfort of occupants. Although glare-induced visual discomfort can be mitigated by using shading devices (e.g. blinds and curtains), they could also reduce useful solar heating and daylighting, which may increase the loads of heating and artificial lighting. Considerable endeavours have been devoted to improving the window performance. Windows integrated with photovoltaic (PV) or concentrating PV (CPV) devices can offer effective solar shading and cooling load reduction, while also allowing the conversion of solar energy into electricity. In contrast to conventional windows with static shading devices, smart windows exploiting thermotropic materials can adjust the amount of solar heat and light through it to adapt to the changed environmental conditions (ambient air temperature and solar irradiation). The intelligent control of solar heat gain and daylighting ensures greater thermal and visual comfort for occupants and contributes to significant energy savings. Combining BIPV glazing and thermotropic smart material into a single window for both electricity generation and adaptive solar radiation control is an innovation concept, which was proposed and numerically studied by Wu et al. [123] but has not been thoroughly investigated. Neither prototype has been developed, nor experiment has been conducted to prove the concept and validate the numerical models. To explore this idea further, this research project designed and developed a novel BIPV smart window system, which consisted of an optically switchable thermotropic hydrogel layer with integrated PVs. This system was comprehensively evaluated by Monte-Carlo ray-tracing simulation (**Chapter 2** & **Chapter 3**), indoor experimental characterisation (**Chapter 2** & **Chapter 4**), outdoor experimental characterisation (**Chapter 5**) and building performance simulation (**Chapter 6**).

7.1 Conclusions

7.1.1 Proof-of-concept preliminary studies

In the early stage of this research (**Chapter 2**), a thermotropic hydrogel potentially suitable for the BIPV smart window application was synthesised with the formula: 6 wt.% Hydroxypropyl Cellulose (HPC) and 1.5 wt.% Gellan Gum type F (GGF) mixed in distilled water, and first evaluated by spectroscopic measurement. A validated wavelength-dependent Monte-Carlo optical model with the measured spectral properties was applied to guide the design and development of the proposed BIPV smart window system. With the aid of the optical simulation and design, a prototype for the BIPV smart window system was fabricated and subsequently evaluated by the experiments of I-V

characterisation and solar transmission measurement under controlled indoor conditions. From the spectroscopic measurement, an optical switching temperature of 40.5°C was recorded for the 6 wt % HPC and 1.5 wt % GGF based thermotropic membrane. Its average visible light reflectance was observed to increase from below 10% to over 47%, with the membrane temperature increasing from 25 to 58°C. Based on the optical simulation and indoor experiment, some key findings and conclusions are presented below:

- The optical concentration ratio of the BIPV smart window system can be affected by various factors including the reflectance of the thermotropic membrane and the aperture area and thickness of its front glass cover.
- The short-circuit current and maximum power output of the BIPV smart window system (6 wt % HPC) increase by 18.6% and 16.5% respectively, with the membrane temperature increasing from 40 to 50°C; meanwhile, a 70.9% reduction in the intensity of light transmitted through the window was observed.
- The maximum power output of the BIPV smart window system (6 wt % HPC) is up to 17.4% higher than that of the counterpart system with no thermotropic membrane applied.
- Increasing the concentration of HPC from 2 to 6 wt % results in an improved power output and reduced light transmittance for the BIPV smart window system when the thermotropic membrane is in the light-scattering state.

7.1.2 An advanced optical model for window design and performance prediction

In **Chapter 3**, an advanced optical model, which combines a Monte-Carlo (MC) ray-tracing technique with an Inverse Adding-Doubling (IAD) method, has been developed for further investigating the light-scattering behaviour of the HPC-GGF based thermotropic membrane and thus enhancing the reliability and robustness of the system design via optical simulation. In contrast to the previous optical models where the thermotropic membrane was assumed as a Lambertian reflector (i.e., uniform reflectance in all directions), the IAD-MC coupled optical model considered the angular distribution of light scattered from the thermotropic membrane. In so doing, the IAD method combined with a Double-Integrating-Sphere (DIS) measurement was first applied to derive the volume scattering properties of the thermotropic membrane under various temperature conditions, which were subsequently applied in a Monte-Carlo ray-tracing model for light-scattering analysis. The IAD-MC coupled optical model has been validated by experiment and showed its applicability for the design and optimisation of the proposed BIPV smart window system.

The light-scattering study revealed that increasing either the temperature or HPC concentration of the thermotropic membrane leads to a higher scattering coefficient and a lower anisotropy factor, i.e.,

stronger scattering of incident light in the backward direction. From the window design and performance analysis, it was found that the enhanced backward light scattering from the thermotropic membrane contributes to a higher optical power density at the integrated PV cells in the BIPV smart window system, thereby a higher electrical power output. In addition, the performance can potentially be further improved by careful optimisation of different design parameters, such as geometric concentration ratio, thermotropic membrane thickness and glass refractive index.

7.1.3 Further development of the thermotropic membrane for practical applications

In the preliminary studies, the HPC-GGF based thermotropic hydrogels have been shown to be promising for application in BIPV windows to improve electricity generation and daylighting control. However, due to high transition temperatures (approximately 40°C), these hydrogels may not switch efficiently to the light-scattering state and provide efficient overheat/glare protection in the mild summer climates (e.g. the UK). Therefore, further development of the thermotropic hydrogels to adapt to a wide range of climatic conditions is required.

Chapter 4 describes an experimental method to optimise the performance of the BIPV smart window system in terms of transition temperature, solar modulation ability and electric power output. A novel thermotropic membrane was developed on the basis of HPC-GGF hydrogel, to which a certain concentration of sodium chloride (NaCl) salt was added to adjust its transition temperature. The result showed that the thermotropic membrane made of 6 wt.% HPC, 0.5 wt.% GGF and 4.5 wt.% NaCl has a transition temperature of 30.5°C with a large modulation of solar transmittance (up to 76.2% difference between the transparent and light-scattering states) and good reversibility during heating-cooling cycles. In addition, the NaCl-added thermotropic membrane exhibits stronger backward scattering than the salt-free thermotropic membrane in the light-scattering state, therefore enabling better electrical performance of the BIPV smart window system.

7.1.4 Window performance in real weather conditions

After the indoor experimental characterisation, the BIPV smart window system comprised of the HPC-GGF-NaCl based thermotropic membrane with the transition temperature at 30.5°C was further evaluated under dynamic outdoor environmental conditions in Nottingham, the UK (**Chapter 5**). The outdoor experiment was carried out in summer days based on a small-scale test cell, where the BIPV smart window system and its counterpart system with no thermotropic membrane were installed on the south wall. The diurnal variations in the electrical properties of the systems and the solar radiation transmission into the test cell with weather factors (e.g. solar irradiation and ambient temperature) were measured and analysed. The main results are summarised below:

- The variation of the short-circuit current and electric power generated by the systems follow similar patterns as the variation of the solar irradiance during the days.
- It was found that the maximum power output of the BIPV smart window system (50 mm × 50 mm) facing south at a tilt angle of 45° is up to approximately 12% higher in comparison to its counterpart system with no membrane.
- Further outdoor tests on a large-scale window system (120 mm × 120 mm) confirm that the BIPV smart window system can passively control the solar radiation transmitted into the interior space with variation in membrane temperature.
- In the middle of a sunny summer day, the use of the BIPV smart window system (120 mm × 120 mm) could reduce the amount of solar radiation transmitted into the test cell by up to 80%, when compared to its counterpart system with no thermotropic membrane, indicating more effective overheat and glare protection for the building interior.

7.1.5 Potentials in improving building energy efficiency and occupant comforts

In the final stage of this research (**Chapter 6**), a comprehensive numerical model was established in EnergyPlus to predict the overall energy and daylight performance of the proposed BIPV smart window system when applied in buildings. The BIPV smart window system was designed (consisting of a PV-membrane glass laminate, an air gap and a low-e glass pane) and assumed to be installed in a cellular office room under the climatic condition of Nottingham, the UK. The thermal, optical and electrical properties of the designed system were calculated and then used as input data to the EnergyPlus model to quantify its behaviour. From the simulation, the potentials of the BIPV smart window system in adaptively modulating daylight transmission and solar heat gain, reducing building energy consumption, supplying renewable energy and improving visual comfort of occupants were evaluated. The following conclusions can be drawn:

- The solar heat gains through the BIPV smart window system are similar as those through the counterpart BIPV window and the low-e double-glazed window in cold seasons, while significantly lower in warm seasons.
- The BIPV smart window system shows better energy and daylight performance than the other two windows. For example, when the Window-to-Wall Ratio (WWR) of the office room is 25%, installing the BIPV smart window system on the south façade contributes to an annual net energy saving of 39.0% when compared with the counterpart BIPV window and 49.6% when compared with the low-e double-glazed window.
- The installation of the BIPV smart window system on the south façade of the office room provides the largest energy savings, followed by the installations on the roof, west façade and

east façade. Moreover, the energy savings by the BIPV smart window system become more significant with increasing the WWR.

- Using a lower transition temperature for the BIPV smart window system results in a lower annual cooling load but a higher annual heating load of the office room. Because of this, the reduction in annual net energy consumption becomes insignificant when the transition temperature is decreased below 24°C.

When compared with the counterpart BIPV window, the BIPV smart window has an additional cost for the HPC based hydrogel layer. For example, the cost of a hydrogel layer (6 wt % HPC) with dimensions of 1 m x 1 m x 0.001 m is estimated to be around £40. The cost of an ordinary double-glazed window (1 m x 1 m) is £300-400 and the cost of a similar-size BIPV window can be over £400. Therefore, the cost of the BIPV smart window might be less than 10% higher than that of a similar-size BIPV window; however, the benefits brought about by the BIPV smart window include reduced cooling energy demand, better daylighting control and higher electricity generation, which could offset the additional cost.

7.2 Recommendations for future work

This study showed a promising glimpse of the proposed BIPV smart window system for building energy conservation, on-site renewable energy generation and adaptive daylighting control. However, there are still some works that need to develop in future research in order to optimise and fully characterise the system. The recommendations for future work are presented below:

- The thermotropic hydrogel could potentially be further optimised in these aspects: (1) optimising the abilities of light scattering and solar modulation by changing the physical properties of the hydrogel components (e.g. the particle size and refractive index of the HPC polymer) [213]; (2) enhancing the spectral selective performance (i.e., accepting visible light but shielding NIR light) by combining the thermotropic hydrogel with a NIR absorption based photothermal material (e.g. cesium tungsten bronze (Cs_xWO_3)) [189]; (3) improving the long-term operational stability, resistance to UV radiation and weatherability by adding UV-stabilisers, antioxidants and/or weathering agents [90].
- The power generation capability of the BIPV smart window system could be enhanced by the methods: (1) Integrating solar cells with a higher power conversion efficiency; (2) replacing the mono-facial solar cells with bi-facial solar cells to take advantage of the light scattered to the solar cell back surfaces [71].

- Detailed and more accurate visual comfort predictions in terms of UDI, daylight uniformity and daylight glare probability need to be made. The complementary daylight model can be developed using the validated light simulation tool, RADIANCE [212, 214].
- The BIPV smart window system needs to be manufactured in large scales and installed in a real office room or an outdoor test facility with HVAC and artificial lighting systems for annual field tests. This would be beneficial for the validation of the developed EnergyPlus models.
- The window performance needs to be assessed in different climatic conditions.
- A life-cycle cost analysis needs to be conducted.

The above recommendations for future work would contribute to a more complete understanding or a more optimised design of the BIPV smart window system. The future work may also provide insights and references for the design and development of advanced window systems with similar structures, materials or working mechanisms.

References

1. Skandalos, N. and D. Karamanis, *PV glazing technologies.* Renewable and Sustainable Energy Reviews, 2015. **49**: p. 306-322.
2. Hee, W., M. Alghoul, B. Bakhtyar, O. Elayeb, M. Shameri, M. Alrubaih, and K. Sopian, *The role of window glazing on daylighting and energy saving in buildings.* Renewable and Sustainable Energy Reviews, 2015. **42**: p. 323-343.
3. Kamalisarvestani, M., R. Saidur, S. Mekhilef, and F. Javadi, *Performance, materials and coating technologies of thermochromic thin films on smart windows.* Renewable and Sustainable Energy Reviews, 2013. **26**: p. 353-364.
4. Rezaei, S.D., S. Shannigrahi, and S. Ramakrishna, *A review of conventional, advanced, and smart glazing technologies and materials for improving indoor environment.* Solar Energy Materials and Solar Cells, 2017. **159**: p. 26-51.
5. Gorgolis, G. and D. Karamanis, *Solar energy materials for glazing technologies.* Solar Energy Materials and Solar Cells, 2016. **144**: p. 559-578.
6. Favoino, F., M. Overend, and Q. Jin, *The optimal thermo-optical properties and energy saving potential of adaptive glazing technologies.* Applied Energy, 2015. **156**: p. 1-15.
7. Whole Building Design Guide. *Window Film Fundamentals*. 2016 [cited 2021. 3.31]; Available from: https://www.wbdg.org/resources/window-film-fundamentals.
8. Tällberg, R., B.P. Jelle, R. Loonen, T. Gao, and M. Hamdy, *Comparison of the energy saving potential of adaptive and controllable smart windows: A state-of-the-art review and simulation studies of thermochromic, photochromic and electrochromic technologies.* Solar Energy Materials and Solar Cells, 2019. **200**: p. 109828.
9. Piccolo, A. and F. Simone, *Performance requirements for electrochromic smart window.* Journal of Building Engineering, 2015. **3**: p. 94-103.
10. Casini, M., *Smart buildings: Advanced materials and nanotechnology to improve energy-efficiency and environmental performance*. 2016: Woodhead Publishing.
11. Leftheriotis, G. and P. Yianoulis, *3.10 - Glazings and Coatings*, in *Comprehensive Renewable Energy*. 2012, Elsevier: Oxford. p. 313-355.
12. Jelle, B.P., S.E. Kalnæs, and T. Gao, *Low-emissivity materials for building applications: A state-of-the-art review and future research perspectives.* Energy and Buildings, 2015. **96**: p. 329-356.
13. Goia, F., M. Zinzi, E. Carnielo, and V. Serra, *Spectral and angular solar properties of a PCM-filled double glazing unit.* Energy and Buildings, 2015. **87**: p. 302-312.
14. Chow, T.-T., C. Li, and Z. Lin, *The function of solar absorbing window as water-heating device.* Building and Environment, 2011. **46**(4): p. 955-960.
15. Gao, T., T. Ihara, S. Grynning, B.P. Jelle, and A.G. Lien, *Perspective of aerogel glazings in energy efficient buildings.* Building and Environment, 2016. **95**: p. 405-413.
16. Skandalos, N. and D. Karamanis, *Investigation of thermal performance of semi-transparent PV technologies.* Energy and Buildings, 2016. **124**: p. 19-34.
17. Peng, J., D.C. Curcija, A. Thanachareonkit, E.S. Lee, H. Goudey, and S.E. Selkowitz, *Study on the overall energy performance of a novel c-Si based semitransparent solar photovoltaic window.* Applied energy, 2019. **242**: p. 854-872.
18. Husain, A.A., W.Z.W. Hasan, S. Shafie, M.N. Hamidon, and S.S. Pandey, *A review of transparent solar photovoltaic technologies.* Renewable and sustainable energy reviews, 2018. **94**: p. 779-791.
19. Wu, L.Y., Q. Zhao, H. Huang, and R. Lim, *Sol-gel based photochromic coating for solar responsive smart window.* Surface and Coatings Technology, 2017. **320**: p. 601-607.
20. Baetens, R., F., Bianco, L., Cascone, Y., Perino, M., Serra, V., 2014. Experimental analysis of an advanced dynamic glazing prototype integrating PCM and thermotropic layers. Energy

Procedia 48, 1272–1281. doi:10.1016/j.egypro.2014.02.144, B.P. Jelle, and A. Gustavsen, *Properties, requirements and possibilities of smart windows for dynamic daylight and solar energy control in buildings: A state-of-the-art review.* Solar Energy Materials and Solar Cells, 2010. **94**(2): p. 87-105.
21. Alrashidi, H., A. Ghosh, W. Issa, N. Sellami, T.K. Mallick, and S. Sundaram, *Thermal performance of semitransparent CdTe BIPV window at temperate climate.* Solar Energy, 2020. **195**: p. 536-543.
22. Cannavale, A., L. Ierardi, M. Hörantner, G.E. Eperon, H.J. Snaith, U. Ayr, and F. Martellotta, *Improving energy and visual performance in offices using building integrated perovskite-based solar cells: A case study in Southern Italy.* Applied energy, 2017. **205**: p. 834-846.
23. Cannavale, A., M. Hörantner, G.E. Eperon, H.J. Snaith, F. Fiorito, U. Ayr, and F. Martellotta, *Building integration of semitransparent perovskite-based solar cells: Energy performance and visual comfort assessment.* Applied energy, 2017. **194**: p. 94-107.
24. Ghosh, A., S. Sundaram, and T.K. Mallick, *Thermal Performance Analysis of BIPV-PDLC Window.* 2019.
25. Jelle, B.P., C. Breivik, and H.D. Røkenes, *Building integrated photovoltaic products: A state-of-the-art review and future research opportunities.* Solar Energy Materials and Solar Cells, 2012. **100**: p. 69-96.
26. Xu, S., W. Liao, J. Huang, and J. Kang, *Optimal PV cell coverage ratio for semi-transparent photovoltaics on office building facades in central China.* Energy and buildings, 2014. **77**: p. 130-138.
27. Chen, M., W. Zhang, L. Xie, Z. Ni, Q. Wei, W. Wang, and H. Tian, *Experimental and numerical evaluation of the crystalline silicon PV window under the climatic conditions in southwest China.* Energy, 2019. **183**: p. 584-598.
28. Andreani, L.C., A. Bozzola, P. Kowalczewski, M. Liscidini, and L. Redorici, *Silicon solar cells: toward the efficiency limits.* Advances in Physics: X, 2019. **4**(1): p. 1548305.
29. Chae, Y.T., J. Kim, H. Park, and B. Shin, *Building energy performance evaluation of building integrated photovoltaic (BIPV) window with semi-transparent solar cells.* Applied Energy, 2014. **129**: p. 217-227.
30. Gao, Y., F.T. Si, O. Isabella, R. Santbergen, G. Yang, J. Dong, G. Zhang, and M. Zeman. *Performance Optimization of Semi-Transparent Thin-Film Amorphous Silicon Solar Cells*. in *2017 IEEE 44th Photovoltaic Specialist Conference (PVSC)*. 2017. IEEE.
31. Meillaud, F., M. Boccard, G. Bugnon, M. Despeisse, S. Hänni, F.-J. Haug, J. Persoz, J.-W. Schüttauf, M. Stuckelberger, and C. Ballif, *Recent advances and remaining challenges in thin-film silicon photovoltaic technology.* Materials Today, 2015. **18**(7): p. 378-384.
32. Liao, W. and S. Xu, *Energy performance comparison among see-through amorphous-silicon PV (photovoltaic) glazings and traditional glazings under different architectural conditions in China.* Energy, 2015. **83**: p. 267-275.
33. Ogbomo, O.O., E.H. Amalu, N. Ekere, and P. Olagbegi, *A review of photovoltaic module technologies for increased performance in tropical climate.* Renewable and Sustainable Energy Reviews, 2017. **75**: p. 1225-1238.
34. Luceño-Sánchez, J.A., A.M. Díez-Pascual, and R. Peña Capilla, *Materials for photovoltaics: State of art and recent developments.* International journal of molecular sciences, 2019. **20**(4): p. 976.
35. Green, M.A., E.D. Dunlop, D.H. Levi, J. Hohl‐Ebinger, M. Yoshita, and A.W. Ho‐Baillie, *Solar cell efficiency tables (version 54).* Progress in Photovoltaics: Research and Applications, 2019. **27**(7): p. 565-575.
36. Alrashidi, H., A. Ghosh, W. Issa, N. Sellami, T.K. Mallick, and S. Sundaram, *Evaluation of solar factor using spectral analysis for CdTe photovoltaic glazing.* Materials letters, 2019. **237**: p. 332-335.

37. Sharma, K., V. Sharma, and S. Sharma, *Dye-sensitized solar cells: fundamentals and current status.* Nanoscale research letters, 2018. **13**(1): p. 381.
38. Fung, T.Y. and H. Yang, *Study on thermal performance of semi-transparent building-integrated photovoltaic glazings.* Energy and Buildings, 2008. **40**(3): p. 341-350.
39. Park, K., G. Kang, H. Kim, G. Yu, and J. Kim, *Analysis of thermal and electrical performance of semi-transparent photovoltaic (PV) module.* Energy, 2010. **35**(6): p. 2681-2687.
40. Miyazaki, T., A. Akisawa, and T. Kashiwagi, *Energy savings of office buildings by the use of semi-transparent solar cells for windows.* Renewable energy, 2005. **30**(3): p. 281-304.
41. Wang, M., J. Peng, N. Li, L. Lu, T. Ma, and H. Yang, *Assessment of energy performance of semi-transparent PV insulating glass units using a validated simulation model.* Energy, 2016. **112**: p. 538-548.
42. Sun, Y., K. Shanks, H. Baig, W. Zhang, X. Hao, Y. Li, B. He, R. Wilson, H. Liu, S. Sundaram, J. Zhang, L. Xie, T. Mallick, and Y. Wu, *Integrated semi-transparent cadmium telluride photovoltaic glazing into windows: Energy and daylight performance for different architecture designs.* Applied Energy, 2018. **231**: p. 972-984.
43. Lee, H.M. and J.H. Yoon, *Power performance analysis of a transparent DSSC BIPV window based on 2 year measurement data in a full-scale mock-up.* Applied Energy, 2018. **225**: p. 1013-1021.
44. Chemisana, D., *Building integrated concentrating photovoltaics: a review.* Renewable and Sustainable Energy Reviews, 2011. **15**(1): p. 603-611.
45. Abu-Bakar, S.H., F. Muhammad-Sukki, D. Freier, R. Ramirez-Iniguez, T.K. Mallick, A.B. Munir, S.H.M. Yasin, A.A. Mas' ud, and N.M. Yunus, *Optimisation of the performance of a novel rotationally asymmetrical optical concentrator design for building integrated photovoltaic system.* Energy, 2015. **90**: p. 1033-1045.
46. Shanks, K., S. Senthilarasu, and T.K. Mallick, *Optics for concentrating photovoltaics: Trends, limits and opportunities for materials and design.* Renewable and Sustainable Energy Reviews, 2016. **60**: p. 394-407.
47. Chemisana, D., J. Rosell, A. Riverola, and C. Lamnatou, *Experimental performance of a Fresnel-transmission PVT concentrator for building-façade integration.* Renewable energy, 2016. **85**: p. 564-572.
48. Kim, J.M. and P.S. Dutta, *Optical efficiency–concentration ratio trade-off for a flat panel photovoltaic system with diffuser type concentrator.* Solar Energy Materials and Solar Cells, 2012. **103**: p. 35-40.
49. Kasezawa, T., H. Horimai, H. Tabuchi, and T. Shimura, *Holographic window for solar power generation.* Optical Review, 2016. **23**(6): p. 997-1003.
50. Kerrouche, A., D. Hardy, D. Ross, and B. Richards, *Luminescent solar concentrators: From experimental validation of 3D ray-tracing simulations to coloured stained-glass windows for BIPV.* Solar Energy Materials and Solar Cells, 2014. **122**: p. 99-106.
51. Wiegman, J. and E. Van der Kolk, *Building integrated thin film luminescent solar concentrators: detailed efficiency characterization and light transport modelling.* Solar Energy Materials and Solar Cells, 2012. **103**: p. 41-47.
52. Zhu, L., Z. Shao, Y. Sun, V. Soebarto, F. Gao, G. Zillante, and J. Zuo, *Indoor daylight distribution in a room with integrated dynamic solar concentrating facade.* Energy and Buildings, 2018. **158**: p. 1-13.
53. Yamada, N., K. Kanno, K. Hayashi, and T. Tokimitsu, *Performance of see-through prism CPV module for window integrated photovoltaics.* Optics express, 2011. **19**(104): p. A649-A656.
54. Sabry, M., *Prismatic TIR (total internal reflection) low-concentration PV (photovoltaics)-integrated façade for low latitudes.* Energy, 2016. **107**: p. 473-481.
55. Sellami, N. and T.K. Mallick, *Optical efficiency study of PV crossed compound parabolic concentrator.* Applied Energy, 2013. **102**: p. 868-876.

56. Baig, H., N. Sarmah, K.C. Heasman, and T.K. Mallick, *Numerical modelling and experimental validation of a low concentrating photovoltaic system.* Solar Energy Materials and Solar Cells, 2013. **113**: p. 201-219.
57. Uematsu, T., Y. Yazawa, K. Tsutsui, Y. Miyamura, H. Ohtsuka, T. Warabisako, and T. Joge, *Design and characterization of flat-plate static-concentrator photovoltaic modules.* Solar energy materials and solar cells, 2001. **67**(1): p. 441-448.
58. Yoshioka, K., K. Koizumi, and T. Saitoh, *Simulation and fabrication of flat-plate concentrator modules.* Solar energy materials and solar cells, 2003. **75**(3): p. 373-380.
59. Weber, K., V. Everett, J. MacDonald, A.W. Blakers, P. Deenapanray, and J. Babaei, *Modelling of silver modules incorporating a lambertian rear reflector.* 2004.
60. Smestad, G. and P. Hamill, *Concentration of solar radiation by white backed photovoltaic panels.* Applied optics, 1984. **23**(23): p. 4394-4402.
61. Morimoto, M. and T. Maruyama, *Static solar concentrator with vertical flat plate photovoltaic cells and switchable white/transparent bottom plate.* Solar energy materials and solar cells, 2005. **87**(1): p. 299-309.
62. Leow, S.W., C. Corrado, M. Osborn, and S.A. Carter. *Monte Carlo ray-tracing simulations of luminescent solar concentrators for building integrated photovoltaics*. in *SPIE Solar Energy+ Technology*. 2013. International Society for Optics and Photonics.
63. Leow, S.W., C. Corrado, M. Osborn, M. Isaacson, G. Alers, and S.A. Carter, *Analyzing luminescent solar concentrators with front-facing photovoltaic cells using weighted Monte Carlo ray tracing.* Journal of Applied Physics, 2013. **113**(21): p. 214510.
64. Corrado, C., S.W. Leow, M. Osborn, E. Chan, B. Balaban, and S.A. Carter, *Optimization of gain and energy conversion efficiency using front-facing photovoltaic cell luminescent solar concentratordesign.* Solar Energy Materials and Solar Cells, 2013. **111**: p. 74-81.
65. Kim, N., S. Lee, X.G. Zhao, D. Kim, C. Oh, and H. Kang, *Reflection and durability study of different types of backsheets and their impact on c-Si PV module performance.* Solar Energy Materials and Solar Cells, 2016. **146**: p. 91-98.
66. Liu, X., Y. Wu, X. Hou, and H. Liu, *Investigation of the Optical Performance of a Novel Planar Static PV Concentrator with Lambertian Rear Reflectors.* Buildings, 2017. **7**(4): p. 88.
67. Uematsu, T., Y. Yazawa, T. Joge, and S. Kokunai, *Fabrication and characterization of a flat-plate static-concentrator photovoltaic module.* Solar energy materials and solar cells, 2001. **67**(1): p. 425-434.
68. Uematsu, T., K. Tsutsui, Y. Yazawa, T. Warabisako, I. Araki, Y. Eguchi, and T. Joge, *Development of bifacial PV cells for new applications of flat-plate modules.* Solar energy materials and solar cells, 2003. **75**(3): p. 557-566.
69. Weber, K., V. Everett, P. Deenapanray, E. Franklin, and A. Blakers, *Modeling of static concentrator modules incorporating lambertian or v-groove rear reflectors.* Solar energy materials and solar cells, 2006. **90**(12): p. 1741-1749.
70. Chou, C.-H., J.-K. Chuang, and F.-C. Chen, *High-performance flexible waveguiding photovoltaics.* Scientific reports, 2013. **3**: p. 2244.
71. Hezel, R., *Novel applications of bifacial solar cells.* Progress in Photovoltaics: Research and Applications, 2003. **11**(8): p. 549-556.
72. Zhang, Y., S. Sun, R. Kang, J. Zhang, N. Zhang, W. Yan, W. Xie, J. Ding, J. Bao, and C. Gao, *Polymethylmethacrylate-based luminescent solar concentrators with bottom-mounted solar cells.* Energy Conversion and Management, 2015. **95**: p. 187-192.
73. Kerrouche, A., D.A. Hardy, D. Ross, and B.S. Richards, *Luminescent solar concentrators: From experimental validation of 3D ray-tracing simulations to coloured stained-glass windows for BIPV.* Solar Energy Materials and Solar Cells, 2014. **122**: p. 99-106.
74. Bergren, M.R., N.S. Makarov, K. Ramasamy, A. Jackson, R. Guglielmetti, and H. McDaniel, *High-performance CuInS2 quantum dot laminated glass luminescent solar concentrators for windows.* ACS Energy Letters, 2018. **3**(3): p. 520-525.

75. Yu, X., Y. Su, H. Zheng, and S. Riffat, *A study on use of miniature dielectric compound parabolic concentrator (dCPC) for daylighting control application.* Building and Environment, 2014. **74**: p. 75-85.
76. Baig, H., N. Sarmah, D. Chemisana, J. Rosell, and T.K. Mallick, *Enhancing performance of a linear dielectric based concentrating photovoltaic system using a reflective film along the edge.* Energy, 2014. **73**: p. 177-191.
77. Shanks, K., A. Knowles, A. Brierley, H. Baig, H. Orr, Y. Sun, Y. Wu, S. Sundaram, and T. Mallick, *An experimental analysis of the optical, thermal and power to weight performance of plastic and glass optics with AR coatings for embedded CPV windows.* Solar Energy Materials and Solar Cells, 2019. **200**: p. 110027.
78. Baig, H., N. Sellami, D. Chemisana, J. Rosell, and T.K. Mallick, *Performance analysis of a dielectric based 3D building integrated concentrating photovoltaic system.* Solar Energy, 2014. **103**: p. 525-540.
79. Baig, H., N. Sellami, and T.K. Mallick, *Trapping light escaping from the edges of the optical element in a Concentrating Photovoltaic system.* Energy Conversion and Management, 2015. **90**: p. 238-246.
80. Paul, D.I., *Characterisation of solar concentrating systems for photovoltaics and their impact on performance*. 2011, University of Ulster.
81. Ramirez-Iniguez, R., J. Deciga-Gusi, D. Freier, S.H. Abu-Bakar, and F. Muhammad-Sukki, *Experimental evaluation of a solar window incorporating rotationally asymmetrical compound parabolic concentrators (RACPC).* Energy Procedia, 2017. **130**: p. 102-107.
82. Zacharopoulos, A., P.C. Eames, D. McLarnon, and B. Norton, *Linear dielectric non-imaging concentrating covers for PV integrated building facades.* Solar Energy, 2000. **68**(5): p. 439-452.
83. Mallick, T.K. and P.C. Eames, *Design and fabrication of low concentrating second generation PRIDE concentrator.* Solar Energy Materials and Solar Cells, 2007. **91**(7): p. 597-608.
84. Su, Y., G. Pei, S.B. Riffat, and H. Huang, *A novel lens-walled compound parabolic concentrator for photovoltaic applications.* Journal of solar energy engineering, 2012. **134**(2).
85. Sharaf, O.Z. and M.F. Orhan, *Concentrated photovoltaic thermal (CPVT) solar collector systems: Part I–Fundamentals, design considerations and current technologies.* Renewable and Sustainable Energy Reviews, 2015. **50**: p. 1500-1565.
86. Sarmah, N., B.S. Richards, and T.K. Mallick, *Design, development and indoor performance analysis of a low concentrating dielectric photovoltaic module.* Solar Energy, 2014. **103**: p. 390-401.
87. Sarmah, N. and T.K. Mallick, *Design, fabrication and outdoor performance analysis of a low concentrating photovoltaic system.* Solar Energy, 2015. **112**: p. 361-372.
88. Sharma, S., A. Tahir, K. Reddy, and T.K. Mallick, *Performance enhancement of a Building-Integrated Concentrating Photovoltaic system using phase change material.* Solar Energy Materials and Solar Cells, 2016. **149**: p. 29-39.
89. Casini, M., *Active dynamic windows for buildings: A review.* Renewable Energy, 2018. **119**: p. 923-934.
90. Resch, K. and G.M. Wallner, *Thermotropic layers for flat-plate collectors—A review of various concepts for overheating protection with polymeric materials.* Solar Energy Materials and Solar Cells, 2009. **93**(1): p. 119-128.
91. Allen, K., K. Connelly, P. Rutherford, and Y. Wu, *Smart Windows—Dynamic Control of Building Energy Performance.* Energy and Buildings, 2017.
92. Muehling, O., A. Seeboth, T. Haeusler, R. Ruhmann, E. Potechius, and R. Vetter, *Variable solar control using thermotropic core/shell particles.* Solar Energy Materials and Solar Cells, 2009. **93**(9): p. 1510-1517.
93. Seeboth, A., R. Ruhmann, and O. Mühling, *Thermotropic and thermochromic polymer based materials for adaptive solar control.* Materials, 2010. **3**(12): p. 5143-5168.

94. Lanzalaco, S. and E. Armelin, *Poly (n-isopropylacrylamide) and copolymers: A review on recent progresses in biomedical applications.* Gels, 2017. **3**(4): p. 36.
95. Zhou, Y., Y. Cai, X. Hu, and Y. Long, *Temperature-responsive hydrogel with ultra-large solar modulation and high luminous transmission for "smart window" applications.* Journal of Materials Chemistry A, 2014. **2**(33): p. 13550-13555.
96. Seeboth, A., J. Schneider, and A. Patzak, *Materials for intelligent sun protecting glazing.* Solar energy materials and solar cells, 2000. **60**(3): p. 263-277.
97. Schneider, J. and A. Seeboth, *Natural thermotropic materials for solar switching glazing.* Materialwissenschaft und Werkstofftechnik, 2001. **32**(3): p. 231-237.
98. Wang, M., Y. Gao, C. Cao, K. Chen, Y. Wen, D. Fang, L. Li, and X. Guo, *Binary solvent colloids of thermosensitive poly (n-isopropylacrylamide) microgel for smart windows.* Industrial & Engineering Chemistry Research, 2014. **53**(48): p. 18462-18472.
99. Maiorov, V., *Optical Properties of Thermotropic Hydrogels (a Review).* Optics and Spectroscopy, 2020. **128**: p. 367-386.
100. Nun, N., S. Hinrichs, M.A. Schroer, D. Sheyfer, G. Grübel, and B. Fischer, *Tuning the size of thermoresponsive poly (N-isopropyl acrylamide) grafted silica microgels.* Gels, 2017. **3**(3): p. 34.
101. Mizuntani, M., K. Satoh, and M. Kamigaito, *Degradable poly (N-isopropylacrylamide) with tunable thermosensitivity by simultaneous chain-and step-growth radical polymerization.* Macromolecules, 2011. **44**(7): p. 2382-2386.
102. Jin, X., H. Kang, R. Liu, and Y. Huang, *Regulation of the thermal sensitivity of hydroxypropyl cellulose by poly (N-isopropylacryamide) side chains.* Carbohydrate polymers, 2013. **95**(1): p. 155-160.
103. Du, H., R. Wickramasinghe, and X. Qian, *Effects of salt on the lower critical solution temperature of poly (N-isopropylacrylamide).* The Journal of Physical Chemistry B, 2010. **114**(49): p. 16594-16604.
104. Li, X.-H., C. Liu, S.-P. Feng, and N.X. Fang, *Broadband light management with thermochromic hydrogel microparticles for smart windows.* Joule, 2019. **3**(1): p. 290-302.
105. Gladen, A., S. Mantell, and J. Davidson, *Numerical evaluation of the optical properties of encapsulated phase change particles for thermotropic materials.* Journal of Thermal Science and Engineering Applications, 2015. **7**(3).
106. Yang, Y.-S., Y. Zhou, F.B.Y. Chiang, and Y. Long, *Temperature-responsive hydroxypropylcellulose based thermochromic material and its smart window application.* RSC advances, 2016. **6**(66): p. 61449-61453.
107. Connelly, K., Y. Wu, J. Chen, and Y. Lei, *Design and development of a reflective membrane for a novel Building Integrated Concentrating Photovoltaic (BICPV) 'Smart Window' system.* Applied Energy, 2016. **182**: p. 331-339.
108. Connelly, K., Y. Wu, X. Ma, and Y. Lei, *Transmittance and Reflectance Studies of Thermotropic Material for a Novel Building Integrated Concentrating Photovoltaic (BICPV)'Smart Window'System.* Energies, 2017. **10**(11): p. 1889.
109. Cao, D., C. Xu, W. Lu, C. Qin, and S. Cheng, *Sunlight-Driven Photo-Thermochromic Smart Windows.* Solar RRL, 2018. **2**(4): p. 1700219.
110. YAO, J. and C.-W. YAN, *Development and analysis of a novel kind of smart thermotropic material.* Functional Materials Letters, 2010. **3**(02): p. 135-139.
111. Watanabe, H., *Intelligent window using a hydrogel layer for energy efficiency.* Solar Energy Materials and Solar Cells, 1998. **54**(1): p. 203-211.
112. Watanabe, H., *Laminate-controlling light autonomously and window using the same*. 2007, Google Patents.
113. Nishio, Y., R. Chiba, Y. Miyashita, K. Oshima, T. Miyajima, N. Kimura, and H. Suzuki, *Salt addition effects on mesophase structure and optical properties of aqueous hydroxypropyl cellulose solutions.* Polymer journal, 2002. **34**(3): p. 149-157.

114. Xia, X., S. Tang, X. Lu, and Z. Hu, *Formation and volume phase transition of hydroxypropyl cellulose microgels in salt solution.* Macromolecules, 2003. **36**(10): p. 3695-3698.
115. Nitz, P. and H. Hartwig, *Solar control with thermotropic layers.* Solar Energy, 2005. **79**(6): p. 573-582.
116. Yao, J. and N. Zhu, *Evaluation of indoor thermal environmental, energy and daylighting performance of thermotropic windows.* Building and environment, 2012. **49**: p. 283-290.
117. Jian, Y. *Modeling and simulation for the optimal switching temperature of double-glazed thermotropic window*. in *Industrial Mechatronics and Automation (ICIMA), 2010 2nd International Conference on*. 2010. IEEE.
118. Ma, R.-H. and Y.-C. Chen, *BIPV-powered smart windows utilizing photovoltaic and electrochromic devices.* Sensors, 2012. **12**(1): p. 359-372.
119. Kwon, H.K., K.T. Lee, K. Hur, S.H. Moon, M.M. Quasim, T.D. Wilkinson, J.Y. Han, H. Ko, I.K. Han, and B. Park, *Optically switchable smart windows with integrated photovoltaic devices.* Advanced Energy Materials, 2015. **5**(3).
120. Murray, J., D. Ma, and J.N. Munday, *Electrically controllable light trapping for self-powered switchable solar windows.* ACS Photonics, 2016. **4**(1): p. 1-7.
121. Zhou, J., Y. Gao, Z. Zhang, H. Luo, C. Cao, Z. Chen, L. Dai, and X. Liu, *VO 2 thermochromic smart window for energy savings and generation.* Scientific reports, 2013. **3**: p. 3029.
122. Li, C., M. Chen, L. Zhang, W. Shen, X. Liang, X. Wang, and H. Yang, *An electrically light-transmittance-switchable film with a low driving voltage based on liquid crystal/polymer composites.* Liquid Crystals, 2020. **47**(1): p. 106-113.
123. Wu, Y., K. Connelly, Y. Liu, X. Gu, Y. Gao, and G.Z. Chen, *Smart solar concentrators for building integrated photovoltaic façades.* Solar Energy, 2016. **133**: p. 111-118.
124. Moehlecke, A., F. Febras, and I. Zanesco, *Electrical performance analysis of PV modules with bifacial silicon solar cells and white diffuse reflector.* Solar Energy, 2013. **96**: p. 253-262.
125. Paul, D.I., M. Smyth, A. Zacharopoulos, and J. Mondol, *The design, fabrication and indoor experimental characterisation of an isolated cell photovoltaic module.* Solar Energy, 2013. **88**: p. 1-12.
126. Abu-Bakar, S.H., F. Muhammad-Sukki, D. Freier, R. Ramirez-Iniguez, T.K. Mallick, A.B. Munir, S.H. Mohd Yasin, A. Abubakar Mas'ud, and N.A. Bani, *Performance analysis of a solar window incorporating a novel rotationally asymmetrical concentrator.* Energy, 2016. **99**: p. 181-192.
127. Hamadani, B.H. and B. Dougherty, *Solar cell characterization*, in *Semiconductor Materials for Solar Photovoltaic Cells*. 2016, Springer. p. 229-245.
128. Nyeinga, K., D. Okello, and O.J. Nydal, *A ray tracer model for analysis of solar concentrating systems.* Journal of Energy in Southern Africa, 2019. **30**(1): p. 8-20.
129. Sarmah, N., B.S. Richards, and T.K. Mallick, *Evaluation and optimization of the optical performance of low-concentrating dielectric compound parabolic concentrator using ray-tracing methods.* Applied optics, 2011. **50**(19): p. 3303-3310.
130. Meinardi, F., F. Bruni, and S. Brovelli, *Luminescent solar concentrators for building-integrated photovoltaics.* Nature Reviews Materials, 2017. **2**(12): p. 1-9.
131. Montes, R. and C. Ureña, *An overview of BRDF models.* University of Grenada, Technical Report LSI-2012, 2012. **1**.
132. Jensen, H.W., J. Arvo, P. Dutre, A. Keller, A. Owen, M. Pharr, and P. Shirley. *Monte Carlo ray tracing*. in *ACM SIGGRAPH*. 2003.
133. Burgers, A., L. Slooff, R. Kinderman, and J. Van Roosmalen. *Modelling of luminescent concentrators by ray-tracing*. in *Presented at the 20th European Photovoltaic Solar Energy Conference and Exhibition*. 2005.
134. Li, X., Y. Liang, and L. Xu, *Bidirectional reflectance distribution function based surface modeling of non-Lambertian using intensity data of light detection and ranging.* JOSA A, 2014. **31**(9): p. 2055-2063.

135. Schaepman-Strub, G., M.E. Schaepman, T.H. Painter, S. Dangel, and J.V. Martonchik, *Reflectance quantities in optical remote sensing—Definitions and case studies.* Remote sensing of environment, 2006. **103**(1): p. 27-42.
136. Simonot, L., *Photometric model of diffuse surfaces described as a distribution of interfaced Lambertian facets.* Applied optics, 2009. **48**(30): p. 5793-5801.
137. Rubin, M., K. Von Rottkay, and R. Powles, *Window optics.* Solar energy, 1998. **62**(3): p. 149-161.
138. Nitz, P., J. Ferber, R. Stangl, H.R. Wilson, and V. Wittwer, *Simulation of multiply scattering media.* Solar energy materials and solar cells, 1998. **54**(1-4): p. 297-307.
139. Lambda Research Corporation, *TracePro, Software for Opto-Mechanical Modeling, User's Manual.* 2020.
140. Ahmadi, S., N. Asim, M. Alghoul, F. Hammadi, K. Saeedfar, N.A. Ludin, S.H. Zaidi, and K. Sopian, *The role of physical techniques on the preparation of photoanodes for dye sensitized solar cells.* International Journal of Photoenergy, 2014. **2014**.
141. Chen, C.-C. and C.-C. Ting, *Photoelectrode fabrication of dye-sensitized nanosolar cells using multiple spray coating technique.* International Journal of Photoenergy, 2013. **2013**.
142. Xuan, Q., G. Li, Y. Lu, B. Zhao, X. Zhao, Y. Su, J. Ji, and G. Pei, *Overall detail comparison for a building integrated concentrating photovoltaic/daylighting system.* Energy and Buildings, 2019. **199**: p. 415-426.
143. Baig, H., H. Kanda, A.M. Asiri, M.K. Nazeeruddin, and T. Mallick, *Increasing efficiency of perovskite solar cells using low concentrating photovoltaic systems.* Sustainable Energy & Fuels, 2020.
144. Li, G., Y. Su, G. Pei, H. Zhou, X. Yu, J. Ji, and S. Riffat, *An outdoor experiment of a lens-walled compound parabolic concentrator photovoltaic module on a sunny day in Nottingham.* Journal of solar energy engineering, 2014. **136**(2).
145. Nilsson, J., *Optical Design and Characterization of Solar Concentrations for Photovoltaics*. 2005: Lund University Lund, Sweden.
146. BS EN 410:2011, *Glass in building – determination of luminous and solar characteristics of glazing. In: Determination of characteristics*. 2011.
147. Al-Khazzar, A.A.A., *Behavior of four Solar PV modules with temperature variation.* International Journal of Renewable Energy Research (IJRER), 2016. **6**(3): p. 1091-1099.
148. Gray, J.L., *The physics of the solar cell.* Handbook of photovoltaic science and engineering, 2003. **2**: p. 82-128.
149. Brano, V.L., A. Orioli, G. Ciulla, and A. Di Gangi, *An improved five-parameter model for photovoltaic modules.* Solar Energy Materials and Solar Cells, 2010. **94**(8): p. 1358-1370.
150. Audenaert, J., F.B. Leloup, B. Van Giel, G. Durinck, G. Deconinck, and P. Hanselaer, *Impact of the accurateness of bidirectional reflectance distribution function data on the intensity and luminance distributions of a light-emitting diode mixing chamber as obtained by simulations.* Optical Engineering, 2013. **52**(9): p. 095101.
151. Neuman, M. and P. Edström, *Anisotropic reflectance from turbid media. I. Theory.* JOSA A, 2010. **27**(5): p. 1032-1039.
152. Shenoy, M.R. and B.P. Pal, *Method to determine the optical properties of turbid media.* Applied optics, 2008. **47**(17): p. 3216-3220.
153. Correia, A., P. Hanselaer, H. Cornelissen, and Y. Meuret, *Radiance based method for accurate determination of volume scattering parameters using GPU-accelerated Monte Carlo.* Optics express, 2017. **25**(19): p. 22575-22586.
154. Hu, D., R. Lu, Y. Huang, Y. Ying, and X. Fu, *Effects of optical variables in a single integrating sphere system on estimation of scattering properties of turbid media.* Biosystems Engineering, 2020. **194**: p. 82-98.

155. Pickering, J.W., S.A. Prahl, N. Van Wieringen, J.F. Beek, H.J. Sterenborg, and M.J. Van Gemert, *Double-integrating-sphere system for measuring the optical properties of tissue.* Applied optics, 1993. **32**(4): p. 399-410.
156. Prahl, S.A., M.J. van Gemert, and A.J. Welch, *Determining the optical properties of turbid media by using the adding–doubling method.* Applied optics, 1993. **32**(4): p. 559-568.
157. Córreia, A., H. Cornelissen, S. Leyre, P. Hanselaer, and Y. Meuret, *Determination of volume scattering parameters that reproduce the luminance characteristics of diffusers.* Optics Express, 2016. **24**(11): p. 11727-11738.
158. Correia, A., P. Hanselaer, and Y. Meuret. *Accurate and robust characterization of volume scattering materials using the intensity-based inverse adding-doubling method*. in *Modeling Aspects in Optical Metrology VII*. 2019. International Society for Optics and Photonics.
159. Leyre, S., F.B. Leloup, J. Audenaert, G. Durinck, J. Hofkens, G. Deconinck, and P. Hanselaer, *Determination of the bulk scattering parameters of diffusing materials.* Applied optics, 2013. **52**(18): p. 4083-4090.
160. Sardar, D.K., B.G. Yust, F.J. Barrera, L.C. Mimun, and A.T. Tsin, *Optical absorption and scattering of bovine cornea, lens and retina in the visible region.* Lasers in medical science, 2009. **24**(6): p. 839-847.
161. Cen, H. and R. Lu, *Optimization of the hyperspectral imaging-based spatially-resolved system for measuring the optical properties of biological materials.* Optics express, 2010. **18**(16): p. 17412-17432.
162. Bellini, S., R. Bendoula, E. Latrille, and J.-M. Roger, *Potential of a spectroscopic measurement method using adding-doubling to retrieve the bulk optical properties of dense microalgal media.* Applied spectroscopy, 2014. **68**(10): p. 1154-1167.
163. Assadi, H., R. Karshafian, and A. Douplik, *Optical scattering properties of intralipid phantom in presence of encapsulated microbubbles.* International Journal of Photoenergy, 2014. **2014**.
164. Prahl, S., *Everything I think you should know about Inverse Adding-Doubling.* Oregon Medical Laser Center, St. Vincent Hospital, 2011: p. 1-74.
165. Rowe, P.I., R. Künnemeyer, A. McGlone, S. Talele, P. Martinsen, and R. Seelye, *Relationship between tissue firmness and optical properties of 'Royal Gala'apples from 400 to 1050 nm.* Postharvest biology and technology, 2014. **94**: p. 89-96.
166. Wang, W. and C. Li, *Measurement of the light absorption and scattering properties of onion skin and flesh at 633 nm.* Postharvest biology and technology, 2013. **86**: p. 494-501.
167. Ionescu, A., J. Cardona, I. Garzón, A. Oliveira, R. Ghinea, M. Alaminos, and M. Pérez, *Integrating-sphere measurements for determining optical properties of tissue-engineered oral mucosa.* Journal of the European Optical Society-Rapid publications, 2015. **10**.
168. Wróbel, M.S., A.P. Popov, A.V. Bykov, V.V. Tuchin, and M. Jędrzejewska-Szczerska, *Nanoparticle-free tissue-mimicking phantoms with intrinsic scattering.* Biomedical optics express, 2016. **7**(6): p. 2088-2094.
169. Leyre, S., Y. Meuret, G. Durinck, J. Hofkens, G. Deconinck, and P. Hanselaer, *Estimation of the effective phase function of bulk diffusing materials with the inverse adding-doubling method.* Applied optics, 2014. **53**(10): p. 2117-2125.
170. Xie, B., Y. Cheng, J. Hao, W. Shu, K. Wang, and X. Luo, *Precise optical modeling of quantum dots for white light-emitting diodes.* Scientific reports, 2017. **7**(1): p. 1-10.
171. Prahl, S.A., M.J.C. van Gemert, and A.J. Welch, *Determining the optical properties of turbid media by using the adding–doubling method.* Applied Optics, 1993. **32**(4): p. 559-568.
172. Prahl, S.A., *The adding-doubling method*, in *Optical-thermal response of laser-irradiated tissue*. 1995, Springer. p. 101-129.
173. Wróbel, M.S., A.P. Popov, A.V. Bykov, M. Kinnunen, M. Jędrzejewska-Szczerska, and V.V. Tuchin, *Measurements of fundamental properties of homogeneous tissue phantoms.* Journal of biomedical optics, 2015. **20**(4): p. 045004.

174. Rowe, R.C., P. Sheskey, and M. Quinn, *Handbook of pharmaceutical excipients*. 2009: Libros Digitales-Pharmaceutical Press.
175. Wüstenberg, T., *Cellulose and cellulose derivatives in the food industry: fundamentals and applications*. 2014: John Wiley & Sons.
176. Wang, J., C. Xu, A.M. Nilsson, D.L. Fernandes, M. Strömberg, J. Wang, and G.A. Niklasson, *General method for determining light scattering and absorption of nanoparticle composites.* Advanced Optical Materials, 2019. **7**(4): p. 1801315.
177. Fortin, S. and G. Charlet, *Phase diagram of aqueous solutions of (hydroxypropyl) cellulose.* Macromolecules, 1989. **22**(5): p. 2286-2292.
178. Varma, S., L. Bureau, and D. Débarre, *The conformation of thermoresponsive polymer brushes probed by optical reflectivity.* Langmuir, 2016. **32**(13): p. 3152-3163.
179. Wang, Q., L. Liu, Y. Wang, P. Liu, H. Jiang, Z. Xu, Z. Ma, S. Oren, E.K. Chow, and M. Lu, *Tunable optical nanoantennas incorporating bowtie nanoantenna arrays with stimuli-responsive polymer.* Scientific reports, 2015. **5**: p. 18567.
180. Gladen, A.C., J.H. Davidson, and S.C. Mantell, *Selection of thermotropic materials for overheat protection of polymer absorbers.* Solar Energy, 2014. **104**: p. 42-51.
181. Modest, M.F., *Radiative heat transfer*. 2013: Academic press.
182. Gueymard, C.A., *Spectral effects on the transmittance, solar heat gain, and performance rating of glazing systems.* Solar Energy, 2009. **83**(6): p. 940-953.
183. Mazhar, A., D.J. Cuccia, T.B. Rice, S.A. Carp, A.J. Durkin, D.A. Boas, B. Choi, and B.J. Tromberg, *Laser speckle imaging in the spatial frequency domain.* Biomedical optics express, 2011. **2**(6): p. 1553-1563.
184. Sellami, N. and T.K. Mallick, *Optical characterisation and optimisation of a static Window Integrated Concentrating Photovoltaic system.* Solar Energy, 2013. **91**: p. 273-282.
185. Weißenborn, E. and B. Braunschweig, *Hydroxypropyl cellulose as a green polymer for thermo-responsive aqueous foams.* Soft matter, 2019. **15**(13): p. 2876-2883.
186. Fischer, T., H.R. Holzbauer, and A. Seeboth, *Influence of inorganic salts on optical transmission behaviour of thermotropic hydrogels.* Materialwissenschaft und Werkstofftechnik: Entwicklung, Fertigung, Prüfung, Eigenschaften und Anwendungen technischer Werkstoffe, 1999. **30**(8): p. 473-477.
187. Nakamura, C., T. Yamamoto, K. Manabe, T. Nakamura, Y. Einaga, and S. Shiratori, *Thermoresponsive, Freezing-Resistant Smart Windows with Adjustable Transition Temperature Made from Hydroxypropyl Cellulose and Glycerol.* Industrial & Engineering Chemistry Research, 2019. **58**(16): p. 6424-6428.
188. Lu, X., Z. Hu, and J. Schwartz, *Phase transition behavior of hydroxypropylcellulose under interpolymer complexation with poly (acrylic acid).* Macromolecules, 2002. **35**(24): p. 9164-9168.
189. Wu, M., Y. Shi, R. Li, and P. Wang, *Spectrally selective smart window with high near-infrared light shielding and controllable visible light transmittance.* ACS applied materials & interfaces, 2018. **10**(46): p. 39819-39827.
190. Jain, K., R. Vedarajan, M. Watanabe, M. Ishikiriyama, and N. Matsumi, *Tunable LCST behavior of poly (N-isopropylacrylamide/ionic liquid) copolymers.* Polymer Chemistry, 2015. **6**(38): p. 6819-6825.
191. Joshi, S.C., *Sol-gel behavior of hydroxypropyl methylcellulose (HPMC) in ionic media including drug release.* Materials, 2011. **4**(10): p. 1861-1905.
192. Yao, R., J. Xu, X. Lu, and S. Deng, *Phase transition behavior of HPMC-AA and preparation of HPMC-PAA nanogels.* Journal of Nanomaterials, 2011. **2011**.
193. Quantum Northwest, *User Manual of Qpod-2e: Temperature-Controlled Sample Compartment for Fiber Optic Spectroscopy*.
194. Seeboth, A. and D. Lötzsch, *Thermochromic and thermotropic materials*. 2013: Jenny Stanford Publishing.

195. Wirth, H., *Crystalline silicon PV module technology*, in *Semiconductors and Semimetals*. 2013, Elsevier. p. 135-197.
196. Kolokotroni, M. and R. Giridharan, *Urban heat island intensity in London: An investigation of the impact of physical characteristics on changes in outdoor air temperature during summer.* Solar Energy, 2008. **82**(11): p. 986-998.
197. Warwick, M.E., I. Ridley, and R. Binions, *The effect of variation in the transition hysteresis width and gradient in thermochromic glazing systems.* Solar Energy Materials and Solar Cells, 2015. **140**: p. 253-265.
198. Butcher, K.J., *CIBSE Guide B - Heating, Ventilating, Air Conditioning and Refrigeration*. CIBSE.
199. American Society of Heating Refrigerating and Air Conditioning Engineers, *ANSI/ASHRAE Standard 55-2013: Thermal Environmental Conditions for Human Occupancy*. 2013, ASHRAE: New York.
200. ISO 10077-1:2006, *Thermal performance of windows, doors and shutters — Calculation of thermal transmittance — Part 1: General.* 2006.
201. ISO 9050, *Glass in Building-Determination of Light Transmittance, Solar Direct Transmittance, Total Solar Energy Transmittance, Ultraviolet Transmittance and Related Glazing Factors.* 2003.
202. Sun, Y., K. Shanks, H. Baig, W. Zhang, X. Hao, Y. Li, B. He, R. Wilson, H. Liu, and S. Sundaram, *Integrated semi-transparent cadmium telluride photovoltaic glazing into windows: Energy and daylight performance for different architecture designs.* Applied energy, 2018. **231**: p. 972-984.
203. Lawrence Berkeley National Laboratory. *IGDB Database Detailed Installation / Update Instructions*. 2019 [cited 2021. 3.31]; Available from: https://windows.lbl.gov/tools/knowledge-base/articles/igdb-database-detailed-installation-update-instructions.
204. Liang, R., *Development of an adaptive façade for visual comfort, daylight and thermal control element, PhD Thesis*. 2018, University of Nottingham, UK.
205. Liang, R., D. Liu, Y. Sun, X. Luo, D. Grant, G. Walker, and Y. Wu. *Investigation of Mg-Y coated gasochromic smart windows for building applications*. in *Building Simulation*. 2019. Springer.
206. Ye, H., L. Long, H. Zhang, B. Xu, Y. Gao, L. Kang, and Z. Chen, *The demonstration and simulation of the application performance of the vanadium dioxide single glazing.* Solar Energy Materials and Solar Cells, 2013. **117**: p. 168-173.
207. U.S. Department of Energy. *EnergyPlus™ Version 9.5.0 Documentation, Engineering Reference*. 2021 [cited 2021. 3.31]; Available from: https://energyplus.net/assets/nrel_custom/pdfs/pdfs_v9.5.0/EngineeringReference.pdf.
208. Kalogirou, S.A., *Solar energy engineering: processes and systems*. 2013: Academic Press.
209. Duffie, J.A. and W.A. Beckman, *Solar engineering of thermal processes*. 2013: John Wiley & Sons.
210. Ministry of Housing Communities & Local Government, *Approved Document L2A: conservation of fuel and power in new buildings other than dwellings, 2013 edition with 2016 amendments*. 2016.
211. Korolija, I., L. Marjanovic-Halburd, Y. Zhang, and V.I. Hanby, *UK office buildings archetypal model as methodological approach in development of regression models for predicting building energy consumption from heating and cooling demands.* Energy and Buildings, 2013. **60**: p. 152-162.
212. Sun, Y., D. Liu, J.-F. Flor, K. Shank, H. Baig, R. Wilson, H. Liu, S. Sundaram, T.K. Mallick, and Y. Wu, *Analysis of the daylight performance of window integrated photovoltaics systems.* Renewable Energy, 2020. **145**: p. 153-163.
213. Gladen, A., S. Mantell, and J. Davidson, *Numerical Evaluation of the Optical Properties of Encapsulated Phase Change Particles for Thermotropic Materials.* Journal of Thermal Science and Engineering Applications, 2015. **7**(3): p. 031002.

214. Sun, Y., R. Liang, Y. Wu, R. Wilson, and P. Rutherford, *Development of a comprehensive method to analyse glazing systems with Parallel Slat Transparent Insulation material (PS-TIM).* Applied Energy, 2017. **205**: p. 951-963.